Micro-Mechanics of Irradiated Fe-Cr Alloys for Fusion Reactors

Christopher David Hardie
University of Oxford

Supervised by Prof S.G. Roberts and Prof S. Dudarev

EPSRC
Engineering and Physical Sciences Research Council

OxfordMaterials

CCFE
CULHAM CENTRE FOR FUSION ENERGY

PREFACE

This thesis describes work carried out by the author in the Department of Materials, University of Oxford from October 2009 to September 2013. This project was supervised by Prof. S.G. Roberts and Prof. S. Dudarev and was jointly funded by the Engineering and Physical Sciences Council (EPSRC) and Culham Centre for Fusion Energy (CCFE) in the form of an industrial CASE Studentship.

No part of this thesis has been previously submitted for a degree at this or any other university. The work of other authors has been drawn upon and has been referenced and acknowledged in the text. A list of references has been given at the end of this thesis.

The following papers report on work conducted as part of this thesis:

C.D. Hardie, C.A. Williams, S. Xu, S.G. Roberts, Effects of irradiation temperature and dose rate on the mechanical properties of self-ion implanted Fe and Fe–Cr alloys, J. Nucl. Mater. 439 (2013) 33-40.

C.D. Hardie, S.G. Roberts, Nanoindentation of model Fe–Cr alloys with self-ion irradiation, J. Nucl. Mater. 433 (2013) 174-179.

C.D. Hardie, S.G. Roberts, A.J. Bushby, Mechanical Behavior of Ion-Irradiated Fe-Cr Alloys Investigated by Spherical Indentation, Proc MRS. 1424 (2012).

A.J. Bushby, S.G. Roberts, C.D. Hardie, Nanoindentation investigation of ion-irradiated Fe–Cr alloys using spherical indenters, Journal of Materials Research (2011).

ABSTRACT

In the absence of a fusion neutron source, research on the structural integrity of materials in the fusion environment relies on current fission data and simulation methods. Through investigation of the Fe-Cr system, this detailed study explores the challenges and limitations in the use of currently available radiation sources for fusion materials research.

An investigation of ion-irradiated Fe12%Cr using nanoindentation with a cube corner, Berkovich and spherical tip, and micro-cantilever testing with two different geometries, highlighted that the measurement of irradiation hardening was largely dependent on the type of test used. Selected methods were used for the comparison of Fe6%Cr irradiated by ions and neutrons to a dose of 1.7dpa at a temperature of 288°C. Micro-cantilever tests of the Fe6%Cr alloy with beam depths of 400 to 7000nm, identified that size effects may significantly obscure irradiation hardening and that these effects are dependent on radiation conditions. Irradiation hardening in the neutron-irradiated alloy was approximately double that of the ion-irradiated alloy and exhibited increased work hardening. Similar differences in hardening were observed in an Fe5%Cr alloy after ion-irradiation to a dose of 0.6dpa at 400°C and doses rates of 6 x 10^{-4}dpa/s and 3 x 10^{-5}dpa/s. Identified by APT, it was shown that increased irradiation hardening was likely to be caused by the enhanced segregation of Cr observed in the alloy irradiated with the lower dose rate.

These observations have significant implications for future fusion materials research in terms of the simulation of fusion relevant radiation conditions and micro-mechanical testing.

ACKNOWLEDGEMENTS

First and foremost, I would like to thank my supervisor, Steve Roberts for providing me with such an amazing opportunity and allowing me a large amount of independence, even though it meant learning the hard way occasionally. I am highly grateful to my supervisor, Sergei Dudarev at CCFE, who has always shown great interest in my work and contributed with useful discussions.

I would also like to thank collaborators (in order of appearance) Andy Bushby (QMUL), Ed Tarleton, Bob Odette (UCSB), Ceri Williams and Shuo Xu for their assistance with work and provision of data (these are acknowledged and referenced in the text).

I thank staff at the Centre for Advanced Energy Studies (CAES) in Idaho Falls (US) for providing the 'hot' FIB facility and all the gallium in it!

Many thanks to Nianhua Peng and Adrian Cansell at the Surrey Ion Beam Centre, and Shavkat Akhmadaliev at the Rossendorf Ion Beam Center (HZDR) for their assistance with ion implantation and their understanding when asked (probably for the first time) to go as slow as possible!

My DPhil friends in the years below deserve a mention for keeping me youthful, cynical and well watered: Christian Beck, Chris Burrows, Mike Gorley, Ele Grieveson, James Herring, Katie Plumber and Sean Yardley.

Finally a special thanks to my parents for turning a blind eye when I packed my bags for university once again and my girlfriend Sarah for your support and actually listening to me for hours about materials science; you would certainly pass the materials science prelims now.

GLOSSARY OF ABREVIATIONS

AFM	Atomic Force Microscopy
appm	Atomic Parts Per Million
APT	Atom Probe Tomography
ASTM	American Society for Testing and Materials
ATR	Advanced Test Reactor
BCC	Body Centred Cubic
CAES	Centre for Advanced Energy Studies
CALPHAD	Computing Coupling of Phase Diagrams and Thermochemistry
CCFE	Culham Centre for Fusion Energy
CLAM	Chinese Low Activation Martensitic
CMCO	Cambridge Metals, Crystals and Oxides
CSIRO	Commonwealth Scientific and Industrial Research Organisation
CSM	Continuous Stiffness Measurement
CVI	Chemical Vapour Infiltration
DBTT	Ductile-Brittle Transition Temperature
DD	Dislocation Dynamics
DEMO	DEMOnstration Reactor
DFT	Density Functional Theory
DOE	Department of Energy
dpa	Displacements Per Atom
D-T	Deuterium-Tritium
EBSD	Electron Backscattered Diffraction
EDX	Energy-Dispersive X-ray Spectroscopy
EFDA	European Fusion Development Agreement
ENS	Early Neutron Source
EU	European Union
F/M	Ferritic/Martensitic
FCC	Face Centred Cubic
FEA	Finite Element Analysis
FEM	Finite Element Modelling
FEPA	Federation of the European Producers of Abrasives

FFTF	Fast Flux Test Facility
FIB	Focused Ion Beam
GND	Geometrically Necessary Dislocation
HD	High Dose
HDR	High Dose Rate
HFIR	High Flux Isotope Reactor
HFR	High Flux Reactor, Netherlands
HZDR	Helmholtz Zentrum Dresden Rossendorf
IFMIF	International Fusion Materials Irradiation Facility
INL	Idaho National Laboratories
ISE	Indentation Size Effect
ISO	International Organisation for Standardisation
JET	Joint European Torus
KBF	Kinematical Bright-Field
KMC	Kinetic Monte Carlo
LD	Low Dose
LDR	Low Dose Rate
LEAP	Local-Electrode Atom-Probe
LVDT	Linear Variable Differential Transducers
MD	Molecular Dynamics
MD	Medium Dose
MRF	Materials Research Facility
NRT	Norgett, Robinson and Torrens
ODS	Oxide Dispersion Strengthened
PID	Proportional-Integral-Derivative
PKA	Primary Knock On Atom
QMUL	Queen Mary's University, London
RAF	Reduced Activation Ferritic
RAFM	Reduced Activation Ferritic/Martensitic
RIS	Radiation Induced Segregation
RNTS-II	Rotating Target Neutron Source
RPV	Reactor Pressure Vessel
SANS	Small Angle Neutron Scattering

SEM	Scanning Electron Microscopy
SIA	Self-Interstitial Atom
SNS	Spallation Neutron Source
SRIM	Stopping Range of Ions in Matter
SRO	Short Range Ordering
SSTT	Small Specimen Test Technology
TEM	Transmission Electron Microscopy
UCSB	University of California, Santa Barbara
UHP	Ultra High Purity
UMIS	Ultra Micro Indentation System
USE	Upper Shelf Energy

TABLE OF SYMBOLS

Q	Reactor Efficiency
n_e	Electron Density
T_e	Energy Confinement Time
E_p	Collision Energy of Transfer
E_d	Atomic Displacement Energy
υ	Number of Displacements
T	PKA Energy
N	Atomic Density
E_i	Incident Particle Energy
$\phi(E_i)$	Energy-Dependent Particle Flux
$\sigma_D(E_i)$	Energy-Dependent Displacement Cross-section
$\sigma(E_i, T)$	Probability of Incident Particle of Energy E_i imparting an energy T onto a Target Atom
c'	Shear Stiffness Constant
σ_t	Thermal Component of Flow Stress
σ_a	Athermal Component of Flow Stress
σ_y	Yield Stress
G	Shear Modulus
b	Burgers Vector
l_d	Defect Spacing
α	Obstacle Strength
n	Work Hardening Coefficient
ϕ	Ion Fluence
P	Load on Sample
P_{raw}	Raw Load
P_0	Raw Load at Surface
h_{raw}	Raw Displacement
h_0	Displacement at Sample Surface
K_s	Spring Stiffness
h_c	Displacement into Sample Surface
Q	Measured Thermal Drift

K_f	Frame Stiffness
S	Stiffness
P_t	Peak Load
h_t	Displacement at Peak Load
h_r	Final Displacement After Unloading
E_r	Reduced Modulus
A	Contact Area
ν	Poisson's Ratio
E	Elastic Modulus
H	Hardness
C	System Compliance
D	Damping Coefficient
ω	Frequency of Oscillation
m	Mass of Indenter Column
ϕ	Phase Angle
P_i	Load at Increment i
h_m	Measured Displacement
h_i	Displacement at Increment i
R	Tip Radius
P_s	Load at Unload
δ	Elastic Component of Indenter Displacement
R'	Radius of Curvature of Indent Impression
a	Radius of Contact Area
η	Dimension Perpendicular to Tilt Axis
z	Dimension Orthogonal to Imaging Plane
y	Vertical Measured Distance
d	Working Distance
ϕ	Tilt Angle
I	Second Moment of Area
R	Radius of Curvature
M	Bending Moment
M	Maximum Perpendicular Distance from Neutral Axis
w	Beam Width

h	Beam Height
ε_{max}	Maximum Plane Strain
δ	Beam Displacement
l	Beam Length
σ_{max}	Maximum Stress
U	Translational Degree of Freedom
R	Rotational Degree of Freedom
n_{TOTAL}	Number of Match Points
$h_{plastic}$	Plastic Displacement
$\varepsilon_{plastic}$	Plastic Strain
A_{actual}	Actual Measured Contact Area
A_{cc}	Contact Area Measured Between Indent Corners
P_{os}	Oscillating Load
τ_n	Activation Stress for Dislocation Nucleation
τ	Resolved Shear Stress
σ_{proof}	Proof Stress
A_1	Fitted Asymptotic Value of Proof Stress
ρ_{GND}	Density of Geometrically Necessary Dislocations
σ_{PU}	Contribution of Stress Caused by Dislocation Pile-Up at the Neutral Axis
ω	Beam Bending Angle
x	Size of Plastic Zone
λ	Dislocation Source Spacing

CONTENTS

1 INTRODUCTION

By 2050 there will be approximately 10-11 billion people living on the planet [1], the global demand for energy will have more than doubled (approaching 30TWY) and the fossil fuel reserves, which currently supply ~80% of this demand, will have depleted [2]. During this time, increasing atmospheric levels of CO_2 are forecast and will continue to cause deleterious effects on the global climate [3]. This was recognised by the UK who committed to the world's first legally binding long-term framework for cutting carbon emissions, known as the 'Climate Change Act 2008' [4]. Yet, evidence of positive action to deliver this framework is scarce. A recent report from the UK regulatory body Ofgem (Office of Gas and Electricity Markets) highlights the decline in UK electricity production capacity and the risk of power shortages in the near future (~3 to 4 years) [5].

Fusion power generation would be safe, produces no harmful greenhouse gases, produces no long lived radioactive waste and uses an abundant fuel source capable of supplying energy for millions of years. Unfortunately, sustained nuclear fusion is very hard to achieve. The most promising reaction for creating energy on earth is between two heavy isotopes of hydrogen, deuterium (D) and tritium (T) [6]:

$$D + T => {}^{4}He\ (3.56MeV) + Neutron\ (14.03MeV) \qquad \boldsymbol{equation\ 1.1}$$

This reaction requires plasma temperatures to reach of over 100 million degrees Kelvin, held by magnets in a torus shaped chamber known as a tokamak [7]. Lithium is the envisaged fuel to supply the Tritium fuel by the reaction [8]:

$$^{6}Li + n => \ ^{4}He\ (2.1MeV) + T(2.7MeV) \qquad \boldsymbol{equation\ 1.2}$$

With the prospect of Li extraction from sea water, the fuel supply for future fusion nuclear reactors is virtually unlimited [8].

In 1997 the Joint European Torus (JET) reactor achieved the current world record for fusion power generation by producing 16MW of electricity [9] and a gain Q (Power out/Power in) of 0.65. Currently in construction in Cadarache, France, a device called ITER will provide the next step in fusion research by producing roughly 500MW of output power with less than 50MW of input power, $Q{\sim}10$ [7]. Despite some doubts (for example see ref. [10]), this collaboration between seven partners (Japan, US, South Korea, China, the European Union, India and Russia) follows a consistent progression towards a commercial power plant (*figure 1.1*) [7].

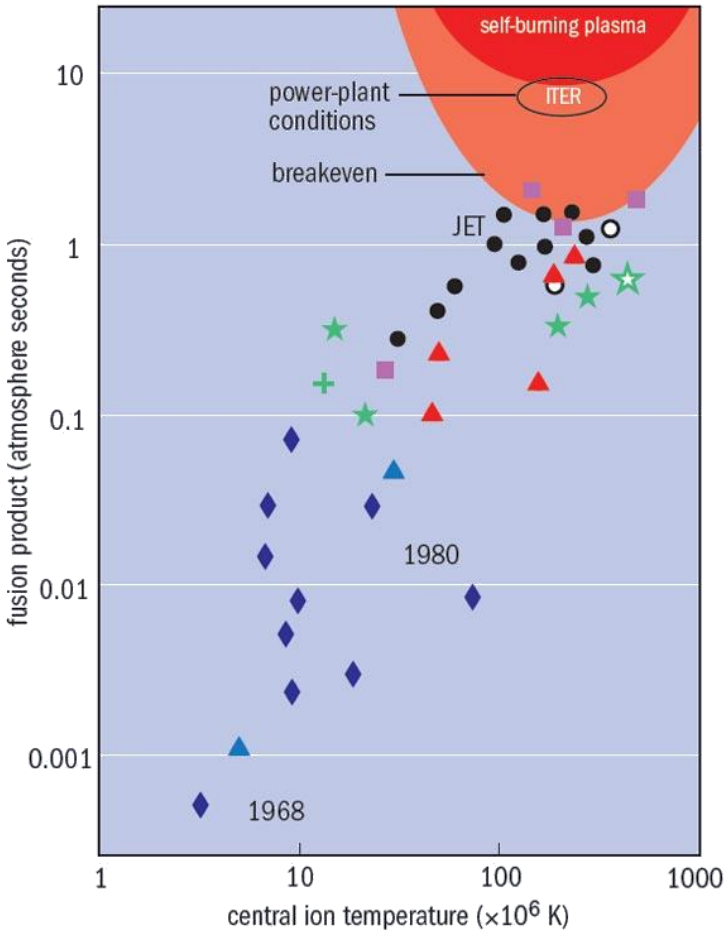

Figure 1.1 - The progress of fusion product[1] vs. temperature for several experimental fusion reactors in the past 50 years. Prediction for ITER is shown in the breakeven region (*Q*>1) [7].

As the science behind nuclear fusion progresses towards technical feasibility, the commercial success of nuclear fusion power generation is becoming increasingly dependent on the development of low-activation materials to withstand the extreme environments within the reactor [11, 12]. The structural materials used will not only play a significant role

[1] The fusion product or Lawson criterion is a measure of plasma conditions for fusion reactions. It is the product of plasma (electron) density (n_e) and energy confinement time (T_e)

in the safety and environmental impact of a fusion reactor, they will also determine operating temperature ranges and downtime required for maintenance/replacement, and thus influence the efficiency and economics of fusion power generation [12].

The work reported in this thesis investigates the use of ion implantation and micron scale testing techniques for the investigation of materials for fusion applications. The first ever direct comparison of ion and neutron irradiation indicates the characteristics of both radiation sources and how irradiated materials plastically deform in micro-scale testing volumes. Accounting for the challenges and limitations discovered with these techniques, *chapter 7* reports on a systematic study investigating irradiation temperature, dose and dose rate on Fe and Fe-Cr alloys. This provides an insight into the role of Cr during irradiation and the mechanisms which control the degradation of mechanical properties commonly observed in steel during operation within a reactor.

2 LITERATURE REVIEW

2.1 Research Context

2.1.1 The Fusion Environment

The structural components within the first wall and divertor with expected lifetimes are shown in *figure 2.1* [13]; these will be subject to large heat loads (up to 20MW/m^2), high-energy 14MeV neutrons, low energy plasma particles and electromagnetic radiation.

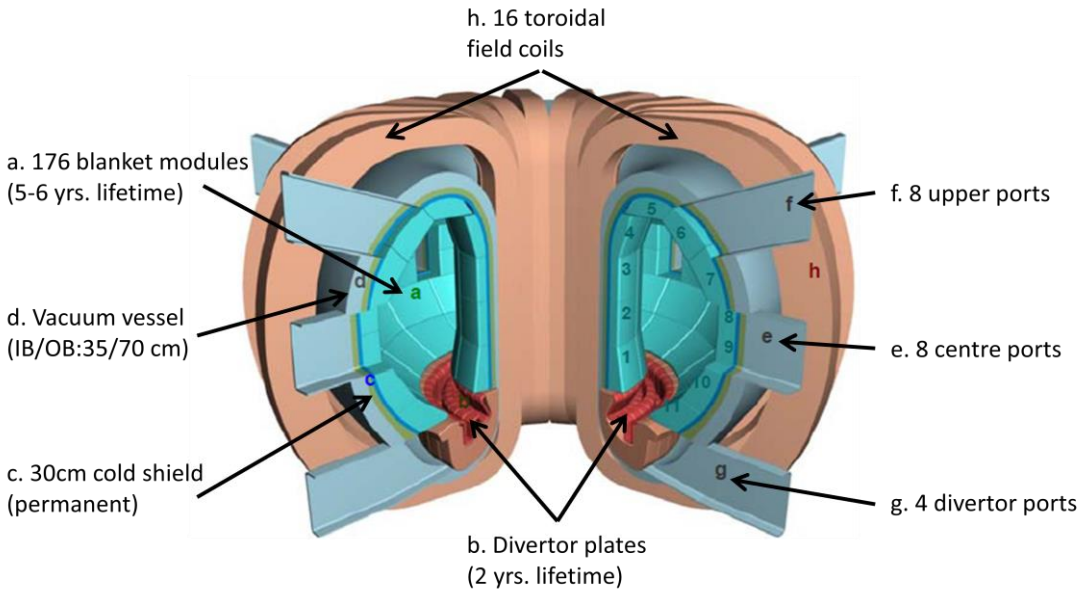

Figure 2.1 – Schematic of future commercial fusion reactor. Redrawn from ref. [13].

This severe radiation environment results in a number of materials-related problems; these problems have been summarised by Schiller [14] in *table 2.1*. In addition to the radiological, thermophysical and strength properties of materials, attention must be given to corrosion and compatibility issues, for example with reactor coolant, and to technical maturity such as fabrication and welding techniques [15].

Table 2.1 – Main materials related problems resulting from the severe radiation environment of a fusion reactor [14].

Component	Plasma interaction	Consequences
First wall and divertor	Sputter erosion	Plasma contamination Reduction of thickness Tritium permeation
	Heat load pulses	Thermal stresses Thermal fatigue
	Neutron flux	Hardening Embrittlement Swelling Radiation creep Activation Creep-fatigue interaction
	Disruptions	Surface melting and Evaporation Reduction in thickness Thermal shocks
Blanket structure	Heat load γ-heating	Thermal stresses
	Neutron flux	Hardening Embrittlement Swelling Radiation creep Activation Tritium permeation
Blanket solid breeder	Neutrons Radiation sintering	Swelling Tritium permeation Activation
	Heat load γ-heating	Thermal stresses
Shield	Low neutron fluence γ-heating	Radiation damage Activation
Insulators	Neutron flux	Change in resistivity Swelling
Optical windows	Neutron flux	Change in transmission

2.1.2 Radiation Damage

The effects of radiation concern many disciplines in science such as Biology, Medical Science, Astronomy and Nuclear Physics. In the present context the term ‘radiation damage’ refers to the changes produced in crystalline lattices resulting from the exposure to radiation in the form of energetic particles. In this review, the majority of attention is given to the radiation-induced physical and chemical defects in metals with special reference to ferritic alloys,

which result in the degradation of the mechanical properties required for application within a fusion environment.

Radiation damage is the product of energetic collisions between incident particles and target atoms which form the bulk of a material. If the transfer of energy (E_p) in a collision is above the displacement energy (E_d), the target atom is displaced from its lattice site [16]. The first target atom which is displaced by a collision with an incident particle is known as a primary knock on atom or PKA. This PKA may then transfer its energy by further collisions, displacing lattice atoms until its energy falls below the displacement energy (E_d). The result of this interaction between the incident particle, PKA and subsequent target atoms is a displacement cascade of self-interstitial atoms (SIA) with a vacancy-rich core [17-19]. The number of displacements, υ, as a function of PKA energy, T, can be described by the model of Kinchin and Pease [20] as defined in *equation 2.1* and shown in *figure 2.2*.

$$\upsilon(T) = \begin{cases} 0 \ for\ T < E_d \\ 1 \ for\ E_d < T < 2E_d \\ \frac{T}{2E_d} \ for\ 2E_d < T < E_c \\ \frac{E_c}{2E_d} \ for\ T \geq E_c \end{cases} \qquad \boldsymbol{equation\ 2.1}$$

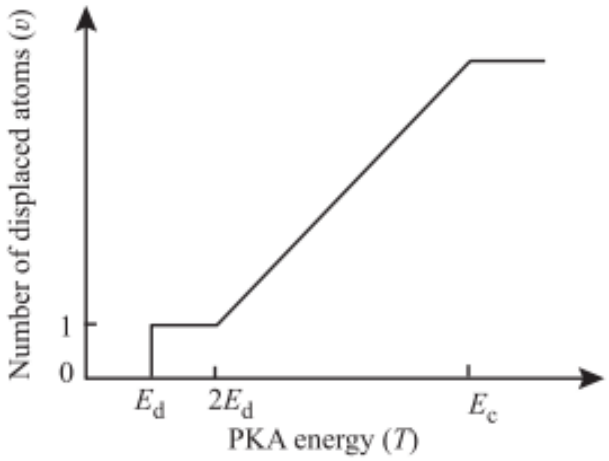

Figure 2.2 - The number of displaced atoms as a function of the PKA energy according to the model of Kinchin and Pease (graph taken from ref. [21]).

The international standard for quantifying the magnitude of displacement damage is 'displacements per atom' (dpa) [22]; that is the number of displacements per unit volume divided by the atomic density, N. For example, a single displacement of every atom from their lattice site in a given volume of target material corresponds to 1dpa.

Displacement damage can be quantified by the damage rate equation [21]:

$$R_d = N \int_{\check{E}}^{\hat{E}} \phi(E_i)\sigma_D(E_i)dE_i \qquad \textbf{equation 2.2}$$

where $\phi(E_i)$ is the energy-dependent particle flux and $\sigma_D(E_i)$ is the energy-dependent displacement cross-section. The displacement cross-section is a probability for the displacement of lattice atoms for each collision event producing a PKA of energy T:

$$\sigma_D(E_i) = \int_{\check{T}}^{\hat{T}} \sigma(E_i, T)\upsilon(T)dT \qquad \textbf{equation 2.3}$$

where $\sigma(E_i, T)$ is the probability that a particle of energy E_i will impart a PKA energy T to a target atom, and $\upsilon(T)$ is the number of displacements produced as defined using the Kinchin and Pease model in *equation 2.1*.

These parameters are discussed in more detail in *section 2.3* and are used for damage calculations in *chapter 6*. As shown in *table 2.1*, the production of displacement point

defects during irradiation can cause dimensional instability such as swelling and creep and degradation of mechanical properties such as hardening and embrittlement. These problems are limiting factors for the operational lifetime and efficiency of a reactor, thus they are briefly described below.

Dimensional Instability

Volume and shape changes can occur as a result of irradiation induced swelling, shrinkage, growth and creep mechanisms. Volume changes are the result of surface erosion, the production of phases with a different density to that of the parent matrix and, more commonly, void formation due to vacancy clustering (light areas shown in *figure 2.3* [23]). Irradiation creep is the enhancement of stress-directed thermal creep due to the constant supply of point defects during displacement damage. Swelling and creep are generally treated together, as both are driven by the same point defect concentrations [24]. In addition to point defect concentrations, transmutation gases, particularly helium, have been found to enhance swelling by enhancing cavity formation [25].

Dimensional instability of materials used within a fusion reactor can have serious consequences to safety and component lifetime. Swelling and creep of components may change engineered dimensions beyond original tolerances and cause the build-up or relief of stresses in components, bolts and clamps. Creep also limits the maximum operating temperature of a material, which reduces reactor efficiency.

Hardening and Embrittlement

During irradiation, the majority of point defects rapidly annihilate with one another; however many migrate within the bulk and can form extended structures such as dislocation loops, voids and clusters (*figure 2.3*) [23, 24]. This produces a population of dislocation loops, which act as obstacles to dislocation glide and cause the material to harden in a similar manner to work hardening. A heightened concentration of mobile defects enhances diffusion, causing radiation induced segregation (RIS) [26, 27], resulting in the segregation of alloying elements to sinks such as grain boundaries, free surfaces and dislocations; in some cases this may cause phase transformation or precipitation.

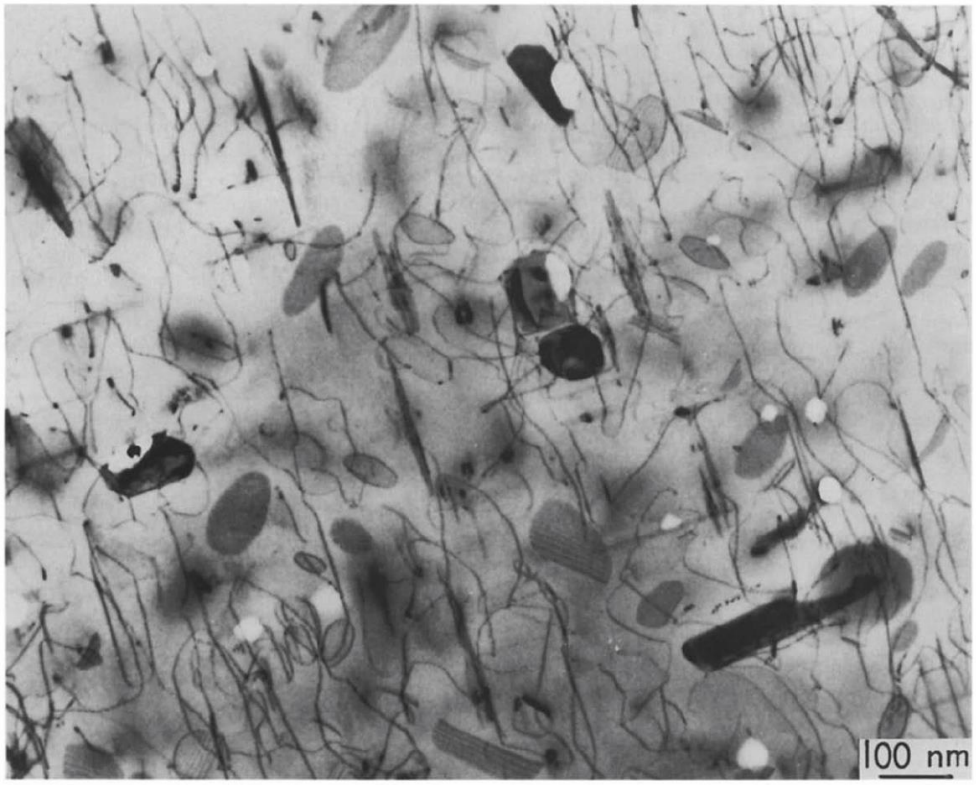

Figure 2.3 – Transmission electron image of a 300 series stainless steel irradiated at 500˚C to a dose of 10dpa [23], showing dislocation loops, voids (light areas) and clusters (black spots).

In addition to the introduction of new phases, entirely new elements may be introduced in the material matrix as a result of transmutation processes. The combination of relatively high energy and nuclear stopping interaction of fusion neutrons, gives rise to a number of inelastic nuclear events. These inelastic events are responsible for the introduction of gaseous transmutation products within the matrix, namely hydrogen and helium, which agglomerate with surviving point defects [28]. The expected concentration of H and He in candidate structural materials after 5 years exposure in a typical first wall environment of a fusion reactor is shown in table 2.2 [29]. H and He are highly insoluble in many materials, causing void and bubble formation in the matrix and at grain boundaries [30].

Table 2.2 – Concentration of transmutation products H and He after 5 years (appm) (data taken from [29]).

	W	**V**	**Fe-9%Cr**	**SiC (50%Si-50%C)**
H	76.3	2580	4920	4250
He	33.6	363	1060	11300

The combined effects of hardening, void formation and gas bubbles results in the embrittlement of several materials, identified by an increase in Ductile to Brittle Transition Temperature (DBTT) in Charpy V-notch tests [15, 31] or a decrease in ductility [32].

2.1.3 Candidate Materials

Currently, three candidate structural material types are under development based on vanadium alloys (V-Cr-Ti), silicon carbide composites (SiC/SiC) and 8-9%Cr ferritic/martensitic steels [11]. These materials, termed 'reduced activation materials', have been developed from the limited number of elements available (see [33]), which will produce acceptable levels of decay heat (for example, during maintenance or loss of coolant accidents) and lower the total level of radioactive waste on component replacement and decommissioning [34].

Radiological Properties

As shown in *table 2.1*, reactor materials are also susceptible to induced activation. In a fusion environment, the energetic 14MeV neutrons interact with the structural materials through elastic collisions, and in comparison to lower energy fission neutrons more frequently through inelastic nuclear events/absorption [15], resulting in transmutation processes (discussed above) and induced activation. In contrast to fission, radioactivity in a fusion reactor is not an inherent product of the fusion reaction itself except for the activity of tritium fuel with a half-life of 12.38 years [35]. In order to maintain the 'non-radioactive waste' appeal of a fusion power plant, all materials (including the coolant, tritium breeder and structural materials) must be made from elements which produce acceptable levels of induced activity caused by transmutation processes [36].

In 1982, the Office of Fusion Energy of the U.S. Department of Energy (DOE) identified three areas for consideration which are strongly influenced by neutron activation. These are [37]:

(i) Long-term management of activated reactor materials after removal from the reactor;

(ii) Hands on contact reactor maintenance (within a reasonably short time after shut down);

(iii) Reactor safety in the case of a severe accident.

It was therefore agreed that the target for low activation materials in fusion power plants is that they are compliant with US DOE Class C waste conditions [37]; they must decay to a low level of radioactivity, equal to or less than the radioactivity of natural uranium, ~25kBq/g [38], within 100 to 500 years.

Vanadium Alloys

Vanadium alloys, particularly the V-Cr-Ti system with principal reference composition V-4%Cr-4%Ti [39], are currently being developed due to attractive thermal properties and swelling resistance [40]. The combination of high thermal conductivity, low thermal expansion and high creep strength permits their operation at temperatures up to ~700˚C, providing a relatively high thermal efficiency which is desirable in a fusion reactor.

Despite such promising characteristics little data exists regarding low temperature hardening and high temperature embrittlement. Initial tensile test results of V-4%Cr-4%Ti show a significant increase in yield stress after exposure to doses as little as 0.1dpa, which approaches nearly a 500% increase after 4-6dpa, above which dose hardening saturation occurs [41]. In addition to low temperature irradiation hardening, the high solubility of interstitial elements such as C, O and H can lead to an increase in strength and loss of

ductility causing cleavage or intergranular fracture, even in the absence of irradiation [42]. This highlights a number of restrictions on the use of certain coolants, notably the use of liquid He and raises concerns regarding the alloy's response to predicted levels of transmutation gases He and H (shown in *table 2.2* [29]). If liquid metal coolants such as Li are to be used, development of an electrically insulating coating is required to reduce possible corrosion and large scale pressure drops in coolant channels associated with magnetohydrodynamic forces [11].

The dependence of mechanical integrity on the impurity content in vanadium alloys leads to important requirements involving the purity of the alloys in fabrication and joining, particularly on an industrial scale. Two large heats of 500kg and 1200kg have been successfully melted and fabricated with similar impurity contents to smaller scale (15kg) laboratory heats [41]. Gas tungsten arc full-penetration welds of V-4%Cr-4%Ti have also been successfully demonstrated without the need for post-weld heat treatment; however, control of strict atmospheric conditions was required [43].

SiC/SiC$_f$ Silicon Carbide Composites

The use of ceramic materials in the design of a fusion reactor was first proposed by Hopkins and Price in 1985 [44], by virtue of the very low induced radioactivity of ceramics during service [34, 45, 46]. However, silicon carbide fibre-reinforced silicon carbide (SiC/SiC$_f$) has a low activation because it has a small cross-section for interaction with neutrons. This enhances neutron penetration and produces a larger volume of active material in comparison to materials with a higher neutron cross-section [47].

SiC/SiC_f composites are under development as a candidate due to their high temperature creep strength and corrosion resistance [48]. SiC/SiC_f composites maintain acceptable mechanical strength at temperatures up to 1000˚C, however, thermal conductivity is decreased considerably as a result of void formation during irradiation [48]. This decrease, shown in *figure 2.4*, reduces the composite's power density capability to far below that of V alloy and F/M steel candidates [15].

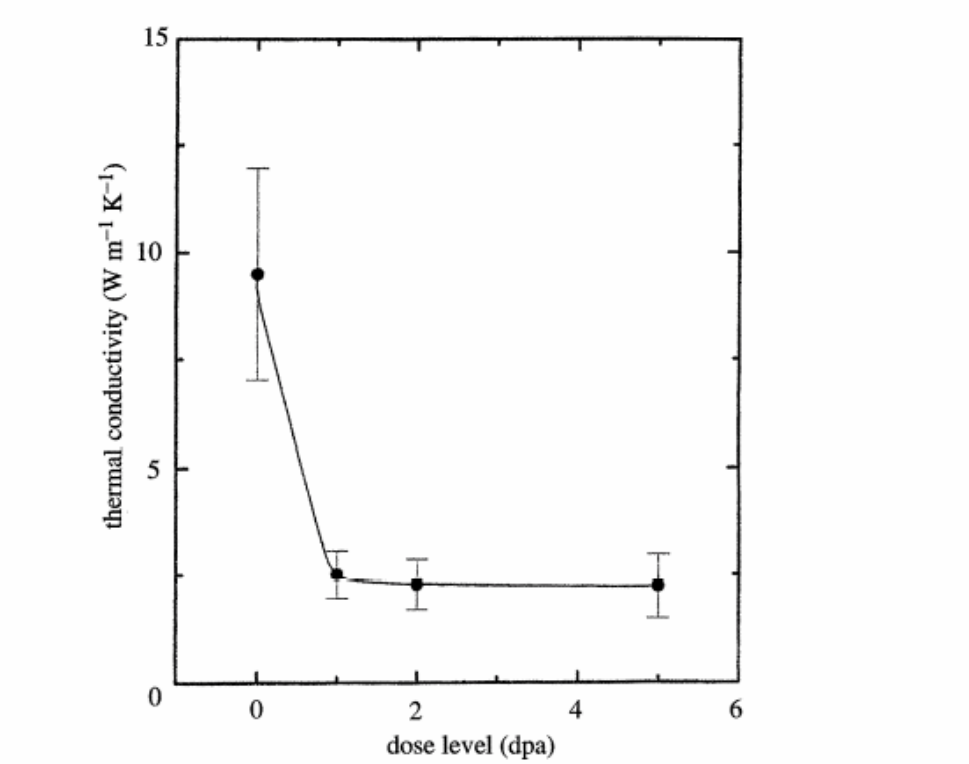

Figure 2.4 – Thermal conductivity of a SiC composite vs. displacement damage ([48] as cited in [15]).

The high strength of SiC/SiC_f composites has been found to decrease dramatically in the presence of He. Hasegawa et al. [49] demonstrated a reduction in strength up to 20% in some composites after He implantations to concentrations as little as 150 – 170 appm. The large cross-sections for in-elastic (n, α) processes in Si causes He concentrations an order of

magnitude larger than that of V-alloys and F/M steels (see *table 2.2*). Thus, reductions in strength at relatively small He concentrations observed by Hasegawa et al. [49], are a major concern when considering He concentrations after extended durations in a fusion reactor. The mechanical properties and dimensional stability in SiC composites are critically dependent on differing rates of swelling/densification of each constituent and the integrity of interfaces between them [48].

SiC/SiC_f composites are synthesised using a chemical vapour infiltration (CVI) method, which provides a gas permeable structure with ~10% void volume fraction, requiring the use of a hermetic sealant [50]. Further development is required to demonstrate large scale manufacture and joining methods.

Ferritic Steels

Ferritic steels are preferred over FCC stainless steels used in fission reactors, due to superior swelling resistance observed under irradiation [51, 52], for example, these steels have been found to exhibit swelling below 2% over the entire temperature range to doses up to 200dpa in the fast flux test facility (FFTF) [53]. However, little is known regarding potential increases in swelling caused by the He and H produced by transmutation reactions from 14 MeV fusion neutrons. Evidence of enhanced swelling in the presence of He has been found in boron doped ferritic F82H alloy [25], and in dual beam implantations in several candidate alloys [54]. The comparison of swelling rates in both materials has rarely taken the effect of dose rate into account, resulting in large scatter of the data [55].

The mechanical properties of ferritic steels subjected to irradiation are a primary focus of this thesis and are discussed in more detail in *sections 2.3* and *2.4*; thus only a brief

introduction is given here. Irradiation hardening occurs at low temperatures (<400°C) [56-58] and on few occasions softening has been observed in some alloys >500˚C [59]. At temperatures below ~400˚C, irradiation hardening results in an increase in DBTT [57, 58, 60]. ΔDBTT is dependent on irradiation temperature, dose, transmutation helium production and Cr content. The pronounced effect Cr content has on ΔDBTT is shown in *figure 2.5* [31, 53, 61]. The radiation-induced increase in DBTT at Cr contents >9% may be due to segregation of the alpha prime (α') phase causing the well-known '475˚C embrittlement' effect [62, 63]. The increase in DBTT in the alloys with decreasing Cr content have also been indicated in Fe-Cr model alloys [64], however the mechanisms controlling this behaviour are not known. The role of Cr in irradiation hardening is a primary concern in the work reported in this thesis.

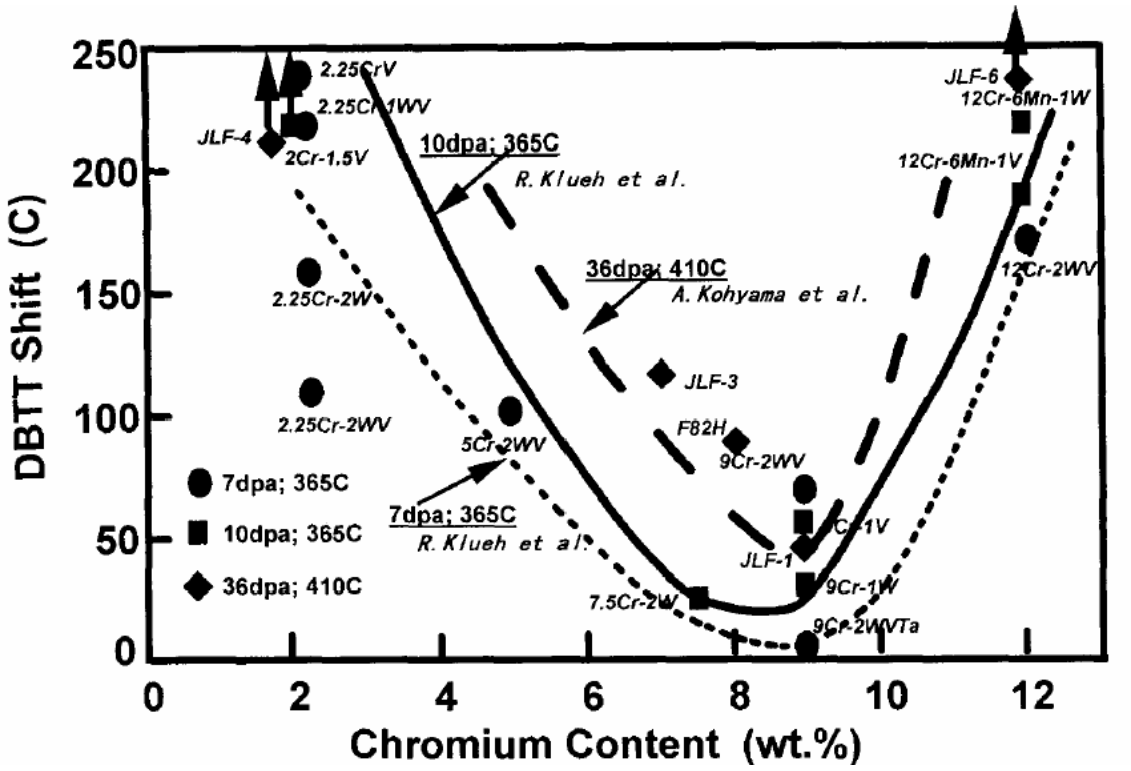

Figure 2.5 – Effect of Cr content on change in DBTT of ferritic alloys after neutron irradiation in FFTF [31].

The database for ferritic steels in a radiation environment is large when compared to that of other candidate fusion materials. Production of these steels with low impurity levels and welding has been demonstrated successfully [65] and a number of alloys have been created specifically for fusion reactors.

ODS Steels

The main disadvantage with ferritic/martensitic steels is the onset of high temperature creep above 550˚C. Oxide dispersion strengthened (ODS) steels are under development, to increase creep resistance and reduce swelling due to the distribution of microstructural traps for helium [65]. These alloys have an ultrafine dispersion of 2nm Ti-, Y- and O- enriched particles formed by a mechanical alloying process, followed by hot extrusion, rolling or hot isostatic pressing [65]. These alloys are early in development; the stability of ODS particles during irradiation and particularly at welds requires further investigation.

2.1.4 Summary

The environment in a fusion reactor is extreme. Components will be subject to large heat loads and radiation from energetic particles, causing several materials related problems which may risk the commercial feasibility of fusion power generation. Of the three candidate structural materials, low-activation ferritic steels are recognised as the most advanced and mature materials [31], and the use of a developed alloy known as EUROFER 97 has been suggested for the blanket design of the first prototype fusion reactor, DEMO [66]. Nevertheless, further work is required to understand hardening and embrittlement mechanisms in these alloys, particularly the role of Cr when subjected to irradiation.

2.2 The Study of Radiation Damage in Solids

Radiation damage in materials include phenomena at time scales from attoseconds (10^{-18}s) to decades, and length scales from angstroms (10^{-10}m) to metres; hence, this discipline requires a multi-scale approach which includes computational modelling [67, 68], microscopy techniques [69] and mechanical testing [70].

2.2.1 Computational Modelling Methods

The development of computational modelling has enabled the simulation of collision events, defect production and migration, microstructural evolution and the resulting effects on the mechanical properties of solids. Investigating the wide range of time and length scales involved is computationally expensive and requires a multi-layered approach, where simulation data are used to pass parameters to subsequent models of a higher scale.

At the smallest time and length scales, density functional theory (DFT) modelling uses quantum mechanics to simulate elementary defects and can be used to develop interatomic potentials. These models are limited to systems with relatively small cell or 'box' sizes of 100-200 transition metal atoms, which are repeated with periodic boundary conditions to represent larger or infinite volumes of material; this limits the complexity and disorder of structures which can be modelled.

Potentials, gained from DFT modelling or fitted to bulk material properties can be used in MD calculations, to simulate collision cascades produced by energetic particles and the microstructural evolution of resultant point defects into clusters and dislocation loops on the order of nm and ps. This may result in improved accuracy in relationships between radiation conditions and defect production, cluster fraction and type (for example see MD simulations of cascades produced by Bacon et al. [71]). More recently, MD simulations have been used to study the complex reactions between glissile dislocations and various radiation defects [72, 73].

To simulate the evolution of cascade products beyond the length and time scales of MD simulations, Kinetic Monte Carlo (KMC) models [74, 75] use statistical mechanics calculations to predict large scale defect evolution resulting from a considerable number of damage events expected in a fusion environment. KMC methods can include complex microstructures, such as the effects of impurities, dislocations and grain boundaries, without the need for excessive computational resources.

Finally, Dislocation Dynamics (DD) coupled with continuum mechanics are employed to model the flow and fracture behaviour of resultant 'damaged' microstructures. In the relatively large scale of these methods (nanometres to micrometres), an accurate simulation of the macroscopic behaviour requires the consideration of several elements which make up the microstructure of the solid, increasing computational demand. At the largest scales, Finite Element Analysis (FEA) models are used with empirical constitutive laws derived for radiation damaged materials.

In the rapidly developing field of materials modelling, care is required not to stretch a model beyond its range of validity [67]. The inherent assumptions, limitations and errors within each model are liable to be exaggerated in parameters which are passed on to subsequent models; this emphasises the importance of experimental methods, to validate the fundamental theory within these models.

2.2.2 Experimental Methods

Methods available to study the effects of radiation damage in solids include a large variety of general techniques established for material science. This section addresses methods for irradiating materials specific to a fusion environment and will provide an overview of the main experimental techniques used to characterise these materials during and after irradiation.

Simulating a Fusion Radiation Environment

The radiation environment at the first wall of a fusion reactor has been detailed in *section 2.1.1*. In order to study the effects of radiation in a fusion environment experimentally, access to a radiation source of some kind is required. In the absence of a working fusion reactor and the much anticipated International Fusion Materials Irradiation Facility (IFMIF) [76], alternative radiation sources for simulating fusion neutron spectra are available; several of these methods have been evaluated by Ishino [77].

The effects of a fusion environment are often studied by using energetic neutrons from current mixed-spectrum and fast fission reactors, requiring correlation with likely effects from fusion spectrum neutrons [78]. In order to successfully apply data from fission reactor studies to the fusion environment, the radiation conditions (such as those discussed in *section 2.3*) must be taken into account; unfortunately, many of the previous studies have recorded such data inaccurately and in some cases important parameters were neither recognised nor documented. Garner et.al [78] showed that when comparing two radiation environments, differences in dose rate are a dominant determinant of an alloy's response. This evidence is particularly concerning when considering the vast range of characteristic dose rates associated with the various radiation sources used for materials research shown in *table 2.3* [11, 79, 80].

Table 2.3 - Various sources of radiation with typical values of dose rate.

Radiation Source	**Dose Rate in iron-based alloys (dpa/s)**
First Generation Fission Reactor Pressure Vessels (RPV) [11]	~ 10^{-11} – 10^{-10}
Rotating Target Neutron Source (RNTS-II) [79]	~ 10^{-10}
Fast Flux Test Facility (FFTF) [79]	~ 10^{-8} – 10^{-6}
Charged Particle Implantation [80]	~ 10^{-5} – 10^{-3}

In addition, M. Kiritani et.al [81] suggested the exposure to neutrons during reactor start up and shut down, producing an irradiation with differing temperature, may result in up to a one hundred percent difference in the final defect structure compared to an irradiation with constant temperature.

Fission based sources have a much lower neutron energy spectra (typically <200KeV) when compared with that envisaged for a fusion reactor. These energies are not sufficient to cause

the 'threshold' reactions which produce the levels of transmutation products expected in fusion reactors, requiring doping of materials prior to irradiation if transmutation products are to be simulated [82, 83]. Typical dopants include nickel, ^{58}Ni and Boron, ^{10}B which form He in mixed-spectrum or high-flux fission reactors[2]; however, these elements produce artefacts, such as B precipitate formation [84], in the alloy during and after irradiation [85].

Other higher energy neutron-based radiation sources include accelerator-based D-T neutron sources, such as the Rotating Target Neutron Source (RNTS-II) facility [86] and Spallation Neutron Source (SNS). These methods can provide similarities to a fusion radiation environment; however a low neutron flux in RTNS-II and broad energy spectrum in SNS limit comparability.

All high energy neutron radiation sources which are used to investigate radiation damage in solids require the use of a 'hot cell'. This involves the transportation of radioactive materials, the hot cell to be onsite with a radiation source and the application of 'hot' testing equipment. A relatively less expensive way to simulate radiation damage in solids can be achieved by ion implantation using a charged particle accelerator, where each incident ion simulates a PKA [87]. The use of heavy ions as a radiation source produces interactions with a considerable increase in the elastic cross-section to that of neutron radiation, which results in a mean free path between collisions in the order of 100Å as opposed to a few centimetres with neutrons. This limits the range of ions into a solid to a few microns, but gives the 'advantage' of high dose rates capable of producing levels of displacement damage

[2] ^{58}Ni forms He by the two-step reaction with thermal neutrons, ^{58}Ni (n, γ) – ^{59}Ni (n, α) – ^{56}Fe. ^{10}B forms He by the reaction, ^{10}B (n, α) – ^{7}Li.

equivalent to a decade in a fusion reactor in a matter of hours. Light particles such as alpha particles, protons, and electrons can be used for increased implantation depth. The fraction of energy lost in the form of electronic stopping is large with lighter ions, producing significant beam heating and low energy transfer in elastic collisions (low PKA energies). Inelastic nuclear events are not directly simulated with charged particle irradiation, requiring subsequent or in-situ dual-beam or triple-beam implantation if transmutation products are to be simulated [88].

In comparison with each other and with conditions expected in a fusion reactor, all currently available irradiation methods have significant differences in radiation environment. The effects of these differences are discussed further in *section 2.3*.

Materials Characterisation

A significant restriction for many experimental techniques available is limited irradiated sample volumes, as a result of volume or technology limitations of the radiation sources or due to maximum activity restrictions. A number of microstructural and chemical characterisation techniques such as Transmission Electron Microscopy (TEM) and Atom Probe Tomography (APT), inherently require sub-micron scale specimens and are commonly used to investigate small volumes of irradiated material. These techniques can be applied to materials which have been irradiated with either neutrons or charged particles; for example, material subjected to charged particle irradiation can be investigated ‘in-situ’ in the TEM for dynamic observations of radiation phenomena [89].

Traditionally, mechanical testing is conducted on specimens of at least several tens of millimetres in size and is defined in several standards. Volume constraints for irradiated materials has resulted in the development of small specimen test technology (SSTT), which involves the miniaturisation of several standard test specimens for different mechanical testing techniques [90]. SSTT uses specimens in the order of a few millimetres; however, test data are subject to scaling effects associated with constraint loss and require adjustment [90].

Micro-mechanical Testing of Irradiated Materials

Micro-mechanical testing of irradiated materials is receiving growing interest for two reasons. Firstly, irradiation of materials by high energy neutrons can cause the formation of radioactive isotopes (such as Mn-54 and Co-60 in structural steels), which complicates handling and testing of large scale test specimens. Secondly, the small volumes of material produced by heavy ion irradiation limits test specimen geometries to dimensions to a few microns. Nanoindentation is increasingly being used for ion-implanted material to study changes in mechanical behaviour of the thin damaged layer at the surface [54, 91-96]. These methods are useful for the quantitative comparison of micro-scale irradiated volumes; however they provide little qualitative information on the micro-mechanical deformation behaviour.

Since the development of focused ion beam (FIB) microscopes, the ability to mill material at a scale as small as a few tens of nanometres has led to the development of site-specific specimen manufacture for TEM and APT analysis [97], as well as various micro-mechanical test geometries [98]. Micro-mechanical techniques can be used on thin damage layers

produced by charged particle irradiation and have the potential to substantially reduce the complexity and expense involved in the mechanical testing of active materials.

Micro-pillar compression is a common micro-mechanical testing method due to its simple geometry; this reduces milling requirements and provides tests with a simple stress state for analysis. Hosemann et al. [70] have used this technique for investigating the end pieces of used tensile test specimens of neutron irradiated HT-9 steel. The volume of neutron irradiated material enabled the testing of relatively large 8 x 8 µm square pillars, results from which agreed well with trends in yield stress found by tensile and micro hardness of the same irradiated material; a direct comparison was not possible due to significant differences in test temperature. For the testing of ion implanted material, pillars must be manufactured lateral to the ion beam. This has been achieved by 'sandwiching' samples for milling into a cross-section of the implantation damage [99] and by implantation of a pre-fabricated FIB milled 5µm thick lamella [100].

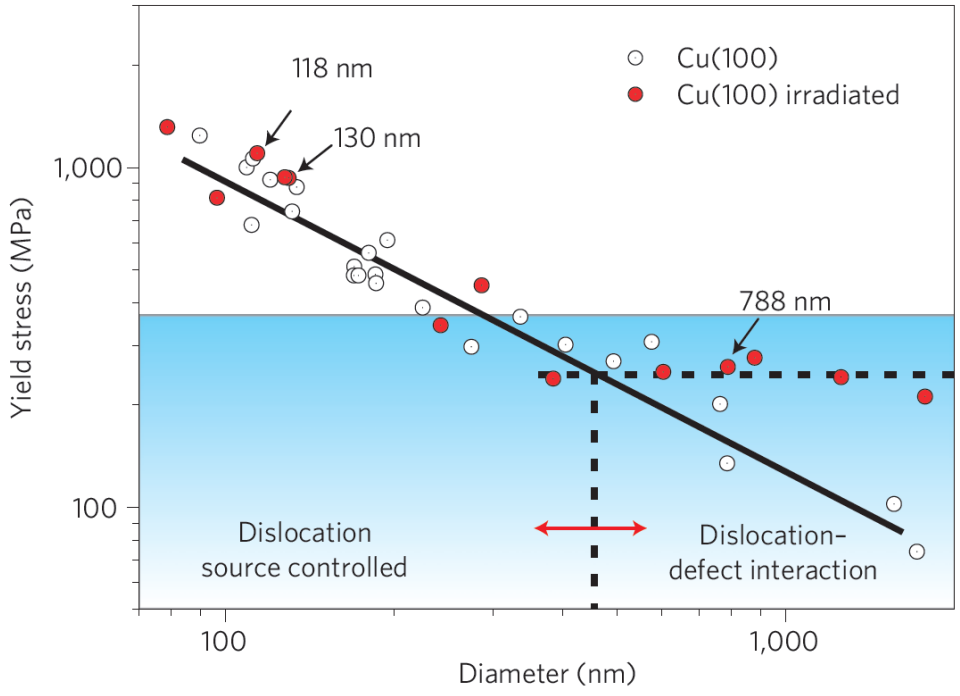

Figure 2.6 - Size-dependent yield stress for (100) orientated irradiated and un-irradiated copper nano-pillar tests [100].

Kiener et al. [100] clearly demonstrated that the measured yield stress in un-irradiated and irradiated copper was dependent on specimen size (*figure 2.6*) and followed the well-established size effect for small scale testing [101]. In the pillars with a diameter smaller than 400nm there was no observable difference in the yield stress between irradiated and un-irradiated Cu and plasticity was dominated by the nucleation of dislocation sources. Above a diameter of 400nm, the irradiated material exhibited a constant yield stress with increasing specimen size, whilst the un-irradiated material continued to exhibit a size effect with decreasing yield stress. The iron-based pillars tested by Grieveson et al. [99] were limited to 1µm in diameter (corresponding to the maximum implantation depth) and a difference in the yield stress between irradiated and un-irradiated iron was not observable; it was suggested that plasticity was controlled by dislocation nucleation similar to the description given by Kiener et al. [100].

The mechanical testing of materials using micro-pillars is hindered by several problems. A poor lateral stiffness due to deformation of material surrounding the base of the beam is a major problem [102] and has led to inaccurate measurements of strain during testing and unrealistic values observed for elastic modulus. Pillars machined by annular milling are prone to having tapered walls leading to a stress gradient along the length of the beam; pillars of this geometry always exhibit plastic deformation only very close to the top of the beam. Scatter in data may occur in some part due to errors in pillar geometry measurements. Pillars machined into a flat surface are usually masked by the edges of the hole they sit in; this necessitates imaging the test specimens with a high angle of incidence and measurement values are weighted heavily on assumptions regarding the orientation of the sample and pillar with respect to the imaging beam column.

The measurement of mechanical properties of ion-implanted material using micro-cantilever testing has been attempted by Halliday et al. [94]. Pure Fe was subjected to ion implantation

using 2MeV followed by 0.5MeV, to average doses of 0.35dpa and 5.33dpa at a temperature of 300°C. Micro-cantilever beams were manufactured by FIB milling and included a 'waist region' 1µm in depth at the fixed end of the beam; this geometry concentrated the stress to a small volume within the implanted layer during testing. As shown in *figure 2.7*, the observed yield stress was found to increase as a function of dose and the work hardening rate was found to increase in the material irradiated to the highest dose. Interestingly, a large increase in the observed elastic modulus was also measured for material irradiated with the highest dose.

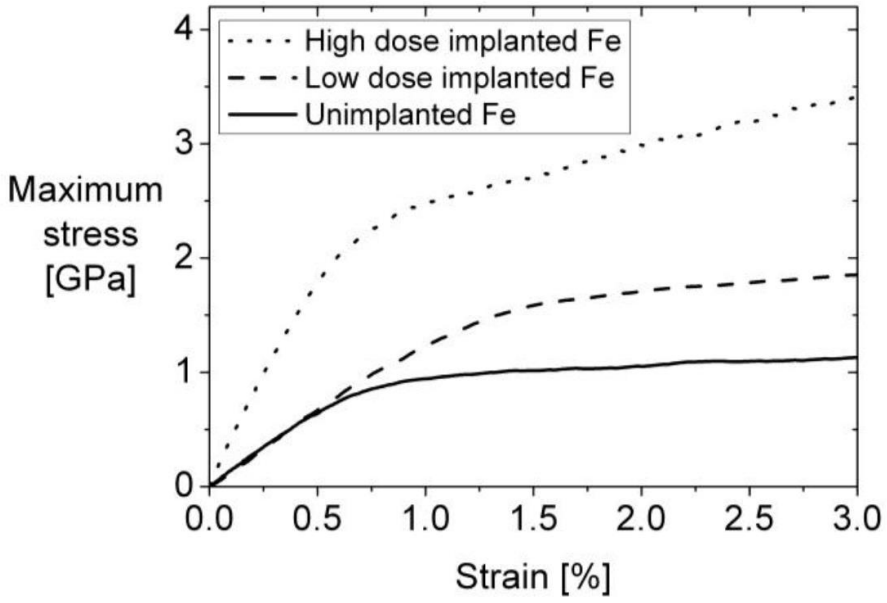

Figure 2.7 - Stress-strain curves for micro-cantilevers close to [0 0 1] in pure Fe, un-irradiated and irradiated to a low dose (0.35dpa) and high dose (5.33dpa) [94].

The data was analysed by using simple beam theory calculations; several assumptions are used in these calculations which may have resulted in significant errors. Most notably the beam is assumed to have a constant cross-section along its length. Differences in the beam stiffness due to the small waist cross-section compared to the relatively large beam cross-section may result in an underestimation of strain. This may have resulted in the calculation

of high elastic modulus in some cases. The fixed end of the beam is assumed to be fully constrained; however the free surface and plastic deformation at the fixed end may cause further complications. Finally, loading should be applied and all deflections should occur in the plane of bending; an image showing a tested beam indicates that the beam may have been subject to torsion stresses during bending (*figure 2.8*).

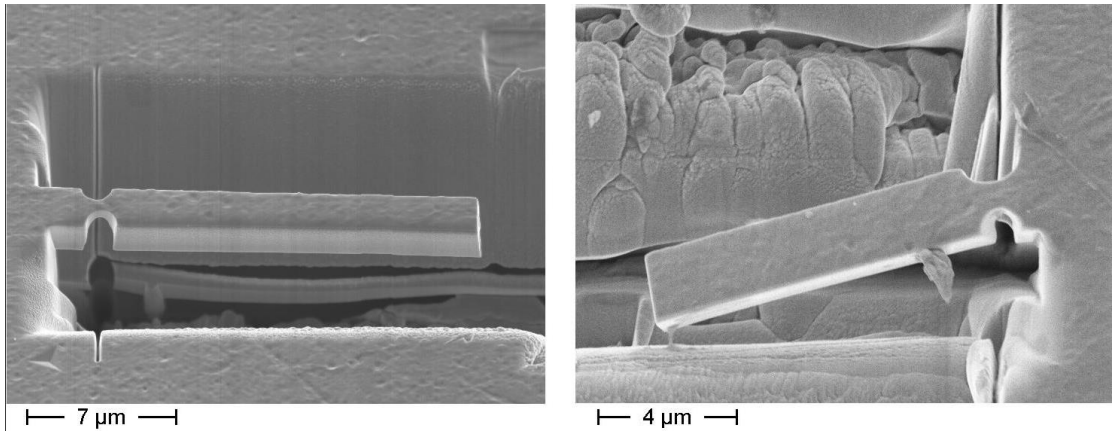

Figure 2.8 – Micro-cantilevers in un-implanted pure Fe before (left) and after (right) testing [94]. Tested beam orientation indicates deformation by both bending and torsion.

2.2.3 Summary

In the absence of a working fusion reactor, there are no radiation sources which accurately simulate a fusion environment requiring the use of various extrapolation methods [78, 81, 83, 103, 104]. In many cases the investigations of radiation effects in materials require the use of experimental techniques at smaller length scales [90]. The use of miniaturised test volumes in laboratories with activity restrictions or for ion implanted materials presents several discrepancies when compared to characteristic bulk behaviour. Observations and test data from each investigation are dependent on the characteristics of the radiation source and characterisation methods used. This is of considerable importance in the work reported in this thesis, which uses ion implantation to produce damage, followed by nanoindentation and micromechanical testing to investigate mechanical properties.

2.3 Radiation Effects – Cascade Damage

The methods described in *section 2.2* have been employed to gain an understanding of the effects of radiation in ferritic materials and develop alloys for nuclear energy applications. This section describes the fundamental processes which control radiation damage, from the production of elementary defects in displacement cascades to the evolution of the damage microstructure. These processes are important for investigating the response of a material, which has been irradiated in a radiation source with characteristic parameters including irradiation temperature, dose and dose rate.

2.3.1 Primary Damage Production

Displacement cascades begin with a ballistic phase, which consists of all displacement collisions resulting from a PKA as described in *section 2.1.2*. This is followed by a thermal spike phase, which includes the cooling of the cascade volume from temperatures exceeding the melting temperature of the alloy. Neutrons have no net electronic charge and transfer energy by direct elastic collisions with atomic nuclei in the target structure; these collisions are commonly modelled equivalent to those of hard spheres [105]. In contrast, charged particles such as those used in ion implantation and PKAs transfer energy by three processes [106]:

(i) Electronic Stopping (e) - Inelastic interactions with bound or free electrons in the target structure;

(ii) Nuclear Collisions (n) - Elastic Coulomb interactions between the 'screened' nuclear charges of charged particle and target atom;

(iii) Charge Exchange (ch) - electron exchange between moving atom and target, during close proximity.

Hence, the total energy loss of an energetic charged particle in a target material is given by:

$$\frac{dE}{dx} = \left(\frac{dE}{dx}\right)_e + \left(\frac{dE}{dx}\right)_n + \left(\frac{dE}{dx}\right)_{ch} \qquad \boldsymbol{equation\ 2.4}$$

At higher energies the majority of energy is lost through electronic stopping which generates heat. However at lower energies, energy is predominantly lost through nuclear collisions which cause atomic displacement [21]. The energy loss due to all interactions with energetic particles (neutrons and charged particles) are calculated with the energy-dependent displacement cross-sections, $\sigma_D(E_i)$, as defined in *equation 2.3*.

2.3.2 Ballistic Phase

The initial ballistic phase of damage production is affected by the ordered array of atoms in a crystalline lattice. Erginsoy et.al [107] used MD and found large differences in threshold displacement energy with crystallographic orientation in iron, as shown in *figure 2.9*. This showed that lattice atoms are displaced at lower energies in collisions along the low index directions and that higher energies are required in high index directions. Similar differences

were later confirmed by resistivity change experiments using electron radiation [108, 109] and simulations with more advanced potentials for both Fe and Fe-Cr [110].

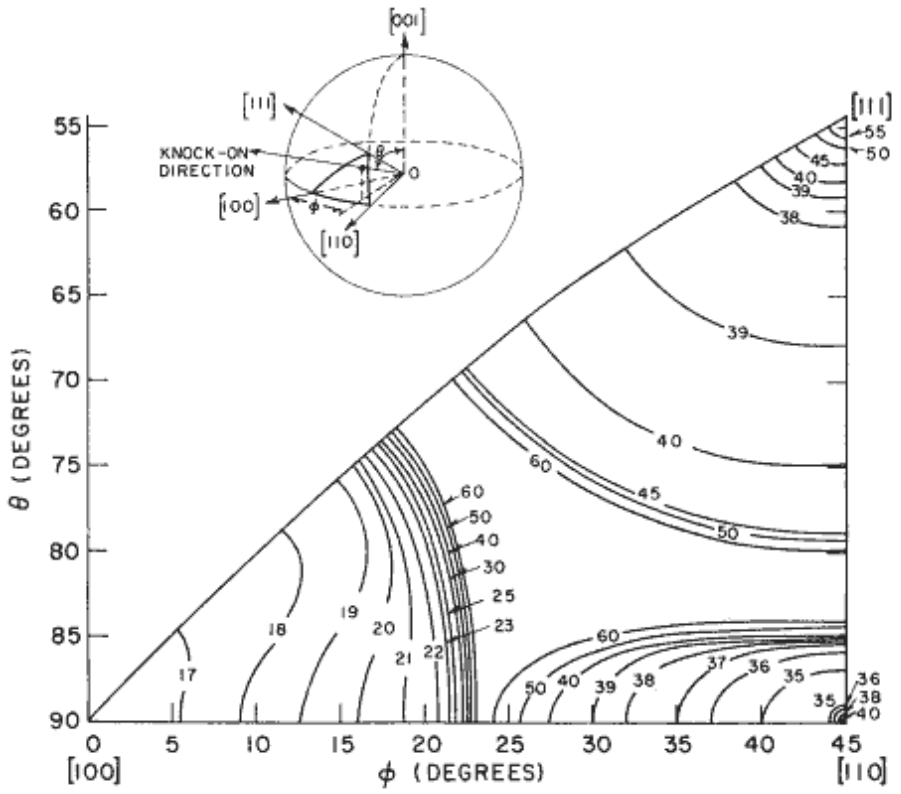

Figure 2.9 – Contours of threshold displacement energies (in eV) in iron with crystal direction in inverse-pole figure [107].

Erginsoy et al. [107] also showed that collision cascades were predominantly the product of a number of supersonic velocity collision chains (‘crowdion transfer’) with preferred close-packed direction of <111> in iron, despite the lower threshold displacement energy in <100>. In addition, long range trajectories of charged particles have been found along low index directions as a result of glancing collisions, which 'steer' the particle within open channels in many different crystalline materials (known as channelling). Beeler [111] used MD simulations to show that channelling, and in particular quasi-channelling of knocked-on atoms of second or higher order, plays a significant role in determining the extent of a

collision cascade in iron. It was shown that channelling is preferred along <110> and <100> directions and collided atom volumes were distributed in these orientations.

Stoller et al. [112] produced a number of MD simulations which directly investigated the effects of crystallography and PKA direction on the number of surviving defects in iron. This investigation showed that the number of surviving defects is lowest in the <100> direction and highest in the <111> direction, as shown in *figure 2.10*. These simulations modelled pure iron in cells equilibrated at 100K and with PKAs of a low energy.

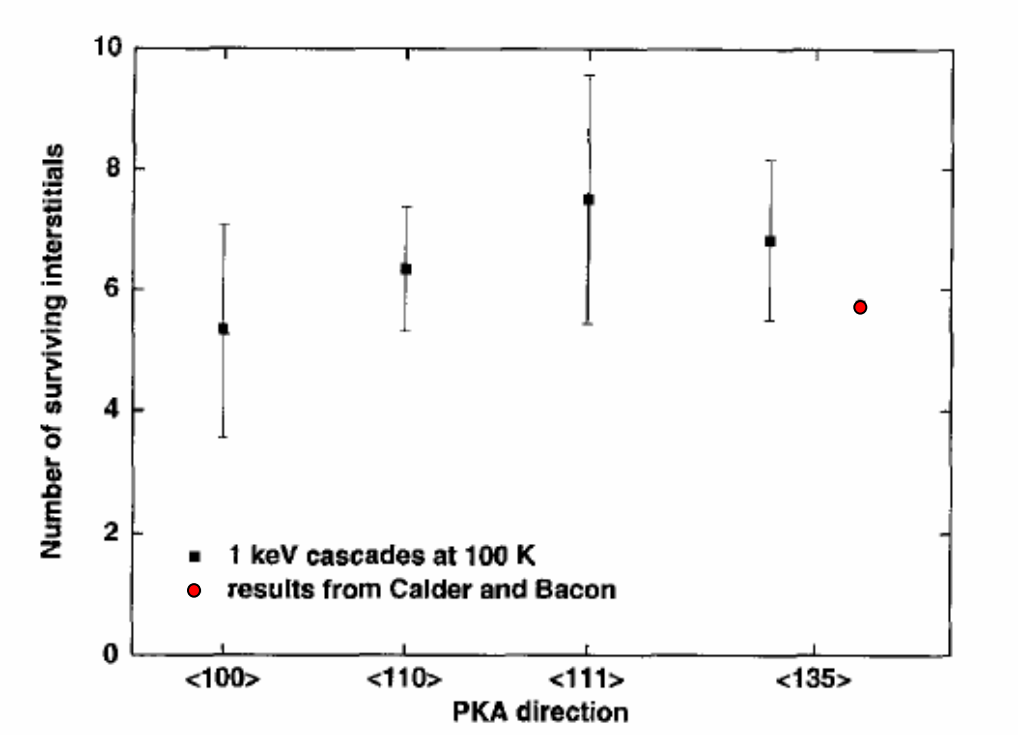

Figure 2.10 – Point defect survival vs PKA direction with standard deviations from six cascade simulations for each PKA direction (redrawn from [112]).

2.3.3 Thermal Spike Phase

In the tens of ps time frame of a displacement cascade, approximately 97% of point defects produced during a displacement cascade annihilate with one another by recombination

[113]. It has been suggested that factors such as material composition and temperature do not have an effect on the ballistic/collision phase of a cascade [110]; however, variation of composition and radiation environment may affect the subsequent recombination (thermal spike) phase, as point defects coalesce forming stable clusters and dislocation loops. The data produced by Stoller et al. [112] were obtained in cascade simulations with an initial temperature of 100K and no boundary atom dampening, which potentially modelled a large temperature increase and a prolonged thermal spike during simulation; this may have resulted in the reduction of the total number of surviving defects.

Experimental and MD investigations into the effects of temperature on the production of cascade defects in iron or related materials are scarce. MD simulations have shown that the number of defects produced decreases by approximately 20-30% with increasing irradiation temperature from 0-900K [114, 115]. This effect is relatively small in the range of cascade energies simulated (2, 5, 10keV), however, appears to increase with increasing cascade energy. This could prove more significant considering the higher cascade energies predicted in a first wall structure.

2.3.4 PKA Energy

PKAs produced by 14MeV fusion neutrons can reach energies up to 1MeV [116] with an average of 0.5MeV [117]. In contrast, PKAs produced in fission reactors have energies up to 200KeV [118]. The incident ions used in self-ion implantation simulates PKAs within the target material at energies equal to the incident ion. For high energy implantations (>0.5MeV), the incident ion is subject to electronic stopping until the energies are low enough for Coulomb interaction with the target atoms. This process is identical for the high

energy PKAs produced by fusion neutrons, thus high energy self-ion implantation create PKA energies which are comparable to those expected in a fusion reactor. Ion implantation at lower energies, such as the 100-150KeV Fe^{+} ions used for the irradiation of TEM foils in ref. [89] are more comparable to PKAs produced in fission reactors. However, both fission and fusion neutron energy spectra include a tail of lower energy PKAs resulting from the range of nuclear stopping events during the path of the neutron. The lower energy PKAs are not represented in ion implantation studies and may produce a difference in the final damage microstructure.

The final number of defects as a function of PKA energy, defined by the fraction of NRT value[3] (defect production efficiency) [22], has been studied by MD simulations [119-122] as shown in *figure 2.11* [119]. The decrease in defect production efficiency with cascade energy up to 10keV may be explained by collision interference, causing an increase in defect recombination within a single cascade. This supports the argument that sub-cascade formation at higher cascade energies results in a saturation in defect recombination and a constant NRT fraction around 0.2-0.3 for energies >10keV [117].

[3] NRT – Norgett, Robinson and Torrens standard formula (modified Kinchin-Pease model) for number of Frenkel pairs (vacancy-interstitial) created by a cascade with PKA energy - $N_{NRT} = 0.8T/2E_d$ (thermal spike effects not included).

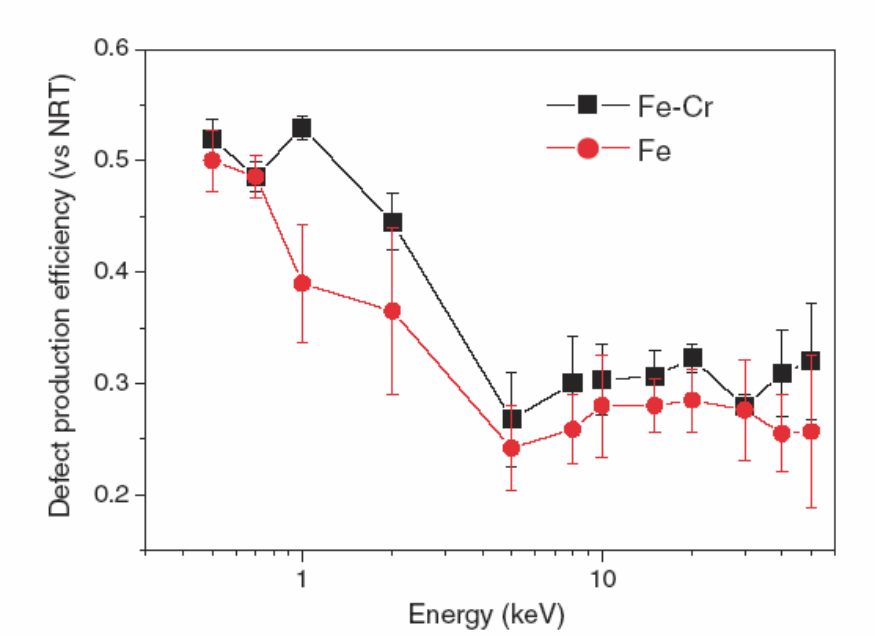

Figure 2.11 – MD simulation data of defect production efficiency – Frenkel pair NRT fraction vs PKA energy [119].

Recent simulations conducted using the HECToR supercomputer [123] modelled displacement cascades produced with PKA energies from 0.1 to 0.5 MeV in iron at 300K [113, 124]. Unlike the sub-cascade formation identified in ref. [117], these simulations found that cascades were in the form of a continuous distribution of damage across 100-130nm for 0.5MeV PKA energies. The NRT fraction of defects was still ~0.3 and consisted of isolated and clustered vacancies and SIAs as shown in *table 2.4*.

Table 2.4 - Defect statistics for 0.1, 0.2 and 0.5 MeV cascade simulations in iron at 300K. The values in brackets shows the standard error over four simulations. Data taken from [113, 124].

Cascade energy	Number of Frenkel pairs (N_F)	NRT fraction of defects	Number of isolated vacancies	Number of isolated SIAs	Number of vacancy clusters	Number of SIA clusters	Largest vacancy cluster	Largest SIA cluster
0.1 MeV	550 (200)	0.55 (0.2)	15 (2)	58 (9)	26 (4)	3 (1)	18	11
0.2 MeV	900 (200)	0.44 (0.11)	70 (5)	65 (4)	17 (1)	46 (7)	54	89
0.5 MeV	1450 (220)	0.29 (0.04)	150 (14)	170 (15)	36 (7)	84 (13)	47	36

2.3.5 Cascades in Fe-Cr Alloys

Information regarding the primary damage production in more complex alloy systems, particularly binary Fe-Cr alloys, is again rather limited. The comparison of pure Fe with Fe-10%Cr is the subject of the majority of MD simulation attempts [119-122]. Fe-10%Cr is chosen due to the lack of a concentration dependent, thermodynamically correct Fe-Cr potential, which correctly describes the tendency for short range ordering (SRO) at C_{Cr}<10%, and phase separation in the miscibility region at C_{Cr}>10%. Despite Fe-10%Cr being considered thermodynamically stable, the interatomic potentials used in many of these simulations have inherent discrepancies with both experimental data and ab-initio calculations. To emphasise this point, Shim et al. [122] produced MD simulations of displacement cascades in pure Fe and Fe-Cr with two different interatomic potentials. It was found that the presence of Cr and thus the potential used did not influence the ballistic phase of a displacement cascade; however, it *did* reduce the subsequent recombination and mobility of SIAs. This provides a good explanation for the large discrepancies in the fraction of Cr in SIAs and clusters between many of the simulations. For example, Terentyev et al. [119] found a 50-70% volume fraction of Cr in interstitial positions (dependent on cascade energy), after cascade recombination in Fe-10%Cr, using an 'embedded-atom' potential in MD. TEM observations of Cr enrichment at the edge of dislocation loops in Fe-Cr alloys by Yoshida et al. [125] were offered as supporting evidence. However, similar more recent simulations carried out by Tikhonchev et al. [120] with a further developed 'manybody' Fe-Cr potential, predicted a Cr fraction in interstitials in the range of 2-5%; a Cr fraction which is essentially lower than that of the base alloy and not in agreement with the simulations by Terentyev et al. [119].

2.3.6 Summary

MD simulations of displacement cascades with various energies have enabled the investigation of elementary defects produced under various irradiation and material parameters. PKAs with energies greater than 10KeV produce cascades with ~30% of the calculated NRT fraction of defects, independent of cascade energy. There is evidence that the number of surviving defects decreases with increasing irradiation temperature due to heightened rates of recombination and that Cr atoms may prefer to occupy interstitial sites in Fe-Cr alloys. However, these simulations are subject to errors associated with the interatomic potentials used.

2.4 Radiation Effects - Microstructural Evolution

The information provided in *table 2.4* shows the elementary defect population formed in high energy cascades in iron. This section concerns the migration and interactions of these defects after a cascade event and the dependence of microstructural evolution of damage on radiation parameters.

With accurate interatomic potentials, MD simulations can provide information on the type and mobility of different defects which coalesce forming extended defects in the microstructure. For example, simulations by Stoller et al. [126] suggested that self-interstitials were most stable in a <110> dumbbell configuration. However, in clusters of two or more interstitials the stable configuration changed from <110> to <111>, with a larger fraction of dumbbells transforming into <111> crowdions with increasing cluster size. Atomistic stacking of interstitials of this nature is consistent with perfect extrinsic dislocation loops with Burgers vector a/2<111>, found in TEM observations of irradiated iron [89, 127, 128].

2.4.1 Dose Rate

The irradiation dose rate may be expressed in the units of dpa/s; i.e. the number of elementary displacement defects (interstitial – vacancy pairs) per atom (dpa) per unit time. The rate of interaction between these defects is dependent on their mobility and is proportional to the square of their density [129].

The types of interaction and fate of these defects can be classified into three possible reaction paths [103]:

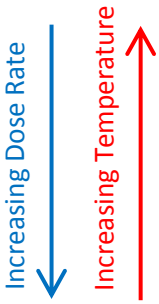

(i) Loss of defects at extended sinks such as dislocations and grain boundaries;

(ii) Growth or shrinkage of defect clusters by the capture of point defects;

(iii) Mutual annihilation by the recombination of a vacancy and interstitial.

Several authors have discussed the dose rate dependence of materials exhibiting sink dominant and recombination dominant regimes [103, 104, 130]. At low dose rates and/or high irradiation temperatures, reaction path (i) (sinks) dominates and at a high dose rates and/or low irradiation temperatures reaction path (iii) (recombination) dominates [103]. The evolution of radiation damage such as dislocation loops and voids and phenomena such as radiation induced segregation, swelling and creep, depend on the fraction of point defects which migrate to sinks, recombine or cluster within the lattice and will be influenced by the reaction path that dominates the microstructural evolution of the material under irradiation.

The relative proportions of these reaction types are directly dependent on the density and mobility of the defects, and hence dependent on dose rate and temperature. Vacancy type defects are generally found to have significantly higher activation energy for migration compared to interstitial type defects in iron; the migration energy for a vacancy is 0.67eV and that of an interstitial is 0.34eV. Defect migration in iron depends strongly on the presence of impurity atoms [131]; carbon forms strongly bound complexes with vacancies

and a vacancy-carbon complex has migration energy of 1.08eV [131]. Depending on temperature, these effects may result in unequal fluxes of mobile interstitials and vacancies, known as a production bias [132], and thus influence the relative fractions of the various reaction paths described above.

The majority of research regarding the dose rate dependence of radiation damage was conducted in the 1980's and reported distinct differences in the swelling and creep rates of austenitic stainless steels irradiated in fission reactors with variations in neutron flux. For example, Seran et al. [133] showed that the swelling incubation period of 316 stainless steel cladding increased from approximately 20 to 70 dpa with increasing dose rate from 5 x 10^{-7} to 25 x 10^{-7} dpa/s. In addition, the creep rate of numerous steels has been shown to decrease with increasing dose rate within the range of 10^{-8} to 10^{-7} dpa/s [134]. This decrease in swelling and creep with increasing dose rate is likely to be due to a reduction in available point defects resulting from heightened rates of defect clustering or, as suggested by Okita et al. [130], a higher fraction of recombination. The rate at which materials are subjected to radiation is less discussed in recent work and the dose rate is often not reported. With strong evidence proving that the radiation response of a material is dependent on dose rate [133-136], this information is crucial for interpreting results.

To identify the effect of dose rate on the damage evolution in the microstructure, Muroga et al. [135] compared the saturated dislocation loop densities in Fe-Cr-Ni austenitic alloys after irradiation with high flux electron, fast neutron and fusion neutron sources. *Figure 2.12* shows the considerable increase in saturated dislocation loop density with increasing dose rate found in the irradiated alloys after irradiation with dose rates from $<10^{-9}$ to $>10^{-4}$ dpa/s.

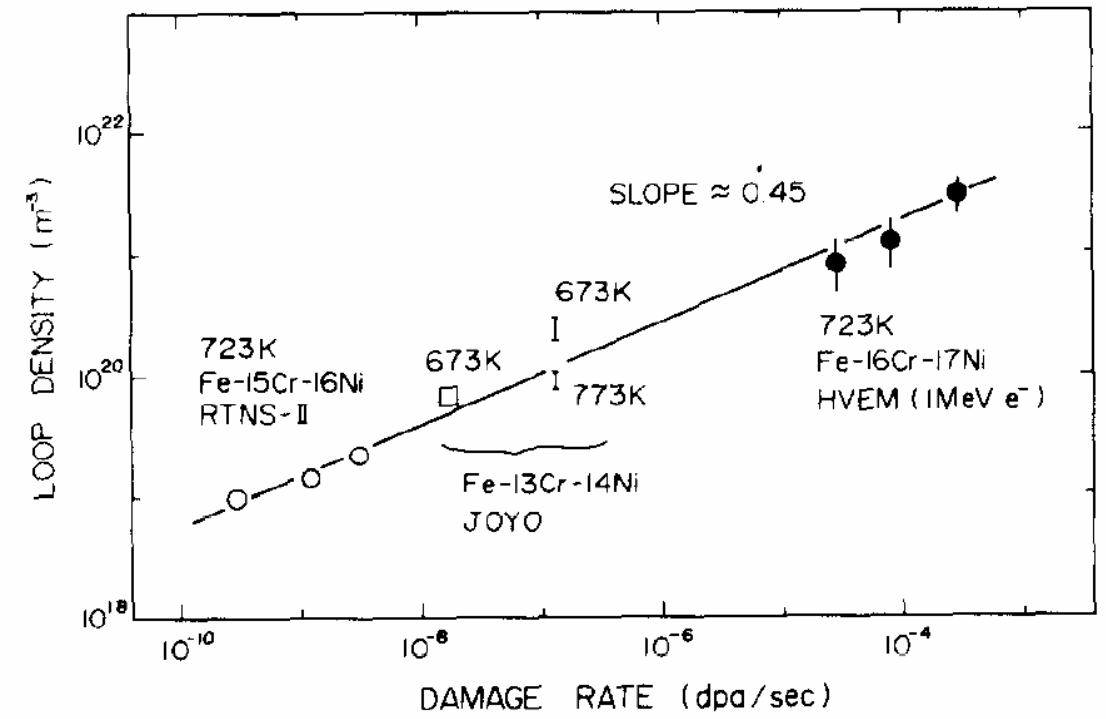

Figure 2.12 – Saturated dislocation loop density in several Fe-Cr-Ni austenitic alloys after electron (●), fast neutron (□) and 14MeV neutron (○) irradiations of various dose rates [135].

Unlike large cascades produced by ions and neutrons, the low PKA energy spectrum characteristic of electrons produce displacements of one Frenkel pair with small SIA-vacancy separation distance. The increase in loop density in *figure 2.12* was thought to be minimised in the higher dose rate region by a higher fraction recombination in the electron irradiations. A later study carried out by Okita et al. [136], investigated Fe-15Cr-16Ni irradiated with 4MeV Ni ions at similar dose rates to the electron irradiations in ref. [135]. At a dose rate of 10^{-4} dpa/s, saturated loop densities were 6.10 x 10^{22}m^{-3} and 2.09 x 10^{21}m^{-3} at 673K and 773K respectively. These larger loop densities associated with ion-implantation strengthens the argument that lower PKA energies in electron-implantation may lead to heightened recombination. The ion implantation data increases the fitted slope gradient on the log

(rate) : log (defect density) plot to approximately 0.5, consistent with values produced elsewhere [79, 130, 135, 136].

The data discussed above exhibit a clear trend in the observed density of dislocation loops with dose rate, yet the data were produced from alloys of various compositions and irradiated at different doses and temperatures. A more systematic study investigating the effect of dose rate in TEM foils of Eurofer and Fe 9%Cr was attempted at 350°C and 550°C using Kr implantation to a target dose of 3dpa [137]. The foils were subjected to dose rates of 1.4 x 10^{-4} dpa/s and 2.8 x 10^{-3} dpa/s; however the results obtained are inconclusive as material subject to the lower dose rate received a larger dose than 3dpa, the value of which is not reported. Unlike the material subject to the lower dose rate, no observable defects were found in Eurofer irradiated with the higher dose rate. Dislocation loops were observed in the model alloy subjected irradiation with both dose rates, with significantly larger loops observed in material irradiated with the lower dose rate. It is not clear whether these observations are a result of a genuine difference in dose rate or the difference in dose.

2.4.2 Radiation Temperature

Rate theory equations have been derived in an attempt to calculate the shift in irradiation temperature required to produce equivalent damage levels for differing dose rates [104, 138]. However, damage evolution in a material depends on multiple reaction processes, each with characteristic activation energies and rates; thus, these equations are usually constricted to a single radiation phenomenon such as swelling.

The investigations by Muroga et al. [135] and Okita et al. [136] discussed in *section 2.4.1* clearly identify a decrease in loop density with increasing irradiation temperature at all dose rates. TEM observations of neutron-irradiated iron by Horiki et al. [139] indicated that whilst the point defect density decreased with increasing irradiation temperature, the average cluster size increased. The increase in irradiation temperature results in higher defect mobility, which causes heightened rates of recombination or annihilation at sinks and accelerated growth/shrinkage of clusters (the three reaction paths discussed in *section 2.4.1*).

In iron and iron-based materials it has been found that the Burgers vector of dislocation loops changes with irradiation temperature. In-situ TEM observations of ion-irradiations in Fe and Fe-Cr alloys by Yao et al. [140] and Jenkins et al. [89] showed a gradual transition from predominantly b = ½<111> loops at ≤300˚C to entirely <100> loops at 500˚C. The fraction of interstitials in loops with ½<111> and <100> Burgers vectors with irradiation temperature is shown in *figure 2.13* for pure Fe [140]. The same trend was also identified for Fe-Cr alloys; however, the microstructure was on a finer scale due to a loss in defect mobility in the presence of Cr (the Cr pinning effect [119, 141]), observed by a reduction in loop hopping in the TEM [89].

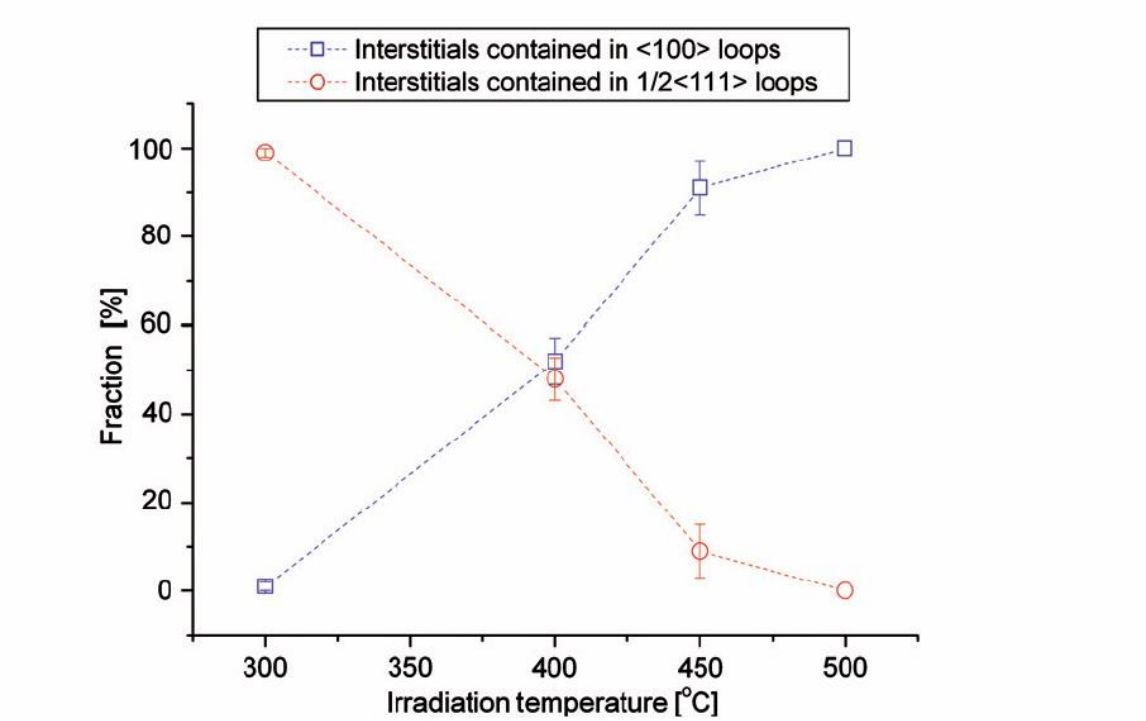

Figure 2.13 – Fraction of interstitials contained in loops of ½<111> and <100> Burgers vector in pure Fe [140].

Loops with b = <100> exhibit significantly lower mobility than with b = ½<111> [142]; thus the in-situ data shown in *figure 2.13* may be susceptible to error resulting from differential loss of defects to the foil surface. In thin foils post-irradiation loop populations are strongly dependent on foil orientation [89]. The loss of glissile ½<111> loops to the foil surface has been observed, despite the orientation of single crystal foils being close to [110] (with two <111> directions in plane of the foil). Particularly at high temperatures, surface losses are likely to result in the underestimation of the ½<111> type fraction shown in *figure 2.13*.

Use of irradiated bulk specimens for TEM foils may prevent the surface losses of defects seen in in-situ experiments. Xu [128] developed a method to thin ion-irradiated bulk Fe and Fe-Cr alloys to access the sub-surface peak damage region typically produced by ions (as shown in *figure 3.3*). The percentage of loops with Burgers vectors of ½<111> observed in ion-irradiated Fe, Fe 8%Cr and Fe 11%Cr bulk materials is shown in *table 2.5* [128].

Table 2.5 – Percentage of ½<111> loops with varying Cr content and irradiation temperature in bulk material (data from [128]).

	300°C	**400°C**	**500°C**
Fe	92% ½<111>	75% ½<111>	5% ½<111>
Fe-8Cr	46% ½<111>		90% ½<111>
Fe-11Cr	37% ½<111>		31% ½<111>

A similar trend to in-situ observations [89, 140], where a small fraction of retained ½<111> loops at higher temperature was identified for pure Fe; however, data for the irradiated bulk Fe-Cr alloys do not follow the same trend as found in in-situ observations. A reduction in defect mobility in the presence of Cr would be expected to result in a decrease in the number of ½<111> loops lost at the surface in in-situ experiments (rather than the observed increase). Therefore, the difference in dislocation type in Fe-Cr alloys between in-situ and ex-situ experiments is difficult to explain. One possible explanation may include the accuracy and reproducibility of sample temperature in the bulk experiments of Xu [128]. The reported temperatures were the result of a temperature calibration undertaken in atmosphere; this is not representative of the thermal conditions in vacuum, particularly the heat transfer at interfaces between the heating element and sample.

Calculations of dislocation loop self-energies in Fe as a function of temperature have been carried out by Dudarev et al. [143, 144]. It was found that the stability of ½<111> and <100> dislocation loops was strongly affected by the elastic instability near the α – γ phase transition temperature (912˚C). Accounting for the reduction in shear stiffness constant c' with increasing temperature, predicts a transition from a dominant occurrence of ½<111>

dislocation loops at lower temperatures to <100> loops at temperatures greater than 550˚C. This may provide an insight into the observations made in the TEM [89, 128, 140]. However <100> loops have been observed in Fe after neutron-irradiation <100˚C [145] and electron-irradiation ~-100˚C [146]. It is possible that the irradiation dose or dose rate may also influence loop Burgers vector; in addition to the magnetic effect proposed by Dudarev et al., several theories exist regarding the mechanisms for the appearance of <100> loops [147-149]. At present, the mechanisms which control the dislocation loop Burgers vector are unknown.

2.4.3 Radiation Dose

A unique phenomenon observed in BCC materials is the absence of visible damage in the TEM up to relatively high doses (doses of approximately $>10^{12}$ ions/cm^2 or 0.01dpa) in low energy self-ion irradiated specimens [127]. This has been associated with a resistance to cascade collapse, the transformation of vacancy-rich cores into dislocation loops, until cascades spatially overlap [127]. This has been later confirmed by in-situ TEM observations, for both irradiated Fe and Fe-Cr alloys by Yao et al. [69], although the threshold dose for visible damage was lower in Fe-Cr alloys than in pure Fe. However, it is likely that the majority of self-interstitials or small interstitial clusters, which are invisible in the TEM, are lost to the surfaces of the thin foils during irradiation. This results in the majority of dislocation loops observed in thin foil experiments being vacancy in nature (as in [127] and [150]). An explanation for the lower threshold for visible damage in bulk Fe-Cr alloys could therefore be related to the reduced mobility of self-interstitials caused by the Cr pinning effect [119, 141], which may prevent defect losses at the surface of the foil.

The effect of foil surface losses suggests that while the microstructural evolution of irradiated thin foils may provide information regarding the type and mobility of defect structures present in bulk materials, such in-situ methods may not provide accurate information on the density and size of dislocation loops representative in bulk materials. *Figure 2.14* shows a comparison made by Matijasevic et al. [64] of defect densities and sizes with radiation dose, in neutron irradiated Fe and Fe-Cr alloys at 573K. The defect density in the Fe-Cr alloys (shown by closed symbols) saturates at <1dpa and decreases slightly with Cr content. These densities are in contrast with the observations by Yao et al. [69], where the loop number densities in ion-irradiated thin foils of different Fe-Cr alloys with 0 to 12%Cr, were an order of magnitude higher than pure Fe for similar damage levels (~1dpa.).

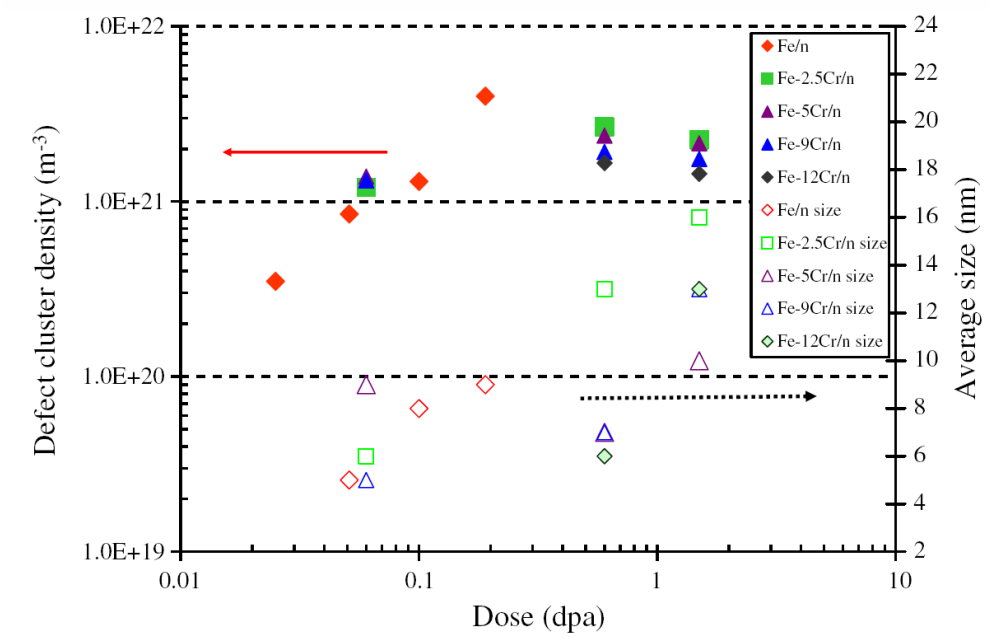

Figure 2.14 – Dose dependence of the defect density (closed symbols) and size distribution (open symbols) in Fe and Fe-Cr [64].

In *figure 2.14* the saturation of defect densities in the Fe-Cr alloys appears to occur at a lower dose than in pure Fe. Despite large scatter in results, defect sizes tend to be smaller in

alloys with the higher Cr content at doses greater than 0.1dpa [64]. This provides further evidence supporting that the mobility of defects is suppressed by Cr pinning.

2.4.4 Void Growth and Transmutation Gas

Void nucleation and growth in Fe and Fe-Cr alloys has been found to be highly dependent on the distribution of point defect traps and microstructural sinks; hence the development of ODS steels. The rate at which interstitials agglomerate forming dislocation loops has a direct influence on the number of vacancies available, which coalesce forming clusters and voids. The crystallography, initial dislocation structure, impurity and solute content have all been found to have a considerable effect on the rate at which voids may nucleate and grow [151, 152]. In addition, Tanaka et al. [153] showed that fusion-relevant levels of transmutation He and H can significantly enhance void swelling. It was shown that whilst H had no effect on void nucleation and growth during dual-beam (Fe^{3+}, H^{+}) implantation, the synergistic effect of He and H with triple-beam (Fe^{3+}, He^{+}, H^{+}) implantation enhanced void growth to almost 5% compared to 0.4% for dual beam (Fe^{3+}, He^{+}) implantation. A good explanation of these effects is given in calculations by Zinkle et al. [154], which show that the presence of gas will stabilise vacancy clusters until void formation, preventing collapse into energetically favourable dislocation loops. This suggests that transmutation H may be of considerable importance, despite observations that a large quantity of H may diffuse out of the material [155]. Caution is required for the interpretation of multi-ion implantation due to evidence of a He dose rate effect [156]. An increase in injection rate was found to result in a decrease in bubble size and increase in bubble number density, similar to the dose rate effect described in *section 2.4.1*.

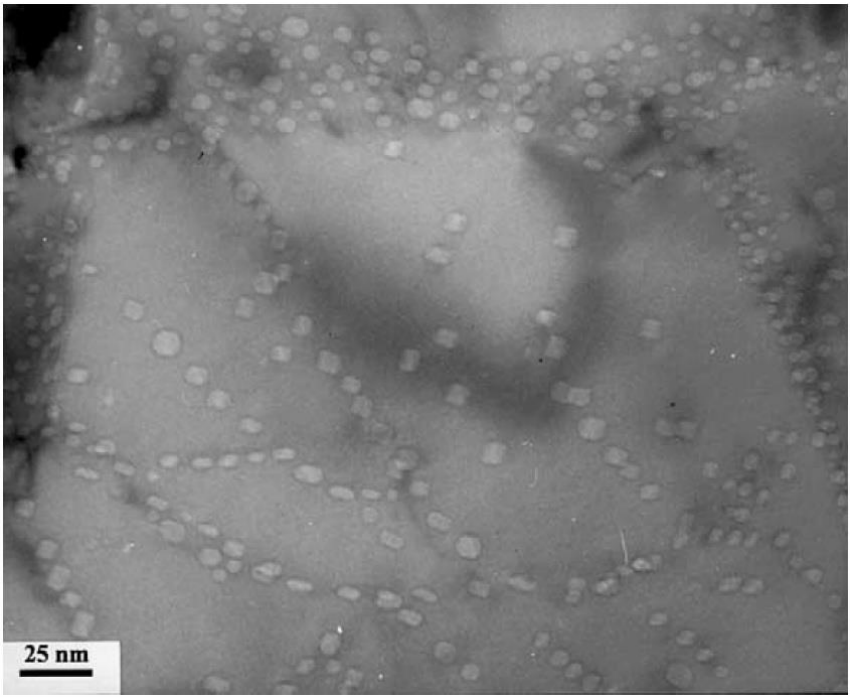

Figure 2.15 – TEM micrograph showing He bubbles distributed along grain boundaries and dislocation lines in 9%Cr-1%Mo martensitic steel after He implantation to 0.5at.%He at 550˚C [30].

In addition to the influence of swelling behaviour, transmutation gases may also affect the structural integrity of the material. *Figure 2.15* shows He stabilised vacancy bubbles distributed along grain boundaries, dislocations and at carbide-matrix interfaces in a 9%Cr-1%Mo martensitic steel [30]. It has been found that these gas bubbles can weaken grain boundaries, resulting in a total loss of ductility associated with a combination of irradiation induced hardening and the onset of intergranular fracture [30].

2.4.5 Cr content – Phase Stability

The microstructural evolution of ferritic steels and less complex Fe-Cr binary alloys is strongly dependent on the radiation environment and material composition. Considerable variation in the density and size of defects, dislocation loops and voids has been observed

with differences in irradiation temperature, dose rate and Cr content. The shape and Burgers vector of dislocation loops created during irradiation is also dependent on these factors. This leads to the strong relationships in radiation induced hardening and embrittlement with temperature and Cr content, as shown in *figure 2.5*. The relatively complex phase diagram of the Fe-Cr system is shown in *figure 2.16* [157]. The diagram defines four stable solid phases: a BCC Fe-rich α and Cr-rich α' phases, a FCC γ phase and a complex σ phase. Within the temperature range of interest for fusion power plants (~300 to 550˚C for steels), there is a miscibility gap between α and α' phases, within which phase separation by precipitation or spinodal decomposition may take place.

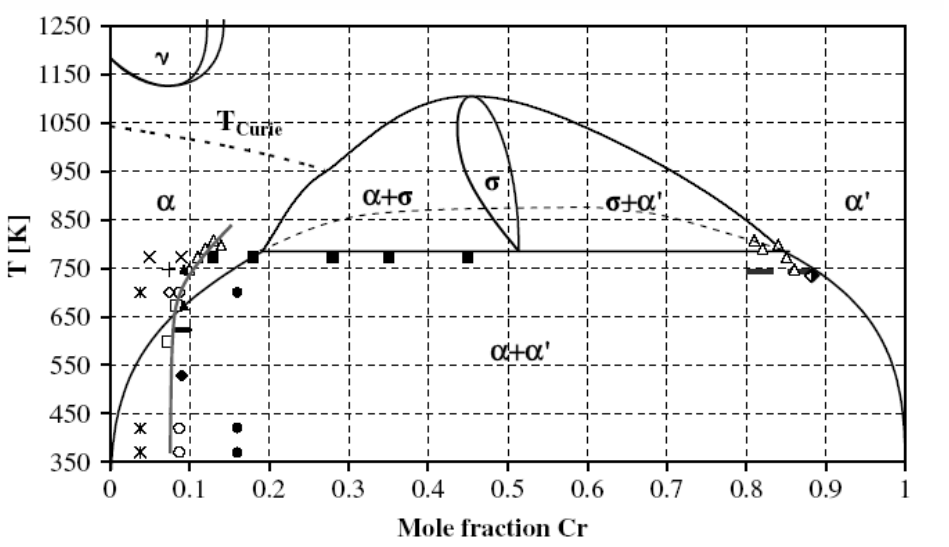

Figure 2.16 – Portion of Fe-Cr phase diagram according to CALPHAD including low temperature and low Cr thermal ageing. Irradiation experimental data (data points) added showing discrepancy in the location of the miscibility region [157].

It has been long identified that steels containing more than 12%Cr are susceptible to hardening and embrittlement after thermal ageing in the region of 500˚C (known as 475˚C embrittlement), as a result of α/α' phase separation [63, 158, 159]. It is commonly proposed that the same mechanism is the cause for the increase in ΔDBTT above 9%Cr (*figure 2.5*) [28].

At first wall operating temperatures of ~350 to 550˚C, alloys with ~9%Cr are situated in close proximity to the miscibility boundary. In this region of the phase diagram, experimental observations, which are also plotted in *figure 2.16*, have placed the predicted location of this boundary under question [157]. However, there is considerable debate as to whether the experimental observations of α/α' un-mixing are radiation enhanced, for example a thermodynamic effect accelerated by irradiation, or radiation induced, that is an effect which does not occur without irradiation.

2.4.6 Summary

The radiation response of a material is significantly dependent on the materials composition and irradiation conditions. These parameters influence the fraction of elementary defects involved with the three reaction paths described in *section 2.4.1*, hence determine the fate of irradiation-induced defects and the extent of irradiation hardening in an alloy. The effect of dose rate is particularly concerning, as this parameter varies dramatically depending on the radiation source (see *table 2.3*).

2.5 Radiation Effects - Structural Integrity

A common goal in fusion materials research programmes is the development of materials to extend performance criteria such as component lifetime and operating temperature range, whilst maintaining structural integrity in the severe radiation environment of a fusion reactor. Hence, mechanical testing provides essential information and has a major role in materials development.

2.5.1 Developed Reduced Activation Ferritic and Ferritic/Martensitic Steels

The development of reduced activation ferritic/martensitic (RAFM) and ferritic (RAF) steels has been predominantly led by the EU and Japan fusion energy programmes [160]. In Japan, reference alloys F82H and JLF-1 are currently under development and in response to initial experience with these alloys and other laboratory heats, the EU developed a reference alloy known as EUROFER-97. In addition to these three reference alloys, several laboratory heats (such as Chinese low activation martensitic steel (CLAM) and EU-OPTIFER), ODS variants, ^{10}B, ^{58}Ni, ^{60}Ni and ^{54}Fe doped material, and conventional ferritic/martensitic steels developed for fission (such as MANET II), are being investigated in several irradiation experiments. The chemical compositions after manufacture of these alloys are shown in *table 2.6* [161, 162]. All compositions under development have a Cr content near 8-9wt%, in response to a superior resistance to embrittlement (*figure 2.5*) [31].

Table 2.6 – Chemical compositions achieved in several RAFM steels and conventional F/M steel (MANET II) (in wt% and ppm) (data from [161, 162]).

	Cr	W	V	Ta	Mo	Ni	Nb	Mn	Si	C	N
EUROFER 97	8.9	1.1	0.2	0.14	10-32	70-280	2-7	0.47		0.11	0.018-0.034
F82H	7.46	1.96	0.15	0	30	200	1	0.21	0.1	0.09	0.023
JLF-1	8.87	1.9	0.19	0.084				0.48	0.24	0.1	0.0244
CLAM	8.98	1.55	0.21	0.15				0.4	0.01	0.11	0.02
OPTIFER V	9.48	0.985	0.245	0.061	50	50	70	0.39	60	0.12	0.0225
MANET II	10.3	-	0.2	-	6100	6800	1400	0.78	1900	0.11	0.031

Several low temperature, fast fission neutron experiments have been carried out in the BR2 reactor (Belgium) in the range of 0.3-2dpa, the HFR (High Flux Reactor, Netherlands) to ~10dpa, and in the Bor60 reactor (Russia) in the range of 30-70dpa [60, 163]. *Figure 2.17a* compares the increase in yield stress of RAFM steels, conventional 9Cr-1Mo steels and ODS variants, after low temperature irradiation (300-330˚C) with doses up to 80dpa [58]. In comparison to conventional steels (9%Cr1%Mo), a superior resistance to low temperature hardening is clearly evident in RAFM steels and is further enhanced in ODS variants. In addition, impact testing of the same materials identified that conventional steels suffered a larger irradiation-induced ΔDBTT compared to that of RAFM steels (*figure 2.17b)* [58].

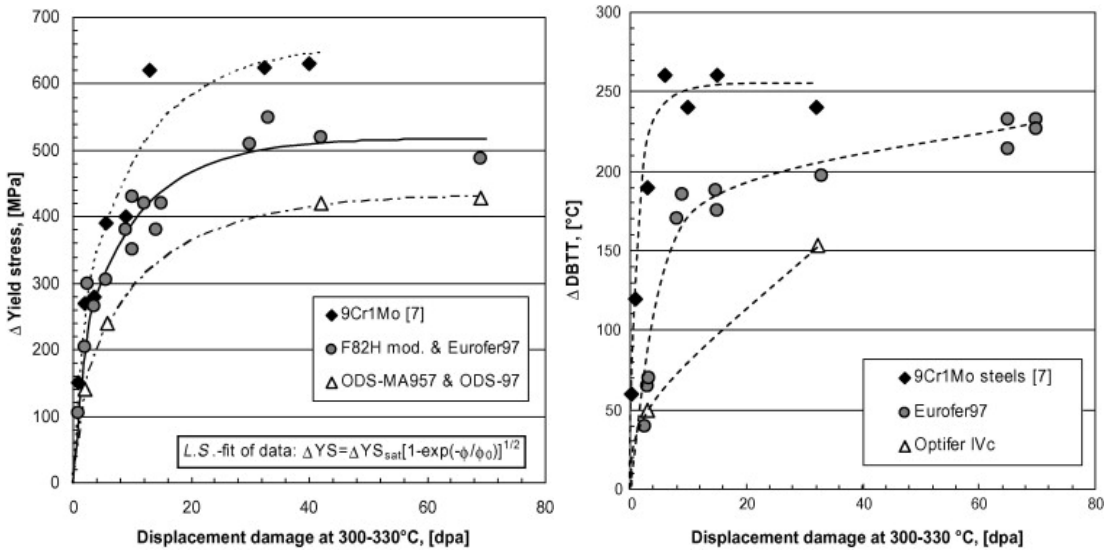

a) **b)**

Figure 2.17 – Variation in mechanical properties with dose in RAFM steels, conventional 9Cr-1Mo steels and ODS, irradiated at 300-330˚C, (a) increase in yield stress (MPa) and (b) increase in DBTT (˚C) [58].

The data shown in *figure 2.17a* suggest that the increase in irradiation hardening saturates with dose, although a slightly higher irradiation temperature for the high dose (~70dpa) RAFM steel of 350˚C [60] may have caused reduced hardening compared to the lower 300-330˚C irradiations. Saturation appears to occur in all materials and irradiation temperatures at approximately 40dpa. This trend is not observed in the impact properties shown in *figure 2.17b*, which shows a large shift in DBTT with dose (~20˚C/dpa) to 10dpa, followed by a much smaller increase (<1˚C/dpa) which has not saturated at >70dpa. This implies that irradiation embrittlement develops by both hardening and non-hardening mechanisms.

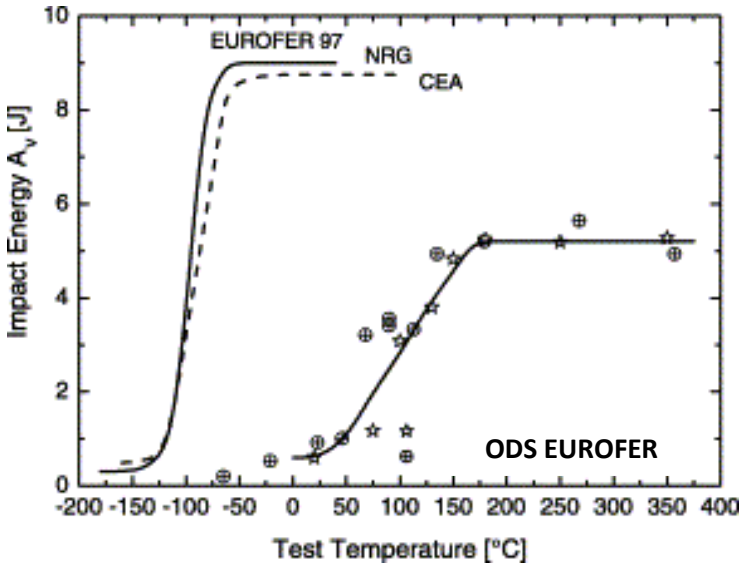

Figure 2.18 – Test temperature dependence and absorbed impact energy vs. test temperature of SSTT specimens of un-irradiated EUROFER-97 and ODS-EUROFER (redrawn from [161]).

Data which present only differences in mechanical properties from the original un-irradiated material, may mask the absolute values of the mechanical properties and may be misleading. Lindau et al. [161] compared the mechanical properties of standard EUROFER-97 and an ODS-EUROFER. Although the ODS-EUROFER alloy had superior creep strength, SSTT impact tests identified poor fracture toughness compared to EUROFER-97 (*figure 2.18*). The reduction in upper shelf energy (USE) from 9J to 5.4J and increase in DBTT from -100˚C to 70-100˚C before irradiation, is unsatisfactory in a structural material for first wall components.

Transmutation Gas – Mechanical Behaviour

The experiments discussed above have been carried out using fast fission neutrons; this may not include the effects of heightened transmutation gas production, which is expected from a 14MeV fusion neutron spectrum. Transmutation gases can dramatically change radiation

damage in materials, and result in an increase in radiation hardening and embrittlement above that of displacement damage alone [11, 15, 28, 50].

Several experiments utilising ^{10}B, ^{58}Ni and ^{60}Ni doped materials[4] to simulate transmutation He (see *section 2.2.2*) have now been undertaken. Klueh et al. [56] identified a 68% larger increase in the DBTT of 9Cr-2WVTa doped with 2%Ni compared to the base alloy after neutron irradiation in the mixed-spectrum high flux isotope reactor (HFIR) to 11dpa. This was attributed to the production of 115appm He in the Ni-doped alloy compared to 5appm He in the base alloy. A similar investigation of EUROFER-97 conducted by Materna-Morris et al. [84], used specimens of EUROFER-97 (natural B<10ppm) and variants of the same alloy doped with 82ppm $^{natural}B$, 83ppm ^{10}B and 1160ppm ^{10}B. The alloys were irradiated in the HFR (Petten, Netherlands) to an average dose of 16.3dpa at various temperatures from 250-450˚C. Tensile testing indicated that radiation induced hardening was higher in the 83ppm ^{10}B-doped alloy (~415appm He) than in the 82ppm $^{natural}B$-doped alloy (~80appm He). Similar strengthening was observed in the 1160ppm^{10}B-doped alloy (~5800appm He) with evidence of intergranular fracture.

Helium production using Ni and B doping methods could be considered inconclusive, due to potential artefacts in the radiation response of these alloys, resulting from the presence of the 'foreign' doping elements. Boron is highly insoluble in the Fe matrix and can form precipitates at preferred sites such as grain boundaries. This results in an inhomogeneous production and distribution of He during irradiation, and may provide an explanation for the small brittle areas found around former B-precipitates, shown in *figure 2.19b* [84]. Dual-ion

[4] ^{10}B, ^{58}Ni and ^{60}Ni are used to simulate fusion levels of transmutation He production with fission-spectrum neutrons.

implantations (Fe^{3+}, He^{+}) in F82H doped with 0, 1 and 2%Ni to doses of 5dpa and 10appm He/dpa, identified that He had no effect on the indentation hardness; however, irradiation-induced hardening increased with Ni content (*figure 2.19a*) [93].

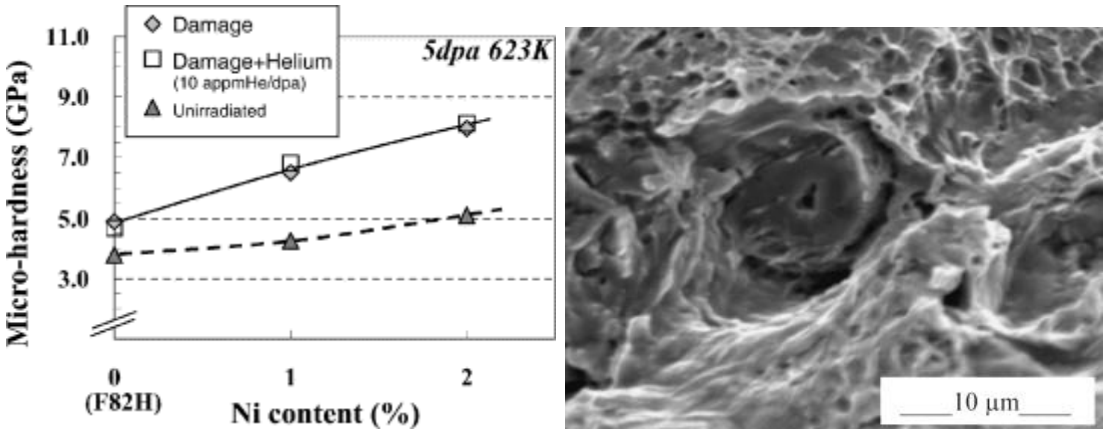

a) **b)**

Figure 2.19 –Micro-hardness increase as a result of He and Ni content in dual-ion implantations [93] (a) and area of brittle fracture around former B-precipitate [84] (b).

The introduction of He through ion-implantation does not involve the use of foreign doping elements and is fairly versatile in terms of He/dpa ratio and irradiation temperature. The small effect of He on irradiation hardening in *figure 2.19a* has been replicated by numerous dual-ion implantation experiments at low doses [93, 164, 165]. However, at doses of 60dpa Ogiwara et al. [166] reported that dual-implantation of Fe^{3+} and He^{+} significantly enhanced radiation hardening. In these experiments, a finer microstructure in the presence of He was observed [166]; the He-enhanced radiation hardening increased with increasing temperature and thermal recovery by annealing was hindered in the dual-implanted material [164, 165]. This suggests that He may reduce defect mobility and microstructural evolution; thus, a longer duration (such as that in neutron irradiation) or higher temperatures are required for defects and He to form stable obstacles such as dislocation

loops or voids. The higher dose rates inherent in ion-implantation methods may have caused the delay in He-enhanced irradiation hardening until higher doses relative to neutron experiments.

In summary, the effect of combined irradiation and production of transmutation gases has been simulated by several different methods. Potential enhancement in irradiation hardening and non-hardening embrittlement has been identified in the presence of H and He, separately and in combination, however, such effects are yet to be realised experimentally with fusion realistic gas/dpa ratios.

2.5.2 Pure Fe and Fe-Cr Alloys

Experimental research of developed candidate alloys is an important process for the fast screening and improvement of materials for the first wall of a fusion reactor. However, the mechanisms which change the radiation response of an alloy are often hard to establish due to the potential range of radiation phenomena in such complex alloy systems. Reducing the number of factors which lead to changes in the radiation response of a system can help in the identification of fundamental mechanisms and their dependent variables. For example, in 1954 Kunz and Holden [167] showed that the activation energy required for the recovery of irradiated single crystal Fe was equal to the activation energy for self-diffusion in Fe at 3.1eV. This led to the conclusion that displacement damage was likely to be in the form of agglomerated stable defects, which require higher activation energy for recovery compared to the diffusion of available single point defects. Analogous to the work of Kunz and Holden, a number of investigations have been carried out on simplified pure Fe and model Fe-Cr alloys, in order to identify fundamental radiation damage mechanisms.

Irradiation Hardening

Ultra-pure polycrystalline iron, neutron irradiated to relatively low doses of ~0.0075-0.375dpa at 320K and 523K, was investigated by Singh et al. [168]. Even at the lowest dose, an increase in yield stress from 235MPa to 275MPa was found at 320K, which further increased with dose up to 414MPa. The magnitude of a yield drop present in both un-irradiated and irradiated specimens was enhanced with dose, and during deformation all of the irradiated specimens showed no or very little work hardening. Suganuma et al. [169, 170] produced neutron-irradiated pure Fe and Fe-Cr alloys to similar low doses of ~0.009-0.0165dpa at ~400K and ~473K. As shown in *figure 2.20*, the radiation-induced increase in yield stress was enhanced with an increase in Cr content and decrease in test temperature. The ductility and total elongation was found to reduce dramatically in the irradiated alloys as test temperature decreased from 283K to 77K and in some cases brittle fracture occurred before deformation took place. Work hardening was found to decrease in the irradiated alloys; this effect was enhanced at lower test temperatures and Cr content. Finally, Luppo et al. [171] also confirmed a comparable radiation-induced increase in yield stress and reduction in work-hardening coefficient, in Fe and Fe-Cr alloys subjected to 590MeV protons at similar low doses of 0.001-0.3dpa.

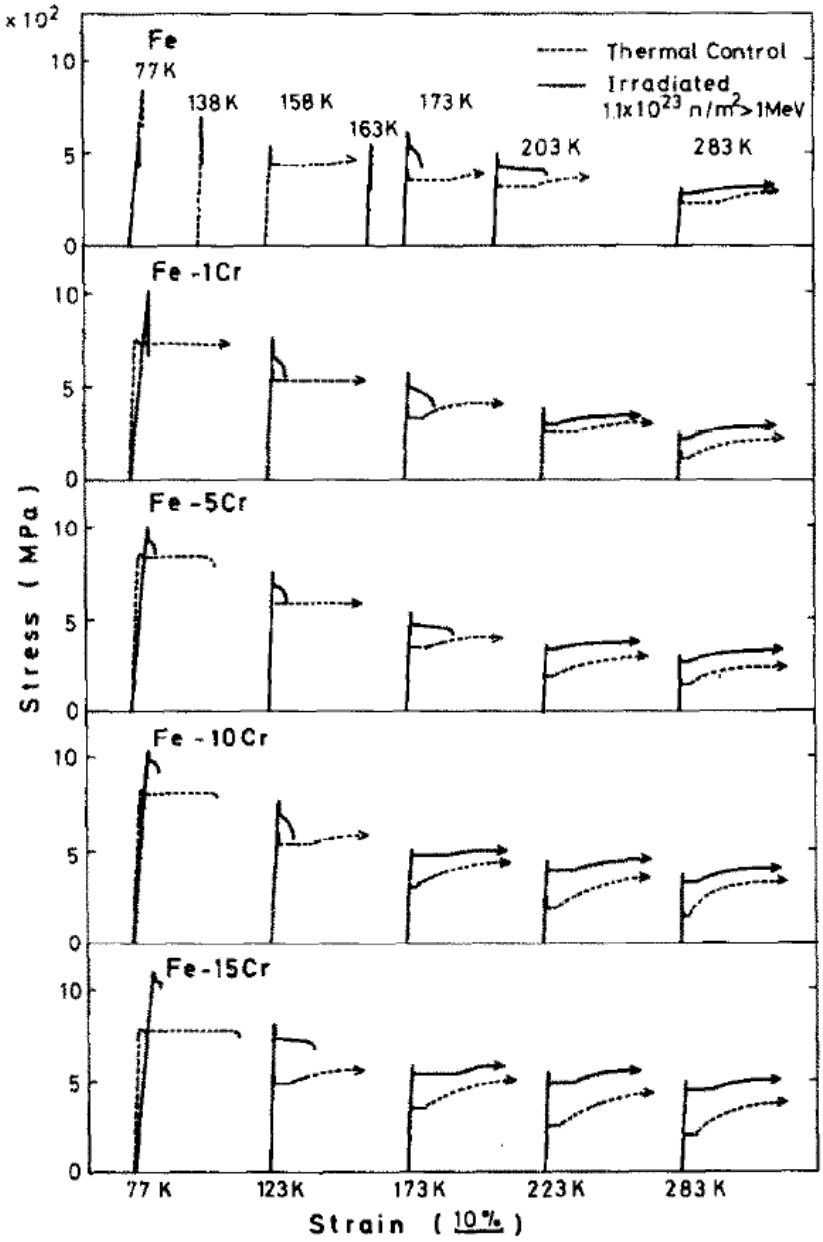

Figure 2.20 - Engineering stress-strain curves before and after irradiation in Fe-Cr alloys [169, 170].

Using the data from various test temperatures, Suganuma et al. [169, 170] divided the radiation-induced increase in flow stress into thermal ($\Delta\sigma_t$) and athermal ($\Delta\sigma_a$) components described by:

$$\Delta\sigma_y = \Delta\sigma_t + \Delta\sigma_a \qquad \boldsymbol{equation\ 2.5}$$

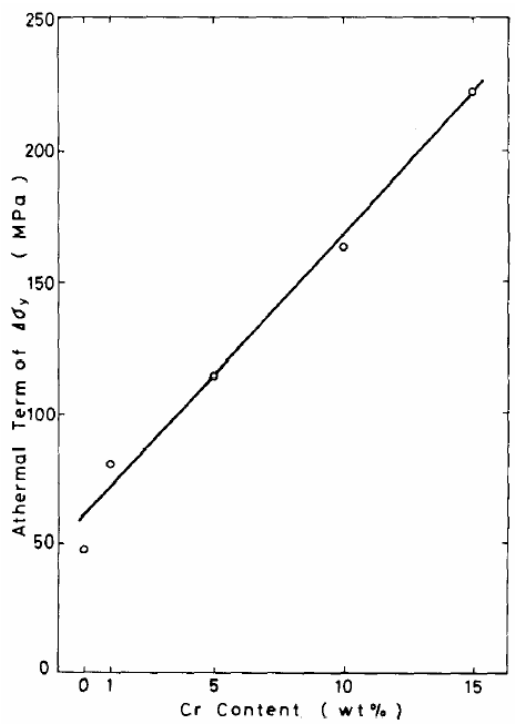

Figure 2.21 – Variation in radiation-induced athermal component ($\Delta\sigma_a$) with Cr content [169].

At a constant dose, the temperature-independent, athermal component was found to increase linearly with Cr content, as shown in *figure 2.21* [169]. This 'mechanical strength' term may be concerned with resistance to dislocation motion (a result of solution hardening and obstacles to dislocation glide), in the absence of free energy contributions in $\Delta\sigma_t$. Suganuma et al. [169, 170] related $\Delta\sigma_a$ to dislocation barrier strengthening and expressed $\Delta\sigma_a$ in the form of the Orowan model:

$$\Delta\sigma_a = \alpha G b l_d^{-1} \qquad \textbf{equation 2.6}$$

where G is the shear modulus, b is the Burgers vector, l_d is the defect (barrier) spacing and α is a constant, which depends on the defect obstacle strength. Initially, it was suggested

that the increasing yield stresses observed in higher Cr content alloys must be due to smaller defect spacing (l_d). However, according to calculations using *equation 2.6* the defect spacing alone did not account for the increased strengthening and that the most probable effect of Cr on $\Delta\sigma_a$ was the modification of defect obstacle strength (α).

Several researchers have made attempts to quantify the barrier strength term, α, in *equation 2.6* [64, 95, 172, 173] and have calculated values from 0.5 to 2.4. By fitting experimental measurements of yield stress taken from neutron irradiated Fe-Cr alloys (with 0-12%Cr) to a dose of 0.06dpa at 300°C, Matijasevic et al. [64] calculated that the defect strength was constant with a value $\alpha = 0.5$. However, calculations of the defect strength for the same alloys irradiated to larger doses identified an increase in α which varied with Cr content. This discrepancy could be produced by several assumptions made in the application of the Orowan mechanism:

(i) Defects which are un-resolvable in the TEM are ignored.

(ii) Defects are sessile and cannot migrate to dislocations during slip, changing l_d.

(iii) All defects produce the same defect obstacle strength, α, regardless of dislocation loop type, Burgers vector, size and composition.

As described in *section 2.5.3*, such assumptions are invalid particularly as defects develop with increasing dose as was the case in the investigations conducted by Matijasevic et al. [64].

The thermal component $\Delta\sigma_t$ in *equation 2.5* is dependent upon available free energy for dislocations to overcome barriers by thermal fluctuations. On the scale of a dislocation core, free energy is in the form of atomic vibration; hence, the resistance to dislocation motion is dependent on both lattice temperature and strain rate. Suganuma et al. [169, 170] suggested that the reduction in $\Delta\sigma_t$ with increasing Cr content was due to the stabilisation and enhanced rigidity of defects such as clusters and loops in the presence of Cr.

The irradiation of Fe and Fe-Cr alloys to higher doses of 7, 38 and 37dpa at temperatures of 365, 403 and 574˚C respectively, was performed by Hamilton and Gelles [174]. Hardening was observed at irradiation temperatures of 365 and 403˚C, with no significant differences between temperatures or Cr content. However, at 574˚C there was no hardening was observed except for Cr>12%. This suggested that at the lower temperatures, hardening mechanisms saturated by 7dpa; while at higher temperatures and doses an additional hardening mechanism took place in the higher Cr content alloys. It was proposed that this may have been due to the formation of σ and/or α' phases as a result of irradiation-induced phase evolution. Evidence of α-α' un-mixing has been identified directly in the TEM in similar ion-irradiation experiments in Fe-12%Cr and Fe-18%Cr [172], and by SANS in neutron-irradiated Fe-9%Cr and Fe-12%Cr [95, 175]. The relatively low saturation doses observed in Fe and Fe-Cr alloys of <7dpa in neutron irradiation [174] and ~1dpa in ion-implantation [95], compared to ~40dpa in RAFM steels (*figure 2.17*) [58], indicates that additional hardening mechanisms, possibly from chemical segregation, exist in more complex alloys.

2.5.3 Deformation Mode

Figure 2.22 shows examples of engineering stress-strain curves in RAFM steels and conventional steels before and after irradiation [176]. The simplification of irradiation-induced hardening into two components in *equation 2.5* provides a good description for the flow stress (lower yield point) of the material; however it does not include the increase in yield drop or change in work hardening behaviour observed in the irradiated alloys shown in *figures 2.20* and *2.22*. Singh et al. [168] proposed that the decoration of 'grown-in' dislocations by mobile SIA clusters could create the radiation-enhanced yield drop behaviour. Yet, despite very low impurity levels reported, a yield drop was observed in the un-irradiated material, suggesting the presence of interstitial impurities (N,C) locking dislocations by a Cottrell mechanism. The influence of Cottrell atmospheres may be enhanced by irradiation, because dislocation loops may be strengthened by N and C impurities in a similar manner. Thus, 'source-hardening' may be the dominant mechanism controlling the deformation behaviour of irradiated ferritic steels.

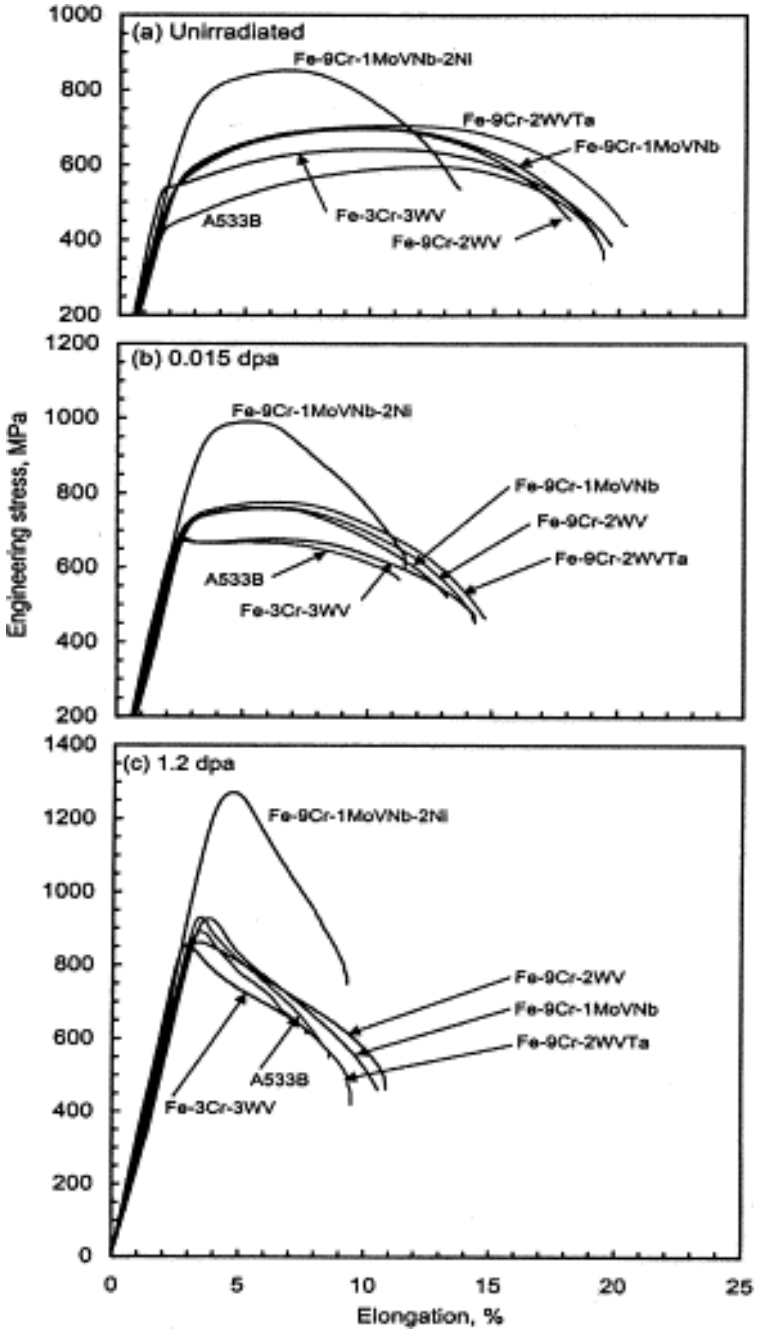

Figure 2.22 – Examples of engineering stress-strain curves before and after irradiation in RAFM and conventional steels [176].

Unusual yielding and work-hardening phenomena have been identified in many irradiation experiments in pure Fe, Fe-Cr alloys [168-171, 174, 177, 178] and developed RAFM steels [58, 84, 176, 179]. Hamilton et al. [178] described yield responses in irradiated Fe-Cr alloys

as 'bumps', which are analogous to the curves in the lower graph of *figure 2.22* and are associated with a reduced work-hardening coefficient. A possible explanation of this behaviour is described by Singh et al. [168]:

"...the decoration of dislocations with gliding SIA clusters becomes more effective with increasing dose. As a result, dislocations could be generated only at the points of singularities with a high stress concentration factor. Once these sources are activated they lead to the formation of cleared channels and most of the plastic deformation occurs in a very localized fashion in these channels."

The relationship between radiation and work-hardening coefficient (n), with evidence of associated dislocation channelling was produced by Luppo et al. [171] using proton irradiations (*figure 2.23*).

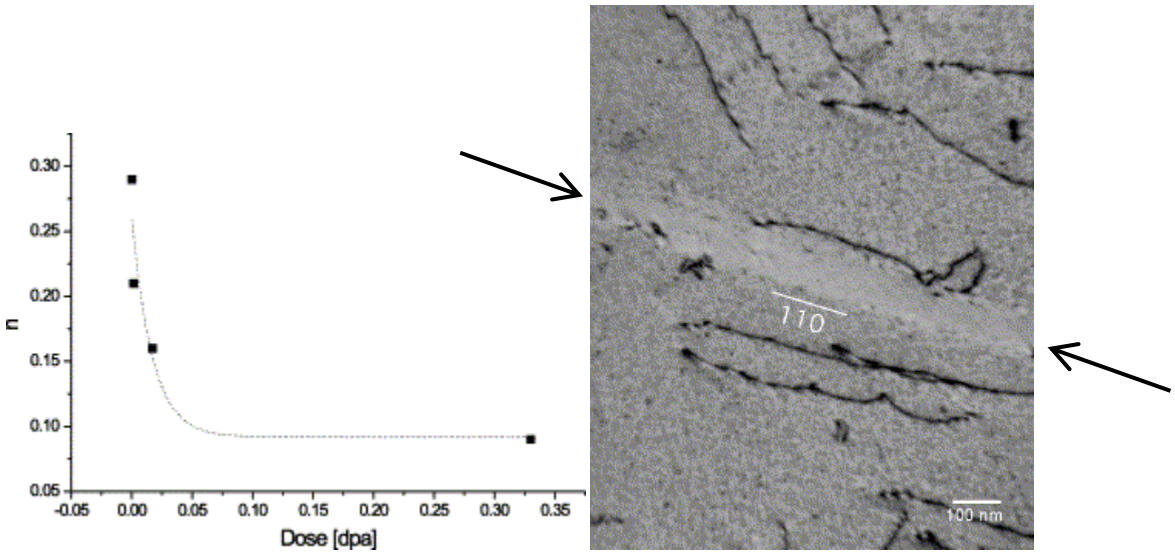

a) **b)**

Figure 2.23 – (a) Work-hardening coefficient (n) vs. dose of pure Fe and (b) TEM image of defect-free channel in deformed Fe-12Cr (590MeV proton irradiated to 0.33dpa) [171].

The removal of defects in the channels identified by Hardie et al. [91] and Luppo et al. [171] is consistent with observed reductions in defect density of TEM samples taken beneath indentations in irradiated ferritic steels [93, 165]. Gelles and Schäublin [180] proposed that the interaction between glissile $a_0/2<111>$ dislocations and $a_0<100>$ loops may remove the entire loop resulting in a significant reduction in energy. It was added that the removal of the $a_0<100>$ loop according to the reaction $a_0/2[111]+a_0[100]=a_0/2<111>$, is sensitive to the sense of the dislocation loop and that interactions with loops of various combinations of <111> and <100> Burgers vectors are not energetically favourable; thus these form a barrier to the glissile dislocation. MD simulations have shown that dislocation loops are attracted to the stress field of a glissile dislocation and can migrate along their Burgers vector towards the slip plane [72, 73]. These simulations support the observation of cleared channels having a thickness in the order of 100nm, due to loop migration over a distance of several tens of nanometres. The interaction between glissile dislocations and loops observed in MD calculations agree with the reaction between a $a_0/2<111>$ glissile dislocation and $a_0[100]$ type loops proposed by Gelles and Schäublin. For loops >100 SIAs, it was observed that the reaction between the dislocation and loop creates a dislocation segment with $b=a_0/2<111>$ for $a_0<100>$ type loops and a sessile $b=a_0<100>$ segment for $a_0/2<111>$ type loops, which glide across the loop habit plane annihilating the loop. The stress required for the absorption of a dislocation loop ranges from <100MPa to nearly 600MPa depending on its Burgers vector, size and composition, and test parameters such as strain rate and test temperature [72, 73].

The migration of loops to glissile dislocations may cause an increase in the number of obstacles and effectively reduce the defect spacing, l_d; this may account for the common overestimation of α in *equation 2.6*. The subsequent annihilation of the dislocation loops

appears to produce defect free channels as shown in *figure 2.23* and the yield drop behaviour in figure 2.18 and 2.20. The sessile a_0<100> segment increases the energy or stress required for $a_0/2$<111> loop annihilation, thus the observed hardening and reduction in work-hardening coefficient may also be influenced by the fraction of both types of loops within the irradiated material.

2.5.4 Non-Hardening Irradiation Embrittlement

Irradiation-induced non-hardening embritlement and the reduction of fracture stress have been observed in both developed alloys and model Fe-Cr alloys. At low temperatures, pure Fe and Fe-Cr alloys neutron-irradiated to relatively low doses (~0.0165dpa) were found to fail by intergranular fracture, cleavage, or a mixture of the two [169]. At room temperature, Fe-Cr alloys with 15 and 18%Cr neutron-irradiated to ~7dpa failed by brittle fracture [174]. Such reduction in fracture stress has been commonly attributed to the presence of transmutation gases [61]. However, there were minimal transmutation reactions during the low dose, low energy neutron irradiations in the examples discussed above, suggesting that other embrittlement mechanisms exist.

UN-IRRADIATED **IRRADIATED**

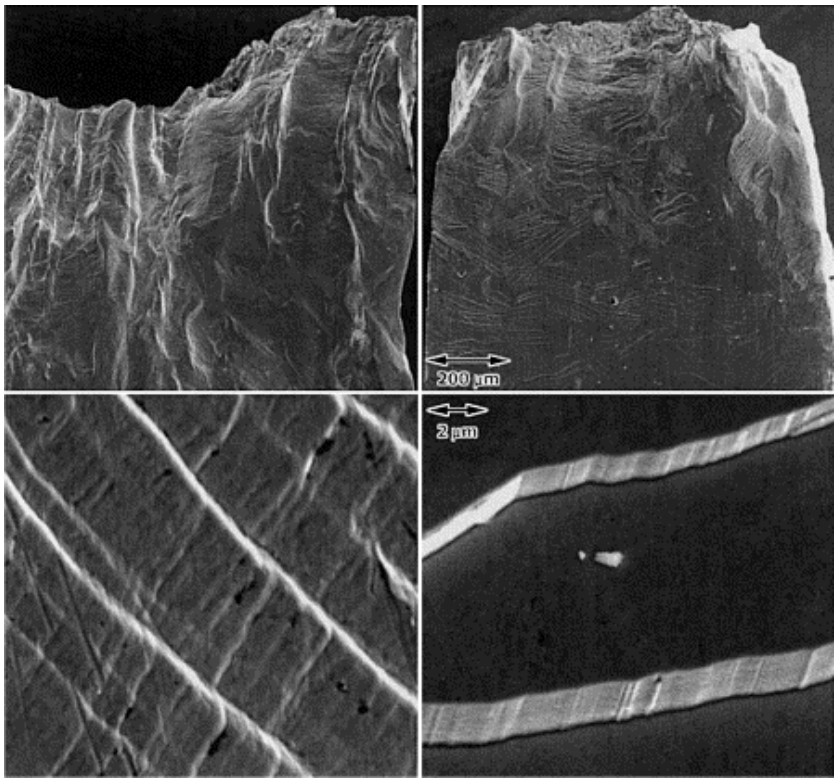

Figure 2.24 – Fracture surfaces of Fe-9%Cr before irradiation (left) and large steps on the fracture surface after irradiation (right) [180].

In the higher Cr content material, α'-phases (and other brittle phases e.g. σ-phases) may be produced by radiation; however, this does not explain radiation embrittlement at low Cr content and in pure Fe. SEM observations of fracture surfaces by Gelles and Schäublin [180] are shown in *figure 2.24*. Large steps were observed on the fracture surface of irradiated Fe 9%Cr. It was suggested that the meeting of dislocation channels at grain boundaries or other interfaces, cause large slip steps, and may lead to high stress concentrations and crack nucleation at these sites [168].

2.5.5 Summary

Mechanical testing has revealed that RAFM steels exhibit complex irradiation hardening and embrittlement compared to model Fe-Cr alloys, which results in the saturation of hardening and further embrittlement at higher doses compared to the model alloys. There are a number of artefacts produced by methods used for the simulation of transmutation gases for all materials; thus enhancement of hardening and embrittlement has been observed in the presence of He, yet the extent of these effects are difficult to quantify.

Irradiation hardening in Fe-Cr alloys is strongly dependent on Cr content. Whilst the athermal component ($\Delta\sigma_a$) of hardening is found to increase linearly with Cr content, the thermal component ($\Delta\sigma_t$) of hardening decreases with Cr content. It was proposed that the decrease in $\Delta\sigma_t$ is caused due to the stabilisation and enhanced rigidity of defects by Cr. There are a number of investigations which have observed unusual plastic behaviour, reductions in work hardening and dislocation channelling caused by defect annihilation by glissile dislocations. This suggests that the interactions between irradiation induced defects and glissile dislocations are dependent on the various types of defects in the material and their impeding energy on the glide of dislocations.

2.6 Conclusion and Research Outline

Reduced Activation Ferritic/Martensitic (RAFM) steels are recognised as leading candidate structural materials for fusion reactors, due to technical maturity and superior properties in a radiation environment. However, further work is required to understand the fundamental mechanisms responsible for the irradiation-induced hardening and embrittlement exhibited in RAFM steels, particularly the influence of Cr in ΔDBTT shown in *figure 2.5*.

In the absence of a realistic radiation environment of a fusion reactor a number of computational and experimental simulation methods are being used. As described in *section 2.2.2*, the small sample volumes inherent in both computational modelling and experimental methods may not include all components of a microstructure which is representative of the bulk material. In addition, various parameters of the radiation environment can have a considerable influence on the radiation response of a material, and can dramatically change structural integrity.

Unlike many microscopical characterisation techniques such as TEM and APT, the use of micro-mechanical testing techniques is early in development and to date little is known regarding its validity for irradiated materials. Thus work conducted in *chapter 5* investigates various micro-scale mechanical testing techniques required for both ion and neutron irradiated materials and the implications of testing at this small scale. Several radiation sources are currently contributing to research on radiation damage in materials; however there are several distinct differences in the radiation parameters between each source, such

as a wide range of dose rates shown in *table 2.3*. The investigation presented in *chapter 6* directly compares a Fe 6%Cr alloy irradiated with both neutrons and ions, to investigate the differences between both radiation sources. C*hapter 7* provides insights into the evolution of damage, irradiation hardening and the role of Cr in Fe-Cr alloys by investigating a series of ultra-high purity Fe-Cr alloys ion-irradiated to different doses (0.06, 0.6 and 6dpa), dose rates ($3x10^{-5}$dpa/s and $6x10^{-4}$dpa/s) and at different temperatures (300-500°C). Finally, *Chapter 8* discusses the implications of these results for fusion materials testing and the influence of Cr on the irradiation-induced hardening of steels.

3 MATERIALS AND EXPERIMENTAL METHODS

This chapter will outline the main experimental techniques used for this work; specific details of individual experiments will be covered in their corresponding chapter.

3.1 Materials and Sample Preparation

The materials and preparation methods used are unique to each investigation undertaken; therefore these details are described at the beginning of the relevant chapter for each investigation.

3.2 Ion Implantation

Ion implantations were conducted by means of electrostatic (Van De Graff) charged particle accelerators at Surrey Ion Beam Centre, UK (*Chapters 5 and 7*) and Helmholtz Zentrum Dresden Rossendorf (HZDR), Germany (*Chapter 6*). Samples were irradiated with Fe ions with multiple charges and energies in order to create a near-uniform damage layer with depth at the sample surface. The ion exposure, temperature and beam current were controlled and measured during implantation, which enabled the investigation of irradiation parameters such as dose, dose rate and irradiation temperature.

3.2.1 Sample Temperature Control

Extensive temperature calibration work was undertaken in Surrey to ensure that the sample temperature during irradiation is accurately controlled and measured. Prior to work conducted for this thesis, the base plate design consisted of a series of components including stainless steel sample clamps, a stainless steel plate, a copper plate and the heating element. Heat was supplied with a tungsten foil element behind the copper plate and controlled by using a power supply with an on/off temperature controller and a K-type thermocouple at the back of the copper plate. Previous calibration work with this arrangement had been conducted at atmospheric pressure and suggested that the temperature of the samples and base plate was near identical to that of the control temperature, i.e. the temperature measured by a thermocouple placed near the heating element.

Figure 3.1a shows data from a base plate heating experiment conducted in the beam line chamber and with a base plate used prior to the investigations reported in this thesis. This data were produced from: (i) the thermocouple positioned by the heating element; (ii) a thermocouple screwed against the front of the base plate and (iii) a pyrometer targeted on the front of the base plate through a viewing port to the side of the main beam line. During heating (0 to 130 minutes), a large difference in the temperature measured between the front and back thermocouples was observed which increased with higher control temperature. The temperature measured by the pyrometer was slightly higher than that measured by the front thermocouple, which may have been caused by additional thermal radiation from the copper plate and surrounding chamber.

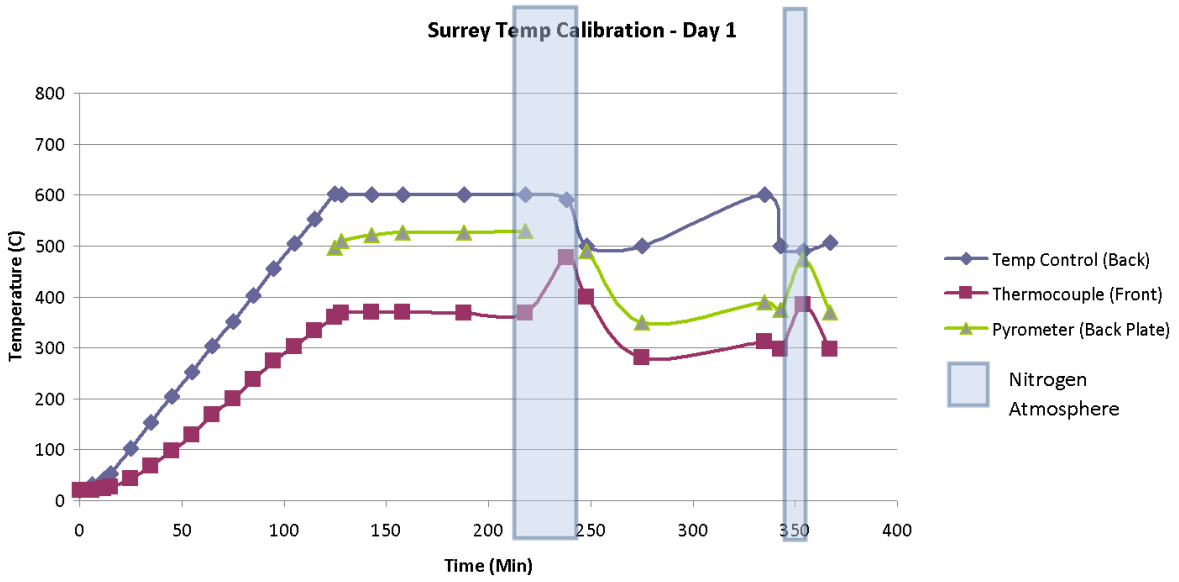

a.

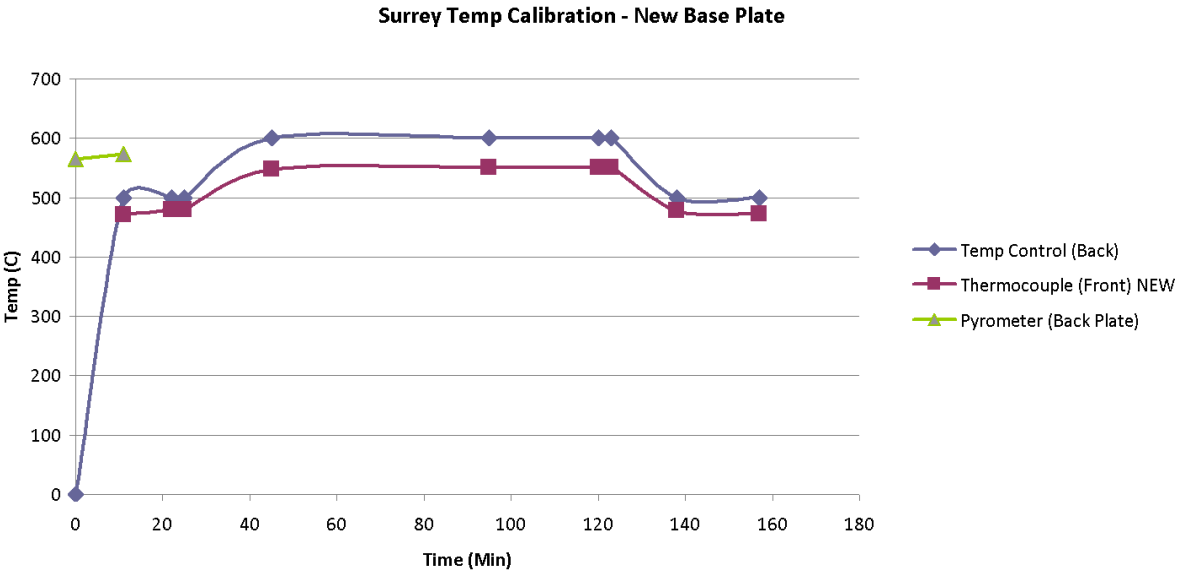

b.

Figure 3.1 – Temperature calibration data for old base plate design (a) and improved design (b).

This experiment was conducted in vacuum pressures typical of those during ion implantation, 10^{-3}Pa (10^{-5}mbar); however, at 210 and 340 minutes the sample chamber was purged with nitrogen to a pressure of $2x10^{4}$Pa (200mbar). Measured temperatures in the presence of a nitrogen atmosphere all tended towards the same value, producing similar

observations to the previous temperature calibrations undertaken in atmosphere. The temperature differences are caused by a low heat transfer coefficient at interfaces between components in vacuum. The heat transfer coefficient is increased by the presence of gas resulting in less heat loss.

New sample clamps and a base plate were designed to overcome these effects. This included the reduction of thermal interfaces from element to sample (by removal of a copper back plate), placing powdered graphite in-between interfaces and fixing a thermocouple into a deep drilled hole in the sample clamp with ceramic epoxy resin. The temperature data for the improved design are shown in *figure 3.1b*.

All implantation experiments reported in this thesis used the temperature measurement from the front thermocouple to control irradiation temperature. The sample arrangement for all implantations at Surrey can be seen in *figure 3.2*. The samples were mechanically secured onto specifically manufactured mild steel clamps, designed to hold the sample against the clamp for good thermal contact whilst preventing any damage to the sample surface. This was achieved by a dove tail section and grub screws machined with a conical end, providing two surfaces which pressed against the outer edges of the sample as shown in *figure 3.2b*. For consistency, a similar design was created for the base plate used at the Rossendorf Ion Beam Centre.

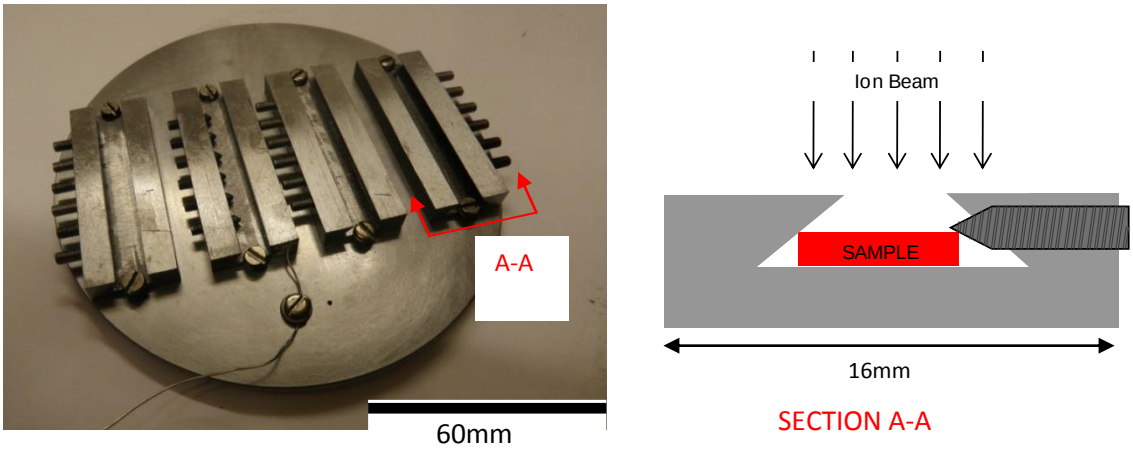

Figure 3.2 – New base plate design with 4 sample clamps (a) and section A-A of a sample clamp showing ion beam direction and a fixed sample (b).

3.2.2 Damage Calculations

For the design of ion beam conditions during implantation the Monte Carlo Code SRIM 2008 (Stopping Range of Ions in Matter) was used to calculate the distribution of damage [181]. These calculations used an average of 1000 ions in pure iron and the recommended displacement energy of 40eV [182]. Chromium has the same displacement energy as iron and has minimal influence on density; therefore, any differences in these damage calculations due to chromium are expected to be minimal.

Damage calculations were conducted using the 'Detailed Calculation with Full Damage Cascades' model, where every collision causing damage is simulated until the incident ion and all recoil atoms are below the displacement energy. Data are averaged for all ions in the simulation in the form of vacancies and replacement collisions with depth (per Angstrom) into the sample surface. Total displacements for each Angstrom layer were calculated by:

$$Displacements\ per\ Ion = Replacement\ Collisions + Vacancies \qquad \textbf{equation 3.1}$$

The dpa as a function of depth, x, was then calculated by:

$$dpa(x) = \frac{\phi v(E_i, x)}{n} \qquad \textbf{equation 3.2}$$

where ϕ is the ion fluence, $v(E_i, x)$ is the displacements produced by incident ion of energy E_i as a function of depth, x, (given by SRIM) and n is the atomic density. The atomic density was calculated by using an interatomic distance of 2.48Å (0.248nm) for Fe [183] to calculate the volume of a BCC unit cell of iron multiplied by two (two atoms in a BBC unit cell).

In all experiments, multiple implantation energies were used, resulting in a more uniform total damage with depth into the sample surface. For a given implantation experiment these calculations were conducted for all implantation energies used and the sum of dpa was taken for all energies as shown schematically for 3 energies in *figure 3.3.*

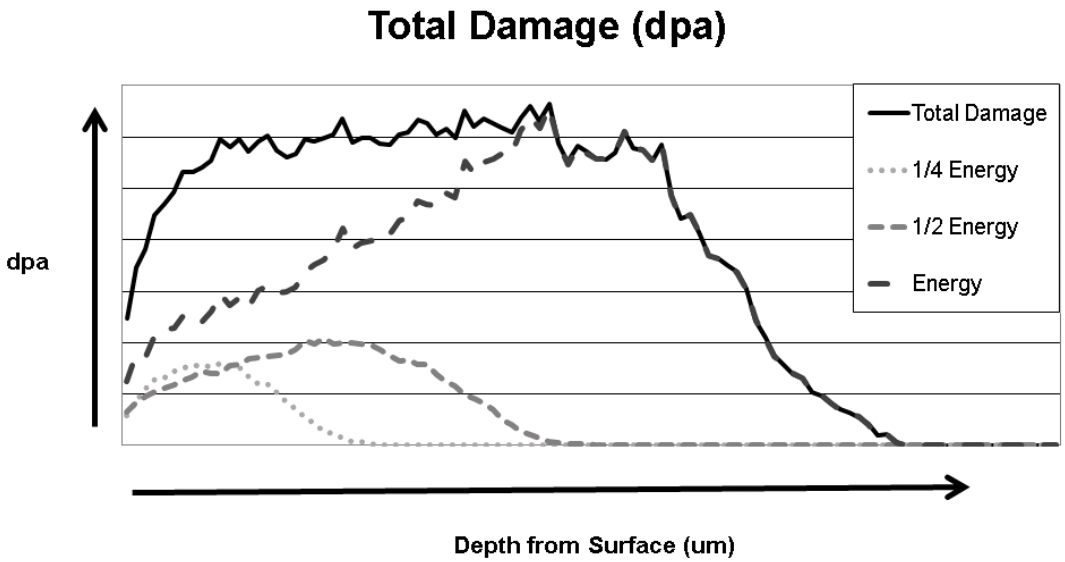

Figure 3.3 - Typical damage as a function of depth into sample surface accumulated with three energies in arbitrary units.

SRIM only calculates the ballistic phase of a collision cascade at 0K and assumes the target material to be amorphous, thus collision chains ('crowdion transfer') and channelling behaviour are not simulated (see *section 2.3.1*). Therefore any differences in the production of damage with crystal orientation are not accounted for in the damage calculations.

3.2.3 Implantation Methods and Known Limitations

Best efforts were made to ensure that radiation damage during ion implantation was produced homogeneously across the volume of the irradiated layer. This is successfully achieved laterally over the area of the samples by raster scanning the 5mm diameter ion beam using a random walk method. The outermost part of the scanned beam area strikes four Faraday cups surrounding an aperture (positioned in front of the samples) shown in *figure 3.4*. This enables the measurement and control of the beam current and total dose during implantation, with accuracy +/- 1%. However, the distribution of damage with depth into the sample surface still remains questionable, due to the use of several energies and assumptions made with SRIM calculations discussed above. It can be seen in *figure 3.3* that the damage produced by the beam of highest energy varies by a factor of 3 over the depth range. During the highest energy irradiation, material at low depths will receive approximately a third of the maximum radiation dose and thus, a third of the maximum dose rate. Subsequently additional lower energies are used to 'top-up' the damage at lower depths and produce a uniform *calculated* damage over the implantation depth range. The production of radiation damage with multiple energies creates layers of material with differing radiation history and may result in local differences in damage microstructures with depth into the sample surface. This may be avoided by the use of a single implantation energy with multiple degrader foils to spread the range of ions and damage into the sample surface; however errors in damage calculations for this type of implantation are increased

with the use of multiple target materials. In addition, access to such an ion beam facility is available at few locations such as JANNUS (CEA, Saclay), which uses a defocused beam. Attempts to use this method produced an implantation with poor lateral homogeneity over the target area resulting in differing dose and dose rate across the range of samples.

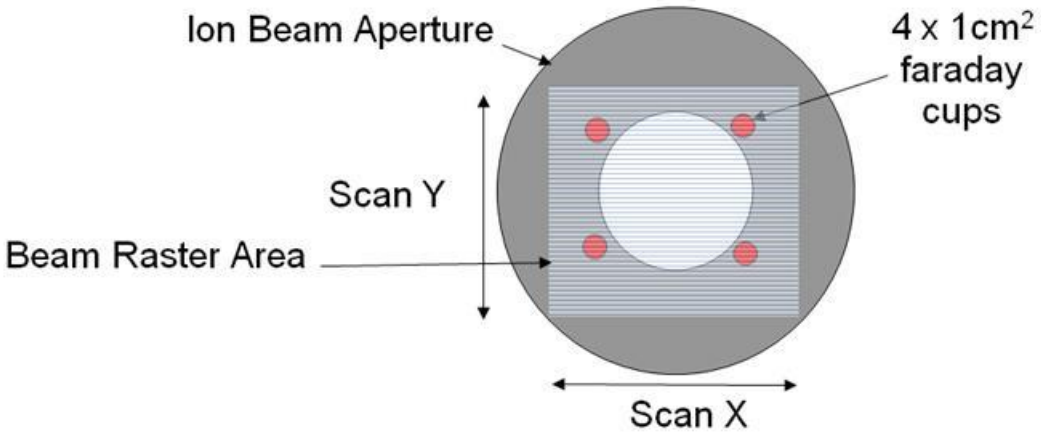

Figure 3.4 – Schematic of a beam line aperture with 4 faraday cups and scanned beam area (shaded). Typical aperture dimensions are 1 to 4 inches.

3.3 Mechanical Testing

Implantation energies available at the Surrey Ion Beam Centre are limited to 2MeV singly-charged ions and produce an implantation depth of approximately 800nm for Fe^{+} in Fe. Measuring the mechanical properties of such a thin layer of material with an un-irradiated substrate required the use of nanoindentation methods and micromechanical testing methods; these are briefly described in the following sections.

3.3.1 Nanoindentation

Nanoindentation, also known as instrumented indentation or depth-sensing indentation, is a convenient tool for measuring mechanical properties of thin layers and was first developed by Pethica et al. [184] to measure the mechanical properties of stainless steel subjected to N^+ implantation in 1982. Instrumentation and methods have since developed and nanoindentation is now the most commonly used technique to measure the mechanical properties of implanted materials. Current systems allow the application and measurement of a specified force or displacement with resolutions as low as 1µN and 0.2nm respectively [185].

Instrumentation

A large fraction of the nanoindentation work reported in this thesis was carried out using an MTS NANO Indenter XP (MTS NANO Oak Ridge Tennessee, USA). This instrument was fitted with the NANO CSM system allowing dynamic measurement of elastic modulus and hardness as a function of indenter depth.

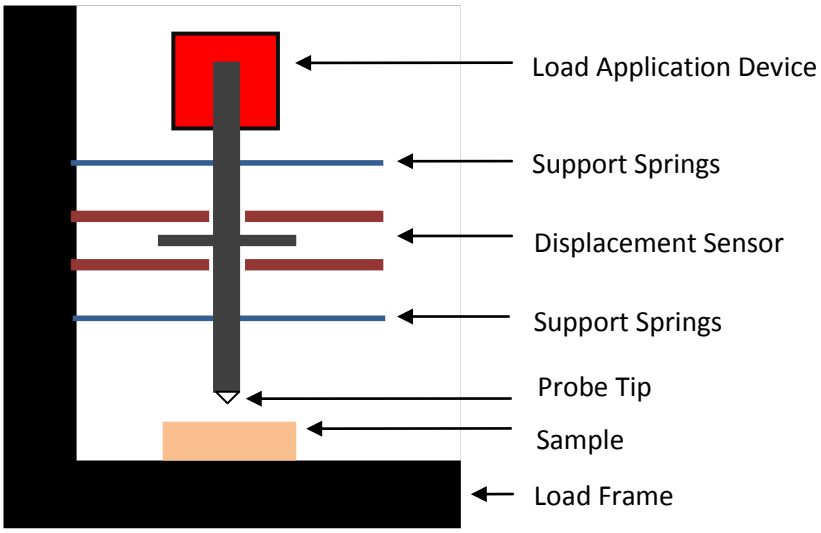

Figure 3.5 - Schematic illustration of a typical nanoindentation system, redrawn from [185].

Figure 3.5 shows a schematic illustration of the hardware installed within the MTS NANO Indenter XP. The indenter column is held in place and restricted from lateral movement by leaf springs, force is applied by using electromagnetic actuation and displacement is measured by a capacitive displacement sensor. The system in *figure 3.5* is inherently a load controlled instrument; however displacement controlled testing can be achieved by using closed loop signal feedback via a proportional-integral-derivative (PID) controller.

During indentation the indenter is driven towards the sample at a constant velocity until contact with the sample surface. This is detected via a change in the stiffness response of the column by using the raw load and raw displacement channels or by using the dynamic stiffness channel (in CSM Mode). The load on the sample was corrected to account for the support spring stiffness by:

$$P = \overbrace{(P_{raw} - P_0)}^{\text{Total Load}} - \overbrace{(h_{raw} - h_0)K_s}^{\text{Reaction Force of Support Springs}} \qquad \textbf{equation 3.3}$$

where P_{raw} is the raw load, P_0 is the raw load at the sample surface, h_{raw} is the raw displacement and h_0 is the raw displacement at the sample surface. K_s is the spring stiffness, $\frac{dP_{raw}}{dh_{raw}}$, measured before contact is made with the sample surface. The displacement into the sample surface was corrected for frame stiffness and for thermal drift and was calculated by:

$$h_c = \overbrace{(h_{raw} - h_0)}^{\text{Total Tip Displacement}} - \overbrace{\frac{P_{raw} - P_0}{K_f}}^{\text{Frame Displacement}} - \overbrace{(t - t_0)Q}^{\text{Thermal Drift}} \qquad \textbf{equation 3.4}$$

Thermal drift is calculated on the unloading part of an indentation at 10% of the maximum load. The indenter is held on the sample whilst displacement data are recorded for 10 seconds, then a least squares fit is used to calculate Q. The frame stiffness K_f is large compared to the stiffness between the indenter tip and sample.

A common component which can significantly degrade nanoindentation data is the sample mounting method which can influence K_f, in particular, differences in sample mounting between the tested and calibration samples. Poor sample mounting can result in an increase the compliance of the load-train; this is identified by a non-linear harmonic contact stiffness or load over stiffness squared, P/S^2 (theoretically independent of indentation depth), with indentation depth during CSM indentation. Several methods were tested prior to the work conducted for this thesis and a thin layer of hot wax was found to produce the best results. Thus, hot wax was used as the mounting method for all experiments reported, however this still had a small effect on the load frame stiffness and mechanical property data as the indentation depth increased. This caused a decrease in the apparent elastic modulus with indentation depth (<10% at 500nm). The use of Berkovich indentation data was restricted to indentation depths <200nm (Surrey 2MeV beam line) and 300nm (Rossendorf 9MeV beam line) for the analysis of ion implanted layers, thus effects of sample mounting in the data are expected to be minimal.

Data Analysis

The load-displacement (P-h_c) data were analysed according to the principles given by Oliver and Pharr [186]. A typical load-displacement curve obtained from a nanoindentation test is shown in *figure 3.6a*. The quantities shown are P_t: peak load, h_t: indentation displacement at peak load, h_r: final displacement after unloading and S: initial unloading stiffness.

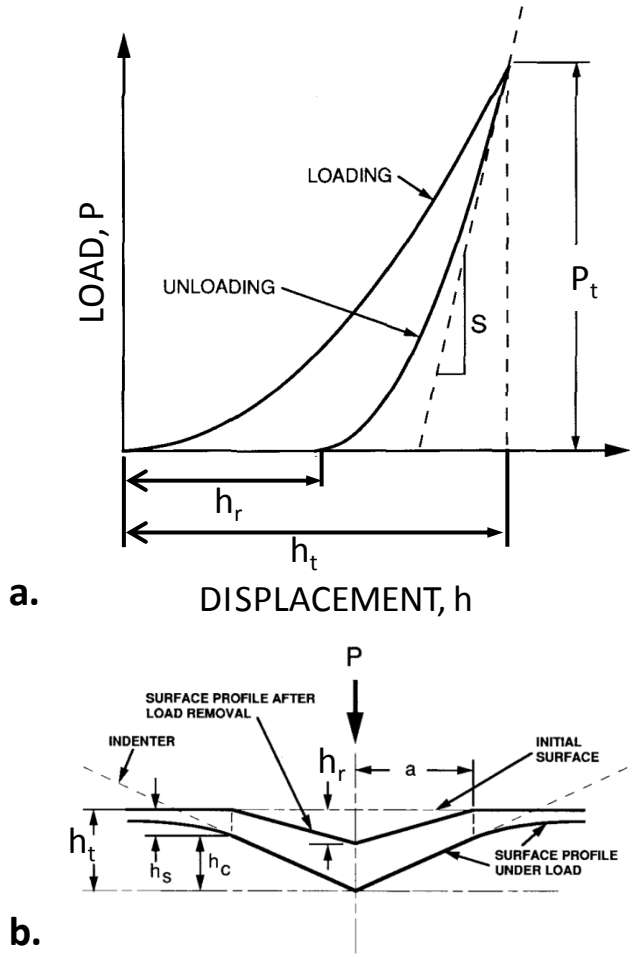

Figure 3.6 – (a) Schematic of a typical load-displacement curve from a nanoindentation test and (b) a schematic representation of a section through an indentation showing quantities used in analysis [186].

Elastic modulus, E_r, is calculated from the stiffness, S, of the initial part of the unloading curve and the area of contact between indentation tip and sample surface, A, by:

$$S = \frac{dP}{dh} = \frac{2}{\sqrt{\pi}} E_r \sqrt{A} \qquad \textbf{\textit{equation}}\ \mathbf{3.5}$$

This can be rearranged to give:

$$E_r = \frac{\sqrt{\pi}}{2} \frac{S}{\sqrt{A}} \qquad \textbf{\textit{equation}}\ \mathbf{3.6}$$

where E_r is called the 'reduced modulus', because the stiffness of the contact upon unloading has contributions from both the sample (E) and the indenter tip (E_i). The sample modulus is therefore calculated by correcting for tip deformation by:

$$\frac{1}{E_r} = \frac{(1-\nu^2)}{E} + \frac{(1-\nu_i^2)}{E_i} \qquad \textbf{equation 3.7}$$

where the elastic modulus, E_i, and Poisson's ratio, ν_i, for a diamond indenter are 1141 GPa and 0.07 respectively [186]. The calculation of hardness also requires knowledge of the contact area and is defined as:

$$H = \frac{P}{A} \qquad \textbf{equation 3.8}$$

Contact Area, A

Standard hardness and micro-hardness testing requires the measurement of the contact area after the test. For nanoindentation, the contact area is calculated from the displacement into surface, h_c, using an area function $A = f(h_c)$ based on tip geometry. Yet, as demonstrated by Pethica et al. in the first depth sensing tests [184], inaccuracies in the definition of tip geometry may lead to large errors in the measurement of mechanical properties. In the experiments reported in this thesis, the shape of each indenter tip was frequently calibrated during its lifetime according to the method proposed by Oliver and Pharr [186]. The method calculates the tip geometry by using data from indentation arrays produced in a reference fused silica material with a known elastic modulus of 72GPa [186]. These data are then used to eliminate the reduced modulus, E_r, in *equation 3.7* and calculate the load frame compliance, C_f, from:

$$C = C_f + C_s \qquad \textbf{equation } 3.9$$

where C is the measured compliance of the system and $C_s$is the sample compliance. The combination of *equation 3.5* and *3.9* can be used to give:

$$C = C_f + \frac{\sqrt{\pi}}{2E_r}\frac{1}{\sqrt{A}} \qquad \textbf{equation } 3.10$$

Provided elastic modulus is constant with indentation depth a plot of C vs. $A^{-0.5}$ is linear and its intercept with the y axis is a direct measure of the load frame compliance. The contact area can then be fitted for all data at the various indentation depths by rearranging *equation 3.10*:

$$A = \frac{\pi}{4}\frac{1}{E_r^2}\frac{1}{(C - C_f)^2} \qquad \textbf{equation } 3.11$$

Values obtained for the indentation area are fitted to an 'area function' in the form:

$$A(h_c) = 24.5h_c^2 + C_1h_c^1 + C_2h_c^{\frac{1}{2}} + C_3h_c^{\frac{1}{4}} + \ \ldots + C_8h_c^{\frac{1}{128}} \qquad \textbf{equation } 3.12$$

where C_1 to C_8 are constants. The first term on the right hand side of *equation 3.12* describes the area function of a perfect Berkovich tip, whilst the following terms account for deviations due to the initial non-ideal shape and blunting of the tip. The exact form of the area function influences the values of both C_f and E_r, thus this step is repeated by an automated process for several iterations until convergence is met.

Figure 3.6b is a schematic representation of a section through an indenter tip in contact with the sample surface and demonstrates how the surface of the sample surrounding the indenter can elastically deform (image taken from [186]). This is known as 'sink-in' and may significantly influence the contact area at a given displacement. Sink-in is accounted for by using the stiffness at peak load and extrapolating to zero load as shown in *figure 3.6a*. The resulting displacement is then used in conjunction with the area function to calculate the contact area at peak load.

Stiffness

Accurate measurement of contact stiffness is important for the calculation of both elastic modulus and contact area. Early analysis methods included the assumption that the initial part of the unloading data is linear [187]; yet it was later shown that the stiffness may change instantly upon unloading in some cases [186]. The instant reduction in stiffness upon unloading is caused by differing elastic recovery over the contact surface of the indent; this results in indent impressions with a slightly larger radius than the tip for spherical indentations, or a slightly larger included tip angle for indentations with pyramidal or conical tips [188]. Thus, the stiffness during unloading is more accurately described by fitting a power law as proposed by Sneddon [189]:

$$P = B(h - h_f)^m \qquad \textbf{equation 3.13}$$

where B and m are constants determined by a least squares fitting procedure. The initial unloading stiffness is then found by differentiating *equation 3.13* and analysing for peak load, P_t, and displacement, h_t.

Continuous Stiffness Measurement (CSM)

The Continuous Stiffness Measurement (CSM) method was developed by Oliver and Pharr [186]. A small sinusoidal oscillation in the force signal measures stiffness dynamically during the indentation sequence and the corresponding displacement signal is monitored. Contact stiffness can be calculated by measuring the phase difference or the amplitude of the displacement signal, accounting for the response of the entire nanoindentation system by the dynamic model shown if *figure 3.7*.

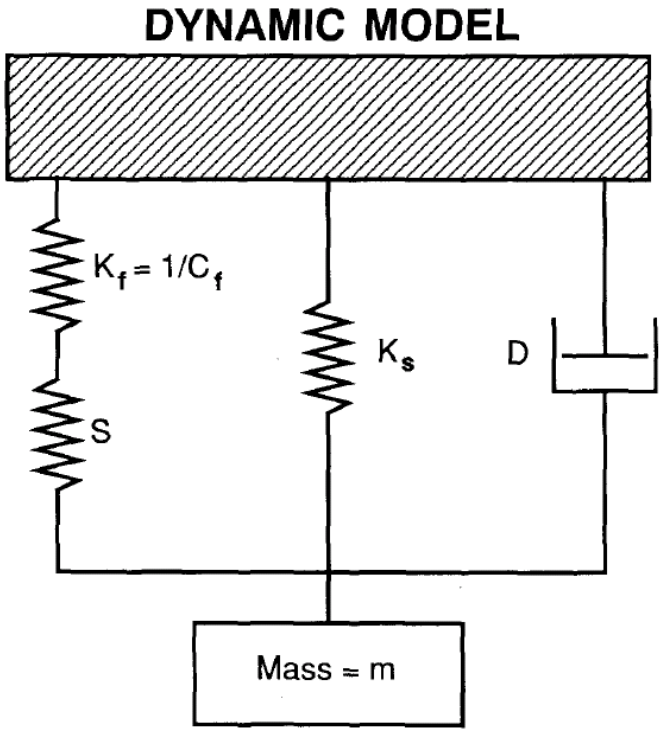

Figure 3.7 - A dynamic model of the nanoindentation system. K_f is the frame stiffness, K_s is the spring stiffness, D is the damping coefficient and S is the contact stiffness [186].

Taking the system components into account, the stiffness of contact, S, can be calculated from the amplitude of the displacement signal from:

$$\left|\frac{P_{os}}{h(\omega)}\right| = \sqrt{\left\{\left(S^{-1} + C_f\right)^{-1} + K_s - m\omega^2\right\}^2 + \omega^2 D^2} \qquad \textbf{equation 3.14}$$

or from the phase difference between the force and displacement signal from:

$$tan(\phi) = \frac{\omega D}{\left(S^{-1} + C_f\right)^{-1} + K_s - m\omega^2} \qquad \textbf{equation 3.15}$$

Where

C_f = the compliance of the load frame

K_s = the stiffness of the column support springs

D = the damping coefficient

P_{os} = the magnitude of force oscillation

$h(\omega)$ = the magnitude of the resulting displacement oscillation (2nm)

ω = frequency of oscillation (45Hz)

ϕ = the phase angle between the force and displacement signals

m = mass of the indenter column

The measurement of mechanical properties with indentation depth is significantly advantageous for the investigation of implanted layers, thus all tests conducted with the MTS NANO Indenter XP reported here have been carried out with CSM.

Spherical Indentation (Load-Unload Method)

Nanoindentation using spherical indenter tips was conducted using a UMIS 2000 instrument (CSIRO, Lindfield, NSW, Australia) with assistance from Dr A Bushby of Queen Mary University London. This system directly measured the displacement of the indenter column and applied load by two linear variable differential transducers (LVDT) and omits correction for support springs.

The displacement into the sample surface, h_i at increment i is given by [190]:

$$h_i = h_m + h_0 - C_f P_i \qquad \textbf{equation 3.16}$$

where h_m is the measured displacement, h_0 is a correction applied for post determination of the tip-surface contact, C_f is the instrument frame compliance and P_i is the load at increment i.

A partial unloading technique analogous to the Oliver and Pharr method was used and the shape of the unloading curve is calculated using Hertzian contact mechanics for each pair of load-unload data [191]. The depth of penetration, h_i, of a sphere into an elastic half space at a load, P_i, is defined as:

$$h_i = Qk \qquad \textbf{equation 3.17}$$

where,

$$Q = \left(\frac{9}{16}\right)^{\frac{1}{3}} \left(\frac{P_i}{E_r}\right)^{\frac{2}{3}} \qquad \textbf{equation 3.18}$$

$$k = \left(\frac{1}{R}\right)^{\frac{1}{3}} \qquad \textbf{equation 3.19}$$

E_r is the reduced modulus and can be used to find the sample modulus using *equation 3.7*. Typical load-unload data of an elastic-plastic material is shown in *figure 3.8*.

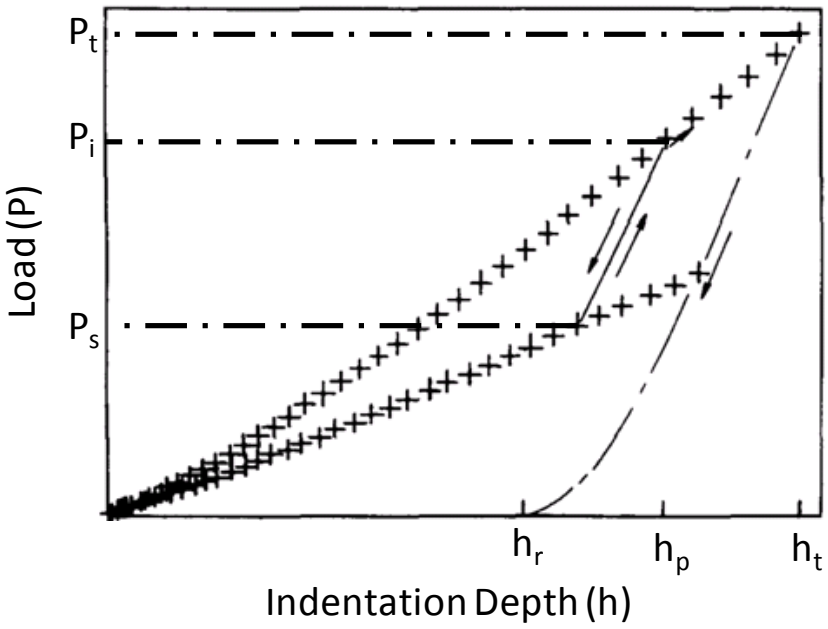

Figure 3.8 - Multiple partial unload data typical of an elastic/plastic material. Graph redrawn from ref. [192].

Partial unloading for each increment, i, in the linear elastic regime (unload to 75% of total load for increment, $P_s = 0.75P_i$) forms a ratio in the form [192]:

$$\frac{(h_i - h_r)}{(h_s - h_r)} = \left(\frac{P_i}{P_s}\right)^{\frac{2}{3}} \qquad \textbf{equation 3.20}$$

The residual indent depth, h_r, was calculated by rearranging *equation 3.20* and extrapolating to zero load with:

$$h_r = \frac{\left[h_s\left(\frac{P_i}{P_s}\right)^{\frac{2}{3}} - h_i\right]}{\left[\left(\frac{P_i}{P_s}\right)^{\frac{2}{3}} - 1\right]} \qquad \textbf{equation 3.21}$$

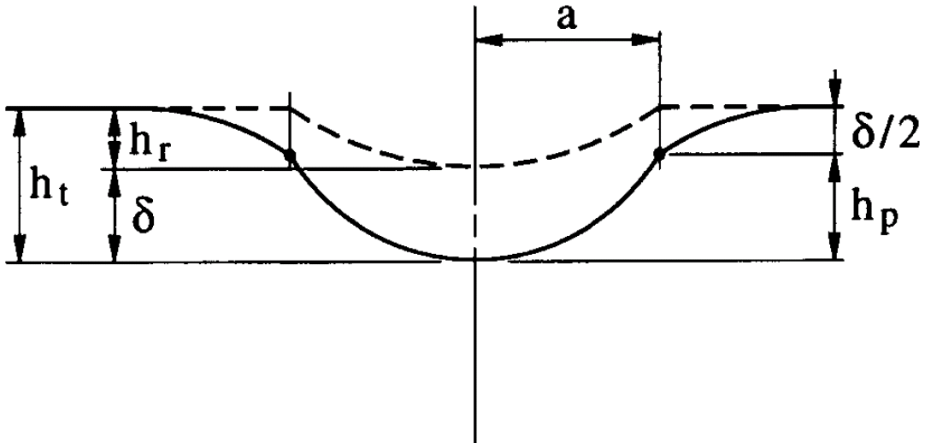

Figure 3.9 - Schematic cross-section through an indent impression with both elastic and plastic deformation. h_t is the total indentation depth, h_r is the residual indentation depth after unloading, δ is the elastic component of displacement and h_p is the tip penetration depth into the sample surface which is used to calculated the contact radius a [192].

As shown in *figure 3.9,* 50% of the elastic component of the total displacement, $\delta = h_t - h_r$, lies above the contact surface; thus the depth of tip penetration into the surface is given by:

$$h_p = \frac{(h_t + h_r)}{2} \qquad \textbf{equation 3.22}$$

and the radius of contact circle may be calculated from:

$$a = \sqrt{\left(2Rh_p - {h_p}^2\right)} \qquad \textbf{equation 3.23}$$

From these calculations the hardness measured at each increment is defined as the mean pressure over the circular area of contact:

$$H = P_m = \frac{P_i}{\pi a^2} \qquad \textbf{equation 3.24}$$

The elastic modulus is proportional to the contact stiffness and requires measurement of load over a displacement range. This is complicated by the relaxation of the residual indent impression on unloading; the radius of curvature of the indent impression, R', is commonly larger than the indenter tip. This is accounted for by adjusting the definition of k in *equation 3.19* to represent the relative curvature between the two surfaces [190]:

$$k = \left(\frac{1}{R} - \frac{1}{R'}\right)^{\frac{1}{3}} \qquad \textbf{equation 3.25}$$

where R' is calculated from the radius of an arc with height, h_r, and width, $2a$:

$$R' = \frac{a^2 + {h_r}^2}{2h_r} \qquad \textbf{equation 3.26}$$

For spherical indentation experiments reported in this thesis, a multiple reference material method was used for calibrating tip geometry and instrument frame compliance (as described in ref. [190]). All indentations were conducted with 60 load-unload increments, with an unloading fraction of 75% of the total increment load (P_i).

3.3.2 Micro-mechanical Testing

A Focused Ion Beam (FIB) microscope was used to mill cantilever beam specimens into the sample surface. These specimens were then imaged for measurement in the Scanning Electron Microscope (SEM) and tested by loading in the MTS NANO Indenter XP. The basic method for each stage in the process will be described below; details of developments for the specific micromechanical tests carried out in this thesis are addressed in *chapter 5*.

Focused Ion Beam (FIB)

The FIB microscopes used for milling work were Zeiss NVision40 and Zeiss Auriga FIB/SEM dual beam systems, and an FEI FIB200-TEM single beam system. Milling of active material was undertaken with a 'hot' FEI Quanta dual beam microscope at the Centre for Advanced Energy Studies (CAES) in Idaho Falls (US). Gallium-based liquid metal ion sources were operated at a primary acceleration voltage of 30kV with an emission of approximately 2μA. In all systems the ion beam current is then reduced by passing through a selected aperture producing a collimated beam from 1pA up to 2μA corresponding to a spot size from approximately 2.5nm to 500nm. Scanning coils are used to raster the focused beam over an area for both imaging and milling operations.

The interactions between the incident Ga^+ ions and sample surface are identical to those described for ion implantation (see *section 2.3*), yet their lower energy results in an interaction volume within a few nm from sample surface. This results in sputtering, whereby atoms are ejected from the target volume due to elastic collisions and lattice displacements at the sample surface. This enables the removal of material on a sub-micron scale and provides a method for machining test specimens in small volumes of irradiated material.

The dual beam microscopes include both an SEM column and FIB column which enables imaging an area independently of Ga^+ milling. This was particularly useful for the manufacture of very small lift-out TEM and APT specimens, where final specimen manufacture stages are sensitive to nanometres of stage/beam drift during milling.

Cantilever Manufacture

Micro-cantilevers were machined in the FIB by a method similar to that used by Di Maio et al. [193]. A U-shaped trench is machined normal to the surface, followed by subsequent undercutting with the sample tilted by 30° from the FIB column. During undercutting from one side, it is very common that a fraction of the sputtered material is re-deposited on the other side of the cantilever beam. This necessitates the use of several undercutting/polishing stages each with reducing beam currents to reduce the fraction of re-deposited material. In addition, final milling procedures with a relatively small Gaussian beam profile provide a means of producing a beam section with small radii at the corners, reducing errors in analysis associated with the assumption of a simple geometry with perfectly sharp corners.

Beam Testing

Micro-cantilever specimens were located in the indenter by using the instrument as an Atomic Force Microscope. A topographical image of the specimen and surrounding sample is produced by bringing the tip into contact with the sample and using a piezoelectric stage to scan the sample beneath the tip. During scanning the indenter maintains a constant scan load (typically 1μN) whilst recording the relative positions of the indenter column and stage. The test specimen is then located and sample coordinates are specified for loading. In the case of all specimens tested for this thesis a method was developed to ensure that test specimens were not damaged during this process. Each beam loading point was located by the AFM imaging of a FIB milled feature (usually a square hole) with a known distance away from the test specimen. Coordinates for loading were then defined relative to the FIB milled feature.

All beams were tested by a displacement control method with constant displacement rate. Load and displacement data were recorded during loading and unloading stages, which were then analysed for the interpretation of mechanical properties according to methods detailed in *Chapter 4*.

Beam Measurement (Stereo Imaging)

As described in *chapter 4*, the response of a beam strongly depends on the accuracy of geometry measurements; however the accurate measurement of FIB milled geometries in an SEM is not trivial. Accuracy is subject to several assumptions regarding the orientation of the sample with respect to the both the Ga^+ beam during milling and electron beam when imaging. For example, when using standard trigonometry to correct an image in an axis perpendicular to the tilt axis, it is commonly assumed that the sample is perfectly flat and parallel to the microscope stage. These assumptions may produce significant errors when imaging geometries in a microscope, particularly when imaging at orientations nearing grazing angles as shown in *figure 3.10*.

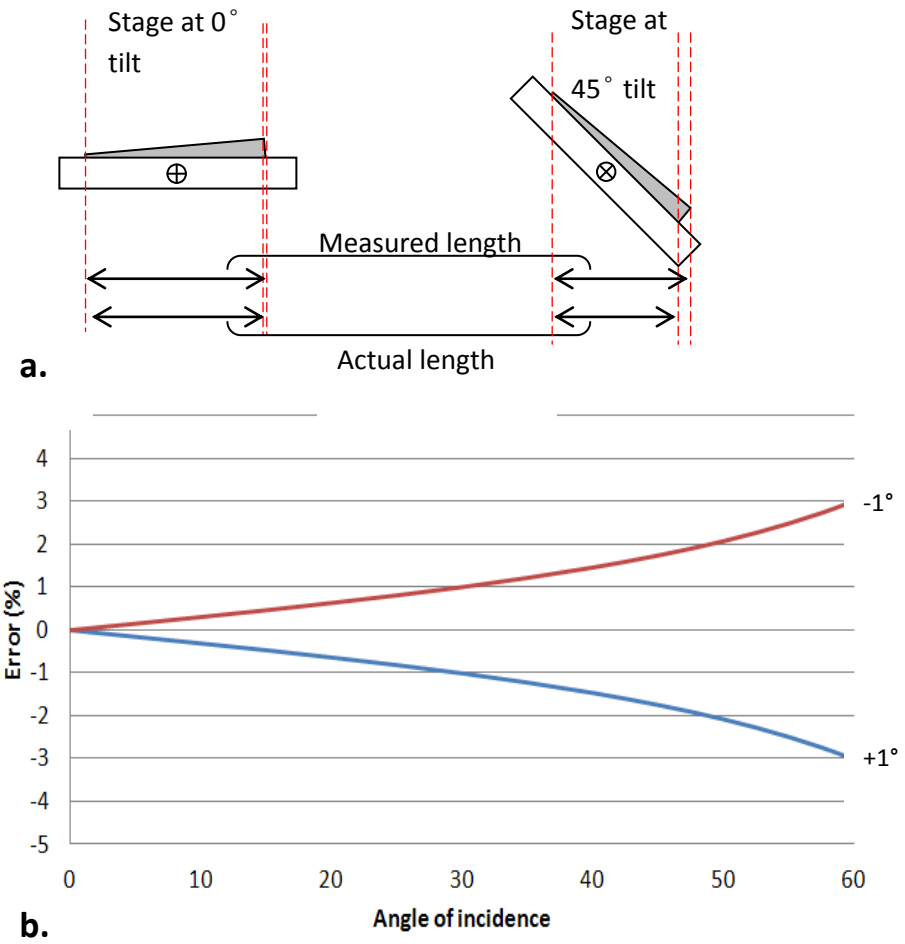

Figure 3.10 - Origin of error in measurements taken with a sample unlevel to the microscope stage (a) and percentage error in measurements taken with a sample orientated +/-1° from the microscope stage (b).

In order to reduce errors associated with unknown orientations with respect to the electron beam, stereo imaging techniques were used. The dimensions of a feature were calculated by imaging at two tilt angles in the SEM. The relative dimensions of features are used to solve actual dimensions perpendicular to the tilt axis in the imaging plane, η, and orthogonal to the imaging plane (at a tilt angle of $\frac{\emptyset_1+\emptyset_2}{2}$) ,z, by using [194]:

$$\eta = \frac{z\{(y_1 + y_2)\cos\Delta\emptyset + (d_1 - d_2)\sin\Delta\emptyset\} - (y_1 d_1 + y_2 d_2)}{(y_1 - y_2)\sin\Delta\emptyset - (d_1 + d_2)\cos\Delta\emptyset} \qquad \textbf{equation 3.17}$$

and

$$z = \frac{(y_1 - y_2)cos\Delta\emptyset + y_1 y_2 \left(\frac{1}{d_1} + \frac{1}{d_2}\right) sin\Delta\emptyset}{sin(2\Delta\emptyset)\left(1 + \frac{y_1 y_2}{d_1 d_2}\right) + cos(2\Delta\emptyset)\left(\frac{y_1}{d_1} - \frac{y_2}{d_2}\right)} \qquad \textbf{equation 3.18}$$

where y_1 and y_2 are the vertical dimensions of the same feature in both images, d_1 and d_2 are the working distances of the microscope when taking each image and $\Delta\phi$ is half the difference in tilt angle between both images. Measurements parallel to the tilt axis are unchanged by tilt and are used as real dimensions of the feature. *Equations 3.17* and *3.18* were used for all measurements of beams in the work reported in this thesis. This proceedure was facilitated by the use of specifically developed MATLAB codes shown in *figure 3.11*.

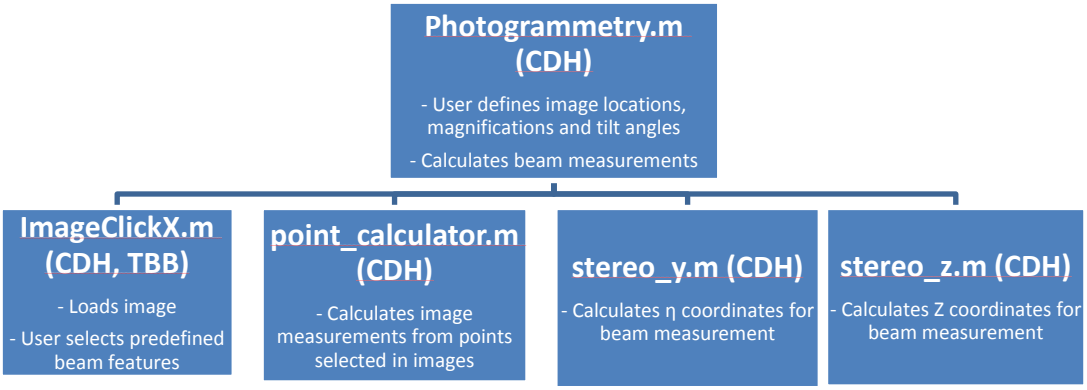

Figure 3.11 - Cantilever beam measurement flow tree showing typical MATLAB files (with author initials) and the functions performed.

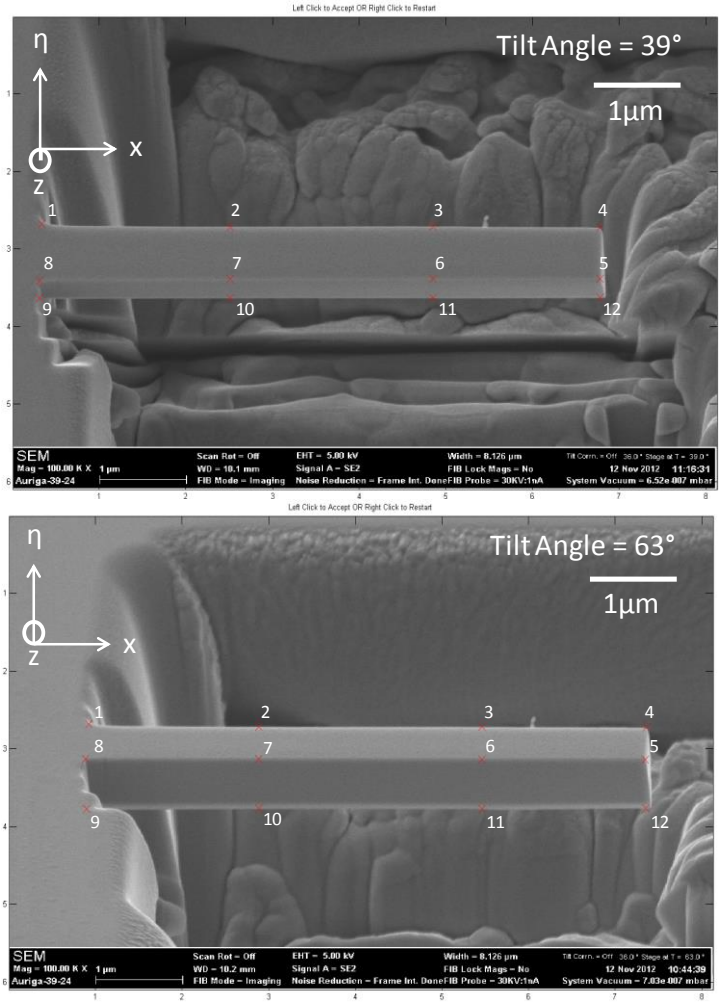

Figure 3.12 - Images of a typical micro-cantilever beam taken at tilt angles of 39 and 63 for stereo-imaging measurement. Numbers represent points selected in MATLAB code to define the beam geometry for measurement. Coordinate system represents coordinates, η and Z as calculated in equations 3.17 and 3.18 respectively. X represents tilt axis.

The 'Photogrammetry.m' code is used for input parameters such as the magnification of the image, which calculates pixel sizes according to the image resolution. The function 'ImageClick.m' enables user selection of predefined points of the beams for each image taken at different tilt angles in the SEM, as shown in *figure 3.12*. 'point_calculator.m' calculates measurments for both images, which are then used with 'stereo_y.m' and 'stereo_z.m' functions, *equations 3.17* and *3.18*, for beam measurement calculation.

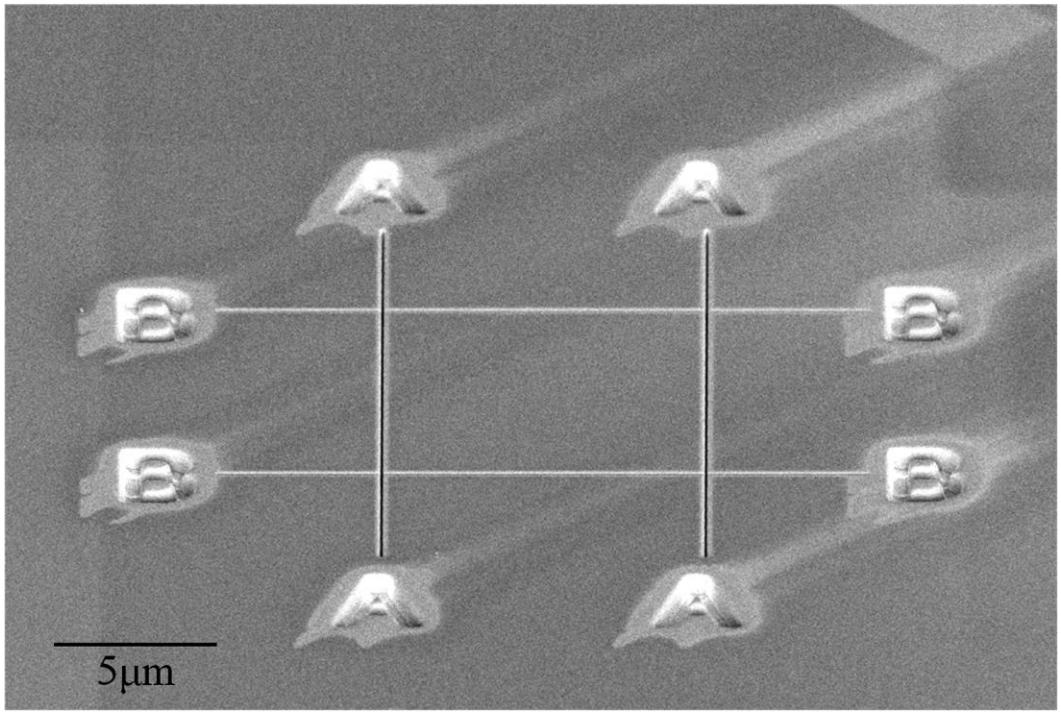

Figure 3.13 – FIB milled grid on sample surface for stereo imaging measurement assessment.

This method was compared to the use of trigonometry by measuring a FIB milled grid onto the sample surface *(figure 3.13*). Images were taken with the stage tilted at 0, 39 and 63° in orientations viewing A-A lines perpendicular to the vertical axis and B-B lines perpendicular to the vertical axis from both sides (stage rotated 180°).

Table 3.1 shows the measured values for the vertical distance between the lines and the calculated dimensions using both trigonometry and stereo imaging techniques. The trigonometry measurement for the distance between both A-A lines changes only slightly as the tilt angle is increased from 0 to 63°, suggesting that the sample surface is relatively level with the stage along the direction perpendicular to the lines A-A. The trigonometry measurement for the distance between lines B-B changes significantly with each stage tilt; this difference has opposite sign when viewing the same lines from the other side (stage rotated 180°). This suggests that the sample is tilted with respect to the stage along the direction perpendicular to the line B-B which produces an error in the trigonometry

measurement of 10% at a tilt angle of 63°. This error is not produced in the measurements calculated by stereo imaging because they are not dependent on assumptions regarding the absolute sample orientation in the microscope.

Table 3.1 – Comparison of FIB milled grid measurements in the SEM by using trigonometry and stereo imaging methods.

Image	Tilt (°)	Lines	Actual Measurement	Trigonometry Measurement	Stereo Measurement			
					Stereo Pair	z	η	Length
1	0	A-A	9.841	9.84	0-39	3.19	9.31	9.84
2	39	A-A	7.718	9.93	39-63	7.65	6.26	9.88
3	63	A-A	4.537	9.99	0-63	5.08	8.43	9.84
4	0	B-B	9.841	9.84	0-39	2.80	9.44	9.85
5	39	B-B	7.969	10.25	39-63	7.35	6.58	9.86
6	63	B-B	4.913	10.82	0-63	4.72	8.65	9.85
Rotated 180° with respect to above measurement of B-B								
7	39	B-B	7.52	9.68	0-39	3.48	9.21	9.84
8	63	B-B	4.279	9.43	39-63	7.79	6.03	9.85
All measurements are in µm.					0-63	5.32	8.28	9.84

Data Analysis

Experimental data were analysed by using either simple beam theory or finite element modelling techniques; these are described in *chapter 4*.

3.4 Atomic Force Microscopy

In order to measure indentation pile-up in some materials, surface topography maps of deformed regions surrounding indents were produced using atomic force microscopy (AFM)

using a Park Autoprobe CP-II AFM with a multitask head. The microscope was fitted with a chip containing 3 beam-shaped cantilevers supplied by Mikromasch (NSC35/AIBS). The sharp tip at the end of each cantilever has a radius of curvature at the apex of typically 10nm. Proprietary software (Veeco, now Bruker) was used to control the microscope during imaging.

The microscope was set up by targeting a laser light produced by a solid state diode onto the end of the cantilever. This light is reflected onto a position-sensitive detector, being a quad-split photodiode, where the error signal is generated by light falling around a set point defined by the upper and lower halves consisting of two closely spaced photodiodes denoted A and B. The detector was adjusted in height so that the output signal of A-B is near zero. Angular displacement of the cantilever during scanning changes the position of the reflected laser light, which is measured by the difference in output signals from the photodiodes.

Imaging was conducted in the tapping mode whereby the cantilever is driven to oscillate at its free-running resonant frequency (no tip-to-surface interaction) by the small piezoelectric element mounted in the tip holder. The amplitude at this frequency is reduced as the tip approaches the sample surface by interaction of the tip and surface through interatomic forces (thereby causing the resonance envelope to shift to a lower frequency). During imaging the probe is scanned over the surface area of interest, whilst the software controls the height of the probe to maintain constant amplitude. The X and Y coordinates lateral to the sample surface and height of the probe are recorded at each pixel in the x-y plane, producing surface topography data.

3.5 Transmission Electron Microscopy (TEM) and Atom Probe Tomography (APT)

All TEM and APT specimen preparation was carried out using a lift-out technique using the Auriga dual beam SEM-FIB; this method is described fully in ref. [195]. This technique enabled the production of site-specific specimens within both irradiated and un-irradiated regions of a sample, and included deformed material surrounding indents and within tested micro-cantilevers.

Lift-out procedure

TEM and APT sample manufacture was conducted by using a lift-out procedure as described in ref. [196]. Platinum was deposited over the area of interest by gas injection locally at the sample surface, which interacts with the microscope beam for deposition. In order to prevent combined milling and deposition during the initial stages, deposition was conducted by firstly using electrons with the SEM beam and secondly using Ga^+ with the FIB. The platinum layer provided protection of the sample surface during lift-out and the use of electrons for initial deposition ensured that this surface is fully preserved during deposition. Subsequently the lift-out is prepared with a similar method to machining micro-cantilevers. Two trenches either side of the area of interest were milled followed by under-cutting at an angle of 45° to produce a cantilever shape supported at one end. At this stage the micro-manipulator needle was positioned with its tip adjacent to the free end of the lift-out beam and attached by Pt deposition. The beam could then been cut away from the sample and moved to either a copper TEM grid or an APT needle holder. Finally, the lift-out is attached to the new holder by Pt deposition and cut way from the micro-manipulator needle. This material was then machined in the FIB to create an electron transparent foil (~100nm thick) for TEM or a needle with a radius of ~100nm for APT.

TEM

All transmission electron microscopy (TEM) was conducted with a Phillips CM20 microscope with an operating voltage of 200kV. All TEM observations reported in this thesis were produced from lift-out samples apart from the TEM observations conducted by Mr S Xu of the University of Oxford presented in *figure 7.10* in *section 7.5.1*. Mr S Xu used the back-thinning method which is briefly described below. Further details regarding the optimization of this method are described in ref. [128].

Back-Thinning Method

Before irradiation, material was mechanically polished to a thickness of approximately 150µm by SiC grit paper. 3mm diameter TEM discs were punched from this material and were further mechanically polished to a thickness less than 100µm. After irradiation, the foils were electro-polished for a few seconds in order to access the peak damage region. This was achieved by a bath polishing technique with accurate temporal control. The samples were then back thinned by electro-polishing into TEM thin foils using a Tenupol 5 Jet-electropolisher.

APT

With assistance from Dr C Williams of the University of Oxford, APT data acquisition was carried out using a Cameca LEAP 3000HR instrument operating in laser-pulsing mode. The specimen base temperature was maintained at 50K with a laser energy of 0.5nJ. An 8µm laser spot size was used at a repetition rate of 200 kHz.

4 MICRO-CANTILEVER DATA ANALYSIS

The micro-cantilever beam tests reported in this thesis were analysed by using simple beam theory and/or Finite Element Modelling. The two geometries of beam tested for experiments reported in this thesis are referred to as a uniform cross-section beam and a 'waisted' beam.

Uniform Cross-Section Beam

A beam with a uniform cross-section (*figure 4.1*) was milled and undercut with a stage tilt of 30° with depths from 0.5 to 7µm.

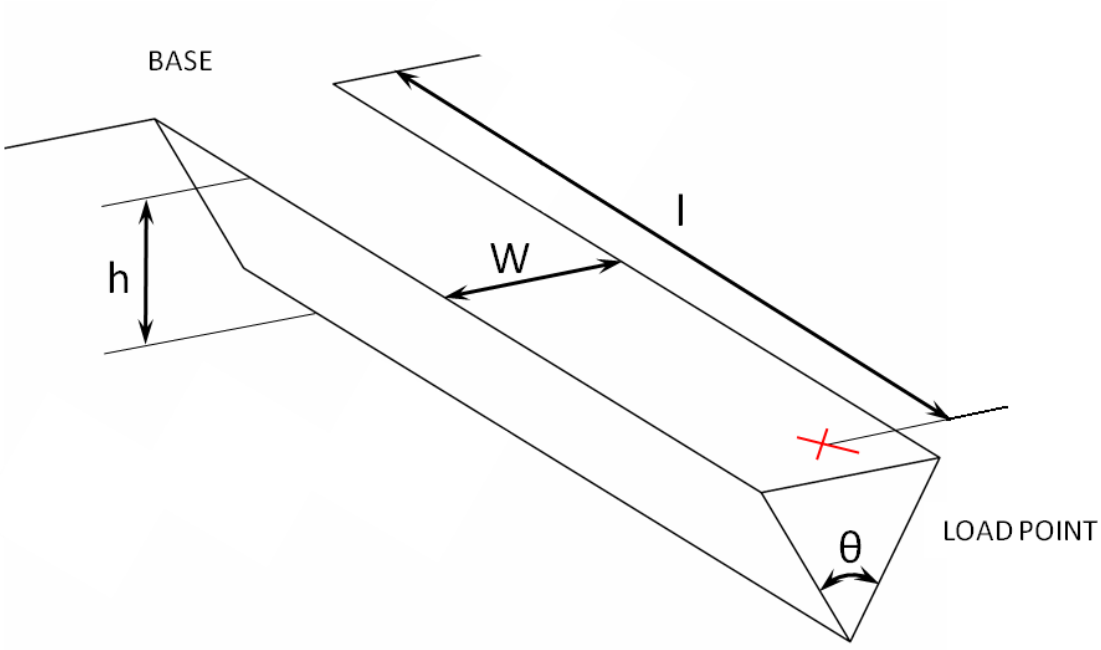

Figure 4.1 – Uniform cross-section beam design showing load point and dimensions used for analysis.

Waisted Beam

The waist or gauge region for the more complex beam geometry used in this study was elongated compared to the geometries used by Halliday et al. [94], to allow plastic deformation to extend along a section of the beam. This beam geometry, shown in *figure 4.2*, was used for materials irradiated at the National Ion Beam Centre at the University of Surrey (UK), which provided a damage layer only 800nm thick at the sample surface. The beam was undercut with a stage tilt of 30° and target dimensions for these beams are shown in the embedded table in *figure 4.2*.

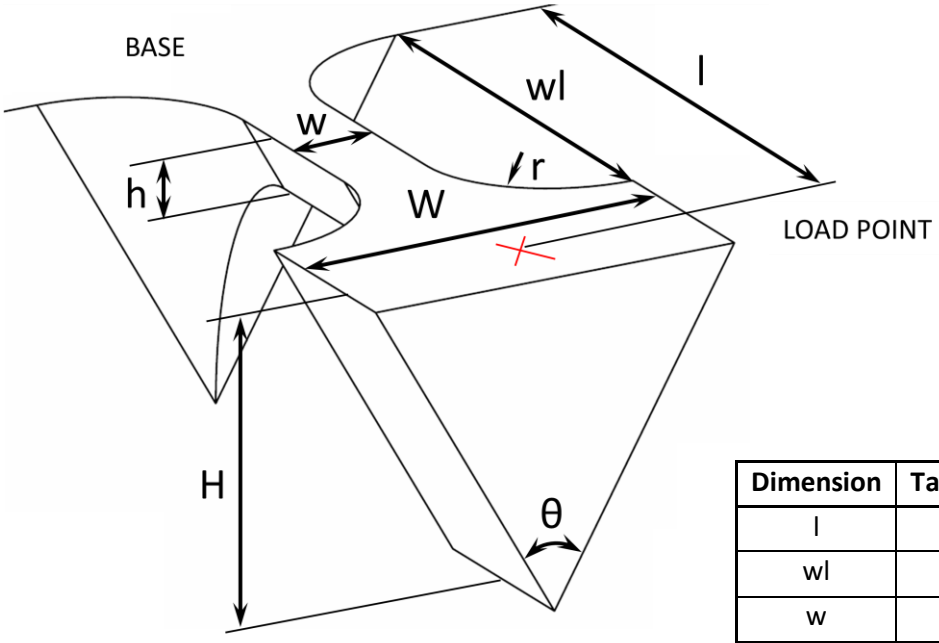

Dimension	Target Length (µm)
l	4.5
wl	3.5
w	0.8
W	3
h	<0.83
θ	60°
H	~2.6
r	1

Figure 4.2 – Elongated waist beam design with table of target dimensions for material irradiated at the National Ion Beam Centre at the University of Surrey (UK).

4.1 Simple Beam Theory

Experimental data produced by uniform cross-section beam tests was analysed by simple beam theory. The stresses and strains within a beam under loading were calculated using the following relationship:

$$\frac{\sigma}{y} = \frac{M}{I} = \frac{E}{R} \qquad \textbf{equation 4.1}$$

where;

σ = the stress due to bending moment, M, occurring at a distance, y, from the neutral axis[5]

y = perpendicular distance from the neutral axis to beam edge in the plane of loading ($y = \frac{2}{3}h$ for a triangular beam).

M = bending moment; load (P) x length (l)

E = Young's modulus

R = radius of curvature of the neutral layer of the beam due to bending moment M

The second moment of area is calculated by summing all areas, a_1, a_2, a_3, … at distances y_1, y_2, y_3, … from a fixed axis ($I = \Sigma a y^2$), so that:

$$I = \int y^2 \, dA \qquad \textbf{equation 4.2}$$

[5] The location of the neutral axis perpendicular to the direction of loading lies coincident with the 'centre moment of area' or centroid of the cross-section.

For the isosceles triangular beam cross-sections of FIB manufactured beams, the centroid/neutral axis is one third the distance from the top surface. The second moment of area, I, for a triangular beam is:

$$I = \frac{wh^3}{36} \qquad \textbf{equation 4.3}$$

where w is the beam width and h is the beam height. Finally, maximum strain is calculated by:

$$\varepsilon_{max} = \frac{2\delta h}{l^2} \qquad \textbf{equation 4.4}$$

and maximum stress by:

$$\sigma_{max} = \frac{24Pl}{ah^2} \qquad \textbf{equation 4.5}$$

This theory is subject to several assumptions as suggested in *section 2.2.2*, which include [197]:

1. The cross-section of the beam has symmetry about the plane of loading. The bending and deflection of the beam occur on this plane (plane of bending).
2. The beam is not affected by irregularities such as geometry near the supports of the beam or at a concentrated load.
3. The beam has a constant cross-section.

Therefore simple beam theory cannot be used for the analysis of micro-cantilevers with complex cross-section geometries and complex stress conditions at the fixed end.

4.2 Finite Element Modelling

Finite Element Modelling (FEM) was also used for the analysis of micro-cantilever tests, where experimental load-displacement data were matched with a simulation by adjusting stress-strain properties of the material in a standard isotropic elastic-plastic model. Abaqus 6.7-1 CAE software was used to generate a mesh representative of the beam geometry, apply material properties and apply boundary conditions including beam displacement during testing. The optimisation of FE models for both beam designs is described below.

4.2.1 The Base

Simple beam theory does not account for stresses and deformation at the base of the beam and this may lead to errors in results. In the experiment the beam is attached to the rest of the sample at its 'fixed end'. In the simulation, a small volume of material, 'a base', was modelled at the fixed end of the beam to represent the sample. The size of the base was optimised by running typical simulations of an experiment using linear tetragonal elements, with various base dimensions. The elastic response was considered sensitive to inaccuracies in the model and was used to determine how each simulation performed.

The base was modelled with a cross-section proportional to that of the cantilever beam, defined by a width and length (corresponding to the beam dimensions). The system was

constrained by removing all degrees of freedom from the surface nodes of the outer faces of the base:

$$U1 = U2 = U3 = 0 \qquad \boldsymbol{equation\ 4.6}$$

$$R1 = R2 = R3 = 0 \qquad \boldsymbol{equation\ 4.7}$$

where $U1, U2$ and $U3$ represent translation along the three Cartesian coordinates (x, y, z) and $R1, R2$ and $R3$ represent rotation about these coordinates.

Several sizes of base were modelled for both beams of typical geometries and analysed in order to assess the size required for accurate simulation. *Figure 4.3* shows the difference in the elastic stiffness of the beams with bases of various sizes. For the uniform cross-section beam the simulation output converges when the base width and depth is approximately twice the beam width. In order to ensure that all simulations remained accurate, the base size was maintained equal to or above 3 times the width of the beam for all uniform cross-section beams of various sizes. For the waisted beam, stiffness deviates from convergence when the base is smaller than a depth of 0.5µm; this would result in an error in the elastic modulus of over 1%. Thus, a base with a width of 4µm and depth of 1µm was used for all simulations of beams with the target size and geometry.

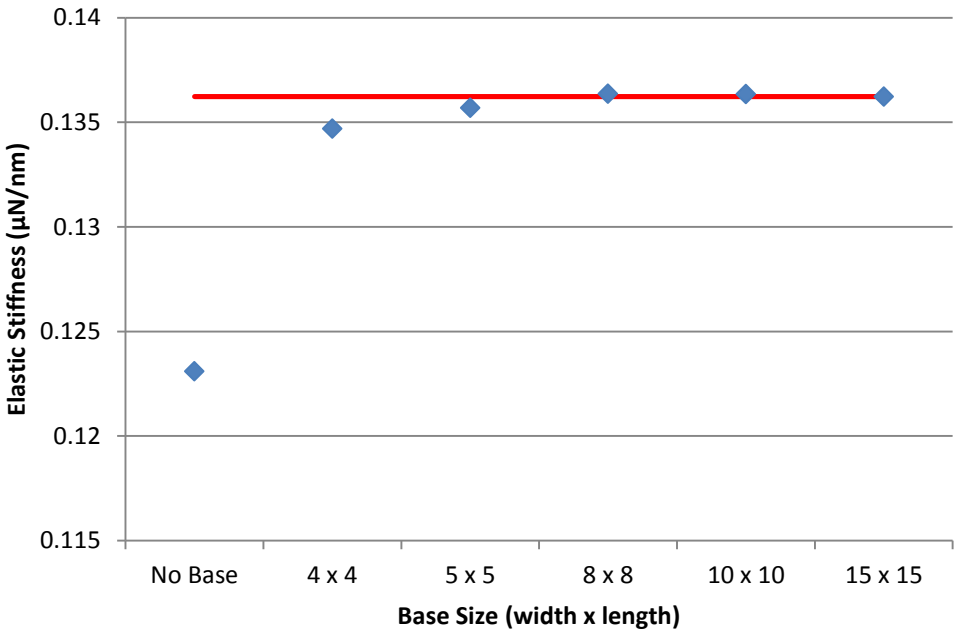

a. Uniform Cross-Section Beam

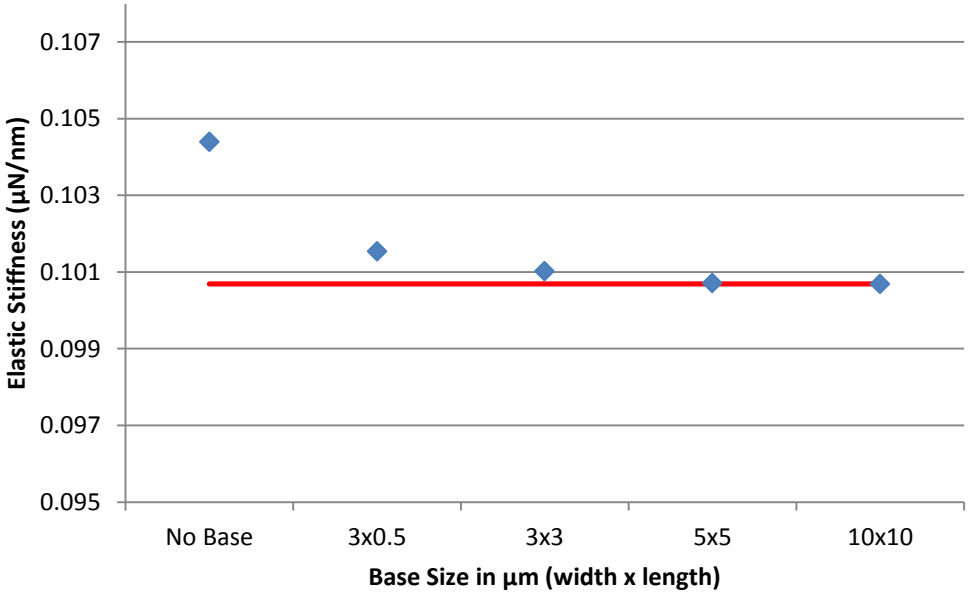

b. Waisted Beam

Figure 4.3 – Elastic stiffness from simulations with various sizes of base for (a) the uniform cross-section beam geometry (3µm width and 15µm length) and (b) waisted beam geometry (target dimensions in *figure 4.2*). The red line is an empirical asymptote representing convergence.

4.2.2 Loading Point

Experimentally, the beams are tested by applying a force with the nanoindenter tip. The tip may embed itself slightly into the top surface of the beam, thus deformation of material directly beneath the indenter tip may influence the load-displacement response.

Loading at the end of the beam was simulated by applying a displacement to a single node and to a line of nodes on the beam's top surface. For waisted and uniform cross-section beams <1µm in depth, the difference in gradient of the load-displacement data between these two methods was <0.5%. The larger beams reported in *chapter 6* were subjected to higher loads during deformation and interactions between the indenter tip and beam surface may be significant. In order to avoid complicating the FEA model with deformations at the loading point of the beam, tip-beam surface interactions were considered separate to the FEA model for large micro-cantilever tests and are discussed in *chapter 6*. Thus, the application of a displacement over a line across the surface of the beam was in used all FEA models.

4.2.3 The Mesh

To maintain accuracy of the simulation, the number of elements used to model the beams was optimised for both beam geometries. Initial simulations with either tetrahedral (waisted geometry) or hexahedral element types and either first-order (linear) or second-order (quadratic) interpolation were carried out to assess the performance of each element type. *Figure 4.4* shows the elastic stiffness from simulations of simple and waisted type beams using a range of element sizes with either first or second-order interpolation. A higher

stiffness exhibited in the simulation using first-order tetrahedral elements (*figure 4.4b*) was caused due to a severe locking behaviour common to this type of element [198]. Displacement interpolation is linear in first-order elements, thus simulations which include strain gradients such as bending problems require a fine mesh for accuracy.

For the uniform cross-section beam model, the simulation output converges when $N^{1/3}$ is greater than ~30 for first-order elements; this corresponds to simulations with <33 000 elements and an average element size of ~0.25µm for a beam 3µm in width. In comparison, convergence was attained with a relatively coarse mesh and lower computational time for simulations using the second-order elements. It is likely that stress concentration due to the sharp changes in geometry where the beam is connected to the base, cause large stress gradients; these are calculated with greater accuracy when using the quadratic term in second-order elements. Thus, all uniform cross-section beam models were meshed with second-order hexahedral elements and values of $N^{1/3}$>16 were maintained. This value corresponds to >4250 elements for each model.

For the waisted beam model, the second-order elements converge with a coarser mesh than the first-order, however the computational time was >5 times larger for the tetrahedral elements and >8 times larger for the hexahedral elements with the same element size. Thus first-order hexahedral elements with a mesh refined to $N^{1/3}$>50 in the critical regions were used for the 'waisted' beam finite element model.

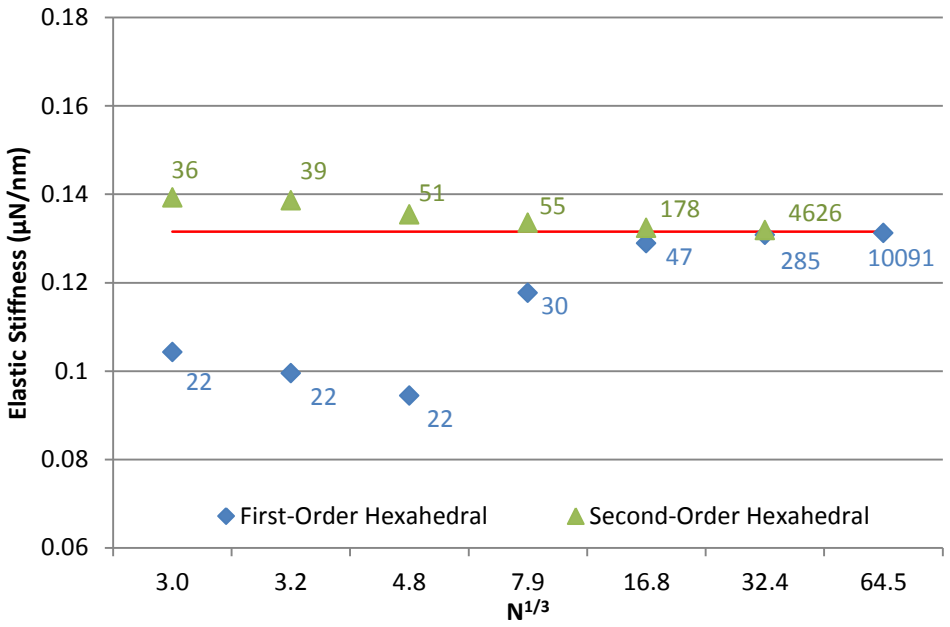

a. Uniform Cross-Section Beam

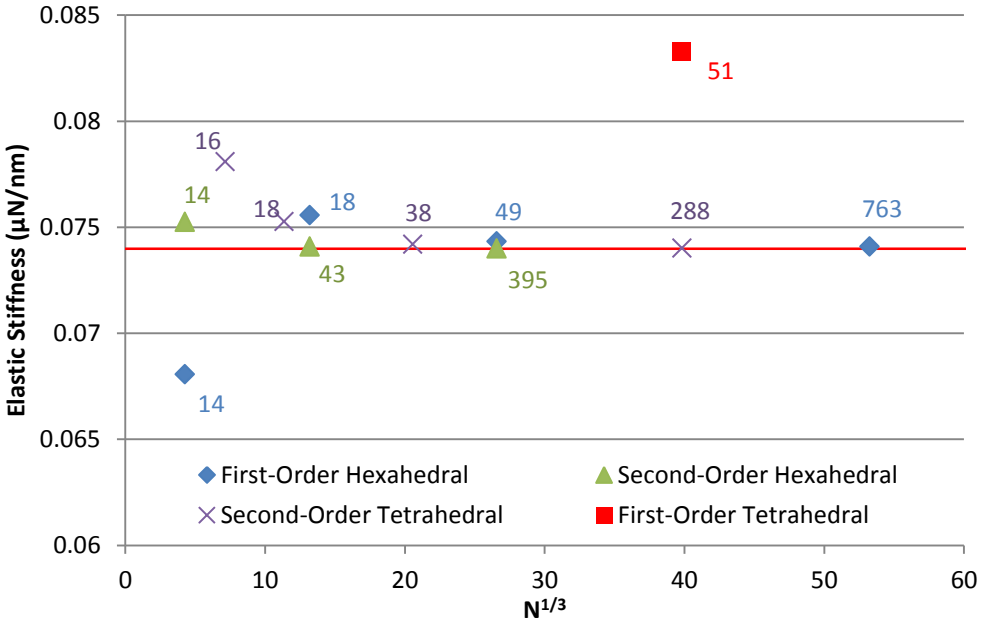

b. Waisted Beam

Figure 4.4 – Element type and size analysis, showing the elastic stiffness compared to the number of simulation elements (N) produced from simulations of (a) a 3µm beam displacement of a uniform cross-section beam of 3µm width and 15µm length and (b) 600nm beam displacement of a waisted beam with target dimensions in *figure 4.2*. Simulation duration in seconds indicted by data labels.

4.2.4 Experimental Data Analysis Tools

The simulation load-displacement data from the FEA models described above were fitted to the experimental data via a process of progressive convergent approximation. For each beam this involved several tens of simulations for an accurate fit and was time consuming. A series of analysis tools were written in MATLAB for automation of experimental data interpretation and FEA simulation fitting. *Figure 4.7* shows a flow tree of the processes and corresponding functions written in MATLAB. Some of the processes integrated codes created by Dr TB Britton of the University of Oxford (marked as TBB in *figure 4.5*).

The analysis tools were operated from **Input_Deck.m**, where an analysis folder for all files, the file locations for test and model data, and individual cantilever test numbers are specified. The regions of raw data before tip-surface contact and elastic region of the test are defined by the user by manually selecting points on a graph showing the load-displacement data via the code **ImageClick.m**. The **CurveFitting.m** code converts the raw load-displacement data into beam load-displacement data for each of the beam tests to be analysed. Raw data was corrected for spring stiffness and surface find using *equations 3.3* and *3.4*. Values for K_s, P_0 and h_0 were defined by calculating the intersection of straight lines fitted to the P-h data before and after (beam elastic region) surface contact. The corrected load-displacement data are then used for the calculation of elastic modulus and stress-strain data by simple beam theory (if applicable) and FEA simulation.

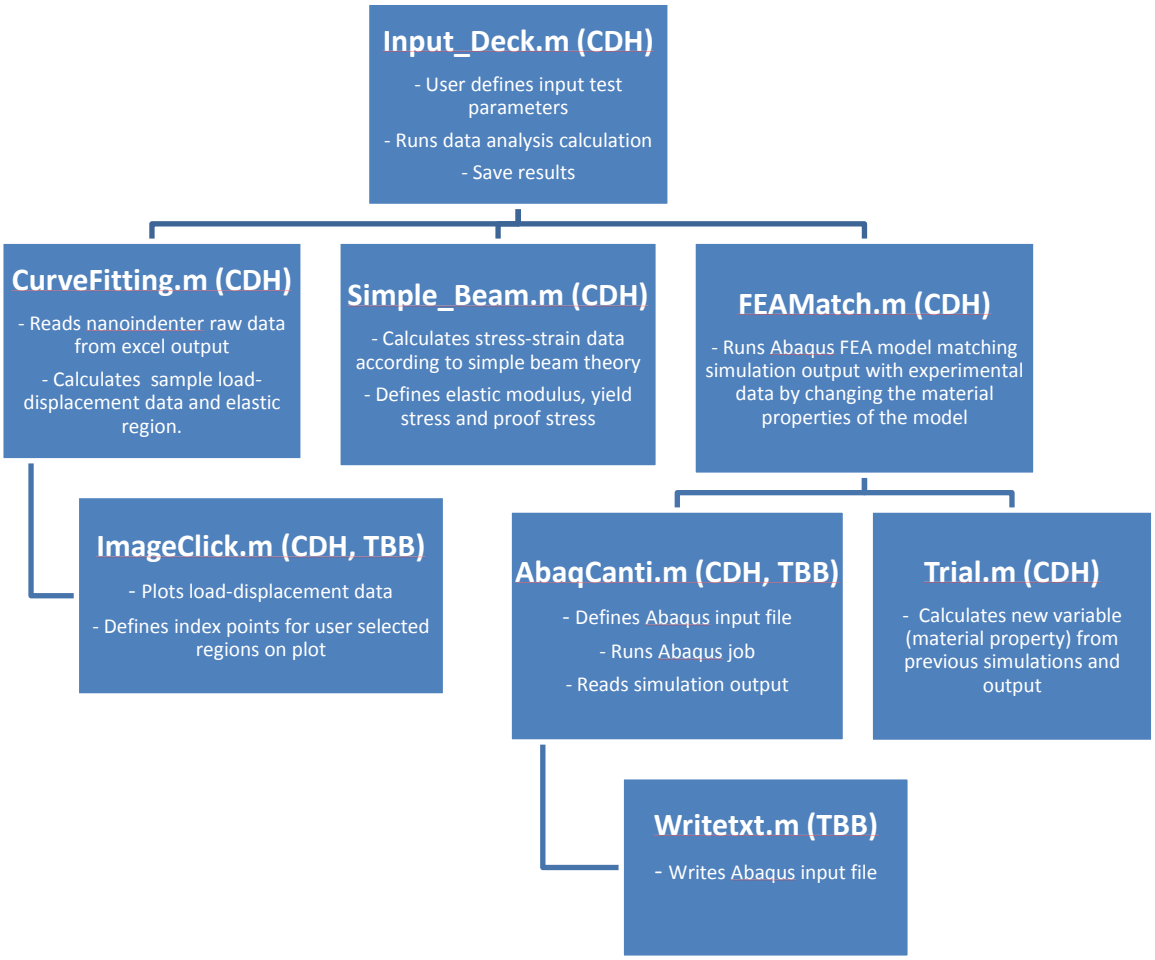

Figure 4.5 - Cantilever Analysis flow tree showing all MATLAB files (with author initials) and the functions performed. Shared authorship of some files exists due to the use of code from Dr TB Britton of the University of Oxford (TBB).

Simple_Beam.m calculates stress by using the relationship defined in *equation 4.5*. The elastic modulus is defined by the linear gradient of a fitted line between the indices selected previously in the **ImageClick.m** code. Yield stress is defined as proposed by Armstrong [199], the stress at the data point where the moving gradient of the stress-strain data (averaged over 20 data points) falls below 10% of the elastic modulus. Additionally, the proof stress with a 0.2% strain offset was calculated.

FEA simulations were conducted in addition to simple beam theory. **FEAMatch.m** amends the model material properties to fit the simulation load-displacement output with the experimental load-displacement data. Firstly the elastic region is simulated by specifying initial estimates of mechanical properties in the **AbaqCanti.m** code; then the model materials elastic modulus is amended until the load-displacement gradients are within 0.2% of each other. As shown in simple beam theory, load and displacement are proportional to stress and strain respectively, thus the elastic modulus in the model should be fitted to the experimental data to within 0.2%.

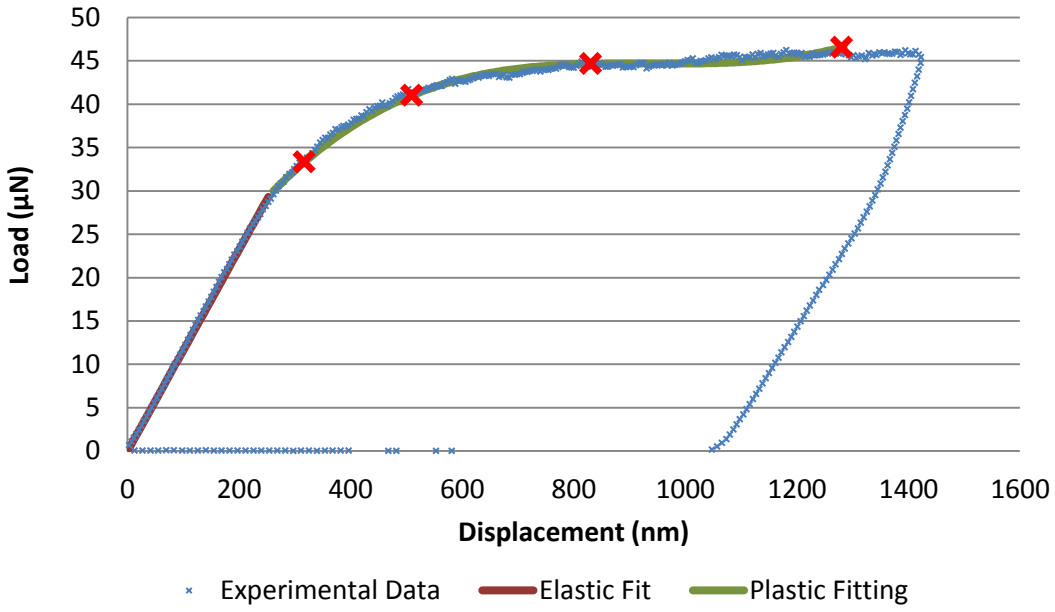

Figure 4.6 - Typical experimental load-displacement data for a cantilever beam, showing elastic and plastic fitting and four plastic match point locations for fitting with FEA simulations (red crosses).

The plastic region of the load-displacement data was defined by a 4th degree polynomial in the **CurveFitting.m** code to give a smooth function, omitting fluctuations in the load resulting from individual plastic events which are typical in micro-mechanical tests. The

plastic behaviour of each cantilever was analysed by dividing the plastic displacement region ($h_{plastic}$) of the experimental data into a specified number of match points (n_{TOTAL}) and matching the simulation load with the experimental load at the end of each increment (*figure 4.6*).

Table 4.1 - Schematic of table used which defines plastic properties of the FEA model.

Increment (i)	Stress (σ)	Plastic Strain ($\varepsilon_{plastic}$)
1	σ_{yield} (yield stress)	$\varepsilon_{plastic1}$ (=0)
2	σ_2	$\varepsilon_{plastic2}$
3	σ_3	$\varepsilon_{plastic3}$

Match points are spaced with a power function ($n^x h_{plastic}/{n_{TOTAL}}^x$) where x can be adjusted to vary the match point spacing at the region of initial yielding. For matching with experiment, the isotropic plastic material properties in the simulation are adjusted in order to change the simulation load at each match point. These properties are defined in *table 4.1*, as values which state the stress (σ_i) required for plastic deformation at a given plastic strain ($\varepsilon_{plastici}$). The simulation load data is matched with the load at each increment via a process of progressive convergent approximation in **Trial.m**. After two initial simulation runs, a linear relationship between the two closest values of stress at $\varepsilon_{plastic}$ are used to define the plastic value for the next simulation. This proceeds until the simulation load is within a defined percentage of the experimental load for each increment. The first value states the yield stress (stress at $\varepsilon_{plastic} = 0$), which is calculated at the first match point. After each increment the maximum plastic strain ($\varepsilon_{plastic}$) is taken from the simulation output and used to define the plastic strain for the next increment. The result is a table of values which define the plastic region of the stress strain properties of the material in the simulation. The

simulation and experimental load-displacement curves with corresponding flow stress convergence graphs of a typical progressive convergent analysis with 6 match points are presented in *figure 4.7* for match points 1 to 3 and *figure 4.8* for match points 4 to 6.

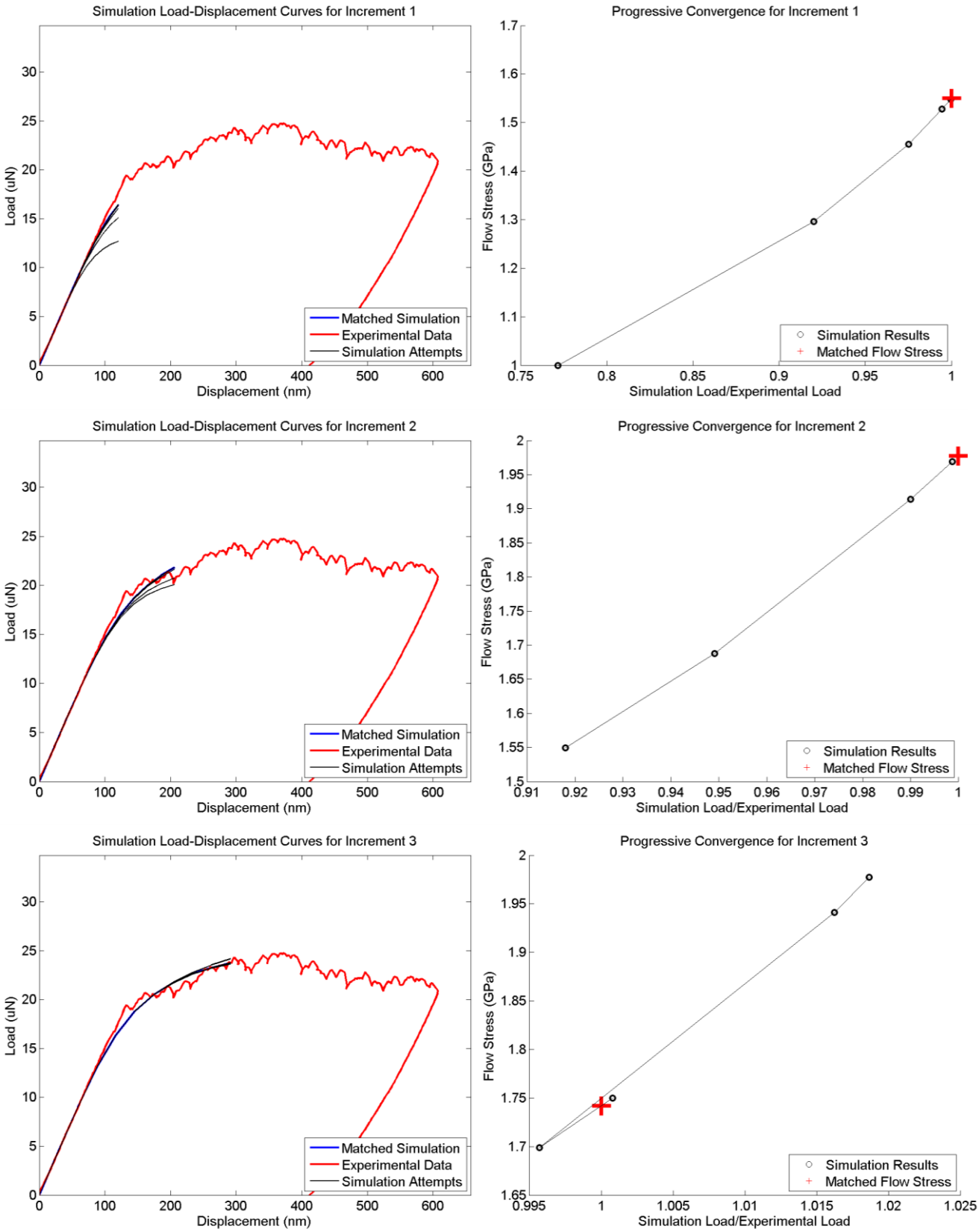

Figure 4.7 - Simulation and experimental load-displacement curves with corresponding flow stress convergence graphs for match points 1 to 3 of a typical progressive convergent analysis with FEA simulations.

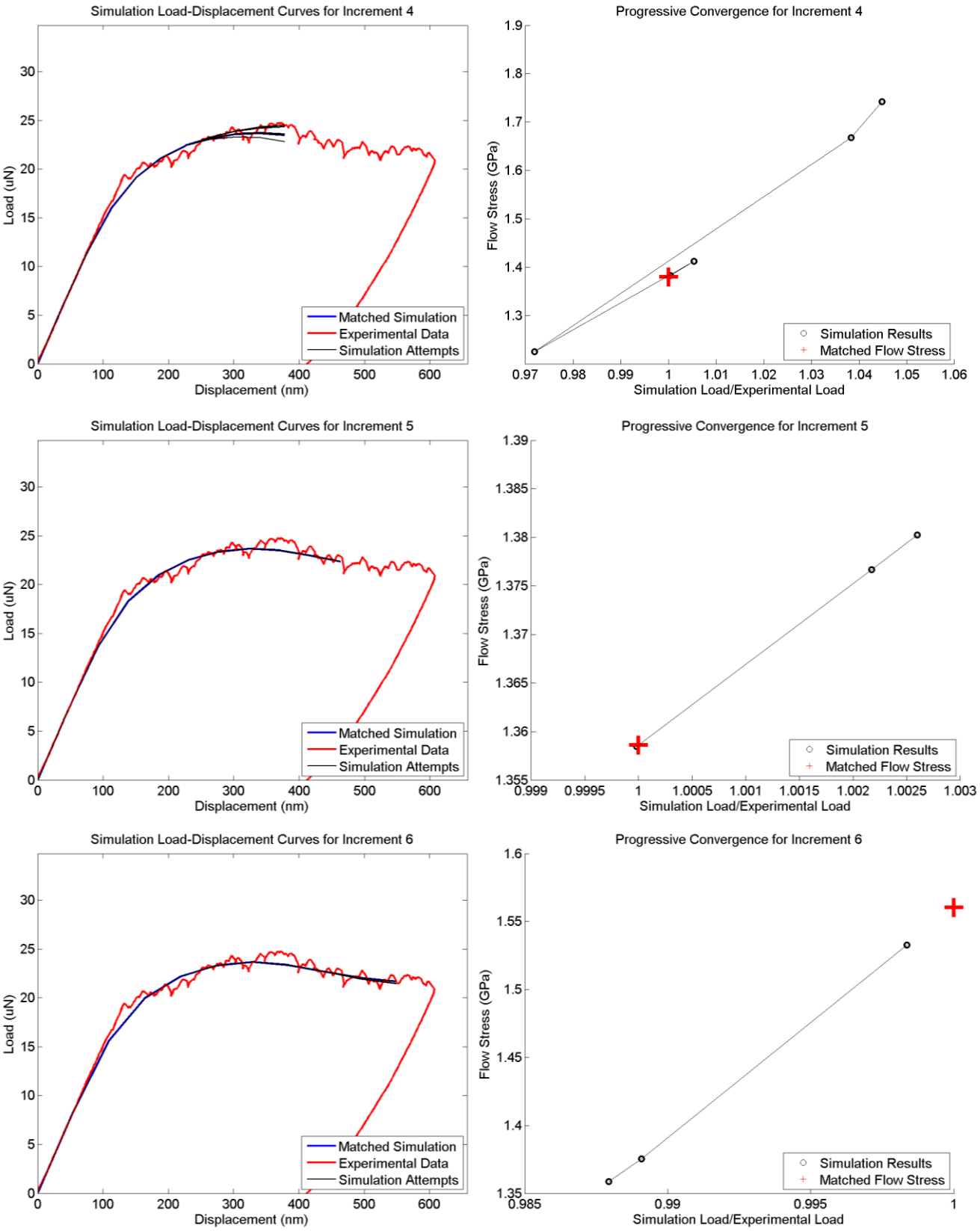

Figure 4.8 - Simulation and experimental load-displacement curves with corresponding flow stress convergence graphs for the match points 4 to 6 of a typical progressive convergent analysis with FEA simulations.

5 MECHANICAL CHARACTERISATION OF IRRADIATED MATERIALS ON THE MICRON SCALE

Ion implantation is becoming an increasingly popular tool to investigate irradiation damage in solids. As discussed in *section 2.2.2*, microstructure and chemical characterisation methods such as TEM, APT and PAS investigate volumes of material which are inherently small relative to that produced by ion irradiation. Thus the limited irradiated volume produced by implantation presents little or no additional challenges when using these techniques. In contrast, there are few methods available for the characterisation of mechanical properties on a micro-scale, and analyses regarding the validity of using these techniques for irradiated materials are scarce. This chapter investigates several methods available for the analysis of an 800nm damage layer of ion-irradiated Fe12%Cr alloy implanted at the National Ion Beam Centre, Surrey. These methods include nano-indentation using cube corner, Berkovich and spherical tips, and micro-cantilever testing methods using both the uniform cross-section and waisted beam designs as described in *chapter 4*. Both simple beam theory and FEA were used to analyse the experimental data produced by tests using the uniform cross-section beam design, and FEA analysis was used for data produced from tests using the waisted beam design.

5.1 Experimental Details

5.1.1 Material and Sample Preparation

An Fe 12%Cr alloy was manufactured by Cambridge Metals Crystals and Oxides (CMCO) with final cold rolling into sheet at a thickness of approximately 1mm. These materials were manufactured from powders with 99.999% purity, yet comet-tailing from polishing, Energy-Dispersive X-ray spectroscopy (EDX) and APT (not reported here) indicated that these materials contained significant impurity content. A full manufacturing history and chemical analysis are unavailable for this alloy.

The Fe12%Cr alloy was cut into a rectangle sample of approximately 4 x 8mm, and then annealed within an evacuated sealed quartz silica tube at 830°C +/-10°C for 72 hours to develop a large equiaxed grain structure. A series of lapping stages using SiC abrasive papers from FEPA P120 to P4000 grades was used to produce a smooth surface with a thin layer of polishing damage. Finally a chemo-mechanical polish with a colloidal silica suspension (0.05µm) was used to provide a surface with minimal polishing damage and of a quality suitable for electron backscattered diffraction (EBSD). Grain diameters were determined by EBSD to be in the range of 20 to 450µm, with a mean grain size of 189µm.

5.1.2 Ion Implantation

The sample was irradiated with Fe^{+} ions at 320°C to an average dose of 6.18dpa (0-800nm depth). Two implantation energies of 2MeV and subsequently 0.5MeV were used in an

attempt to produce a uniform distribution of damage with depth. The ion beam and environmental conditions for the implantation are shown in *table 5.1* and SRIM calculations of damage with depth into the sample surface are presented in *figure 5.1*.

Table 5.1 - Ion beam conditions at the Surrey Ion Beam Centre (UK).

Implantation Energy	0.5 MeV	2 MeV
Implantation Dose (ions/cm^2)	1.5 x 10^{15}	3 x 10^{15}
Radiation Damage (avg.)	6.18 dpa	
Radiation Damage (max.)	8.36 dpa	

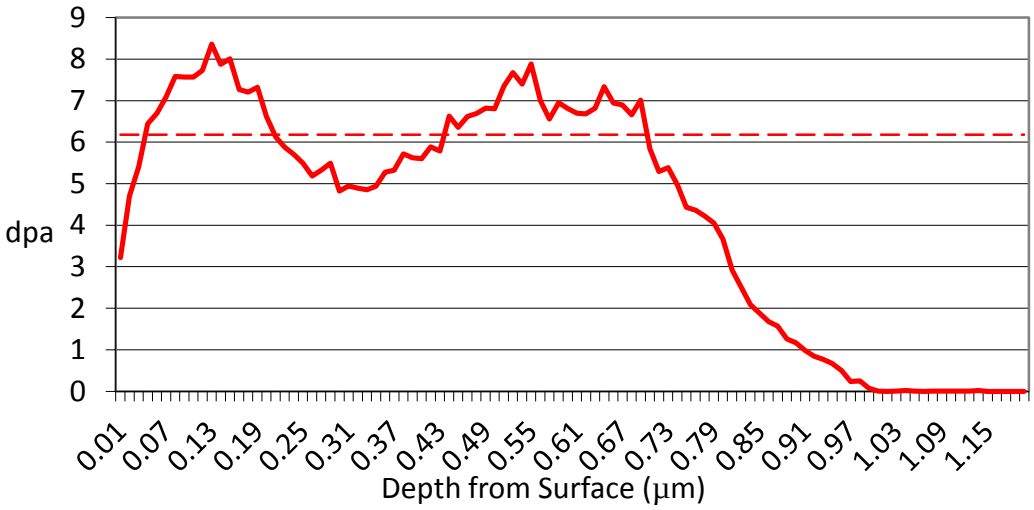

Figure 5.1 - Irradiation damage versus depth from the sample surface as calculated by SRIM with a displacement energy of 40eV for iron [200].

Figure 5.2 shows a TEM cross-section of the radiation damage layer at the sample surface. The micrograph includes the protective Pt layer deposited in the FIB before foil thinning, a

region of dense dislocation loops forming the damage layer and the underlying un-irradiated substrate. It is evident that the visible damage extends to a depth no more than 600nm at the sample surface which is slightly less than that predicted by the SRIM calculations. The beam current varied slightly with ion source life, resulting in a variation in the peak dose rate of 3.5-7.5 x 10^{-4} dpa/s (average ~5 x 10^{-4} dpa/s). The sample clamp described in *section 3.2.1* produced a sample with areas both exposed to and shielded from the beam. After implantation, the region of the sample exposed to the beam was clearly visible in secondary electron images by a darker in contrast with the rest of the sample. This enabled the FIB milling of marker lines, visible under an optical microscope, at the implanted/un-implanted boundary, enabling mechanical testing adjacent to the boundary of the implanted and un-implanted regions within same grain. This provided the advantage of eliminating differences in observed mechanical properties due to any anisotropy associated with crystallographic orientation and variation in the quality of polishing and sample mounting conditions.

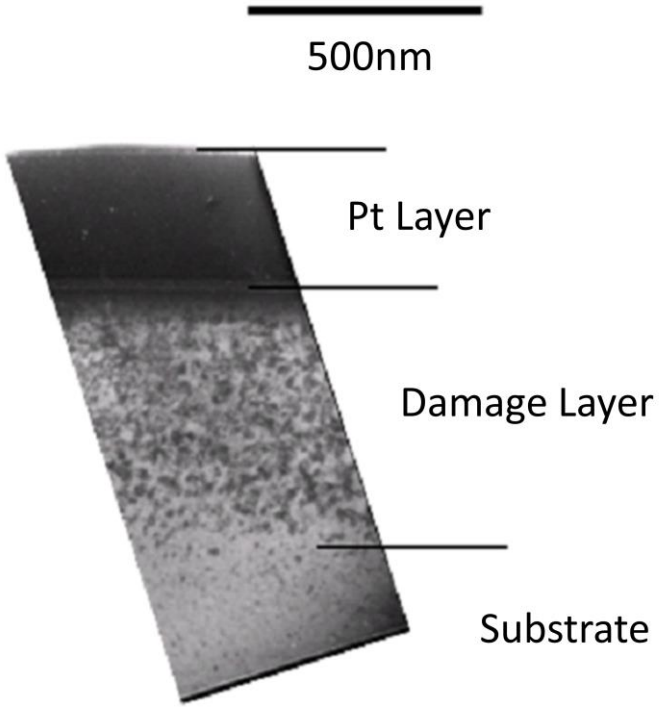

Figure 5.2 - Cross-sectional TEM image of the damage layer produced in Fe12%Cr by Fe^{+} implantation at 2MeV and 0.5MeV.

5.2 Nanoindentation of Ion Implanted Layers

Several commercial suppliers of nanoindentation equipment, such as Hysitron and Aglient Technologies, offer general guidance in the selection of tip geometries for nanoindentation. For each of the three tip geometries tested for this work, a brief overview of the information is given [201, 202]:

Cube Corner

As its name suggests a cube corner tip is a three-sided pyramid with its faces arranged in a similar manner to the corner of a cube. The angle between the tip centreline and face is 34.3° and it is the 'sharpest' of the tips used in the work reported in this thesis.

Berkovich

The Berkovich tip is a relatively blunt three-sided pyramid with a centreline to face angle of 65.3°; this produces the same area to depth ratio as the Vickers hardness tip geometry. This tip is the most frequently used and is a standard for nanoindentation. This tip is commonly used for thin films (>100nm thick) and bulk materials.

Sphere

Unlike pyramidal tips, where the indenter shape is constant with depth, the geometry of the spherical tip and therefore strain, changes continuously with indentation depth. As a result, information regarding the transition from elastic to plastic deformation and work hardening can be examined. The size of plastic deformation is relatively large with spherical indenters and their uses on thin films are limited due to the difficulties in the manufacture of high quality spheres at the micron scale [201].

Important tip dependent parameters such as the size of the plastic zone, stress distribution, contact area and strain rate must be considered for the interpretation of results. This involves a number of additional techniques for investigating material post indentation; however, these techniques are relatively time consuming and it would be unrealistic to complete such a detailed investigation for all materials tested in this thesis. Thus this work was intended to identify the characteristics of each nanoindentation method on the irradiated and un-irradiated regions of the Fe12%Cr sample.

5.2.1 Plastic Zone Size

The volume of material which is deformed by elastic and plastic processes is an important parameter in the interpretation of indentation data and is particularly important for tests on thin films such as ion-implanted layers. There have been several investigations which model the distribution of stresses surrounding the indenter tip [203] and which examine plastic deformation directly [204-206]. The latter consists of several methods such as AFM for the observation of the plastic zone size laterally at the sample surface and/or FIB manufactured cross-sectional specimens for EBSD and TEM of deformation beneath the indenter tip. This work shows that the development of a plastic zone surrounding a *nano*-scale indent is dependent on the material, crystal orientation, tip geometry and indentation depth [204]. Therefore, the multiplication factors (ranging from 4 to 10) which relate indentation depth with the plastic zone size [207, 208] provide a somewhat simplified case and are of limited value for systems where the thickness of a layer/coating presents a significant limitation.

Cross-sectional TEM analysis of nanoindents produced with a range of depths and loads were conducted to determine the size and shape of the plastic zone surrounding the three different types of indenter tip. For all tips, indents were produced within the same grain to avoid differences in plasticity due to variations in crystallographic orientation. For each region, the indents of increasing depth were produced in a line (*figure 5.3a*) so that a large foil containing cross-sections of all the indents could be manufactured, as shown in *figure 5.3b*. Deformation below each indent is produced by a flat surface of the tip on right and a tip edge on the left. Cross-sections of spherical indents were only produced in the irradiated material due to the large indentation pop-in events in the un-irradiated material as described in *section 5.2.3*. This indentation behaviour prevented plastic deformation occurring in the un-irradiated material at indentation depths less than 150nm, preventing a comparison with the irradiated material.

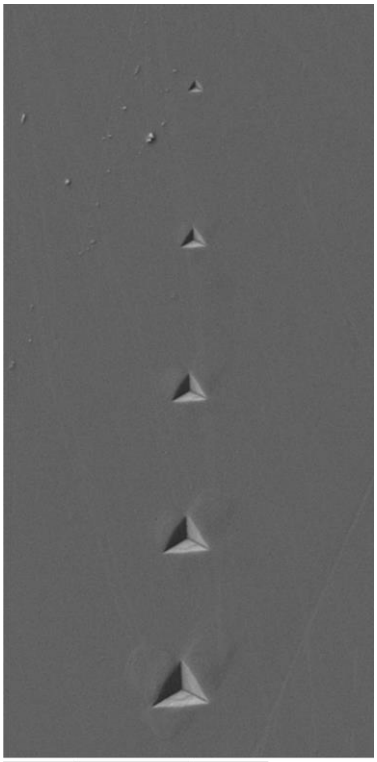

a. **b.**

Figure 5.3 - (a) Line of indents produced at various depths with a Berkovich tip and (b) indent cross-section showing TEM foil orientation with respect to the indents produced on the sample surface.

An overview of cross-sectional TEM images of both irradiated and un-irradiated regions, showing the plastic zones surrounding indents produced by the cube corner, Berkovich and spherical tips, is presented in *figure 5.4, figure 5.5* and *figure 5.6* respectively.

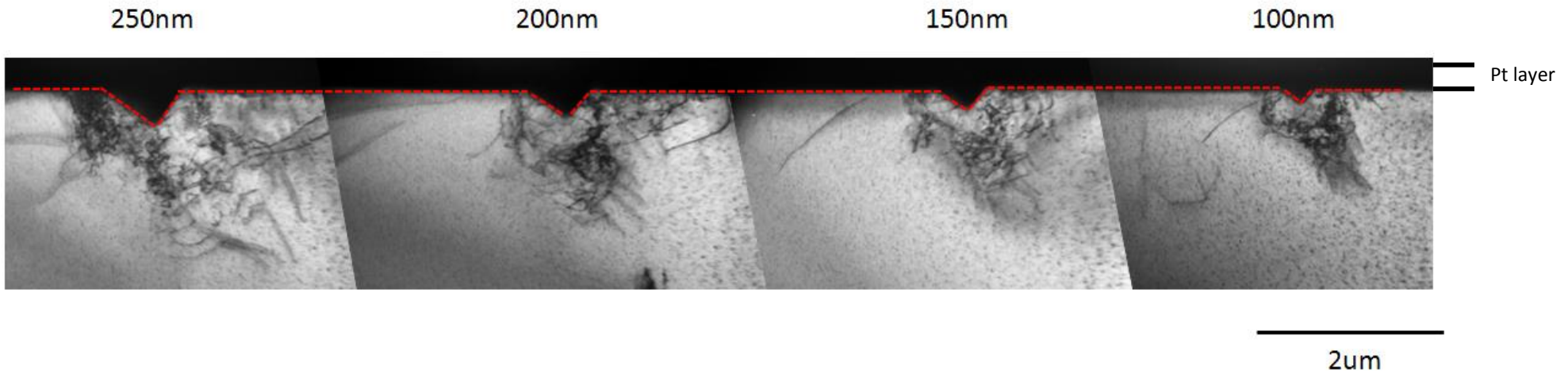

a. UN-IRRADIATED

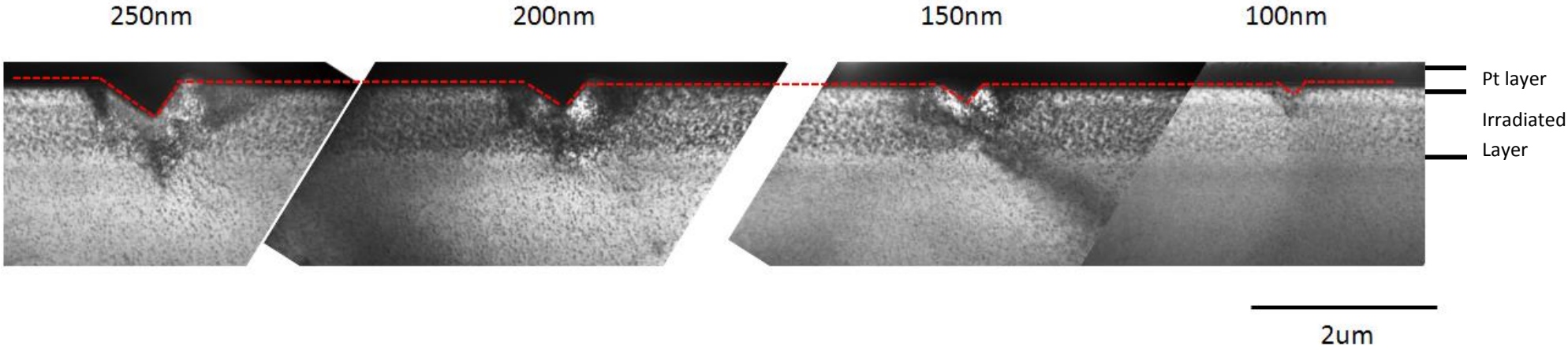

b. IRRADIATED

Figure 5.4 - Cross-sectional images through the centre of indents with depths from 100 to 250nm produced by a cube corner tip in (a) un-irradiated and (b) irradiated regions of the same grain in the Fe12%Cr sample.

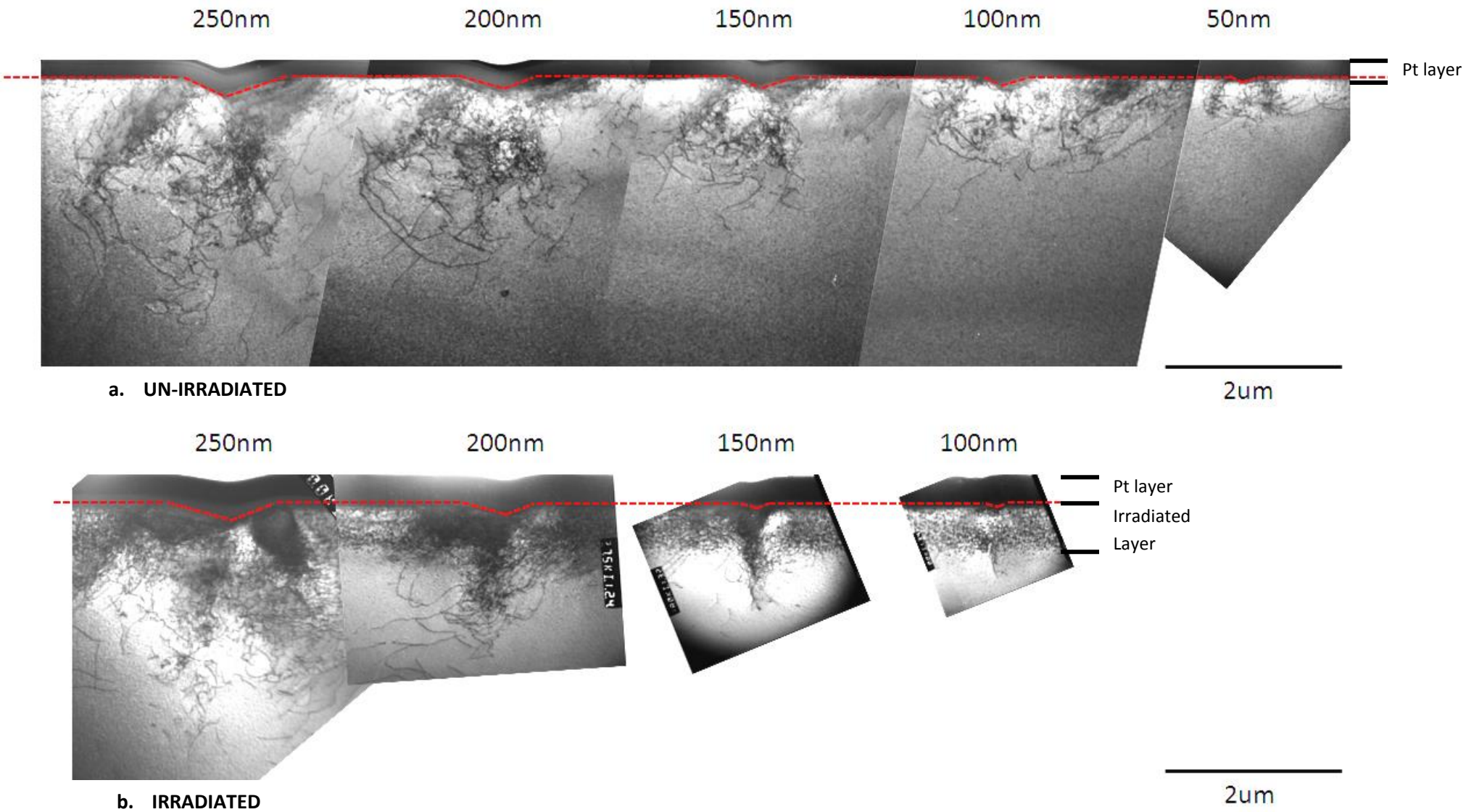

Figure 5.5 - Cross-sectional images through the centre of indents with depths from 50 to 250nm produced by a Berkovich tip in (a) un-irradiated and (b) irradiated regions of the same grain in the Fe12%Cr sample.

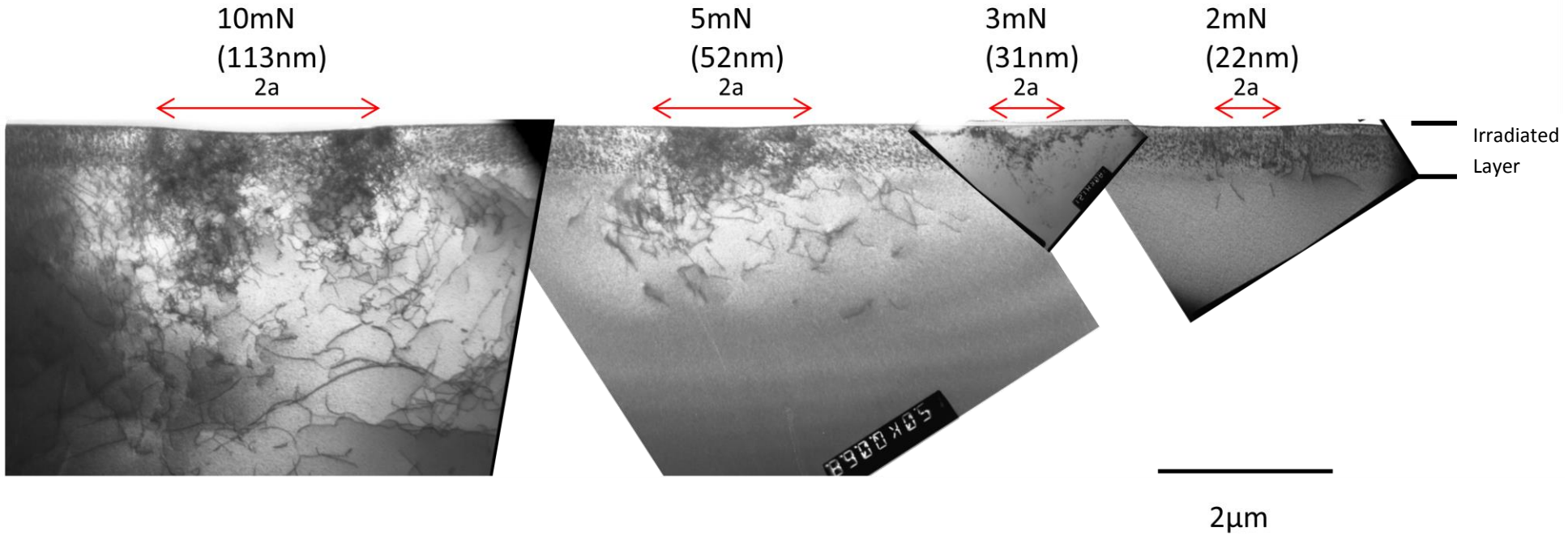

Figure 5.6 - Cross-sectional images through the centre of spherical indents produced in the irradiated region of the Fe12%Cr sample. Indents produced with loads from 2 to 10mN (with corresponding depths from 22 to 113nm) produced by a spherical tip with nominal radius of 10µm. The contact area under load has diameter 2a in each case.

At similar indentation depths the size of the plastic zone, observable by a network of dislocations, changes dramatically as a function of the tip depth-area ratio (the tip sharpness). For the pyramidal tips, the plastic zone size in irradiated material is suppressed in comparison to the un-irradiated material by the presence of the damaged layer. This effect is reduced at larger indentation depths where the plastic zone appears to penetrate through the damage layer into the underlying un-irradiated material. In all cases it is evident that the deformation has developed into multiple regions, such that dislocations are formed into separate lobes where plastic strain has been accommodated by favourable slip systems. This evolving and irregular shape of deformation means that measurement of the plastic zone is difficult to define for such small indentations in a single crystal.

5.2.2 Indentation Sink-in and Pile-up

Before cross-sectioning, AFM scanning and SEM imaging of the plastic deformation surrounding the residual indent impressions was conducted to investigate the evolution of sink-in or pile-up with indentation depth. Both sink-in and pile-up of material surrounding the indenter tip influence the actual contact area and can cause errors and/or artefacts in mechanical property measurements which are calculated using a calibrated tip area function (see *section 3.3.1*).

The extent of sink-in or pile-up is closely related to the proximity of the plastic deformation in relation to the indenter tip. For standard tests this behaviour is dependent on the ratio of elastic modulus to yield stress, E/σ_{yield}, and the work hardening coefficient, n, of the material (where $\sigma = K\epsilon^n$) [209, 210]. In addition, pile-up/sink-in can be more prominent in

indentation tests which include a thin coating on an underlying substrate [207]. Plastic deformation may take place in the substrate (away from the tip) for indentation in hard coatings on a soft substrate or adjacent to the tip for indentation in a soft coating on a hard substrate [211]. Thus, the substrate beneath thin damage layers produced by ion-implantation may influence the sink-in/pile-up behaviour during indentation. Differences in sink-in/pile-up properties between irradiated and un-irradiated materials may obscure the observation of irradiation-induced changes in mechanical properties.

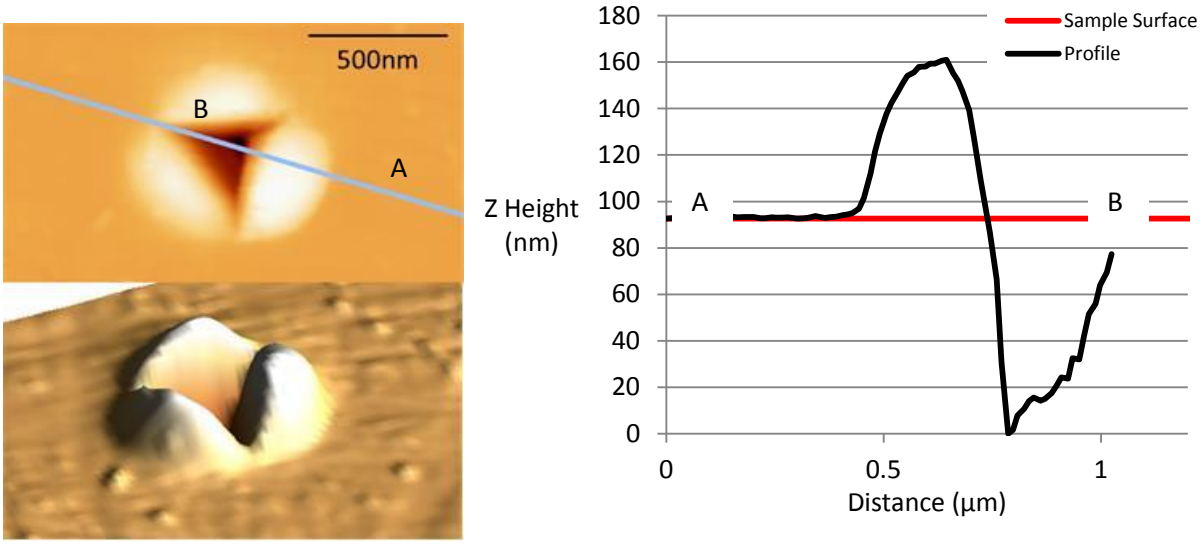

Figure 5.7 – AFM tomography of a 200nm depth indent with a cube corner tip in an irradiated region of Fe12%Cr shown in 2D with line profile marker and 3D (a) and height data from line profile (b).

The surface topography surrounding each indent was observed by AFM to investigate the evolution of pile-up with indentation depth. A typical 3D image of the surface topography surrounding a cube corner indent is given in *figure5.7a*, which clearly shows the pile-up morphology corresponding to the three flat surfaces of the indenter tip. Line profiles were

taken through the centre of each indent; a typical example of surface data from each line profile is shown in *figure 5.7b*. For pyramidal tip indentations, the position of the line profiles (as indicated on *figure 5.7a*) provided surface height data through an apex of the indentation (where two flat surfaces of the tip meet) and through the flat edge of the indentation with adjacent pile-up lobe. AFM data showing pile-up lobe sizes for indentation depths of 50-250nm produced by both pyramidal tips are shown in *figure 5.8*.

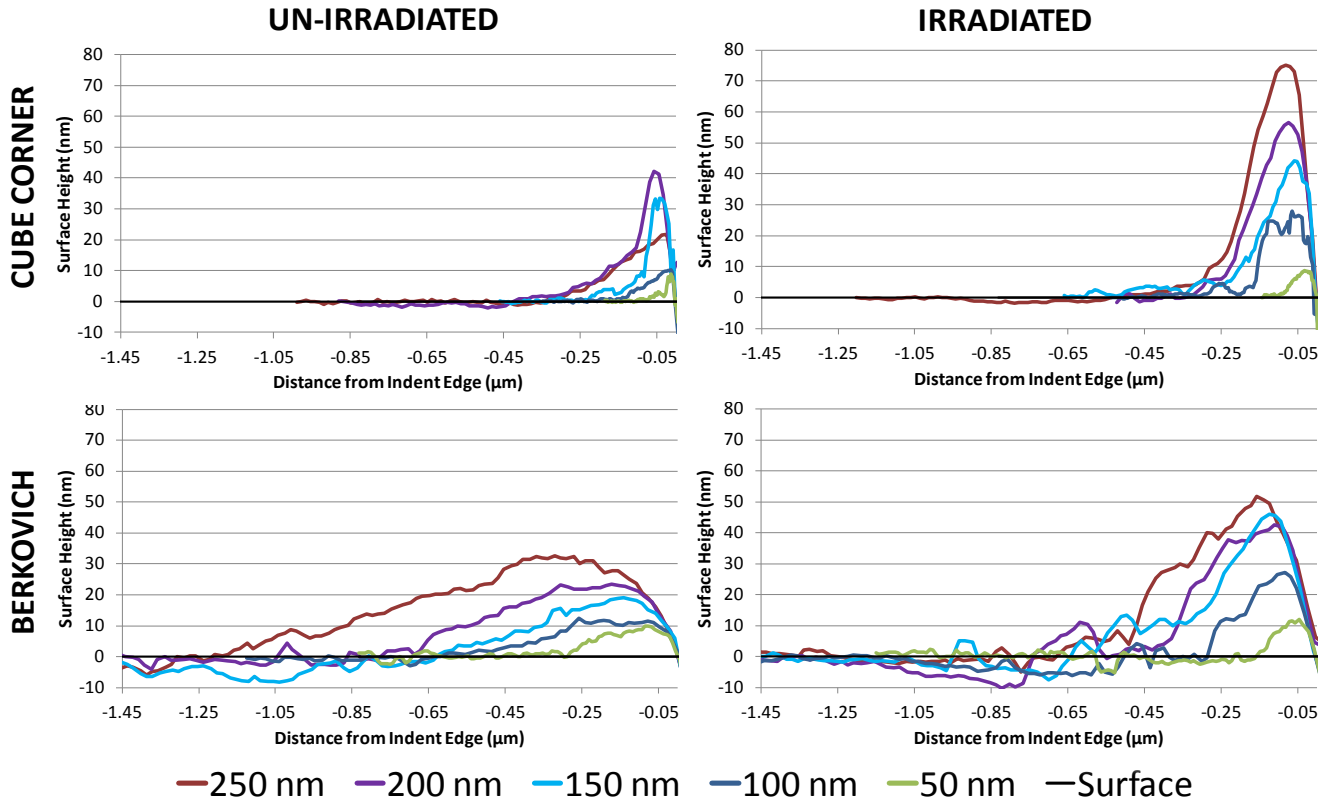

Figure 5.8 - AFM line profile through pile-up lobes of indentations of depths from 50 to 250nm produced by both Berkovich and cube corner tips. Profiles corrected for surface height and alignment with flat surface of indenter tip on the right in each case.

All indents produced by the pyramidal tips produced pile-up adjacent to the flat edges of the indenter tip and pile-up extended to greater heights in the irradiated material. The residual impressions produced in the irradiated material by spherical indentation of several loads

were also investigated by AFM in QMUL [212] and line profiles taken through the deepest point in the impression are shown in *figure 5.9*. In contrast to indentations produced by the pyramidal tips, sink-in was observed for indentations produced at low loads and pile-up only developed once the indent had reached a load of 50mN.

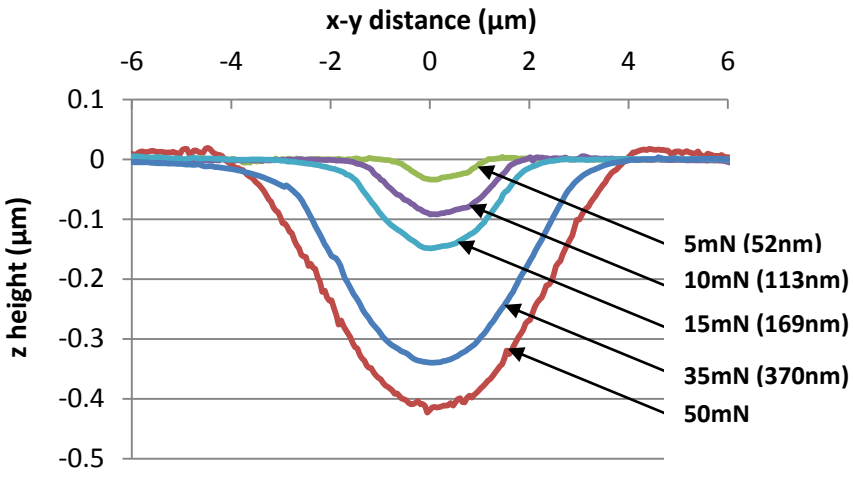

Figure 5.9 - AFM line traces through deepest pixel of indentation for indents produced by a spherical tip (nominal radius 10µm) at loads of 50mN, 35mN, 15mN, 10mN and 5mN (corresponding indentation depth in brackets). Data redrawn from ref. [212].

For the spherical tip, the actual contact area was calculated by defining a new contact radius (a), identified by the point of inflection in the AFM profiles [213]. Measuring the contact area by the AFM line profiles for the pyramidal tips was attempted according to a method proposed by Kese et al. [214]. This approach assumed that the additional contact area was in the form of a semi-ellipse with a chord length equal to the flat edge of the indentation impression and a segment height equal to width measurements of the pile-up in contact with the tip. SEM images of the Berkovich and cube corner indents in the un-irradiated and irradiated material are shown in *figure 5.10*.These images show that the semi-ellipse assumption cannot be used for small, single crystal indents due to in-homogeneous plastic deformation and pile-up behaviour. The actual contact area accounting for the pile-up was

evaluated by the direct measurement of area using SEM imaging as shown in *figure 5.10*, in a similar method to that proposed by Tsui et al. [211].

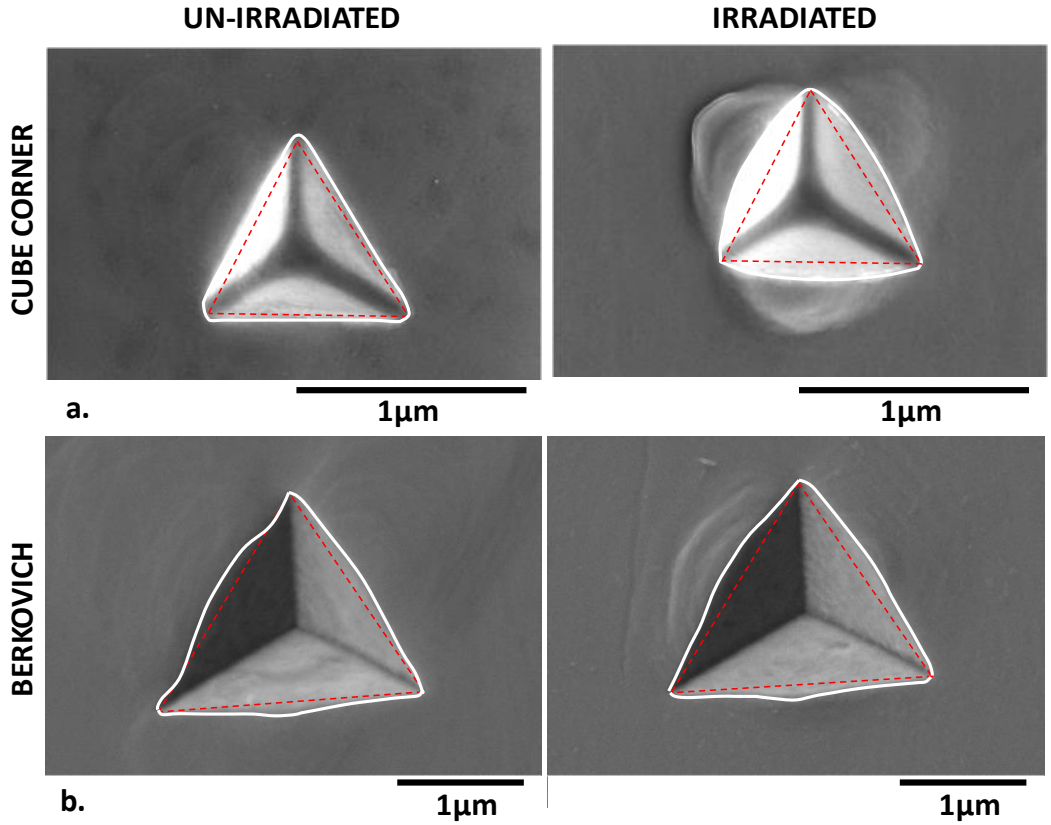

Figure 5.10 - SEM images showing corner-to-corner measurement (A_{cc}) of contact area (red dashed) and actual (A_{actual}) contact area (white solid) for 250nm deep cube corner (a) and Berkovich (b) indents in irradiated and un-irradiated regions of the same grain.

Figure 5.11 shows the ratio of actual contact area to the corner-to-corner measurement of contact area (no pile-up) for the pyramidal tips, and actual contact area to depth-sensing measurements for the spherical indents with increasing depth; this ratio represents sink-in for values <1 and pile-up for values >1. Data are shown for both irradiated and un-irradiated regions of the sample apart from the spherical indentations where indent impressions were limited to depths >150nm due to large pop-in events in the un-irradiated material (described in *section 5.2.3*).

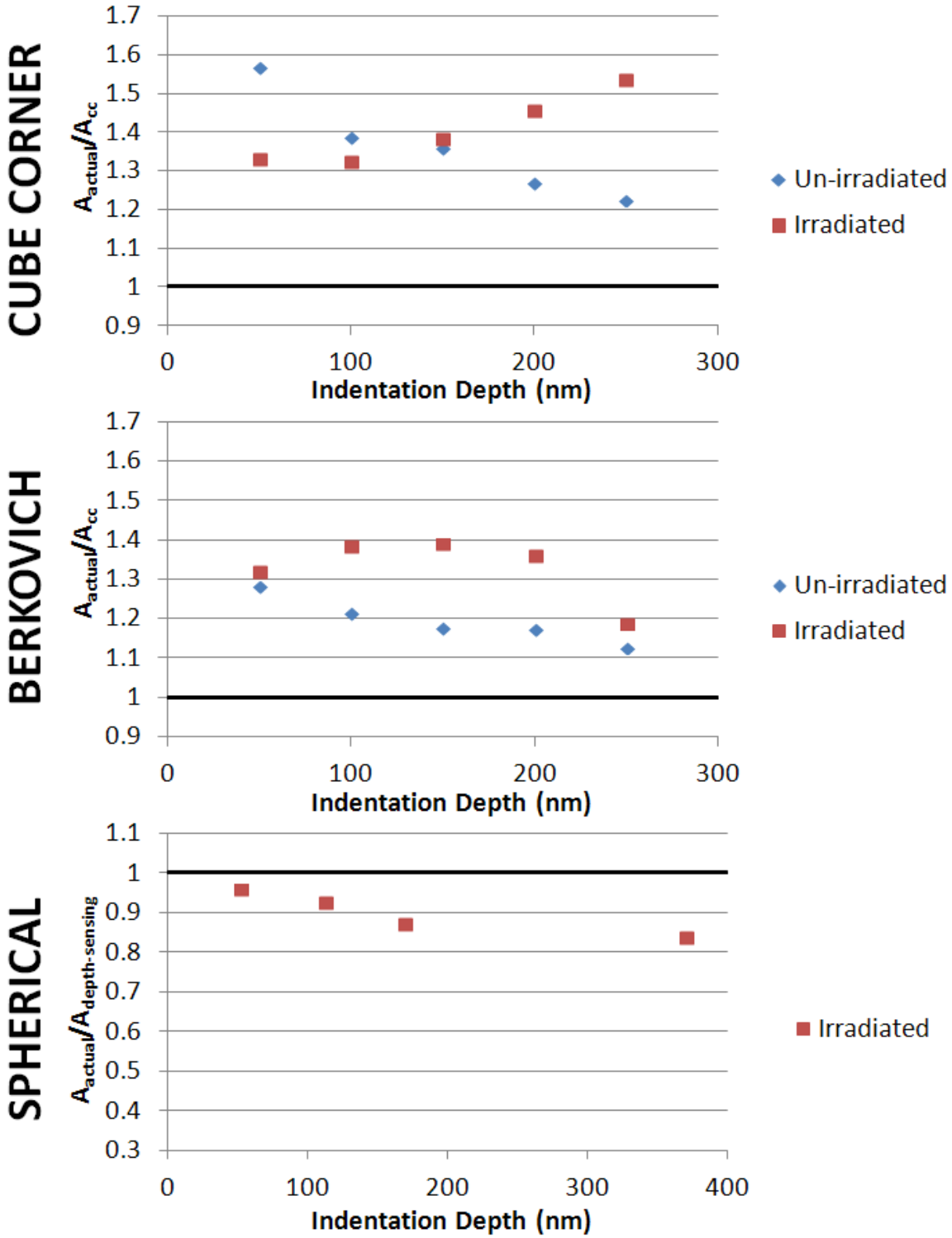

Figure 5.11 - Ratio of actual contact area (A_{actual}) to the corner-to-corner (A_{cc}) measurement (A_{actual}/A_{cc}) of indentations produced by the cube corner and Berkovich tips. A_{cc} is replaced with the depth-sensing calculation ($A_{actual}/A_{depth\text{-}sensing}$) for indentations produced by the spherical tip. Data are plotted against indentation depth (nm) for all tips.

The additional contact area due to pile-up (A_{actual}/A_{cc}) surrounding the pyramidal tips was significant. For both pyramidal tips, A_{actual}/A_{cc} in the un-irradiated material decreases as the indentation depth increases. For indentation depths from 50 to 250nm, A_{actual}/A_{cc} produced by the cube corner and Berkovich tips range from ~60 to 20% and ~30 to 10%. For the cube corner tip, A_{actual}/A_{cc} in the irradiated material increases from >30% to >60% over the same depth range. Similarly, A_{actual}/A_{cc} for the Berkovich tip increases with indentation depth to a depth between 50 and 200nm and then decreases dramatically. For spherical indents, the material surrounding the indenter tip exhibited sink-in (A_{actual}/A_{cc} <0), which increased with indentation depth.

According to *equations 3.6* and *3.8* in *section 3.3.1*, the variation in contact area produced by pile-up/sink-in will cause an error of $E/(A_{actual}/A_{cc})^{-1/2}$ in elastic modulus and $H/A_{actual}/A_{cc}$ in hardness. The next section will assess the effect of pile-up and sink-in in the mechanical property measurements produced using the depth sensing technique.

5.2.3 Indentation Data

Figure 5.12 shows nanoindentation data produced by using the cube corner, Berkovich and spherical tips. For each tip arrays of indents were produced in the un-irradiated and irradiated regions of the same grain. The indentation data presented for the pyramidal tips is an average of ~8 indents and error bars plot the standard deviation. Due to the 'pop-in' nature of the spherical indents (discussed below), the data presented for the spherical tip is from a single indent. The total indentation depth (h_t) was set to 2000nm for the pyramidal tips, which produced maximum loads (P_t) of 25mN for cube corner indents and 138mN for

Berkovich indents. Spherical indentation (using the UMIS 2000 instrument) was conducted under a load-control method with a maximum load (P_t) of 35mN; for indents which exhibited plastic deformation, this produced an indentation depth (h_t) of approximately 400nm.

For all three tips, the indentation load at a given indentation depth was higher in the irradiated material; this translates to a higher hardness measurement, which tends towards that of the un-irradiated material as the indentation depth increases. The spherical indentation exhibited a large elastic stresses. In the majority of cases the indentation response in the un-irradiated material remained entirely elastic up to 35mN with the spherical tip (shown on *figure 5.12g*); at this load the indentation depth was ~150nm producing a mean pressure (P_m) of up to 7.8GPa beneath the indenter tip.

For both pyramidal tips, the elastic modulus appears to be higher in the irradiated material; but as shown in *figure 5.14* this is entirely accounted for when using the data with the actual contact area which corrects the data for contributions from pile-up. The elastic modulus measured with the Berkovich tip decreases with indentation depth, which is likely to be caused by poor compliance in the sample mounting method (hot wax) which decreases the apparent contact stiffness at the high loads produced with the Berkovich geometry (138mN).

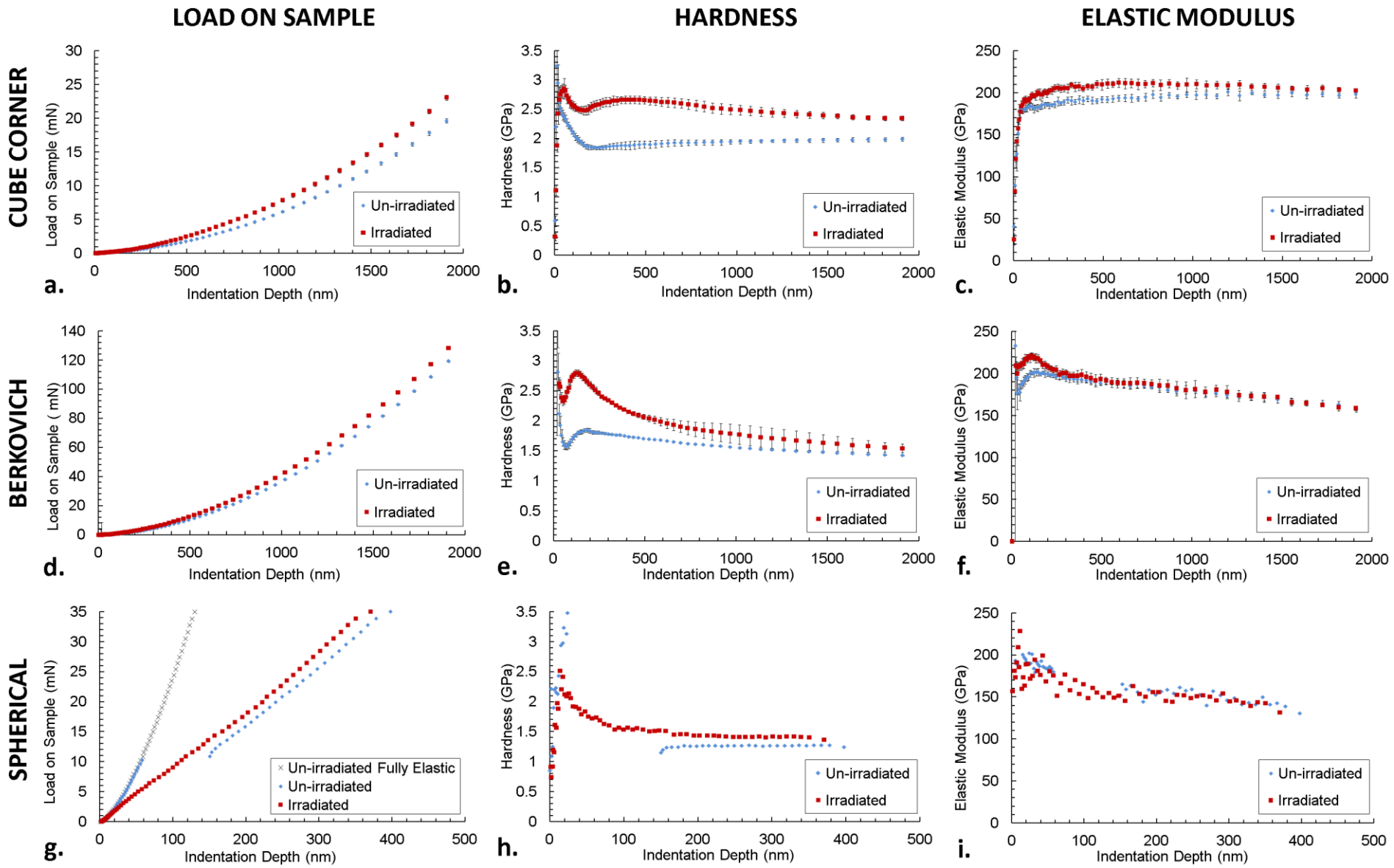

Figure 5.12 - Load on sample, hardness and elastic modulus indentation data for un-irradiated and irradiated regions of Fe 12%Cr, produced by cube corner, Berkovich and spherical tips.

Indentation Pop-in

The elastic-plastic transition behaviour of indents produced by all three indenter tips can be observed in the load-depth data at low indentation depths in *figure 5.13*. In every case, the irradiated material exhibited a smooth transition from elastic to plastic deformation. In the un-irradiated material, the initiation of plastic deformation can be identified by a number of discrete jumps in the tip displacement known as pop-in events; these are produced by the nucleation of the first dislocations, relieving strain beneath the tip [215]. At very early indentation depths (before the first pop-in), all three tips are essentially spherical in shape due to blunting of the pyramidal tips and the load-depth data exhibit Hertzian contact behaviour (as plotted for the spherical tip in *figure 5.13*). The magnitude of the pop-ins are similar for the two pyramidal tips, however the smallest jump in tip displacement in the data produced by the spherical tip was significantly larger (from 58nm to 151nm).

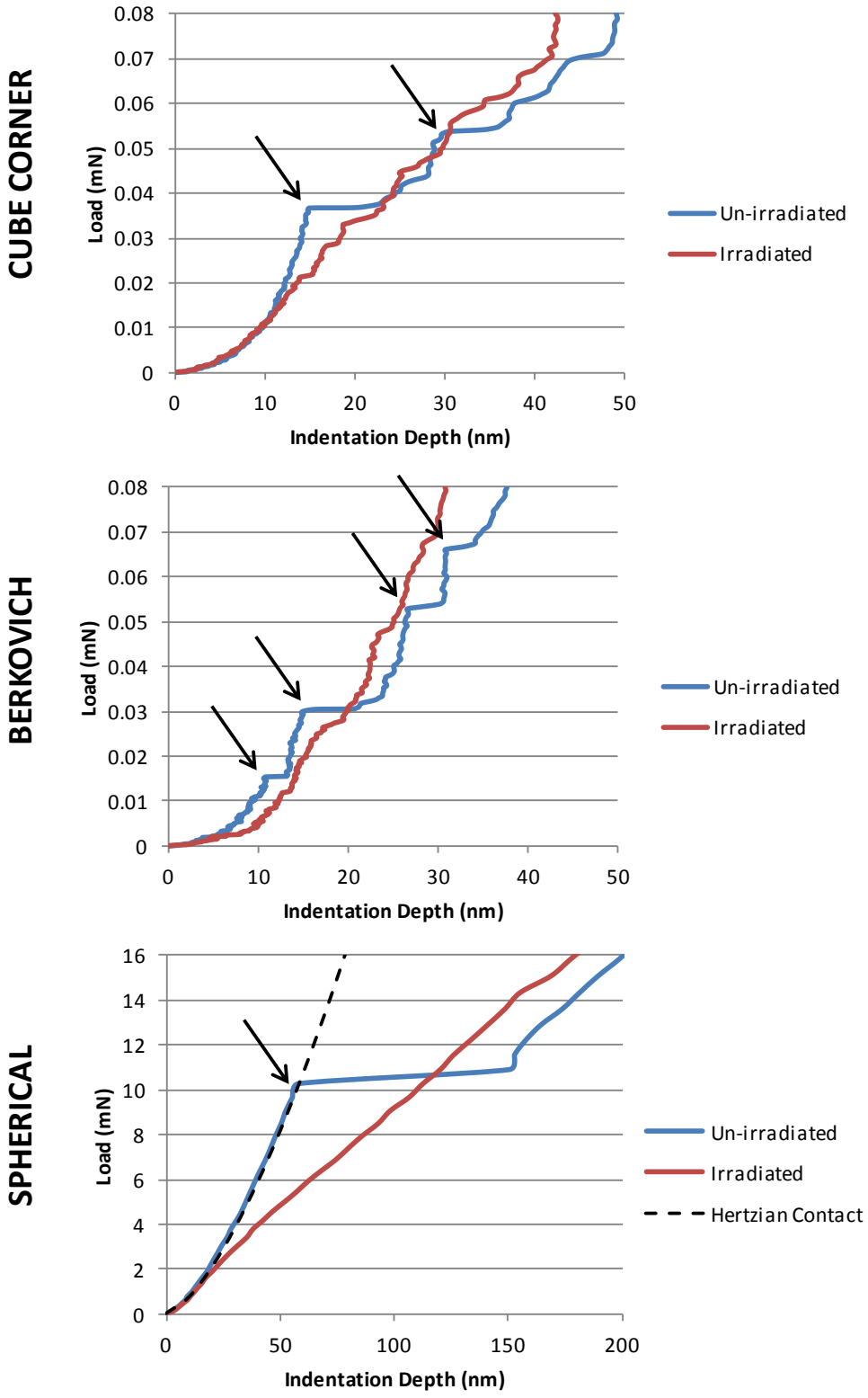

Figure 5.13 - Typical load-depth data produced with indentation with the cube corner, Berkovich and spherical tips; black arrows indicate pop-in events in the un-irradiated material.

Elastic Modulus

As shown in *figure 5.14* the apparent elastic modulus calculated by depth sensing data produced by both pyramidal tips is larger for the irradiated material. This is accounted for entirely when recalculating the same indent data with SEM measurements of the actual contact area (*section 5.2.2*). The additional area produced by pile-up (A_{actual}/A_{cc}) increases the apparent elastic modulus by approximately 10 to 30%. The elastic modulus measured with the spherical tip decreases with increasing load; this is entirely accounted for by the sink-in of material identified by area corrections from the AFM measurements discussed in *section 5.2.2*. Sink-in decreases the apparent elastic modulus by ~30% at the highest load (35mN). Elastic modulus data from an indent which remained entirely elastic in the un-irradiated region are also plotted in *figure 5.14*. The elastic response of this indent is not affected by plastic sink-in and should therefore remain independent of depth. In contrast to the un-irradiated data which was in an elastic-plastic regime at a depth greater than 51nm, the measured elastic modulus remains close to the corrected value of 190GPa (+/- 2.7GPa). Data from fully elastic indents are subject to noise at indentation depths below 50nm and the total indentation depth is limited due to reaching the maximum load of 35mN.

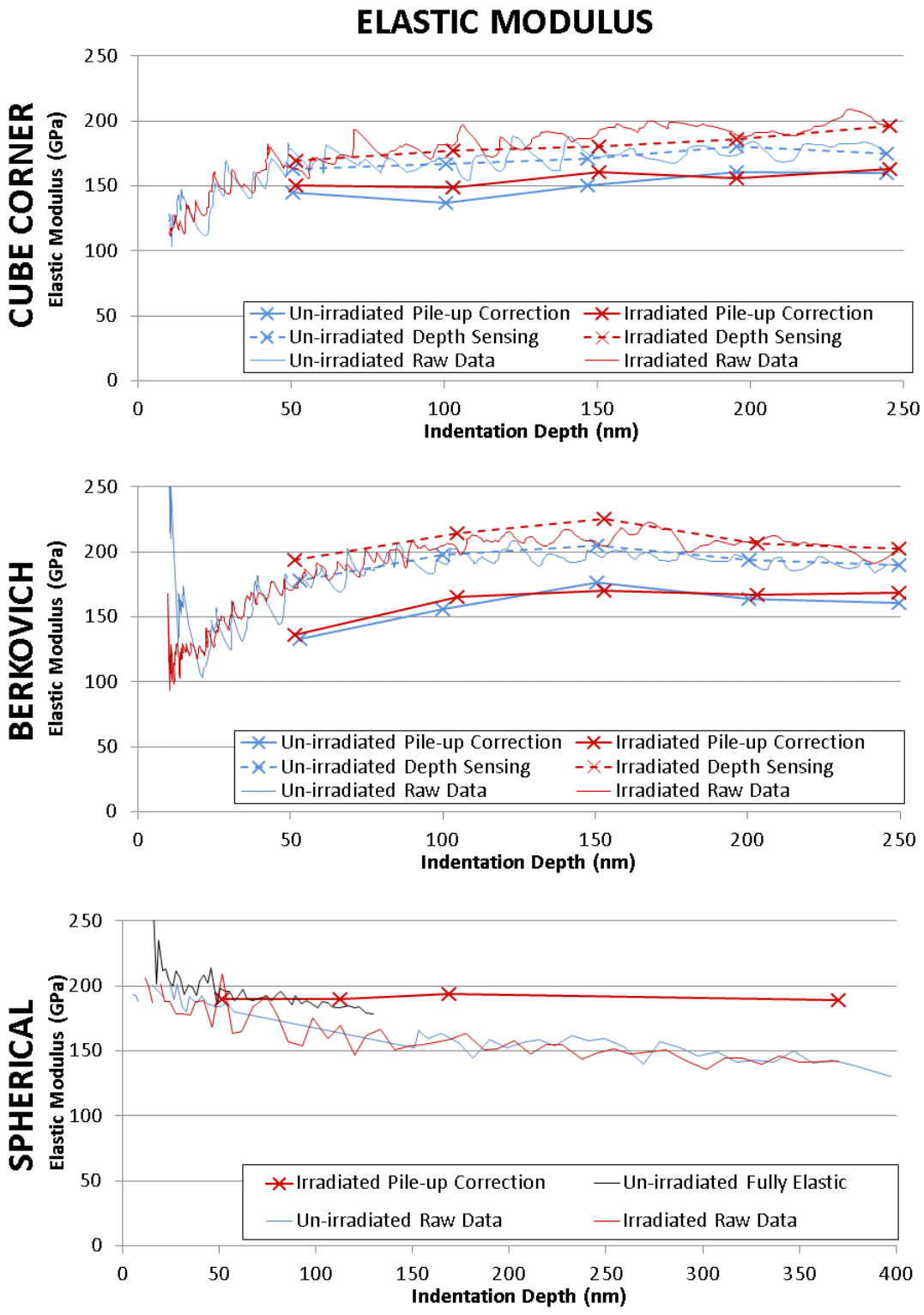

Figure 5.14 - Elastic modulus data produced with indentation by the cube corner, Berkovich and spherical tips. Original data plotted against data corrected for pile-up (pyramidal tips) and sink-in (spherical tip).

Hardness

Figure 5.15 shows the hardness measurements from the raw CSM data of a typical indent (for pyramidal tips), depth-sensing data taken at P_{max} for the indents with increasing depth and values corrected for the actual contact area accounting for pile-up/sink-in (*section 5.2.2*). In comparison to the corrected measurements, values for hardness using the depth sensing method were up to 41% higher for the cube corner tip, 84% higher for the Berkovich tip and 19% lower for the spherical tip. The corrected hardness values from 50 to 250nm produced an irradiation hardening (ΔH) of ~0.25GPa for cube corner data and ~0.6GPa for Berkovich data. A value of irradiation hardening could not be directly calculated from the data produced by the spherical tip, due to the lack of plastic data until after pop-in at depths of approximately 151nm. The same indentation depth in the irradiated region corresponds to a plastic zone which has expanded well beyond the damage layer into the underlying un-irradiated material.

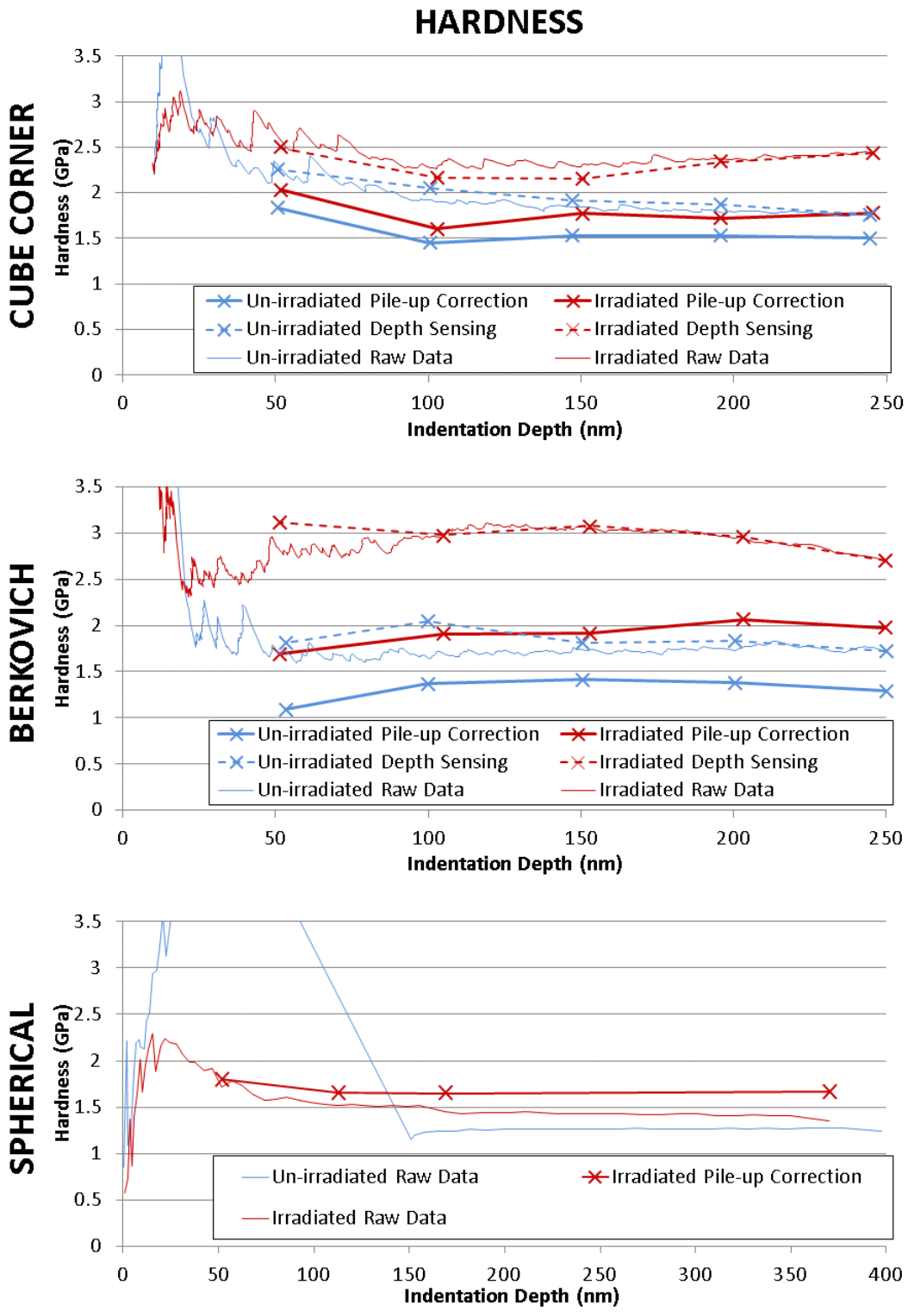

Figure 5.15 - Hardness data produced by indentation with the cube corner, Berkovich and spherical tips. Original data plotted against data corrected for pile-up (pyramidal tips) and sink-in (spherical tip).

5.2.4 Characteristics of Nanoindentation

A primary concern when using nanoindentation for mechanical property measurements of thin surface layers such as ion-implanted surfaces is the range of indentation depth which produce representative mechanical property data of the material within the layer. For the measurement of the 800nm thick irradiated layer discussed here, the useful indentation depth range is limited due to high levels of noise at smaller depths and contribution from the underlying un-irradiated substrate at larger depths. A significant limitation in the use of the spherical tip at smaller depths is set by the prominent pop-in events in the un-irradiated material, which prevent the measurement of plastic properties at depths less than at least 150nm.

Pharr et al. [216] have shown that there are three potential sources of error in the measurement of mechanical properties using the CSM method at indentation depths <100nm:

i. During CSM measurements, the NanoXP system records the mean load rather than the peak load. At low indentation depths, the oscillation in tip displacement can cause a relatively large oscillation in the load resulting in a lower mean load compared to the peak load.
ii. As shown in *equation 3.14* the contact stiffness is calculated from the amplitude of the load and displacement signals ($\Delta P/\Delta h$). This assumes that the unloading load-displacement curve is linear within the range of oscillation, however at low indentation

depths the large oscillation in load may exhibit curvature in the unloading curve resulting in a lower measured stiffness.

iii. At low indentation depths, the indenter tip and surface may not be in full contact throughout the entire displacement range of oscillation.

As shown in the raw data on *figure 5.14*, both pyramidal tips produced low elastic modulus measurements compared to standard Fe measurements, which increased with depth up to a consistent value at ~50-100nm. This happens in both un-irradiated and irradiated material, thus cannot be caused by a reduction in stiffness associated with the pop-in events exhibited in the un-irradiated material.

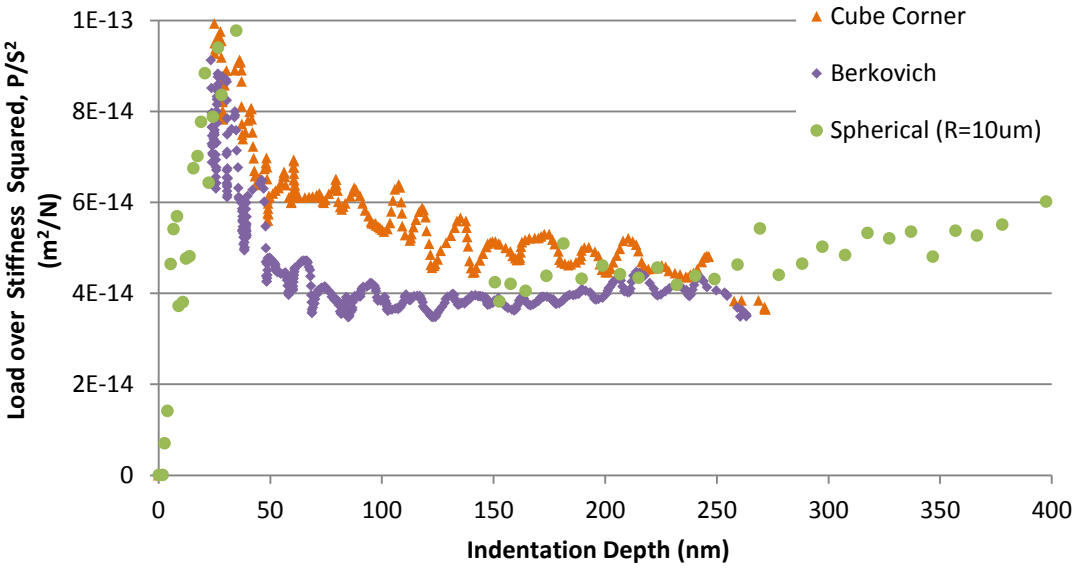

Figure 5.16 - Plots of load over stiffness squared versus indentation depth for indentations in the un-irradiated region of the same grain, produced by the cube corner, Berkovich and spherical tips.

The value of load over stiffness squared (P/S^2) is a useful indentation parameter as it is independent of indentation depth and contact area, provided elastic modulus and hardness do not vary with indentation depth [217]. Therefore, the plot of P/S^2 versus depth can be used for the identification of potential sources of error in nanoindentation data. *Figure 5.16* shows P/S^2 versus depth for indentation data produced in the un-irradiated region of the same grain in the Fe12%Cr sample. The spherical indentation data was not produced by a CSM method and the values for P/S^2, shown in *figure 5.16* for comparison, are constant for the data available in the depth range of 151 to 400nm. The pyramidal tips exhibit higher values of P/S^2 at smaller indentation depths, which appear to stabilise at a depth of ~150-200nm for the cube corner tip and ~50-75nm for the Berkovich tip. At low depths, higher values of P/S^2 may be caused by a reduction in stiffness as a result of (ii) and (iii) described above. From *equations 3.5* and *3.8*, $P_t = f(A)$ and $S = f(A^{\frac{1}{2}})$, thus the resulting load oscillation as a fraction of total load (P_{os}/P_t) produced by the displacement oscillation ($h(\omega)$) of 2nm decreases as indentation depth increases. Without knowledge of the exact tip shape for the first few tens of nanometres of indentation depth it is unclear how the effect of (ii) and (iii) would differ between the two pyramidal tips. As shown in *figure 5.17*, the ratio of load oscillation to total load (P_{os}/P_t) does not differ substantially between the two tips at low depths due to similar levels of blunting. For both tips, the value of (P_{os}/P_t) is greater than 1 for depths up to 30-40nm. It is likely that the tip is not in full contact at these indentation depths and may produce errors in the value of P/S^2 up to approximately 50nm.

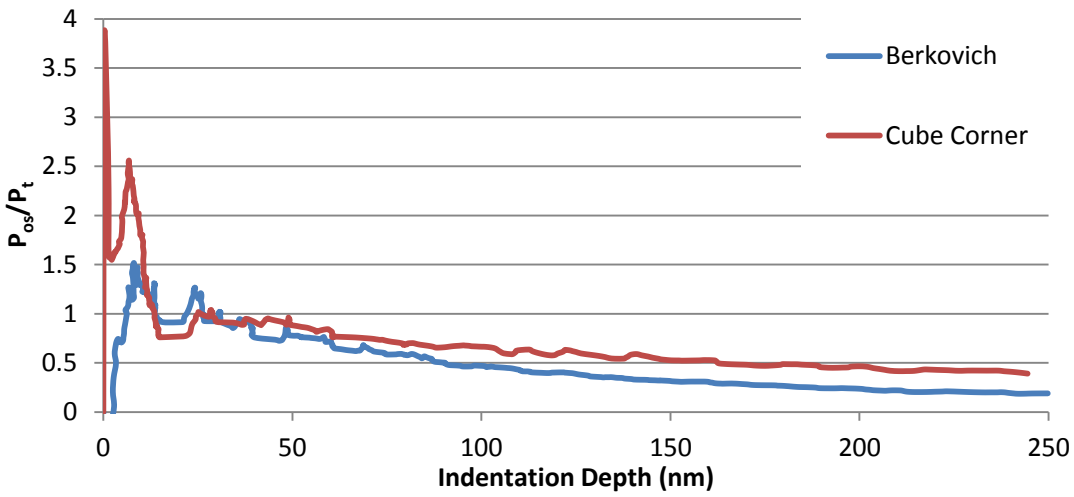

Figure 5.17 - Ratio of load oscillation to total load (P_{os}/P_t) for cube corner and Berkovich tips.

The depth range where P_{os}/P_t>1 cannot explain the decrease in the value of P/S^2 with depth produced by the cube corner tip. The non-linear behaviour may be caused by an indentation size effect (ISE) [218], which is likely to be more prominent in the data produced by the cube corner tip. The size of the plastic zone with indentation depth (*figure 5.4*) is significantly smaller than that produced by the Berkovich and spherical tips and hardness data produced by the cube corner (*figure 5.15*) indicates that an ISE exists.

As described in *section 5.2.1* the expansion of the plastic zone is suppressed by the radiation damage in the irradiated layer. This correlates well with the observations of larger pile-up surrounding the pyramidal tips in *section 5.2.2*, where deformation is constrained closer to the tip compared to the un-irradiated material (*figure 5.8*). As the indentation depth increases the plastic zone extends beyond the damage layer and the hardness tends towards that of the un-irradiated material (*figure 5.12*). The plastic zone beneath the Berkovich indentation extends beyond the damage layer at a depth of approximately 200nm. This is also indicated by the relative drop in the pile-up from 200 to 250nm shown in *figure 5.11*.

The hardness measured in the irradiated material with the Berkovich tip tends towards the un-irradiated value at smaller depths compared to measurements for the cube corner tip. This may be caused by a combination of significant pile-up surrounding the cube corner with increasing depth and a smaller plastic zone in the irradiated material. Due to the large pop-in events, hardness data produced by the spherical tip are limited; however there is only a small difference in hardness between the un-irradiated and irradiated material (0.22GPa) evident after the pop-in event at an indentation depth of 150nm. As shown in *figure 5.6*, the plastic zone has extended well beyond the damage layer at spherical indentation depths greater than ~100nm.

The mechanical property data produced by the three indentation methods are given in *table 5.2*; these will be compared with data from micro-cantilever testing in *section 5.4*.

Table 5.2 - Mechanical property data uncorrected and corrected for pile-up for all three indentation methods. Data averaged over a depth range of 100-250nm for cube corner and 50-200nm for Berkovich tips. Data taken at ~5mN (52nm) for spherical indentation.

HARDNESS		**Un-irradiated**		**Irradiated**	
		Hardness (GPa)	**SD**	**Hardness (GPa)**	**SD**
Corrected	Cube Corner (100-250nm)	1.5	0.04	1.72	0.08
	Berkovich (50-200nm)	1.31	0.15	1.9	0.15
	Spherical (5mN/52nm)			1.8	
Uncorrected	Cube Corner (100-250nm)	1.9	0.12	2.28	0.14
	Berkovich (50-200nm)	1.88	0.11	3.03	0.08
	Spherical (5mN/52nm)			1.72	

ELASTIC MODULUS		**Un-irradiated**		**Irradiated**	
		Elastic Modulus (GPa)	**SD**	**Elastic Modulus (GPa)**	**SD**
Corrected	Cube Corner (100-250nm)	152	11	157	6
	Berkovich (50-200nm)	158	18	160	16
	Spherical (5mN/52nm)			190	
Uncorrected	Cube Corner (100-250nm)	173	6	185	8
	Berkovich (50-200nm)	193	11	210	13
	Spherical (5mN/52nm)	192		209	

5.3 Micro-mechanical Testing of Ion Irradiated Materials

The purpose of this section is to assess micro-cantilever testing methods by using both the simple and 'waisted' beam geometries as described in *chapter 4* on the ion implanted Fe12%Cr sample.

5.3.1 Uniform Cross-Section Beam Testing

An array of 12 uniform cross-section type beams were machined in both un-irradiated and irradiated regions of the Fe12%Cr sample as shown in *figure 5.18a*. The regions are shown divided by a FIB milled line with un-irradiated material bottom left and irradiated material top right. A typical beam with a milled marker box for indenter positioning is shown in *figure 5.18b*.

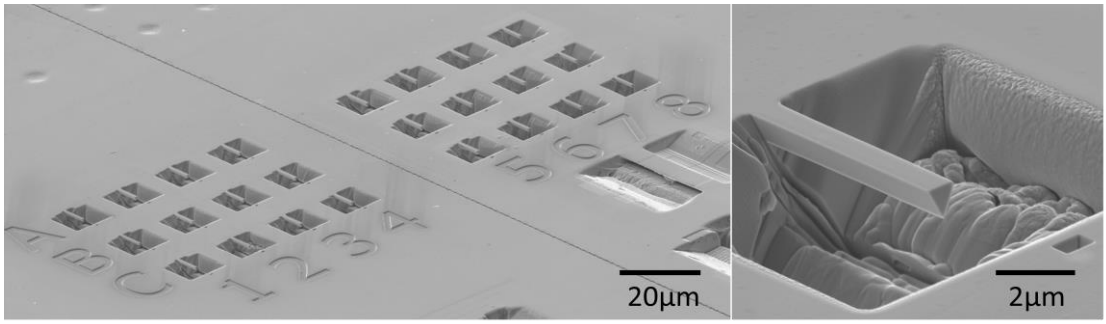

a. **b.**

Figure 5.18 - SEM image showing (a) arrays of uniform cross-section type micro-cantilever beams in un-irradiated (left) and irradiated (right) regions of the sample and (b) a typical beam.

The beams were undercut with a 50pA beam current at 30°, to a target depth of 0.8µm to ensure beams in the irradiated region were fully within the radiation damage layer. Stereo-

imaging measurements showed that the bottom angle of the beam cross-section was ~50.3° due to taper of the Ga^+ beam; thus the actual beam depths were 0.98µm +/- 0.1µm. Each beam was loaded approximately 1µm from its free end and ~5µm from the fixed end resulting in aspect ratios, length/width, of ~5. Tests were conducted with a target strain of 0.05 and strain rate of 2 x 10^{-4}/s, requiring displacements from 700 to 1200nm and constant displacement rates of 2.9 to 4.5nm/s. Maximum loads during testing were in the region of 20 to 30µN, which was not sufficient to leave a visible impression into the surface with the Berkovich tip. The location of the point of loading (where the indenter tip and beam made contact) was observable by a faint contrast mark using the in-lens secondary electron detector in the SEM. The position of this with respect to the free end of the beam was measured by stereo-imaging using the methods described in *section 3.3.2* and the raw load-displacement data for each test was analysed with simple beam theory and with FEA using the methods described in *chapter 4*.

Simple Beam Theory

Typical stress-strain curves for tests conducted in the un-irradiated and irradiated regions of the Fe12%Cr sample are shown in *figure 5.19*. Many tests in the un-irradiated material exhibited large load drops which are likely to be associated with the nucleation of dislocations. Similarly to indentation pop-ins, described in *section 5.2.3*, these strain bursts were not as large in the irradiated material.

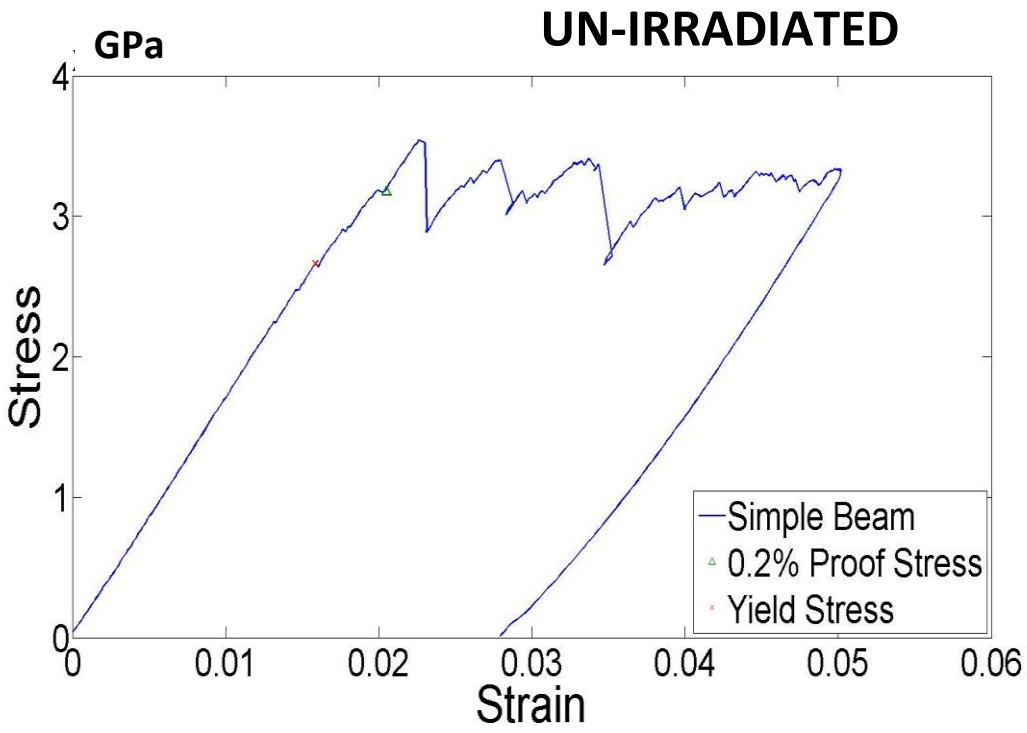

a.

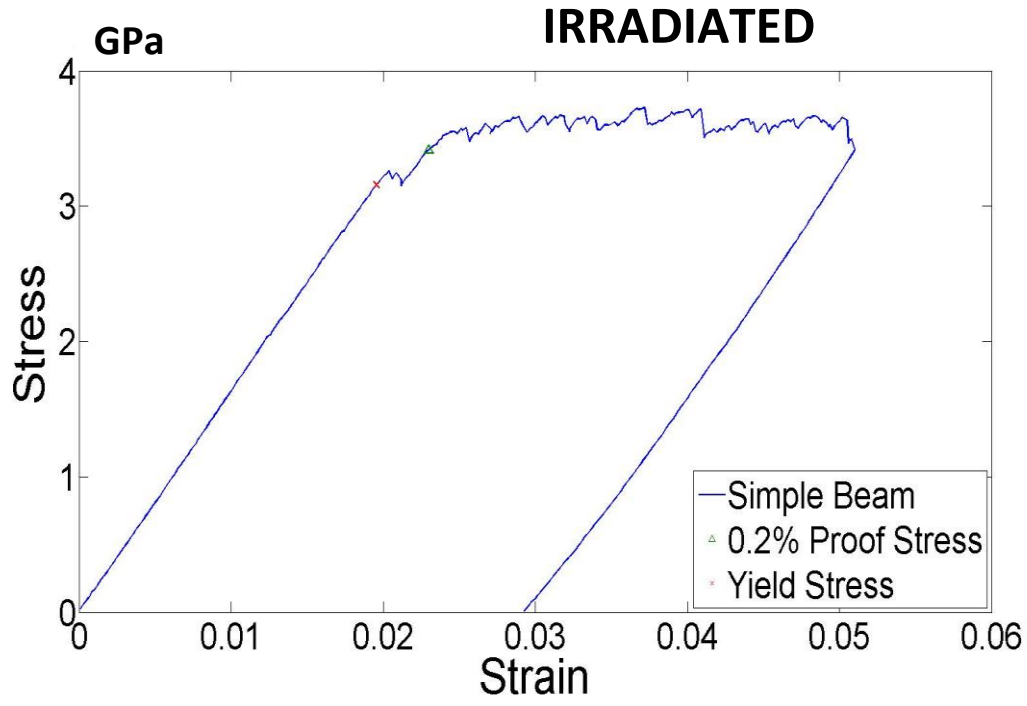

b.

Figure 5.19 - Typical stress-strain behaviour of a micro-cantilever test in the un-irradiated (a) and irradiated (b) region of the Fe12%Cr sample.

Average mechanical property measurements for beams tested in both irradiated and un-irradiated regions of the sample were calculated according to methods described in *section 4.1*. These are shown in *table 5.3*.

Table 5.3 - Average mechanical property measurements produced by simple beam theory from ~12 micro-cantilever tests in un-irradiated and irradiated Fe12%Cr.

		Un-irradiated			Irradiated		
			SD	%		SD	%
Simple Beam Theory	**Elastic Modulus (GPa)**	181	15	8.3	166	26	15.6
	Yield Stress (GPa)	2.78	0.38	13.8	2.75	0.27	9.8
	Yield Strain	0.016	0.001	8.7	0.017	0.002	0.1
	0.2% Proof Stress (GPa)	3.30	0.35	10.8	3.18	0.23	7.2
	0.2% Proof Strain	0.020	0.002	7.7	0.021	0.002	10.0

FEA Analysis

For the FEA analysis, several simulations were conducted using a single set of load-displacement data, to assess the effects of the number of plastic match points (n_{TOTAL}) and match point spacing (see *section 4.2.4*).

Plastic Deformation

The effect of the number and spacing of match points was evaluated for simulation of the plastic deformation. Firstly, several simulations were conducted for matching the model load to within 5% of the experimental load using 1 to 5 equally spaced match points. *Figure 5.20a-e* shows the final simulation load-displacement data, experimental load-displacement

data and match points. As the number of match points increased the simulation matched the experimental load-displacement behaviour with more accuracy.

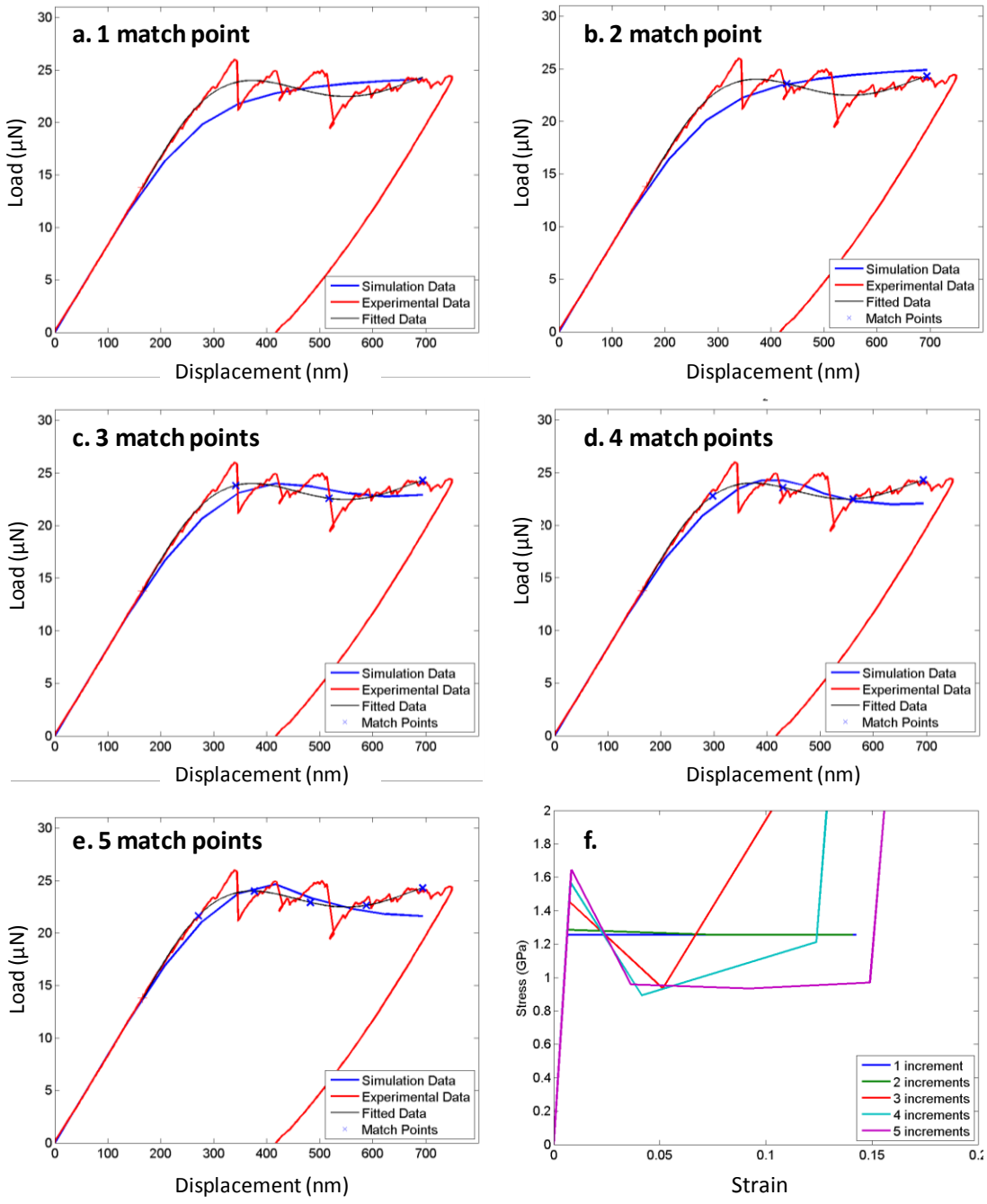

Figure 5.20 - Load-Displacement data showing simulation matched to experiment using a varying number of match points (a-e) and model stress-strain properties calculated for matching (f).

The model yield stress (σ at $\varepsilon_{plastic}$=0) increases as the first match point is positioned closer to the point of initial yield, requiring a large decrease in stress for matching at higher displacements. This can be seen in *figure 5.20f* where the model stress-strain properties are plotted for each matching analysis using a different number of match points. For analysis with greater than 2 match points a large increase in stress (up to 50GPa) was required to fit to the last match point. This stress-strain behaviour is an un-realistic measurement of the material properties and resulted in instabilities in the FEA model. Following this, the match point spacing defined by the power law introduced in *section 4.2.4,* ($n^x hplastic/nTOTAL^x$), was analysed by using 3 match points and varying the value of x from 1 (equal spacing) to 3 as shown in *figure 5.21*. Spacing the match points closer to the yield point of the load-displacement data improved matching to some extent with the best results obtained by using $x = 2$.

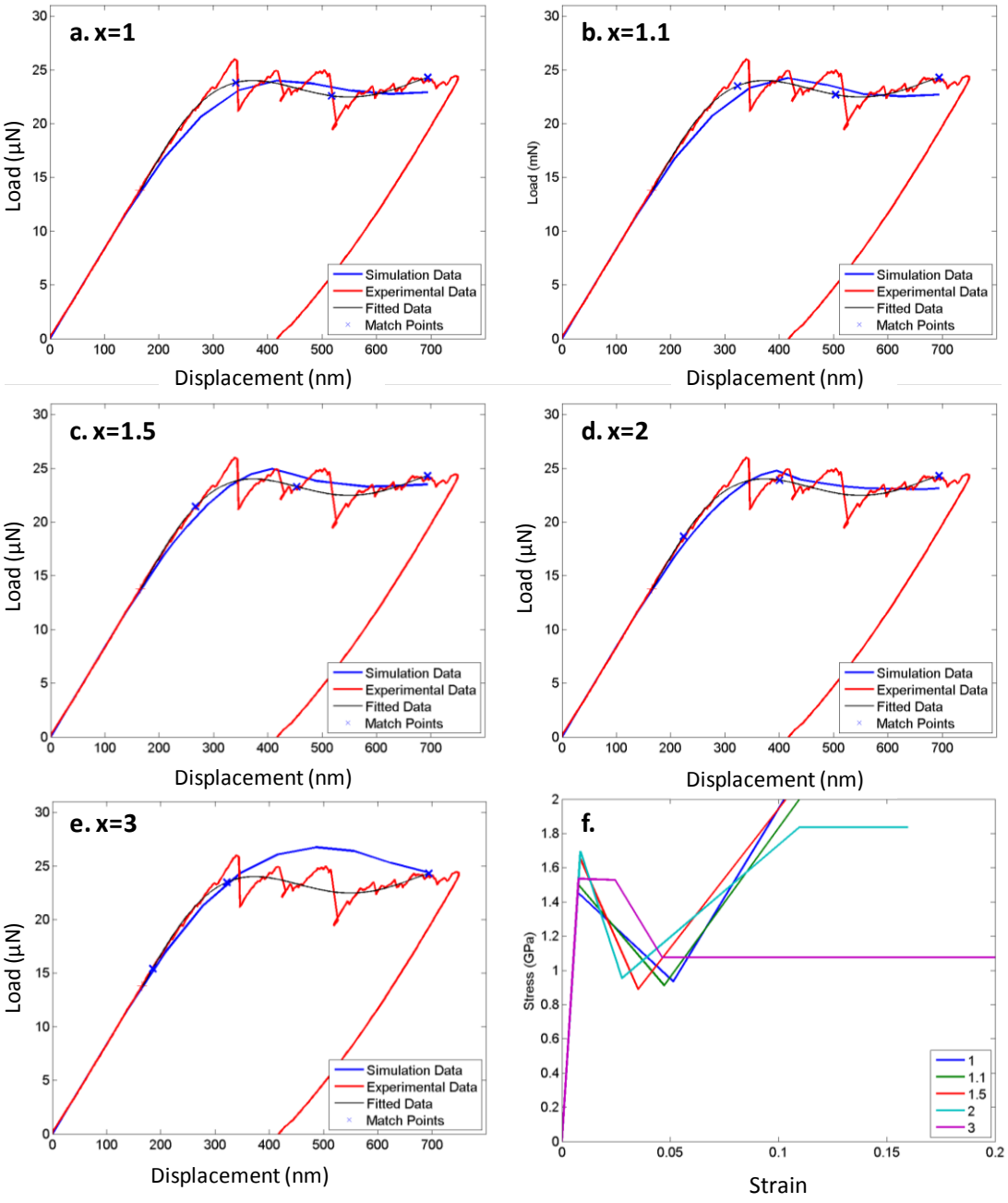

Figure 5.21 - Load-Displacement data showing simulation matched to experiment using a varying number of x in the function $n^x hplastic/nTOTAL^x$ for match point spacing (a-e) and model stress-strain properties calculated for matching (f).

Final Analysis

The optimisation procedure above determined that experimental data could be matched with simulation using 3 match points, with a match point spacing defined by the function $n^2 hplastic/nTOTAL^2$. This technique was used for all uniform cross-section beams tested in the Fe 12%Cr sample and results are shown in *table 5.4*.

Table 5.4 - Average mechanical property measurements produced by FEA analysis for 12 micro-cantilever tests in un-irradiated and irradiated Fe12%Cr.

		Un-irradiated			Irradiated		
			SD	%		SD	%
FEA Analysis	Elastic Modulus (GPa)	205	14	6.7	195	30	15.4
	Yield Stress (GPa)	1.83	0.32	17.6	1.67	0.16	9.6

5.3.2 'Waisted' Beam Testing

In a manner similar to that described in *section 5.3.1* for uniform cross-section beams, arrays of 12 'waisted' type beams were manufactured in both un-irradiated and irradiated regions of the sample. These arrays of waisted beams and a typical beam are shown in *figure 5.22*.

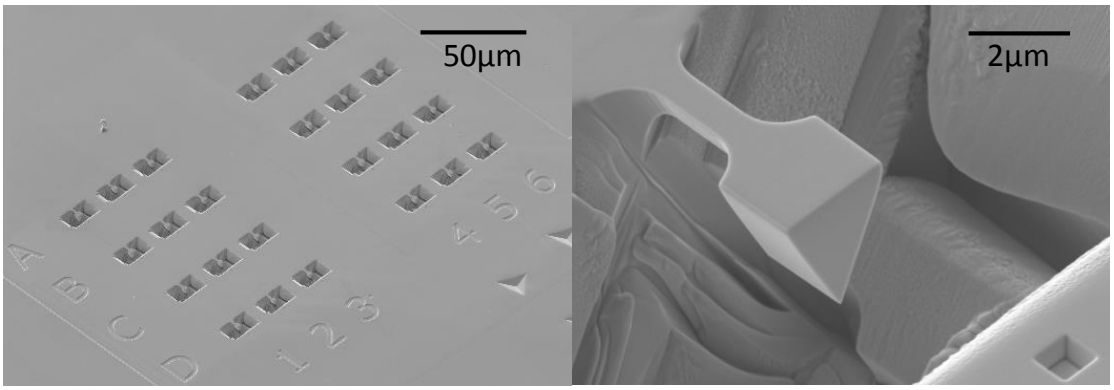

a. **b.**

Figure 5.22 - SEM image showing array of 'waisted' type micro-cantilever beams in un-irradiated and irradiated regions of the sample (a) and image of a typical beam (b).

The beams were milled with a final step at 50pA to produce the 'waist' section. The beams had a depth of 0.81µm +/-0.03 and were loaded approximately 1.5µm from the free end and ~5µm from the fixed end, producing an aspect ratio (length/neck width) of ~5-6.

FEA Analysis

Approximately half of these beams in both regions of the grain were tested with a displacement rate of 5nm/s and the raw load-displacement data was analysed using the FEA methods described in *Chapter 4*. The other half were tested at differing displacement rates and are not reported here.

The elastic-plastic transition behaviour is less prominent in the load-displacement data produced by 'waisted' type beams than in the uniform cross-section beams. This response is better represented in the FEA model than the sharp transition exhibited by uniform cross-section beam geometry and enabled closer fitting criteria. Several simulations were

conducted for matching the simulation output to within 0.2% of the experimental load using 1 to 6 equally spaced match points. *Figure 5.23a-f* shows the final simulation output with experimental data from a single test in the un-irradiated material.

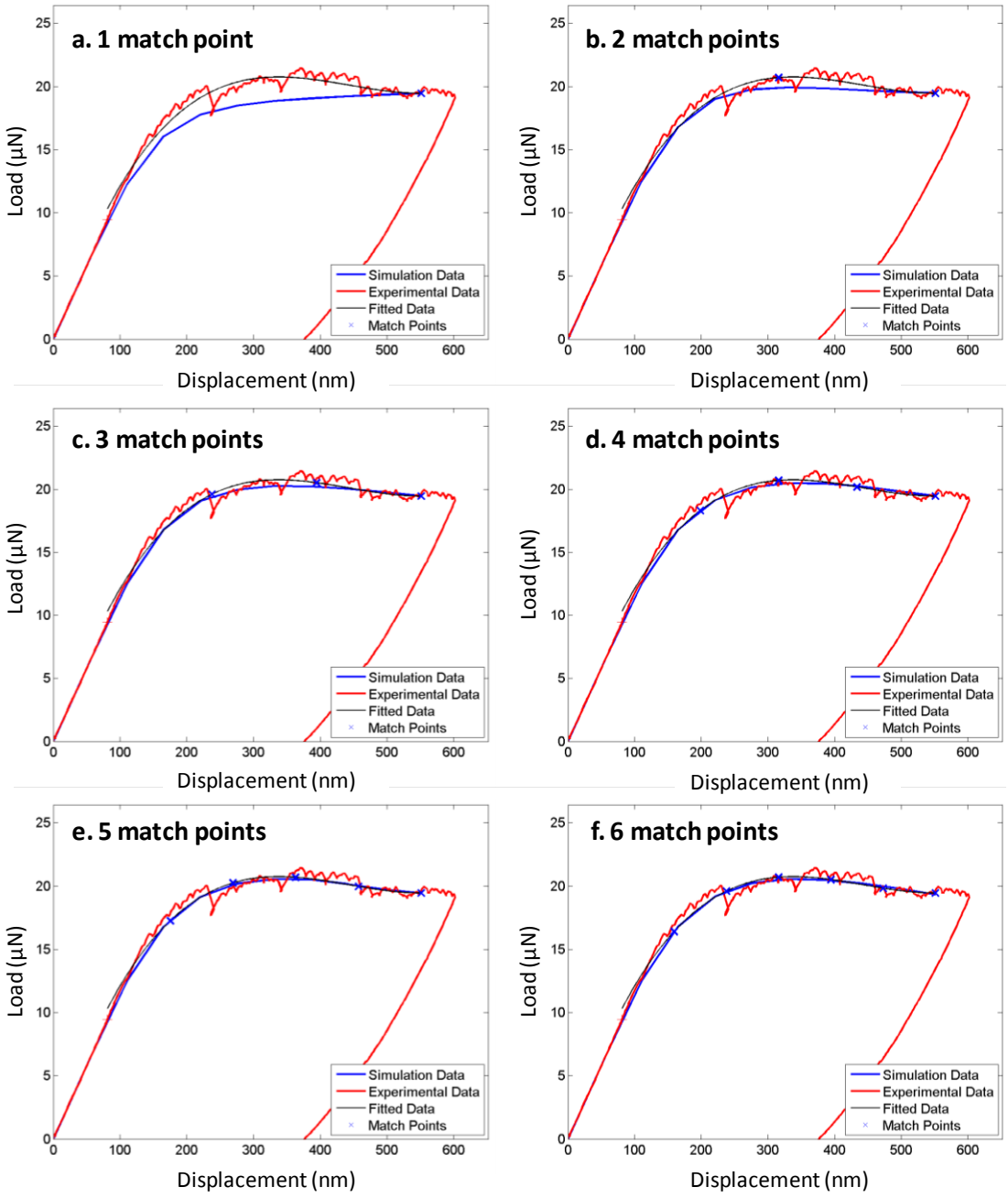

Figure 5.23 - Typical 'waisted' type beam load-displacement data matched to simulation output with various numbers of match points from 1-6 (a-f). Load matched to within 0.2% and match points are positioned with equal spacing.

The model stress-strain properties for each match using a different number of match points can be seen in *figure 5.24*. It can be seen that the match increases in accuracy as the total number of match points is increased. In addition, the resultant model stress-strain output calculated for matching is similar as the number of match points is increased, yet the behaviour fits an increasingly complex trend. The use of more than 5 match points caused the FEA simulation to fail due to instabilities caused by the work softening behaviour of the material and the fit was not improved by adjusting match point spacing.

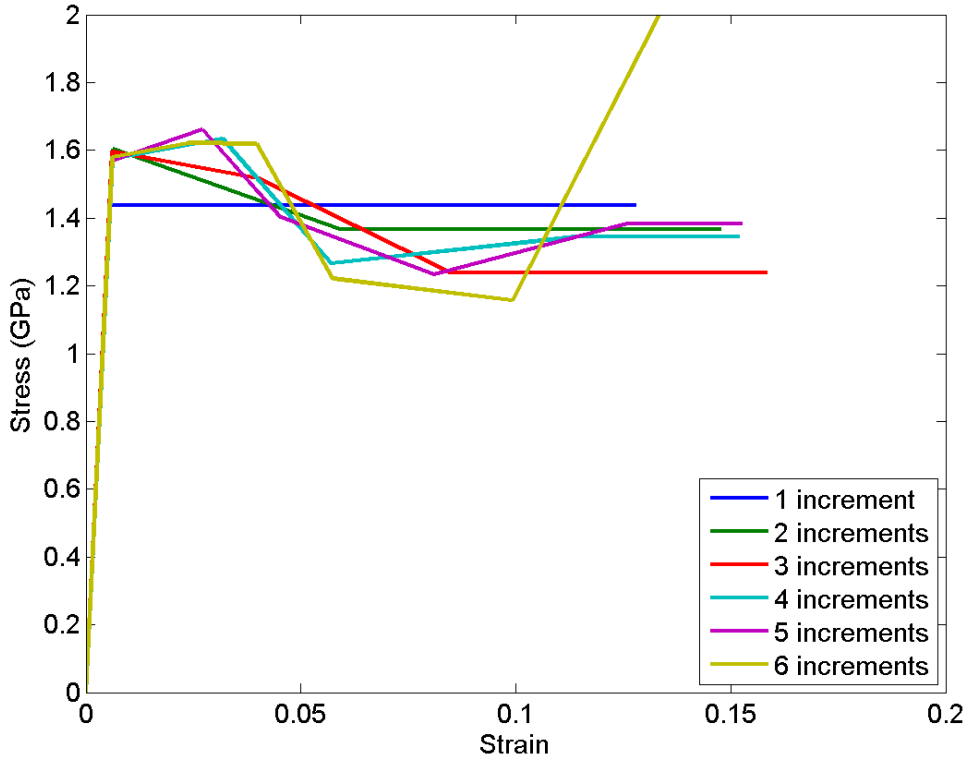

Figure 5.24 - Model stress-strain properties calculated for matching experimental load-displacement data with 1 to 6 match points.

Final Analysis

The optimisation procedure for the 'waisted' type beam modelling determined that experimental data should be matched with simulation using 6 match points with equal

match point spacing. This technique was used for all waisted beams tested in the Fe 12%Cr sample. *Figure 5.25* shows the individual model stress-strain curves for all beams tested in the un-irradiated and irradiated regions of the Fe 12%Cr sample. The average results for these tests are given in *table 5.5*.

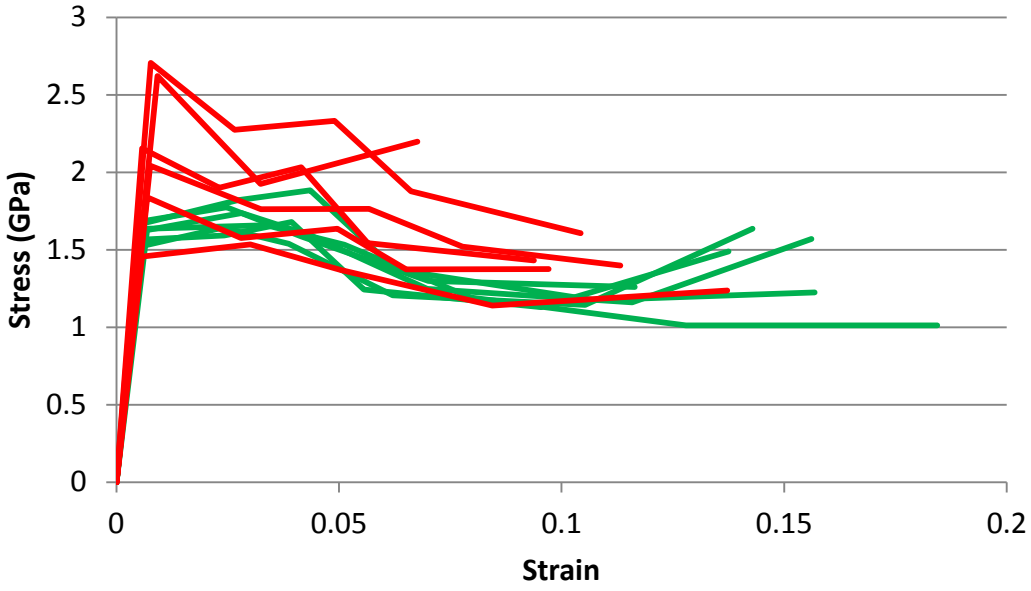

Figure 5.25 - Matched model stress-strain curves for 'waisted' type beams tested in the un-irradiated (shown in green) and irradiated (shown in red) regions of Fe 12%Cr.

Table 5.5 - Average mechanical property measurements from 'waisted' type micro-cantilever testing produced by FEA analysis for un-irradiated and irradiated Fe 12%Cr.

		Un-irradiated			Irradiated		
			SD	%		SD	%
FEA Analysis	Elastic Modulus (GPa)	277	26	9.5	299	50	16.9
	Yield Stress (GPa)	1.62	0.06	3.8	2.14	0.47	22.2

No significant difference in elastic modulus was found between the un-irradiated and irradiated material. The un-irradiated material exhibited strikingly consistent behaviour with an average yield stress of 1.62GPa (+/- 0.06GPa) and some initial work hardening followed by softening. The irradiated material produced a higher average yield stress yet the behaviour was less consistent. Unlike the un-irradiated material, stress decreased instantly after yield which tends towards the un-irradiated stress at ~0.1 strain. Dislocation channelling has been observed in the pile-up lobes surrounding indent impressions in this material, shown in *section 7.6.4*, *figure 7.14* (this work is reported in ref. [91]). Thus, the work softening behaviour may be caused by the annihilation of radiation induced defects by reaction with glissile dislocations [72, 73].

5.3.3 Error Analysis

Several sources of random errors exist in the analysis of the raw load-displacement data from cantilever tests, whether using either simple beam theory or the progressive convergent analysis described in *section 4.2.4*. These sources of error may be produced from inaccuracies in the beam measurement using the stereo imaging techniques (*section 3.3.2*), inaccuracies of load-displacement data produced by the MTS NanoXP instrument, thermal drift and the calculation of spring stiffness.

Table 5.6 - Mean and standard deviation from 10 stereo imaging measurements of a typical uniform cross-section and waisted beam.

	Uniform Cross-Section Beam			Waisted Beam		
	Load Length	Width	Depth	Load Length	Neck Width	Neck Depth
Mean (µm)	5.66	0.866	0.984	5.11	0.726	0.841
Standard Deviation (µm)	0.01	0.019	0.006	0.02	0.011	0.007
Percentage of Mean (%)	0.32	2.15	0.64	0.31	1.50	0.83

Table 5.6 shows the standard deviation from 10 measurements for a typical simple and waisted type beam. These measurements have small scatter due to the variation in the positions of points manually selected in the MATLAB codes described in *section 3.3.2*.

The resolution of the NanoXP DCM II indenter head used for the testing of micro-cantilever beams is 0.0002nm in displacement and 3nN in load. Despite this larger errors exist in the load-displacement data due to the presence of thermal drift and correction for spring stiffness. The testing method included a period to stabilise to an allowable drift rate of 0.05nm/s before proceeding to load the test specimen; for a typical test this may result in an error of up to ~5nm over the duration of elastic loading (~200nm displacement at ~3nm/s). *Figure 5.26* shows load-displacement data of a typical beam after correction for spring stiffness and surface find using methods described in *section 4.2.4*. It can be seen that there is a difference of approximately 1µN in the measured load before and after testing the beam.

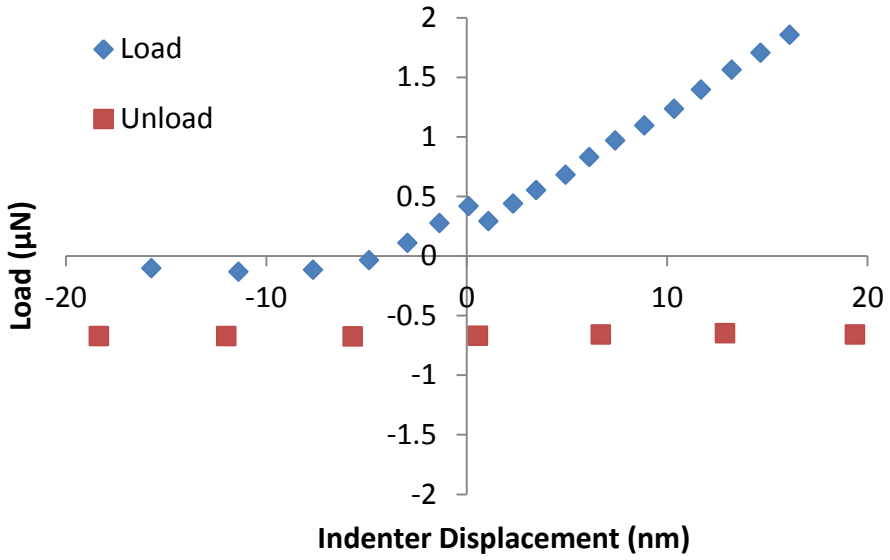

Figure 5.26 - Typical load-displacement data near sample surface showing load and unload data for a uniform cross-section beam test.

Using the random errors given above, the error in the cantilever test results was calculated using a superposition of errors method. By combining *equations 4.4* and *4.5*, the elastic modulus measured by micro-cantilever testing is defined by:

$$E = \frac{\sigma}{\varepsilon} = \frac{4Pl^3}{\delta a h^3} \qquad \textbf{equation 5.1}$$

The error in the elastic modulus measurement, ∂E, is calculated by taking the partial differential of each component in *equation 5.1* multiplied by the error of each component:

$$\partial E = \frac{\partial E}{\partial P}\,\partial P + \frac{\partial E}{\partial l}\partial l + \frac{\partial E}{\partial \delta}\,\partial \delta + \frac{\partial E}{\partial a}\,\partial a + \frac{\partial E}{\partial h}\,\partial h \qquad \textbf{equation 5.2}$$

where,

$$\frac{\partial E}{\partial P} = \frac{4l^3}{\delta a h^3} = \frac{E}{P} \qquad \textbf{equation 5.3}$$

$$\frac{\partial E}{\partial l} = 3\frac{4Pl^2}{\delta a h^3} = \frac{3E}{l} \qquad \textbf{equation 5.4}$$

$$\frac{\partial E}{\partial \delta} = \frac{-4Pl^3}{\delta^2 a h^3} = \frac{-E}{\delta} \qquad \textbf{equation 5.5}$$

$$\frac{\partial E}{\partial a} = \frac{-4Pl^3}{\delta a^2 h^3} = \frac{-E}{a} \qquad \textbf{equation 5.6}$$

$$\frac{\partial E}{\partial h} = -3\frac{4Pl^3}{\delta a h^4} = \frac{-3E}{h} \qquad \textbf{equation 5.7}$$

Substituting equations *5.3* to *5.7* into *equation 5.2* gives:

$$\partial E = \frac{E}{P}\,\partial P + \frac{3E}{l}\,\partial l + \frac{-E}{\delta}\,\partial \delta + \frac{-E}{a}\,\partial a + \frac{-3E}{h}\,\partial h \qquad \textbf{equation 5.8}$$

This approach is considered too pessimistic because it assumes all errors occur with the same sign. Therefore the more conventional approach of summing errors in quadrature was undertaken:

$$\partial E = \sqrt{\left(\frac{E}{P}\right)^2 \partial P^2 + \left(\frac{3E}{l}\right)^2 \partial l^2 + \left(\frac{-E}{\delta}\right)^2 \partial \delta^2 + \left(\frac{-E}{a}\right)^2 \partial a^2 + \left(\frac{-3E}{h}\right)^2 \partial h^2}$$

$$\textbf{equation 5.9}$$

The same method can be applied to the measurement of yield stress given in *equation 4.5*, which gives:

$$\partial\sigma = \sqrt{\left(\frac{\sigma}{P}\right)^2 \partial P^2 + \left(\frac{\sigma}{l}\right)^2 \partial l^2 + \left(\frac{-\sigma}{a}\right)^2 \partial a^2 + \left(\frac{-2\sigma}{h}\right)^2 \partial h^2} \qquad \boldsymbol{equation\ 5.10}$$

Calculations using values for the random errors discussed above produce an error of up to 6.92% in the measured elastic modulus and 2.55% in the yield stress. The value of error for the elastic modulus is similar to the standard deviation of results for the uniform cross-section beam tests in un-irradiated Fe 12%Cr. The standard deviation for the yield stress measurements from the same tests is higher than the calculated error, which suggests that the variation in yield stress is statistically significant. This variation of yield stress may be produced by the random distribution of dislocation sources and source activation stresses within each test specimen.

The errors within the FEA progressive convergent analysis described in *section 4.2.4* cannot be directly calculated; however the same random sources of error described above exist and errors in elastic modulus and yield stress measurements are likely to be similar for both beam types.

5.3.4 Characteristics of Micro-Cantilever Testing

The use of simple beam theory for the uniform cross-section type beams is a fast and efficient method to generate well defined mechanical property data. When comparing to

FEA matching for the same test data, the elastic modulus is slightly lower for simple beam theory due to deformation surrounding the base of the beam. The yield stress calculated by simple beam theory is significantly higher than that calculated by FEA matching. An FEA simulation using a model without a base showed increased stresses at the fixed end of the beam; thus assumptions regarding the fixed end cannot account for the higher yield stresses calculated by simple beam theory. It is possible that this difference exists due to inaccuracies in matching the simulation to where the experimental load-displacement response first deviates from linearity; a typically discrete event corresponding to dislocation source activation.

At the micron scale, plasticity is controlled by a relatively small number of dislocations resulting in several discrete load drop events in the load-displacement curve. The continuum theory used in FEA simulations produces a smooth load-displacement curve and does not capture the stochastic nature of slip produced by these small-scale tests [219]. *Figure 5.27* shows the Von Mises stress distribution at the bottom of the fixed end of the simple and 'waisted' type beams after first increment of simulation. In both simulations the first increment corresponds to bending moments of 32pNm for the uniform cross-section beams and 31pNm for the 'waisted' beam. Stresses are distributed over a larger area in the 'waisted' beam, thus the plastic response of the beam may be produced over a larger volume containing more dislocation sources. The resulting load-displacement response of a waisted beam test is less stochastic and the elastic-plastic transition is less abrupt. In comparison with uniform cross-section beams, this behaviour is better represented by the FEA simulation data.

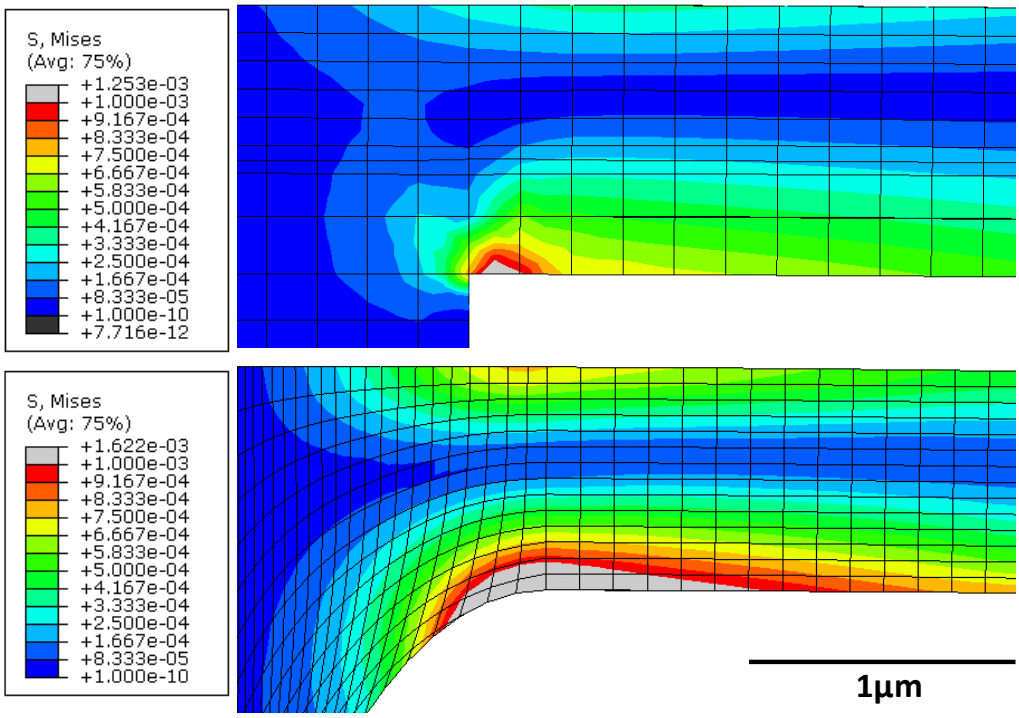

Figure 5.27 - FEA simulation Von Mises stress distribution for simple and 'waisted' type beams after first increment of simulation. Beam displacements correspond to 69nm and 55nm and bending moments are 32pNm and 31pNm for the simple and 'waisted' type beams respectfully. Stresses in TPa.

A more sophisticated approach which simulates the discrete events associated with individual dislocations was conducted with assistance from Dr E Tarleton of the University of Oxford. A 2D discrete dislocation plasticity model coupled with a finite element code using the superposition principle (as described in ref. [220]) was used to model the load-displacement response of the un-irradiated uniform cross-section beam example described in *section 5.3.1*. The plane strain model simulated plasticity in a 2D cross-section of the beam by defining a random distribution of dislocation sources, which simulate a Frank-Read source by nucleating a dislocation dipole when the shear stress at the source is greater than the activation stress (τ_n) for a duration longer than 1ns. The model used a random distribution of 200 sources with a Gaussian profile of activation stresses, a mean τ_n of 350MPa and a

spacing of ~0.2µm; this activation stress is similar to macro-scale yield stresses for Fe12%Cr as reported in refs. [64, 172]. Once nucleated, dislocations glide on slip planes at an angle of 45° when the resolved shear stress (τ) exceeds a friction stress taken at $0.1\tau_n = 35MPa$. Once a dislocation reaches a free surface it is removed from the simulation. The experimental and simulation data are shown in *figure 5.28*. The simulation captures the stochastic nature of plastic events seen in the experiment and exhibits the higher yield stresses observed with tests of this scale [221]. The high yield stress observed in the simulation originates from the lack of dislocation sources in favourable positions. This modelling technique is currently in development for producing 3D simulations, which may be useful in the simulation of micro-mechanical tests of irradiated materials in the future.

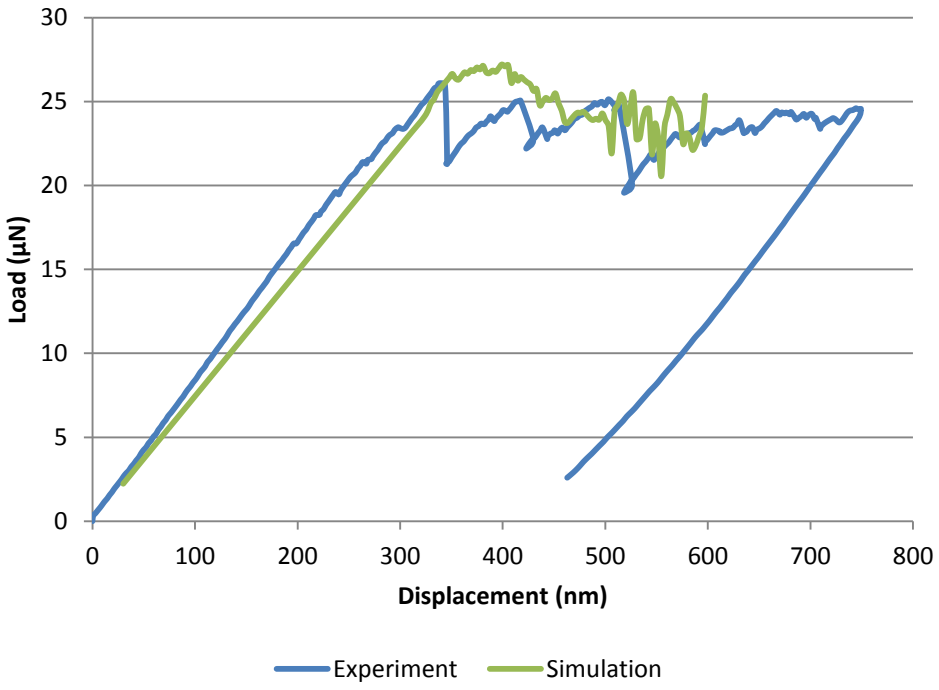

Figure 5.28 - Experimental data for a uniform cross-section beam test in un-irradiated Fe 12%Cr with simulation data from 2D discrete dislocation dynamics model.

5.4 Discussion: The Comparison of Mechanical Testing Methods

Indentation with the cube corner tip provides the advantage of the smallest plastic zone for thin surface layers, however the difference in pile-up between the irradiated and un-irradiated material produces significant errors in the observed irradiation hardening if an area function, rather than direct contact area measurement is used. Due to an increase in strain with depth, spherical indentation provides the potential to observe work hardening characteristics and size effect analysis with multiple tips [212]. The prominent pop-in events produced by the spherical tip prevent a direct comparison between un-irradiated and irradiated materials.

The Berkovich tip provides a good compromise between small pop-in events and exhibits moderate pile-up with a small plastic zone size. Thus, data produced by indentation with a Berkovich tip at depths 50-200nm has been used throughout the investigations described in this thesis. Observable by an apparent increase in elastic modulus, pile-up also produces larger apparent irradiation hardening. This pile-up is caused by the restricted growth of the plastic zone in the damage layer; therefore indentation data which are uncorrected for pile-up are considered a measure of both irradiation hardening and irradiation-induced indentation pile-up.

The complexity of manufacture, measurement and analysis of both micro-cantilever designs were similar. In the time frame of work conducted for this thesis, the analysis of the number of tests reported here would not have been feasible without MATLAB automation. As indicated by nanoindentation pop-in events and load drops in micro-cantilever data, the

onset of plasticity in such small volumes was dominated by the nucleation of dislocation sources. This phenomenon may suppress the observation of differences in the uniform cross-section beam tests of un-irradiated and irradiated material. This compares well with recent micro-pillar compression results, which have also reported no observable differences in the yield stress of iron irradiated to the same dose [99] and results from pillars in copper with diameters <400nm [100] (discussed in *section 2.2.2*). Waisted beam results did identify some irradiation hardening, which may have been due to the smaller strain gradients at the base of the beam, reducing strain bursts associated with dislocation source nucleation.

Average values of flow stress measured by nanoindentation (hardness/3.03 [222]) and yield stress measured by micro-cantilever testing are presented in *figure 5.29*. As discussed in *section 5.2.4*, the nanoindentation methods were constrained to the indentation depth range which omitted noise in the data at small depths and the effect of the un-irradiated substrate at larger depths. Hardness values corrected for pile-up were averaged across the depth range of 50 to 200nm for the Berkovich data and 100 to 250nm for the cube corner data. Data for the spherical indentations were produced by taking the hardness measurements at first yield in the irradiated material, whilst extrapolating the un-irradiated hardness data to the elastic line as reported in ref. [212]. Caution should be taken when comparing the un-irradiated value of hardness for the spherical tip, as this approach excludes depth dependent phenomena such as indentation size effect. Finally, values from the FEA progressive convergent analysis have been used for the comparison of both types of micro-cantilever tests.

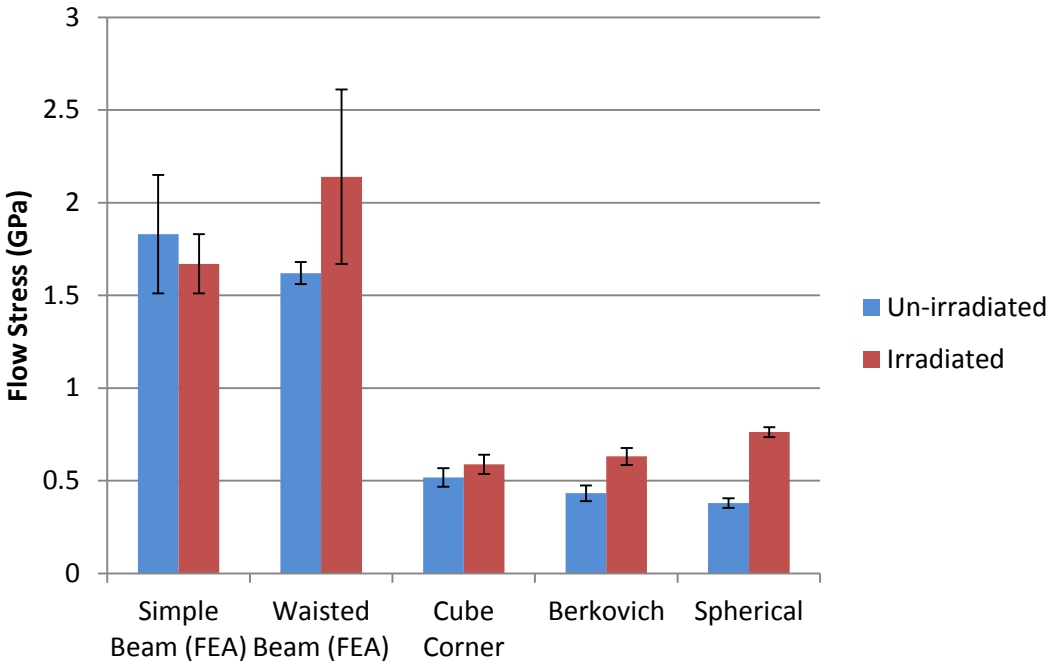

Figure 5.29 - Flow stress for un-irradiated and irradiated Fe 12%Cr, measured by the uniform cross-section beams and waisted micro-cantilever beams, and flow stress (hardness/3.03) measured by cube corner, Berkovich and spherical indentation. Error bars represent +/- one standard deviation.

The flow stress in *figure 5.29* is approximately an order of magnitude higher than that expected for macro-scale testing [64, 172] and the un-irradiated values for flow stress decrease as the test volume increases (from left to right along the x-axis). It is likely that this trend is caused by the size effect in plasticity observed in many materials [101, 221, 223]. It is also apparent that the difference between un-irradiated and irradiated flow stress increases with test volume indicating that irradiation hardening is obscured by the size effect. An investigation into the size effect of un-irradiated and ion-irradiated material has been conducted and is presented in *chapter 6*.

5.5 Summary

i. As shown in *figure 5.2*, TEM measurements of the damage layer produced in Fe12%Cr by 2MeV Fe^{+} ions extended to ~500nm compared to ~800nm as calculated by TRIM.

ii. Cross-sectional TEM measurements of indents at various depths in the un-irradiated and irradiated material in *section 5.2.1*, show that the expansion of the plastic zone beneath the indent is suppressed by the damage layer. The plastic zone size is smallest for the sharper cube corner tip and largest for the spherical tip with nominal radius of 10µm.

iii. Nanoindentation data was significantly affected by differing pile-up contributions to contact area in irradiated and un-irradiated material (*section 5.2.2*). For pyramidal indenter tips, larger pile-up caused an artificial increase in elastic modulus measurements in the irradiated material (shown in *figure 5.14*).

iv. Nanoindentation pop-in events and load drops in micro-cantilever load-displacement data indicates that plasticity at the micro-scale was predominantly controlled by dislocation sources.

v. Scatter in yield stress measurements from cantilever data was higher than the estimated error calculated in *section 5.3.3*.

vi. Negligible irradiation hardening was measured by micro-cantilevers with a depth of 800nm, which may have been obscured by dislocation source nucleation. This effect may be reduced as more dislocation sources are activated, resulting in increased measurements of irradiation hardening as the size of the plastic volume increases as shown in *figure 5.29*.

6 INVESTIGATING IRRADIATION BY IONS AND NEUTRONS, AND THE SIZE EFFECT IN FE6%CR

The use of heavy ion implantation for the simulation of reactor conditions is now common practise, due to the short time scales to reach relatively high damage levels and the absence of induced radioactivity; the latter avoids costly requirements for additional handling precautions and the use of hot cell facilities. Despite this, there are known differences between ion implantation and the conditions expected within a fusion environment. These differences may prove significant for the interpretation of data produced from ion implantation studies, when considering the development of structural materials for fusion reactors.

6.1 Introduction

This chapter reports the first ever systematic study conducted on the differences in mechanical properties between ion and neutron irradiation of the same material. Samples were taken from a single batch of Fe 6%Cr alloy, irradiated with comparable doses and irradiation temperature, and tested by using identical nanoindentation and micro-cantilever methods. In addition, the larger volume of radiation damage available in the neutron irradiated material enabled the manufacture of micro-cantilever specimens with a wide range of sizes. This provided an opportunity to investigate the effect of radiation damage on the mechanisms controlling the commonly observed size effect, which has been indicated in *chapter 5*.

6.2 Experimental Details

Material for this work was sourced by Prof. G.R. Odette of the University California, Santa Barbara (UCSB). Ion irradiation was undertaken at the Ion Beam Centre in Rossendorf and neutron irradiation was undertaken as part of a large scale irradiation experiment designed and carried out by UCSB in the Advanced Test Reactor (ATR) at Idaho National Laboratories (INL).

6.2.1 Material: Fe 6%Cr

A detailed description of the alloy manufacture and characterisation of the microstructure is given by Gelles [224]. A one hundred pound (~45kg) heat of the Fe 6%Cr alloy was melted at the Paul D. Merica Research Laboratory in New York. Compositions provided by the manufacturer and chemical analysis performed by Lukens Steel Company (Pennsylvania) are given in *table 6.1*. The alloys were provided in the form of a 1cm extruded bar, which was then rolled to approximately 0.3cm thick.

Table 6.1 - Elemental analysis provided by the manufacture and separate examination (compositions in weight percent). Data taken from ref. [224].

	Manufacturer	Chemical Analysis
Cr	6.0	
C	0.007	
O_2	0.021	0.001
N_2	0.0014	0.05
P		0.005
Ni		0.1
Mn		0.02

The alloy was annealed under an argon atmosphere at 950°C for 15 minutes followed by air cooling, then tempered at 750°C again followed by air cooling. This produced the microstructure shown in *figure 6.1*.

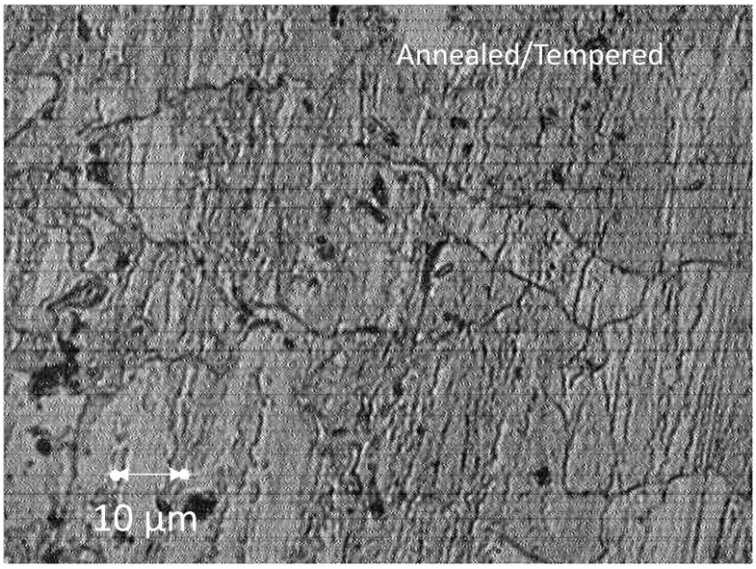

Figure 6.1 - Microstructure of Fe 6%Cr after anneal and temper. Sample polished and etched. Image supplied by Doug Klingensmith (UCSB).

For the un-irradiated and ion irradiated material, sample polishing methods were similar to those described in *chapter 5*. This included a series of lapping stages using SiC abrasive papers from FEPA P120 to P4000 grades followed by a chemo-mechanical polish using a colloidal silica suspension (0.05µm).

The neutron irradiated material was polished by INL staff at INL after irradiation. A 2.3mm disc was punched from a larger sheet and then ground with a series for abrasive papers to a final stage using FEPA P1200 for 3 minutes. The sample was polished for ~2 minutes using a 3µm diamond solution, followed by ~3 minutes using a 1µm diamond solution and finished

by a chemo-mechanical polish using a colloidal silica suspension (0.05µm) for ~5minutes. In an attempt to minimise radioactive waste, these polishing times were significantly less than what was used for the un-irradiated and ion-irradiated material.

6.2.2 Neutron Irradiation

A sample was irradiated in capsule 6A in the ATR1 materials test reactor in INL at a controlled temperature of 288°C ±12°C. The duration of the irradiation cycle was approximately 10 weeks and had a target total dose of 1.7dpa. A discussion on measurements of fluence and damage calculations is given in *section 6.4.1*.

Activity Measurements

To ensure that the material could be analysed at the Department of Materials in Oxford, the sample received from INL was in the form of a 2.3mm diameter, ~0.25mm thick disc. The total activity of the sample was measured at 36MBq; 90% of the departmental limit of 40MBq. *Table 6.2* shows the total activity measurements for the sample. Dose rate measurements were 0.15mSv/hr gamma (15 mrem/hr) and 0.9mSv/hr beta (90 mrem/hr) on contact and 0.01mSv/hr gamma (1 mrem/hr) at 30 cm.

Table 6.2 – Isotope activity measurements for Fe%6Cr sample irradiated in the ATR1 reactor at INL. Isotopes highlighted in yellow were not included in the total activity measurement as these isotopes decay by electron capture. Data provided by Collin Knight (INL).

Isotope	Curies	MBq
HE 6	0.00E+00	0.0
BE 8	0.00E+00	0.0
B 12	0.00E+00	0.0
C 14	3.34E-09	0.0
SC 47	1.29E-18	0.0
SC 48	2.00E-25	0.0
SC 49	0.00E+00	0.0
TI 51	0.00E+00	0.0
V 52	0.00E+00	0.0
V 53	0.00E+00	0.0
V 54	0.00E+00	0.0
CR 51	9.91E-04	36.7
CR 55	0.00E+00	0.0
MN 54	7.50E-04	27.8
MN 56	0.00E+00	0.0
MN 57	0.00E+00	0.0
MN 58	0.00E+00	0.0
FE 55	3.42E-03	127.0
FE 59	1.88E-04	7.0
CO 60	3.57E-05	1.3
CO 60M	0.00E+00	0.0
CO 61	0.00E+00	0.0
Y 90	4.02E-15	0.0
Y 90M	0.00E+00	0.0
Y 91	2.50E-09	0.0
SUM TOTAL	5.38E-03	199.8
TOTAL Activity	9.74E-04	36.1

6.2.3 Ion Irradiation

Ion implantations were conducted at the Ion Beam Center in Rossendorf. The implantation was designed with multiple ion charges, energies and beam currents in an attempt to maintain a constant level of damage and dose rate with depth into the sample. The beam conditions used are shown in *table 6.3*.

Table 6.3 - Ion beam conditions for implantation with multiple energies at the Ion Beam Center, Rossendorf.

Target Temperature	**288 ˚C**

Energy (MeV)	**Dose (ions/cm^2)**	**Ion Charge**	**Dose Rate (ions/cm^2/s)**	**Beam Current (nA/cm^2)**	**Time (hrs)**
0.5	1.16 x 10^{14}	1	1.60 x 10^{10}	2.56	2.02
1	2.18 x 10^{14}	1	1.84 x 10^{10}	2.95	3.29
2	2.18 x 10^{14}	1	2.00 x 10^{10}	3.21	3.03
3	2.18 x 10^{14}	1	2.16 x 10^{10}	3.46	2.80
4.5	2.18 x 10^{14}	2	2.38 x 10^{10}	7.62	2.55
6	2.91 x 10^{14}	2	2.31 x 10^{10}	7.41	3.49
9	8.00 x 10^{14}	3	2.34 x 10^{10}	11.24	9.50

TOTAL	**2.08 x 10^{15}**	**TOTAL**	**26.69**

The implantation temperature was measured and controlled at 288˚C by a thermocouple mechanically clamped adjacent to the samples on the base plate. The beam conditions were designed according to SRIM calculations and produced an average damage of 1.7dpa in a layer 2µm in depth from the sample surface as shown in *figure 6.2a*. Beam currents were maintained during implantation which gave a consistent peak dose rate of 5 x 10^{-5} dpa/s for all energies (*figure 6.2b*).

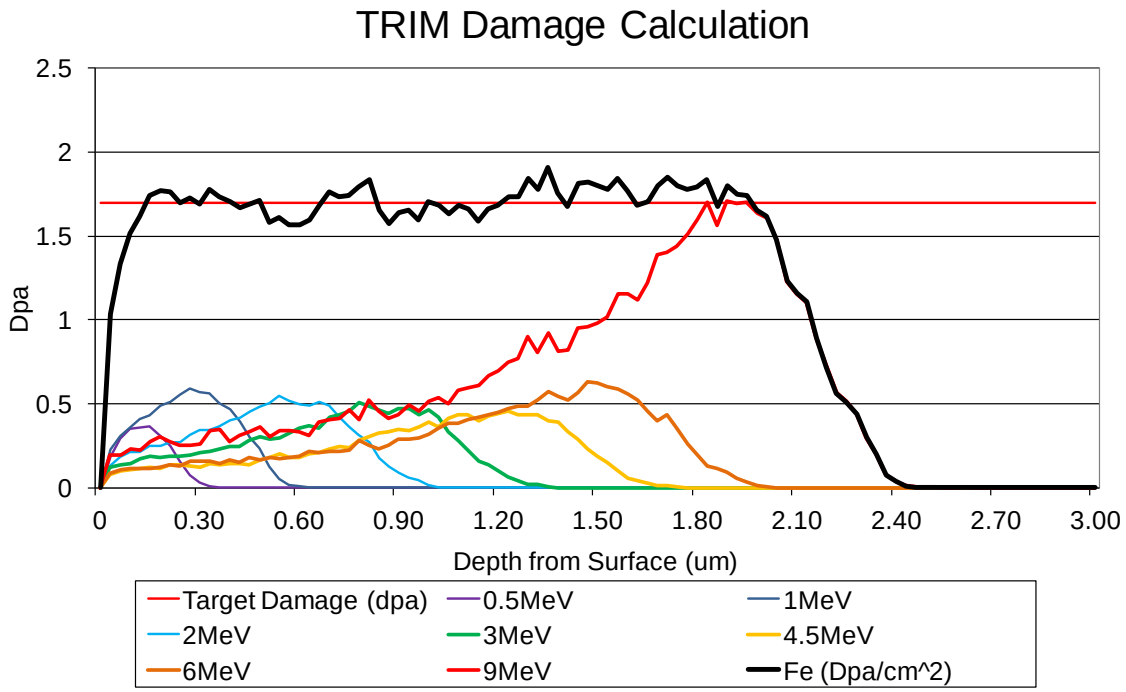

a.

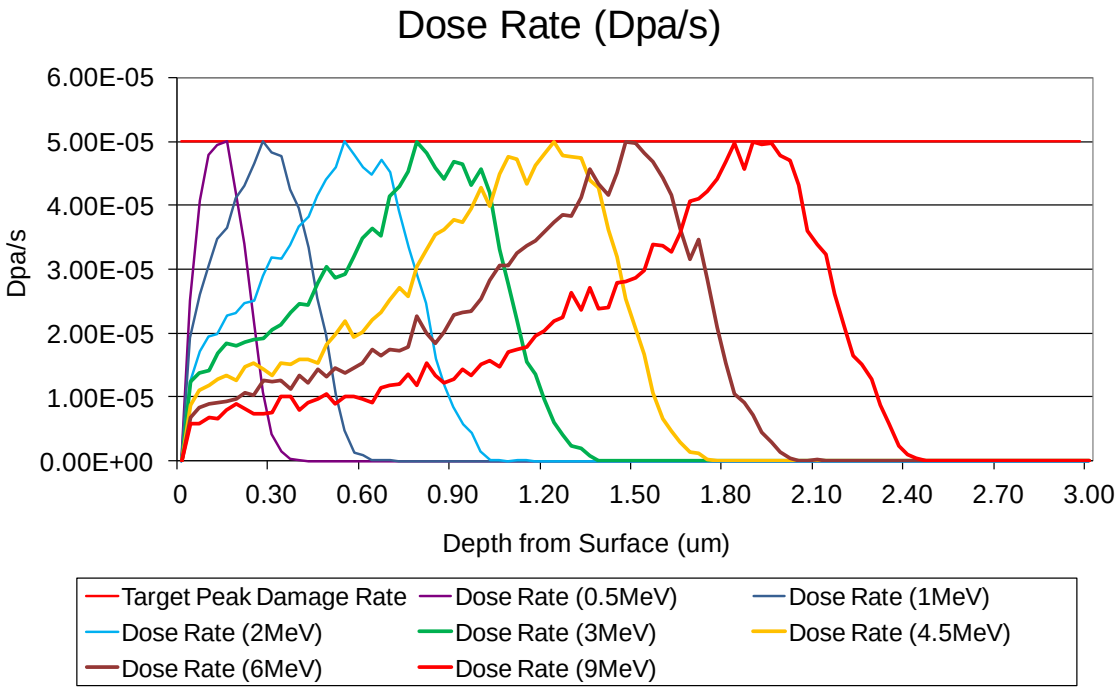

b.

Figure 6.2 - SRIM calculations showing (a) irradiation damage vs. depth into sample surface, including total damage and contributions from each beam energy, and (b) dose rate vs. depth into sample surface for each energy.

6.2.4 Nanoindentation and Micro-Cantilever Testing

Nanoindentation was conducted using the CSM method with a single Berkovich tip and tip calibration for all tests. Arrays of at least 16 indents with a depth of 1000nm and a spacing of 40µm were produced in each sample. Due to the grain size distribution, data from each indent includes the response of several grains which are averaged for all indents using the same methods described in *section 5.2.3*.

'Simple' geometry micro-cantilevers (shown in *figure 4.1*) of various sizes were manufactured in the un-irradiated, ion irradiated and neutron irradiated samples, using the methods described in *section 3.3.2*. The following test specimens were produced for each sample:

i. Neutron irradiated sample - 66 cantilevers with depths from 0.82 to 7.30µm (machined at CAES, Idaho)
ii. Ion irradiated sample - 30 cantilevers with depths from 0.36 to 2.3µm
iii. Un-irradiated sample - 32 cantilevers with depths from 0.53 to 5.11µm

All beams were measured by stereo-imaging techniques as described in *section 3.3.2*. Tests were conducted to a final strain, ε_{max}, of ~0.05 (*equation 4.4*) and a target strain rate of 2 x 10^{-4} /s; taking the varying beam size into account, this required controlled displacement rates from 1.4 to 30nm/s.

6.3 Results

6.3.1 Nanoindentation

Nanoindentation data for elastic modulus versus indentation depth are shown in *figure 6.3*. The measured elastic modulus is higher for the ion and neutron irradiated material in a similar manner to the measurements presented in *section 5.2.3*. At low indentation depths the elastic modulus measurements for ion and neutron irradiated materials are similar. As the indentation depth increases the elastic modulus measurements for the ion-irradiated material tend towards the values for the un-irradiated material. Using the same methods described in *section 5.2.3*, post-indentation contact area measurements of all indent impressions in the un-irradiated and neutron irradiated material were conducted by SEM imaging (*figure 6.4*). Elastic modulus measurements using the post-indentation contact area measurements were produced for each indent; the average values with standard deviation have been plotted on *figure 6.3a*. Unlike the Fe 12%Cr sample investigated in *chapter 5*, the difference in elastic modulus between the un-irradiated and neutron-irradiated material is not fully accounted for by pile-up.

The average values for hardness versus indentation depth and values corrected for post-indentation contact area measurement are shown in *figure 6.3b*. Irradiation hardening is clearly evident in both irradiated alloys; however hardening in the neutron-irradiated material is more than double that of the ion-irradiated material. Larger pile-up surrounding the indenter tip in the neutron-irradiated material has resulted in a slight over estimation of irradiation hardening; however pile-up in the ion-irradiated material (not measured) may also overestimate the irradiation hardening.

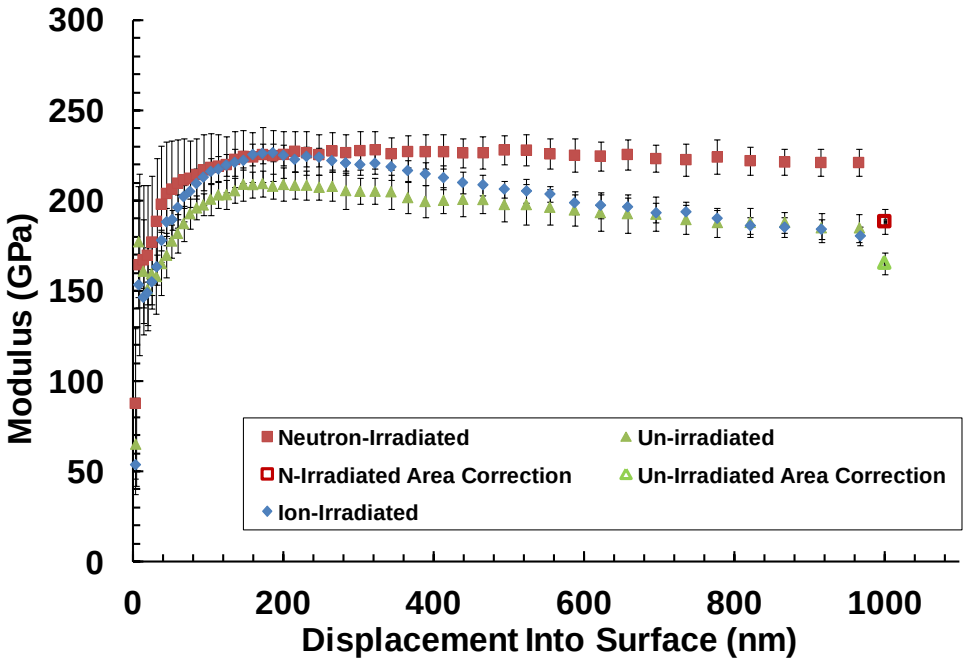

a.

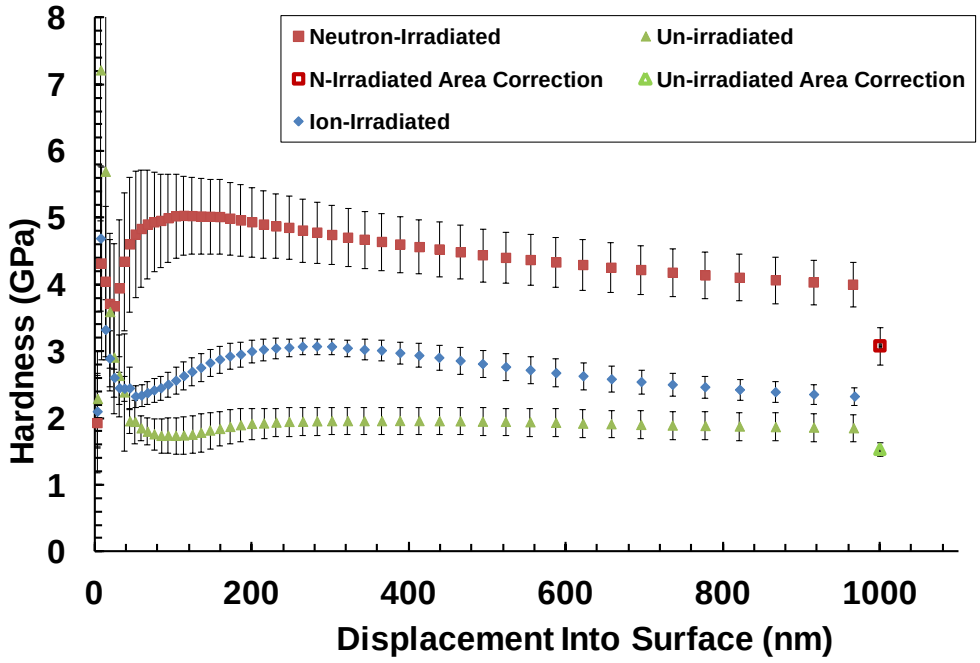

b.

Figure 6.3 - Average elastic modulus (a) and hardness (b) versus indentation depth for indent arrays of at least 16 indents produce in the un-irradiated, ion-irradiated and neutron irradiated Fe 6%Cr. Error bars represent +/- one standard deviation.

Typical SEM images of indent impressions in the un-irradiated and neutron irradiated material are shown in *figure 6.4*. Plastically deformed material forming the pile-up lobes had diffuse wavy slip lines in the un-irradiated material and highly localised slip steps in the neutron-irradiated material.

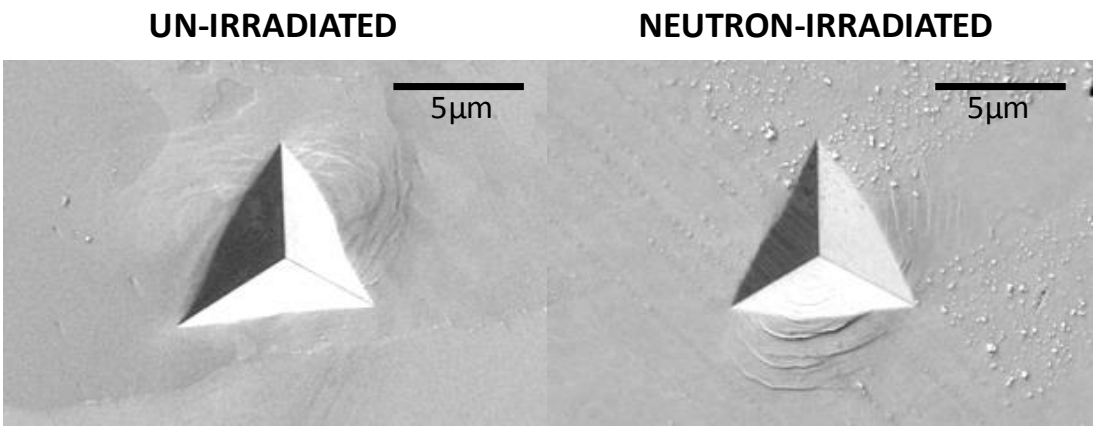

Figure 6.4 – SEM micrographs of typical indent impressions in the un-irradiated and neutron irradiated material.

6.3.2 Micro-cantilever Testing

Typical stress-strain curves for micro-cantilever tests of various sizes are shown in *figure 6.5*. As plastic deformation progressed, large load drops were observed in the un-irradiated material, which tended to increase in magnitude as the beam size increased. They were not observed in both ion and neutron-irradiated alloys where plastic deformation produced smooth variations in load. Very little work hardening was observed in the un-irradiated and ion irradiated material and the stress-strain curve exhibits an almost perfectly plastic response. In comparison, the neutron-irradiated material clearly exhibited work hardening.

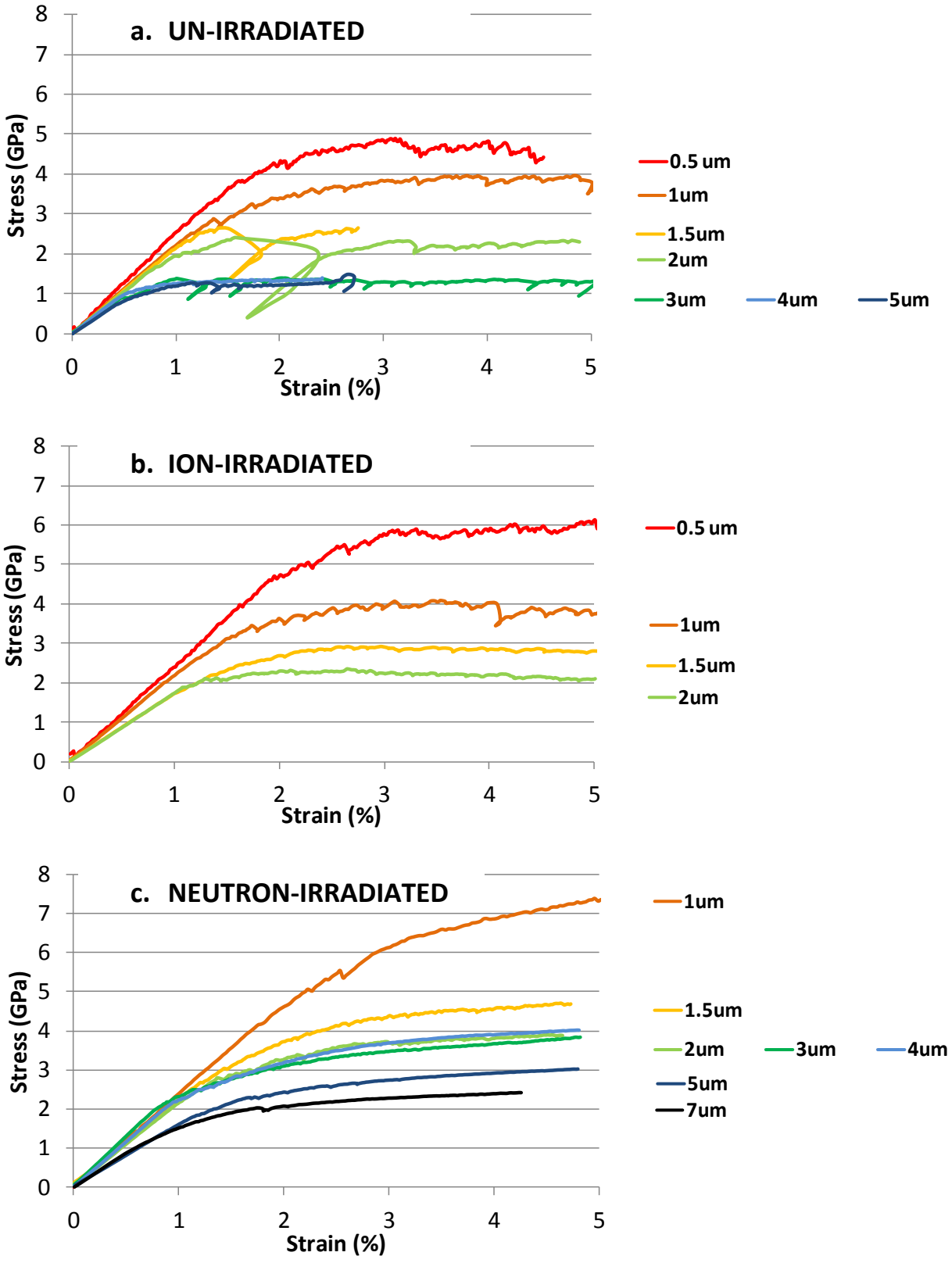

Figure 6.5 - Typical stress-strain curves from micro-cantilever tests of various sizes in: (a) un-irradiated, (b) ion-irradiated and (c) neutron irradiated material. Various rounded beam heights shown with different colours.

The elastic modulus measurements with error bars calculated using the simple beam theory methods described in *section 5.3.3* are plotted in *figure 6.6* for all cantilever tests. A large scatter in the modulus between ~150 and 350GPa was observed in the smallest cantilevers, which may be attributed to variations in crystal orientation across each test. The elastic modulus of pure Fe varies from ~125GPa along the <100> axis to 275GPa along the <111> axis [225]. As the beam size increases, more grains contribute to the elastic modulus measurements and the scatter decreases; these values should tend towards approximately 210GPa [226]. The values of elastic modulus measured in the largest beams appear to be slightly lower than this value; this may be due to lower stiffness measurements caused by the deformation of material at the base of the beam and surrounding the indenter tip. Evidence for the latter was produced by SEM imaging of indent impressions on the beam surface post testing.

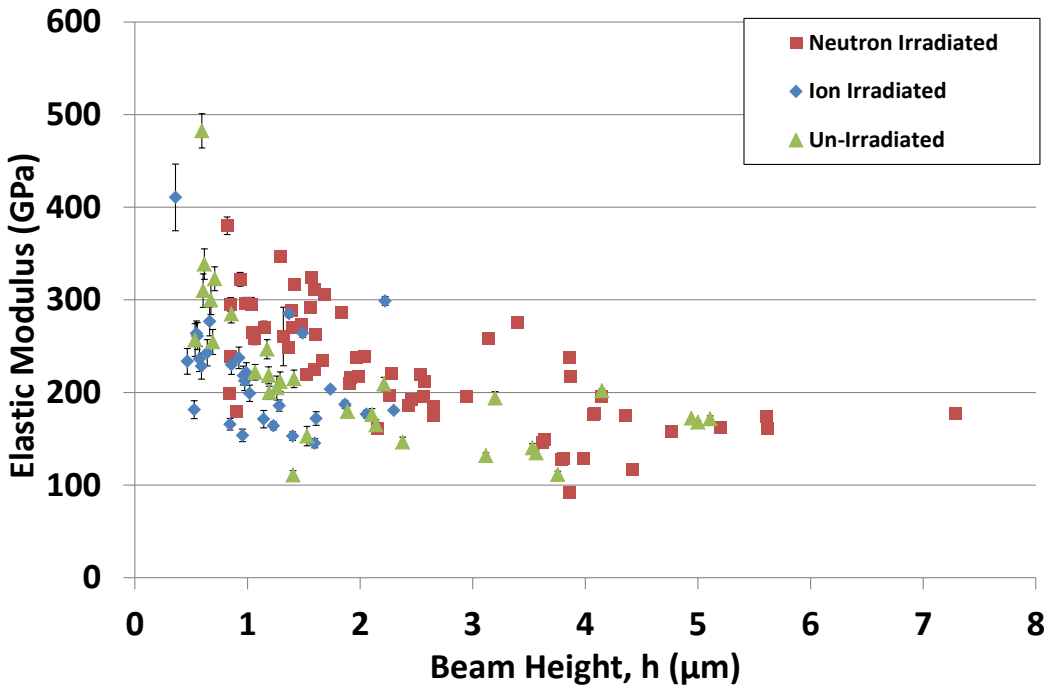

Figure 6.6 - Elastic modulus measurements versus beam height, h, for all micro-cantilevers tested in the un-irradiated, ion-irradiated and neutron-irradiated material. Error bars represent estimated error according to analysis reported in *section 5.3.3*.

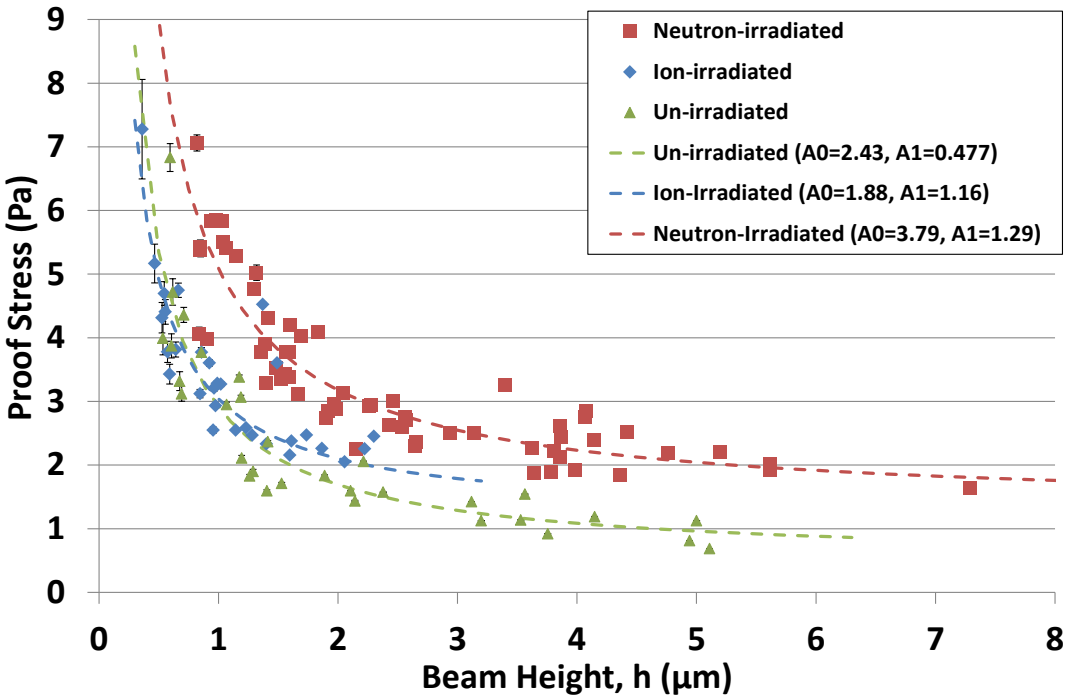

Figure 6.7 - Proof stress measurements versus beam height, h, for all micro-cantilevers tested in the un-irradiated, ion-irradiated and neutron-irradiated material. Error bars represent estimated error according to analysis reported in *section 5.3.3*.

The proof stresses calculated at 0.2% strain offset by simple beam theory versus the beam height are plotted in *figure 6.7,* with error calculated according to methods described in *section 5.3.3*. All three materials exhibited an increase in the measured proof stress as the cantilever size decreased. An irradiation-induced increase in proof stress is clearly evident across the entire range of beam sizes in the neutron-irradiated material, yet no increase in the ion-irradiated material is observed in beams with h<1µm. From testing a number of fitting procedures it was identified that the variation in proof stress, σ_{proof}, was closely proportional to h^{-1}, thus data for each material were fitted to the function:

$$\sigma_{proof} = A_0 h^{-1} + A_1 \qquad \textbf{equation 6.1}$$

where h is the beam height and A_1 is the asymptotic value of proof stress (σ_{proof} at $h = \infty$). The fitted curves are shown in *figure 6.7*. The values for A_0 and A_1 are given in *table 6.4* with the correlation coefficient R; these values are discussed further in *section 6.4.3*.

Table 6.4 - Fitting parameters for *equation 6.1* and correlation coefficient R.

	A_0 (μmGPa)	A_1 (GPa)	R
Un-irradiated	2.43	0.477	0.90
Ion-irradiated	1.88	1.16	0.94
Neutron-irradiated	3.79	1.29	0.91

Typical SEM images of the plastically deformed surfaces at the beam base are shown in *figure 6.8*. In contrast to the larger cantilever beams, no slip steps were observable in the smallest beams. A series of slip steps are observed in both irradiated materials and suggest plasticity progressed within highly localised slip planes. Large beams in the un-irradiated material exhibited fewer large slip steps in the deformed region.

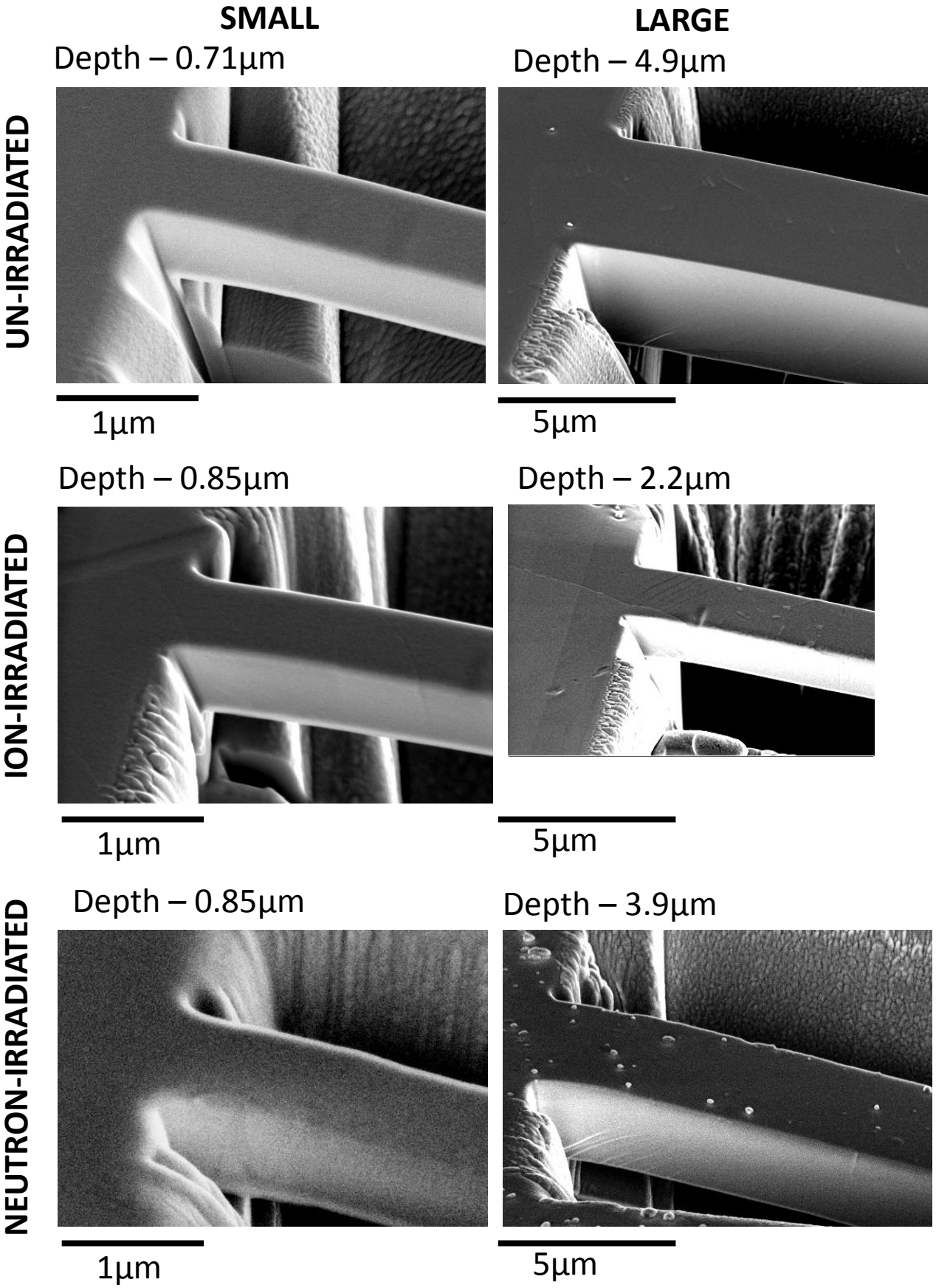

Figure 6.8 - Typical SEM micrographs of plastically deformation on the surfaces of micro-cantilever beams tested in the un-irradiated, ion-irradiated and neutron-irradiated beams.

6.4 Discussion

The experiments described in this chapter were conducted with two objectives. The first objective was to assess the validation of ion implantation as an analogue for neutron irradiation by a direct comparison. The second objective was to investigate the influence of irradiation hardening on the intrinsic size effects on sample strength, by conducting micro-mechanical testing with test specimens of various sizes. The latter was also briefly discussed in *chapter 5*, where a variation in irradiation hardening measurements was observed across several testing methods of different test volumes.

6.4.1 Comparison of Ion and Neutron Irradiation

The production and evolution of radiation damage in a given material depends on several parameters including the type and energy of the irradiating particle, the fluence/dose (number of displacements, dpa), the irradiation temperature and flux/dose rate (damage rate, dpa/s) [103]. The current experiment produced irradiated material with a calculated dose of 1.7dpa and irradiation temperature of 288°C, yet the nanoindentation measurements presented in *figure 6.3b* and micro-cantilever results in *figure 6.7* have identified a clear difference in hardening produced by irradiation with ions and neutrons. This difference may be caused by inconsistencies in damage calculations, differences in dose rates and PKA energy spectra, or the presence of transmutation He and H.

Damage Calculations – Neutron Irradiation

Three different methods were used to calculate the level of radiation damage in the neutron irradiated alloy:

Method 1: Post irradiation fluence measurements as a function of neutron energy and the energy-dependent displacement cross-section for the neutron irradiated material were provided by Mr J.W. Nielsen at INL. Using *equation 2.2* given in *section 2.1.2* produces a value for damage of **1.83dpa**.

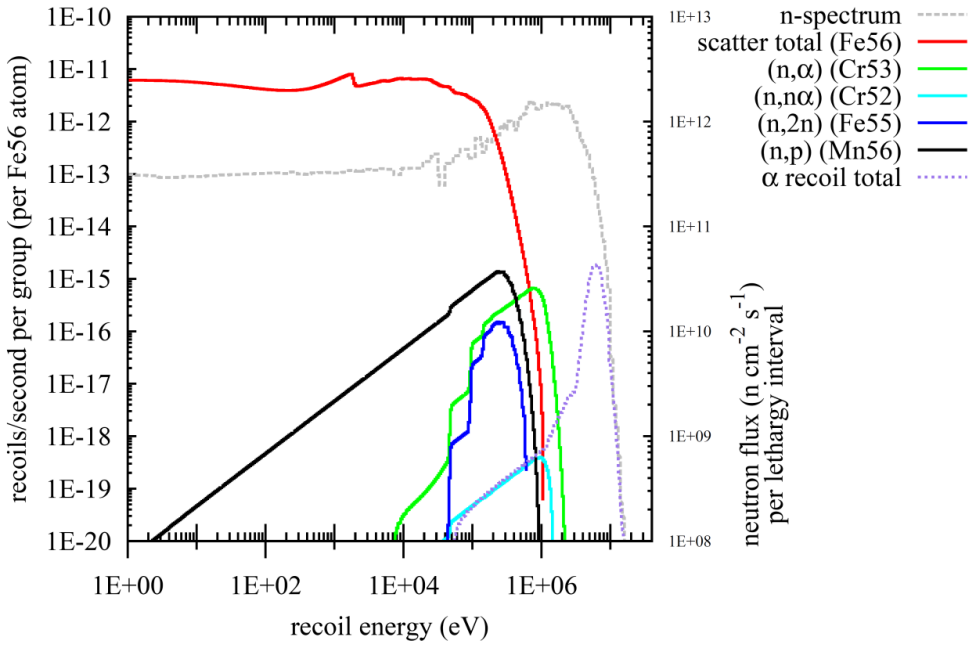

Figure 6.9 - PKA energy spectra for dominant reactions in the ATR1 reactor. Data produced by Dr M Gilbert (CCFE).

Method 2: The PKA energy (recoil) spectra for the neutron irradiated material were calculated by Dr M Gilbert at CCFE using the NJOY-2012 code [227] (to produce recoil probability matrices, $\sigma(E_i, T)$ defined in *equation 2.3*) and SPECTER (to collapse these

matrices with the ATR1 spectrum). The PKA energy spectra for the dominant reactions during irradiation are plotted in *figure 6.9*. The results from a FISPACT-II inventory simulation [228] produced a value for total damage of **1.63dpa**.

Method 3: The damage energy, T, as a function of PKA energy, E_i, in iron was calculated using the data and relationships produced by Dierckx [118]; this is shown in *figure 6.10*. The modified Kinchin and Pease NRT formula [22] (*equation 2.1* multiplied by a 'cascade efficiency factor' of 0.8), produced a value for total damage of **1.72dpa**.

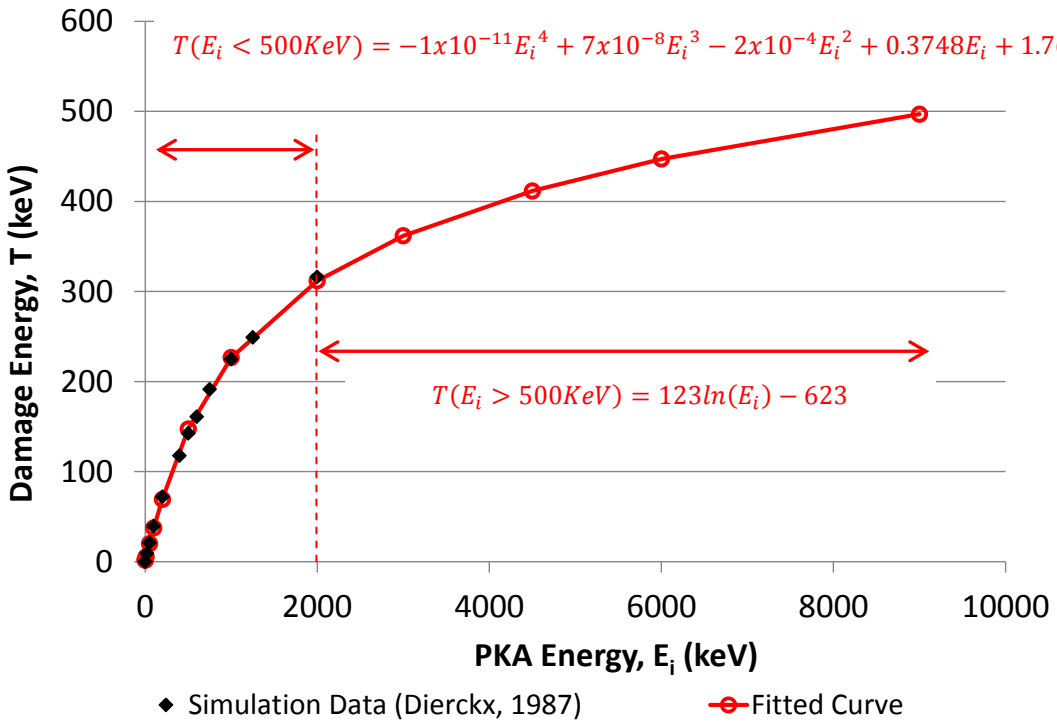

Figure 6.10 - Damage energy, T, as a function of PKA energy, E_i, in iron modelled using the data and relationships produced by Dierckx [118].

All three values are reasonably consistent at 1.7dpa, +/-0.1dpa.

Damage Calculations – Ion Irradiation

Doses for the ion implantation were calculated by using the 'Detailed Calculation with Full Damage Cascades' model in SRIM as shown in *figure 6.2*, producing a damage layer with an average damage of 1.7dpa. However, the application of method 3, by using the same damage energy function produced by Dierckx [118] and NRT formula produces a value of ~0.5dpa. This discrepancy is caused by inconsistencies in the SRIM, which was recently been confirmed by Stoller et al. [229]. As recommended by Stoller, the 'Quick Calculation of Damage' (Kinchin-Pease) model in SRIM was used and the damage energy, T, was calculated by:

$$T = E_i^0 - E_i^I - E_T^I = E_i^P + E_i^B + E_T^P + E_T^B \qquad \textbf{equation 6.2}$$

where the energy of the incident ion is distributed into electronic stopping (superscript I), lattice binding energy (superscript B) and lattice phonons (superscript P), from the incident ions (subscript i) or the target atoms (subscript t). In order to remain consistent with the NRT model used for the neutron irradiation, the lattice binding energy was set to zero and the number of phonons/Å/ion was used to give T. This produced an average damage with depth of 0.82dpa and is shown with the original target of 1.7dpa in *figure 6.11*.

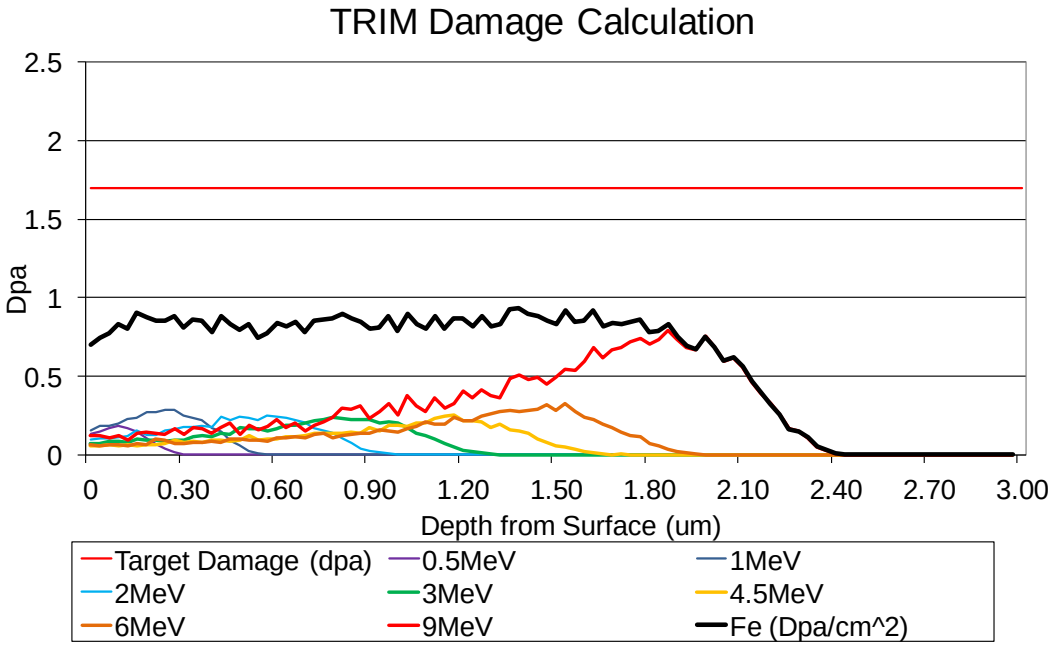

Figure 6.11 – SRIM calculations based on the Kinchin and Pease model showing irradiation damage vs. depth into sample surface, including contributions from each beam energy and total damage.

The damage calculations used for the neutron and ion irradiations are inconsistent in representing the physical exposure to radiation and it is likely that the neutron irradiated alloy was subjected to more displacement damage. Despite this, several ion implantation studies of a similar low purity alloy have identified that irradiation hardening saturates at a dose of 1-2 dpa (calculated by using the 'Detailed Calculation with full Damage Cascades' model) [91, 95]. Thus, a variation in dose alone may not explain the large difference in hardness in the ion and neutron irradiated material.

The Effect of Dose Rate

In chapter 7 it is shown that the microstructural evolution of the primary damage is dependent on the dose rate during irradiation. The rate of damage produced during ion irradiation ($5x10^{-5}$dpa/s) was approximately 150 times faster than in the ATR reactor (~$3x10^{-7}$dpa/s). It is likely that the Fe 6%Cr alloy irradiated in the ATR reactor exhibited radiation-induced segregation of Cr, similar to that observed in the ultra-high purity Fe 5%Cr alloy subjected to a lower dose rate reported in *chapter 7*. There, it was identified that Cr enriched areas were formed after irradiation and that enrichment was suppressed at higher dose rates. Irradiation hardening at the low dose rate was found to be double that of the same alloy irradiated with the higher dose rate. The observed difference in irradiation hardening measured between the ion and neutron irradiated Fe 6%Cr alloy may therefore be caused by the same Cr enrichment mechanism, which may increase the strength of obstacles to dislocation glide. The ion irradiated material in the present investigation was subjected to a similar dose rate to the low dose rate used in chapter 7, which produced the Cr enriched areas. It may therefore be expected that the Fe 6%Cr alloy should exhibit Cr enrichment after ion implantation in the present study. However, the relative purity of the materials discussed in the present investigation compared with those described in *chapter 7*, complicates the comparison of the two experiments. The lower purity Fe6%Cr alloy produced by the Paul D. Merica Research Laboratory will result in the reduced mobility of defects and could suppress Cr enrichment. The comparison of Fe-Cr alloys of various purity and its effects on irradiation hardening are discussed in *section 7.6.3*.

The Effect of PKA Energy Spectra

As discussed in *section 2.3.4*, fission neutrons produce PKA energies of up to 200 keV [118] and have an energy spectrum which includes a tail of lower energies. In comparison, ion

implantation experiments produce PKAs with energies equal to that of the beam energy (up to 9MeV in the current experiment). Using recoil spectra for Fe_{56} and calculations of displacements from method 3 above, the damage as a function of PKA energy produced by the ion and neutron irradiations is shown in *figure 6.12*.

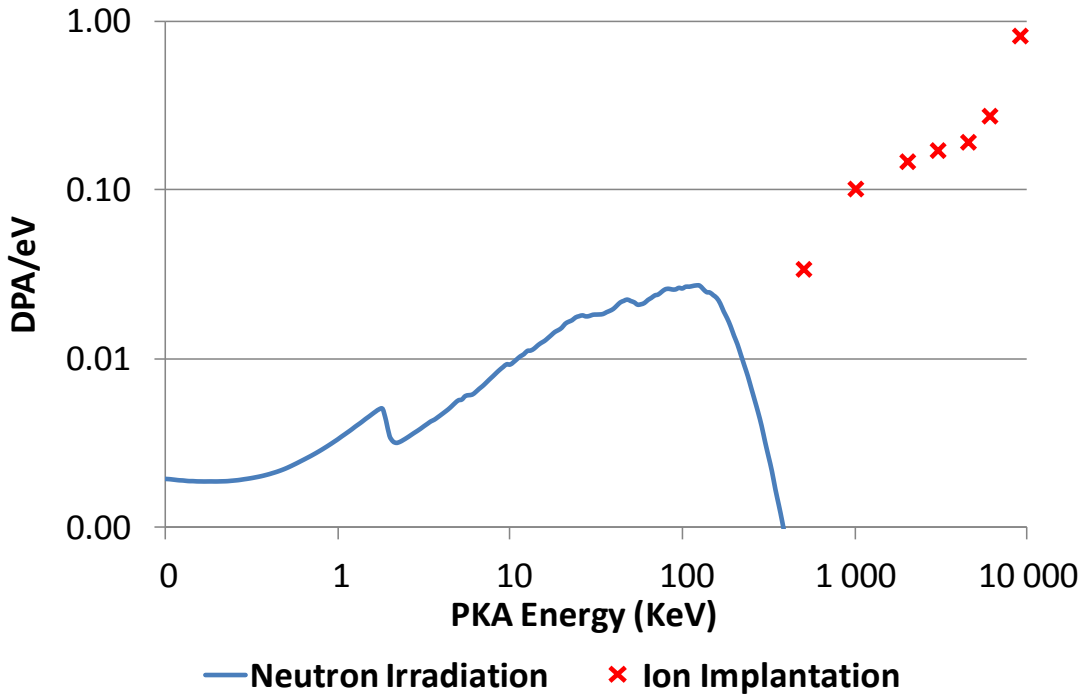

Figure 6.12 – Radiation damage as a function of PKA energy for ion and neutron irradiations.

The difference in the total number of displacements produced by each incident particle should be accounted for in the respective damage calculations for each irradiation; thus, areas beneath data for ions and neutrons in *figure 6.12* are equal to ~1.7dpa. However, the types of primary defects produced by an incident ion or neutron may differ depending on the PKA energy. There is agreement amongst several authors [118, 126, 230, 231] that above a threshold damage energy of approximately 5 to 10KeV, the production of primary defects in a material is independent of damage energy. The threshold energy represents the

transition from the production of Frenkel pairs at the lowest PKA energies to larger cascades and sub-cascade formation (described in *section 2.3.4*) at higher PKA energies. Above this threshold energy, formations of separate sub-cascades produce the same primary defect types and the numbers of these defects remain a constant function of the energy (30% of the NRT value [231]). Contrary to early work, recent MD simulations summarised in *table 2.4* identified that cascades were in the form of a continuous distribution of damage and that the primary defect morphology continues to change as a function of energy up to 0.5 MeV [113].

For the neutron irradiation, the majority of the damage was produced by PKA energies from ~60 to 275keV with a peak at 158keV. In contrast, PKA energies produced during the ion implantation were 0.5 to 9MeV. This suggests that the cascade damage morphology produced by the fission neutrons may be significantly different than that produced by ion implantation. This is likely to influence the fraction of freely migrating defects in both ion and neutron irradiations [232, 233]; that is, the fraction of isolated point defects or defects within small clusters which are mobile.

The lower dose rate and lower PKA energy spectrum during neutron irradiation may have produced more favourable conditions for radiation-induced segregation than ion implantation. These conditions may have caused heightened Cr enrichment as observed in *chapter 7* and contributed to greater irradiation hardening in the neutron irradiated alloy. In addition, the FISPACT-II inventory simulation conducted by Dr M Gilbert indicated that approximately 10appm He and 6.5appm H was produced in the alloy during neutron irradiation. This may have also contributed to the increase in irradiation hardening.

6.4.2 Size Effects in Irradiated Materials

The observed increase in mechanical strength of a material with decrease in test specimen size is a well-known phenomenon. The first observations of size dependence in tensile strength were made by Brenner in 1956 by tensile testing whiskers of iron, copper and silver from 1.2µm to 15µm in diameter [234]. There have been several attempts to characterise the underlying mechanisms which produce this effect, yet at present there is no clear explanation which can account for all of the various observations throughout the literature. A full review of the theories related to size effects would not be appropriate in the context of this thesis, thus only a brief overview is provided below.

The origins of the most common mechanical size effects have been identified as:

i. Strain gradient plasticity theory (beam bending and indentation)
ii. Dislocation starvation
iii. Dislocation truncation
iv. Dislocation pile-up at the beam neutral axis (beam bending only)

A variation of hardness with indentation depth is commonly observed in many materials and provides a method to measure the size dependence of strength in the same test. Nix and Gao [218] developed a law for strain gradient plasticity which suggests that the density of geometrically necessary dislocations (GNDs) required to support the shape of the indent impression is responsible for the indentation size effect (ISE). Assuming a simplified model comprising of a rigid conical indenter and deformation accommodated by circular GNDs in a hemispherical volume beneath the indenter tip, the density of GNDs is defined as:

$$\rho_{GND} = \frac{3}{2bh} tan^2\theta \qquad \textbf{\textit{equation}}\ \mathbf{6.3}$$

where θ is the centreline-to-face angle of the indenter tip, b is the Burgers vector and h is the indentation depth. Thus, as the indenter is driven into the sample surface, ρ_{GND} decreases with indentation depth.

This theory does not apply to the strong size effect observed in micro-pillar tests [101], where there are no strain gradients produced from uniaxial loading. It has been proposed that the lack of dislocation multiplication events during the deformation of such small volumes may lead to a lack of available dislocations, termed dislocation starvation, and requires the nucleation of dislocations at a higher stress [235]. Similarly, dislocation sources require a characteristic volume to operate. The fabrication of test specimens may create surfaces which reduce the length of available dislocation segments and limit the volume available for source operation; these segments and sources may require higher stresses to operate, known as truncation hardening [236].

The theories of source starvation and truncation suggest that plastic deformation is increasingly controlled by the activation of dislocation sources as the size of the test volume decreases. In the work reported here, there are two observations which indicate that the activation of dislocation sources influence plasticity in the tests reported in this thesis. Firstly, discrete pop-in events in the load-displacement behaviour during nanoindentation at small depths (described in *chapter 5),* represents the transformation from elastic to fully plastic deformation by the activation of dislocation sources. Secondly, as commonly

observed in other micro-mechanical tests [221], plasticity in the micro-cantilever tests shown in *figure 6.5* progressed in a stochastic nature exhibiting several drops in load during mechanical testing. These load drops are likely to be related to the activation of individual sources as the deformation progresses.

As shown in *figure 6.5a*, the magnitude of the load drops increased with increasing beam size in the un-irradiated material. The magnitude of the load drop may be proportional to the strain accommodated once a dislocation source has been activated; it is likely that this strain is controlled by the number of dislocations which can be emitted before stresses produced by pile-up at the neutral axis cause the source to shut down. Hence, the increase in magnitude of the load drops with increasing beam size may relate to the longer distance dislocations glide on larger slip planes, which accommodate a greater number of dislocations emitted from a single source. This observation is supported by the appearance of visible slip steps at the surface only in the larger plastically deformed beams in *figure 6.8*, where each slip plane can accommodate a greater number of dislocations.

As discussed in *section 5.4*, load drops in cantilever tests indicate that the stress to activate dislocation sources dominates the observed strength of the material, resulting in no difference in the yield stress between the un-irradiated and ion-irradiated material for beams <1µm depth. A similar observation was made in the only comparable investigation conducted by Kiener et al. [100], where no irradiation hardening in proton irradiated Cu was measured in micro-pillar tests below a diameter of 400nm. Kiener et al. identified that glissile dislocations partially or fully remove the irradiation-induced defects and that plastic deformation developed by localised slip within defect-free channels. The highly localised slip

steps observed in the irradiated material adjacent indents (*figure 6.4*) and at the deformed surfaces of micro-cantilevers (*figure 6.8*) suggests that the material investigated here deforms in a similar manner. This type of plastic deformation has been characterised for the Fe 12%Cr alloy investigated in *chapter 5* (reported elsewhere [91]) and is caused by the annihilation of irradiation-induced defects by glissile dislocations (see discussion on dislocation channelling in *section 7.6.4*). In the presence of high stresses produced to overcome size effect mechanisms, the defects may be annihilated without additional stress and plastic deformation progresses at the same stress as the un-irradiated material. When the size of the test specimen increases above a critical size (~1µm in the present case), the stress determined by the size effect mechanisms is lower than that determined by the irradiation-induced defects and the response of the ion-irradiated material deviates from that of the un-irradiated material. In Kiener's study, this critical size was found to be a pillar diameter of 400nm, above which the yield stress of the irradiated Cu was apparently independent of size. This is clearly not observed in the tests reported here where the yield stress of the irradiated material continues to decrease as the beam depth increases.

Unlike the behaviour of ion-irradiated material, irradiation hardening measured for the neutron irradiated material was not completely obscured in the smallest beams. This suggests that the interaction between glissile dislocations and irradiation induced defects is different for the defects produced by ion-irradiation and neutron-irradiation. As suggested in *section 6.4.1*, the neutron-irradiated material is likely to exhibit Cr enrichment as identified in *chapter 7*. Unlike dislocation loops, areas of Cr enrichment cannot annihilate by reaction with a glissile dislocation, thus may contribute to the stress required for plastic deformation in *addition* to the mechanisms controlling the size effect. Furthermore, the resistance to

annihilation of Cr enriched regions may give rise to the increased work hardening behaviour observed in the neutron-irradiated material.

6.4.3 Comparison with Macro-Scale Properties

The Fe 6%Cr material studied here was also investigated by Vickers micro-hardness testing by Mr T Milot at INL. This method could not be conducted in Oxford, due to the size of specimen required being larger than that allowed by the activity limit of the department. A LECO LM247 AT instrument was operated with a load of 500g, to produce indents into both the un-irradiated and neutron irradiated material. Values of hardness were 117.2Hv (+/- 2.7) for the un-irradiated material and 232.9Hv (+/- 5.8) for the neutron-irradiated material. According to the empirical relationships derived for irradiated austenitic and ferritic steels [222], dividing these values by 3.03 provides an estimate of the macro scale yield stress; this produces a yield stress of 355MPa for the un-irradiated material and 706MPa for the neutron-irradiated material.

The micro-cantilever data described in *section 6.3.2* may provide a means for extrapolation to macro scale properties. The observation that the proof stress is strongly proportional to h^{-1} was also made by Motz et al. [221] for micro-cantilever tests in a copper single crystal. Motz provided an analytical model which accounts for the increase in flow stress produced by the pile-up of dislocations at the neutral axis. This contribution, σ_{PU}, is given by:

$$\sigma_{PU} = \frac{\alpha G}{b}\frac{\omega^2}{x^2}h\lambda^2 \qquad \textbf{equation 6.4}$$

where α is a constant (0 to 1), G is the shear modulus (84GPa for iron), b is the Burgers vector (2.48Å for iron), ω is the beam bending angle, x is the size of the plastically deformed region, h is the beam height and λ is the dislocation source spacing. The assumption that the size of the plastically deformed region can be approximated as the beam thickness ($x = h$) gives:

$$\sigma_{PU} = \frac{\alpha G}{b}\frac{\omega^2}{h}\lambda^2 \qquad \textbf{equation 6.5}$$

According to *equation 6.5* values of A_0 in *equation 6.1* may be described by:

$$A_0 = \frac{\alpha G}{b}\omega^2\lambda^2 \qquad \textbf{equation 6.6}$$

Rearranging *equation 6.6* and using the fitted values for A_0 in *table 6.4* produces an average dislocation source spacing from ~20nm to ~200nm for the three materials at values of α from 0.1 to 0.9. This range corresponds well with the distribution of slip steps in the deformed beams shown in *figure 6.8.*

The values for A_1 in *table 6.4* represents the asymptotic values of proof stress (σ_{proof} at $h = \infty$) of 477MPa for the un-irradiated and 1290MPa for the neutron irradiated material. These values are larger than the values of yield stress calculated from the Vickers hardness data and indicate that additional size effect mechanisms such as source

starvation/truncation may also contribute to the response of the material. This suggests that the extrapolation of yield stress to macro scale properties requires a more complex model of the mechanisms which contribute to the size effect or a larger range of test sizes.

6.5 Summary

i. Fe6%Cr irradiated to a dose of 1.7dpa at 288°C exhibited significantly different irradiation hardening depending on whether the irradiation was by ions or by neutrons.
    a. Nanoindentation results showed that irradiation hardening in the neutron-irradiated material was ~3GPa, whilst it was ~1GPa in the ion-irradiated material.
    b. Unlike the un-irradiated and ion-irradiated material, the neutron-irradiated material exhibited some work hardening in micro-cantilever tests.

ii. The variation of hardening may be caused by:
    a. Inconsistencies in damage calculations between the standard NRT formula for neutron irradiations and 'detailed calculation with full damage cascades' model in TRIM for ion-irradiation. As described in *section 6.4.1*, comparison with similar work suggests that the ion implantation damage is likely to be at or near saturation.
    b. Differences in the dose rate ($5x10^{-5}$dpa/s for ion-irradiation and ~$3x10^{-7}$dpa/s for neutron-irradiation) and/or PKA energy spectrum (see *figure 6.12*), which may cause enhanced Cr enriched regions in the neutron irradiated material. TEM and APT data are required to confirm differences in the damage microstructure.

iii. All materials exhibited a size effect with yield stress varying by up to 700% for beam depths from ~0.5µm to ~7µm (*figure 6.7*). The effect in the ion-irradiated material was such that hardening due to irradiation was obscured by size effects. In the neutron irradiated material, the stronger hardening due to irradiation was not fully obscured by size effects. These differences in strength and irradiation hardening are likely to have been caused by the different types of defect produced by the ion and neutron irradiations, in particular a stronger tendency to produce chromium enriched regions for the neutron irradiation where the dose rate is much lower than for ion irradiation.

iv. Attempts to extrapolate micro-cantilever results to the macro-scale in *section 6.4.3* appear unsuccessful. This is likely to be caused by errors in empirical relationships used for Vickers hardness data and/or multiple size effect mechanisms including source activation and dislocation pile-up at the neutral axis, which require a more complex model.

7 IRRADIATION PARAMETERS AND THE ROLE OF CR IN FE-CR ALLOYS

Investigations reported in *chapter 6* directly compared irradiations produced by ions and neutrons. Results indicated that ion irradiation cannot be used to directly simulate conditions expected within a fusion reactor and irradiation parameters such as dose rate and PKA energy spectrum may have a significant influence on the microstructural evolution and mechanical properties of a given material. Unfortunately, many investigations fail to report or recognise the importance of these parameters; which cause apparent discrepancies in results such as the observed differences between ion and neutron irradiated Fe6%Cr discussed in *chapter 6*.

7.1 Introduction

This chapter presents a systematic investigation of ultra-high purity (UHP) Fe and Fe-Cr alloys subjected to several ion-implantations with various irradiation doses, dose rates and temperatures. The experiments were designed to examine the evolution of radiation damage in the Fe-Cr system, the types of defects which are produced and their contribution to hardening.

7.2 Experimental Details

The experiments reported in this chapter used ultra-high purity material supplied by EFDA (under contract no. EFDA-06-1901) and ion-irradiations conducted at Surrey Ion Beam Centre, UK.

7.2.1 Material: Fe and Fe-Cr Alloys (EFDA)

Pure Fe and Fe-Cr alloys with 5, 10 and 14%Cr were manufactured by EFDA at MINES ParisTech Centre for Material Forming (France). The materials were manufactured by induction melting under a pure argon atmosphere; hot forming by forging ingots with a mechanical hammer at 1000°C (pure Fe) and 1150°C (Fe-Cr alloys); cold forging in a swaging machine and various recrystallisation heat treatments. A chemical analysis of each alloy can be seen in *table 7.1*; for more detail a comprehensive report regarding the manufacture and post analysis of these materials can be seen in ref. [237].

Table 7.1 - Chemical analysis of the alloys after hot forming and in the as-delivered final metallurgical condition (in brackets) [237].

Alloy	C wt ppm	S wt ppm	O wt ppm	N wt ppm	P wt ppm	Cr
Fe	3 (4)	2 (2)	5 (4)	2 (1)	<5	<2 ppm
Fe 5%Cr	3 (4)	3 (3)	4 (6)	3 (2)	<5	5.40 wt%
Fe 10%Cr	4 (4)	6 (4)	3 (4)	3 (3)	<5	10.10 wt%
Fe 14%Cr	4 (5)	6 (7)	4 (4)	5 (5)	<10	14.25 wt%

All materials were cut into small samples approximately 10mm in diameter and 0.5mm thick. Samples were annealed in a vacuum furnace at a pressure of $<10^{-4}$ Pa ($<10^{-6}$mbar) and temperature was increased to 830°C in multiple steps to allow recovery from out-gassing of the sample and chamber. Similar to experiments reported in *chapters 5* and *6*, polishing included a series of lapping stages using SiC abrasive papers from FEPA P120 to P4000 grades used to produce a smooth surface, followed by a chemo-mechanical polish using a colloidal silica suspension (0.05µm). This provided a surface with minimal polish damage with a quality suitable for electron backscattered diffraction (EBSD).

7.2.2 Ion Implantation

A matrix of implantations was designed to provide samples subject to a low dose of 0.06dpa (LD), a medium dose of 0.6dpa (MD) and a high dose of 6dpa (HD); a high dose rate (HDR) of 6 x 10^{-4}dpa/s and low dose rate (LDR) of 3 x 10^{-5}dpa/s; and irradiation temperatures of 300, 400 and 500°C. *Table 7.2* shows each implantation produced with the irradiation conditions.

Table 7.2 - Experiment ion irradiation conditions for EFDA alloys. High dose rate (HDR) refers to 6 x 10^{-4} dpa/s and low dose rate (LDR) refers to 3 x 10^{-5} dpa/s.

		DOSE (dpa)			
		0.06 (LD)	**0.6 (MD)**		**6 (HD)**
TEMPERATURE (°C)	**300**	HDR	HDR	LDR	HDR
	400		HDR	LDR	
	500		HDR	LDR	

Ion beam and environmental conditions for all implantations used are shown in *table 7.3*. Fe^{+} ions were implanted successively with energies of 2MeV, 1 MeV and 0.5MeV to produce a roughly uniform damage profile with depth as shown in *figure 7.1* for all 3 doses used.

Table 7.3 - Ion implantation beam conditions for each energy for specified doses and dose rates.

		Dose			Beam Current			
Temperature	Energy	LD (0.06dpa)	MD (0.6dpa)	HD (6dpa)	HDR (6×10^{-4})		LDR (3×10^{-5})	
(°C)	(MeV)	(ions/cm^2)	(ions/cm^2)	(ions/cm^2)	ions/cm^2/s	nA/cm^2	ions/cm^2/s	nA/cm^2
300, 400 & 500	0.5	5×10^{12}	5×10^{13}	5×10^{14}	1.87×10^{11}	29.9	9.35×10^{9}	1.5
	1	7.5×10^{12}	7.5×10^{13}	7.5×10^{14}	2.16×10^{11}	34.5	1.08×10^{10}	1.73
	2	2.5×10^{13}	2.5×10^{14}	2.5×10^{15}	2.28×10^{11}	36.6	1.14×10^{10}	1.83

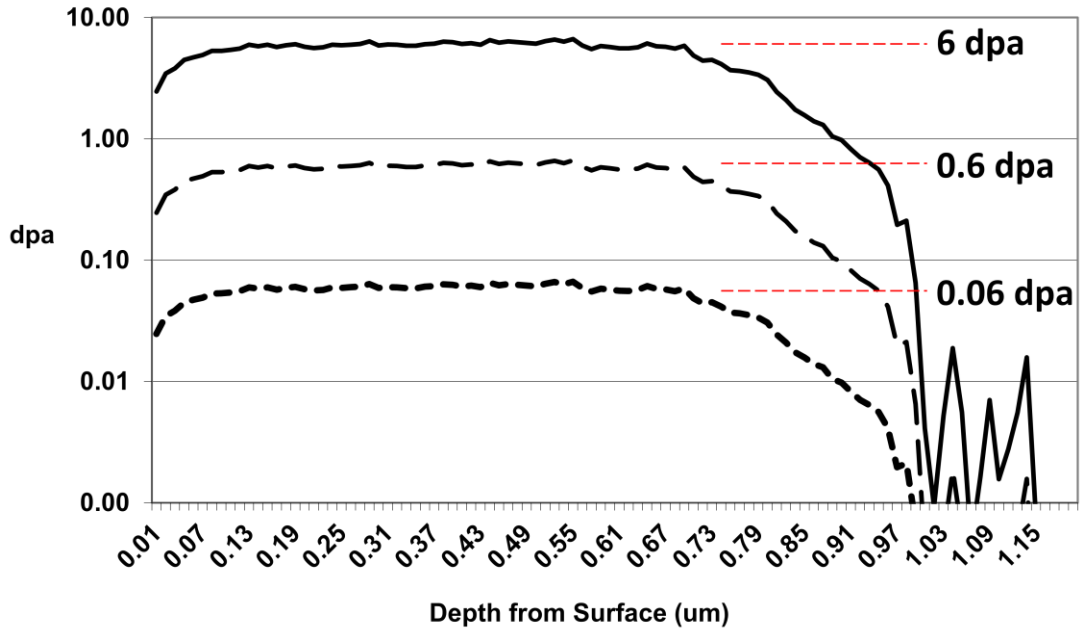

Figure 7.1 - Damage profiles for all samples irradiated with 3 energies to doses of 0.06, 0.6 and 6dpa as calculated by SRIM.

The beam current was maintained for each of the energies used during implantation by adjusting conditions at the source (for a coarse control) and adjusting the size of the beam raster area (for control to within <0.1nA). This enabled beam currents to be held constant for all energies, giving constant peak dose rates shown in *figure 7.2*. The ion beam was focused to a diameter of 5mm and distributed over the implantation area by beam scanning at 4kHz. This produced a localised pulsing of the beam with increased dose rate at doses of 1.5 x 10^{-7}dpa per pulse for the high dose rate and 7.5 x 10^{-9}dpa per pulse for the low dose rate. This is a small fraction of the damage required for cascade overlap, ~0.01dpa [69]; thus localised flux is not considered to influence the formation of damage.

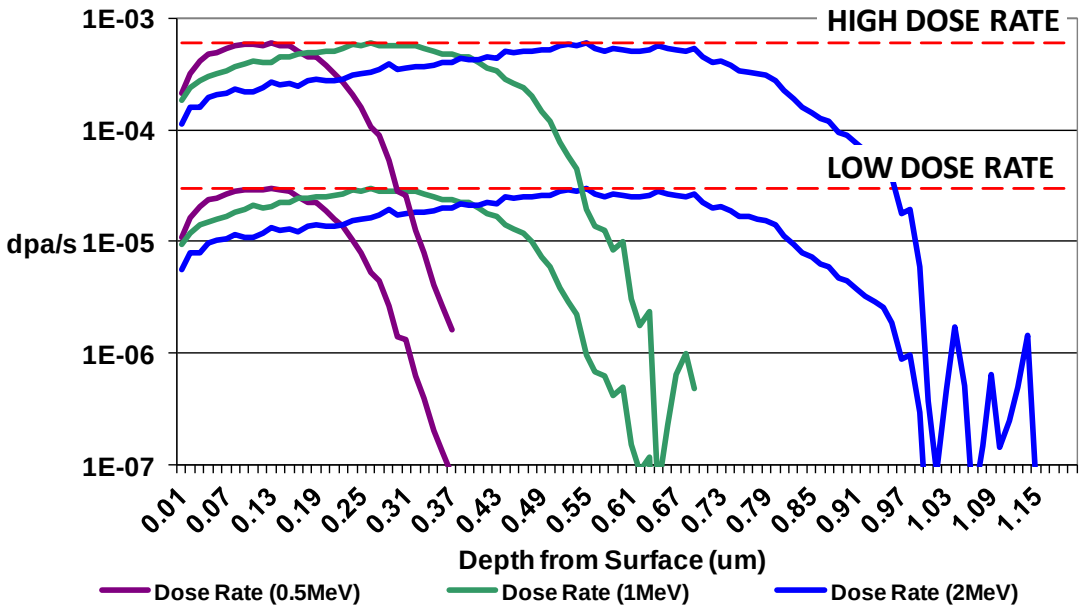

Figure 7.2 - High and low dose rate for each energy as calculated by SRIM.

7.2.3 Mechanical Testing

Nanoindentation was conducted using the CSM technique with a Berkovich tip and a strain rate of 0.05/s. Indents were produced in arrays of approximately 8 indents with 40µm spacing. Micro-cantilever testing was conducted using the waisted beam geometry, stereo-imaging measurement and FEA progressive convergent approximation as described and optimised in *chapters 4* and *5*. Beams were tested at a displacement rate of 5nm/s which produced average strain rates of ~$3x10^{-4}$/s. For material irradiated at 300°C nanoindentation and micro-cantilever tests were conducted in the un-irradiated and irradiated regions of the same grain using the same methods described in *section 5.1.2*. The boundary between the un-irradiated and irradiated material was less visible in the secondary electron images of material irradiated at 400 and 500°C, thus testing was conducted in different grains for both regions.

7.3 Nano-indentation Results

Samples for all irradiation conditions were tested using nanoindentation as described in *section 3.3.1*. For all tests the average elastic modulus and hardness with indenter depth for the un-irradiated and irradiated regions of each sample exhibited a similar form to that shown for the Fe12%Cr alloy presented in s*ection 5.2.3*. The elastic modulus data for two grains in the Fe 5%Cr, MD, HDR, 300°C sample is shown in *figure 7.3*. There is an apparent increase in the observed elastic modulus at early indentation depths, ΔE, which is likely to be caused by differences in pile-up between the un-irradiated and irradiated material as characterised in *chapter 5*. The additional contact area due to pile-up will also influence the hardness data to some extent; however this effect, measured by ΔE, does not change

dramatically over the range of samples. *Figure 7.4* shows the corresponding hardness versus indentation depth data for the same samples. Irradiation hardening is seen for indentation depths less than 200nm, when the plastic zone of the indent is predominantly within the damaged layer (*figure 5.5*). Once the plastic zone expands beyond the damaged layer, the observed hardness tends towards that of the un-irradiated material.

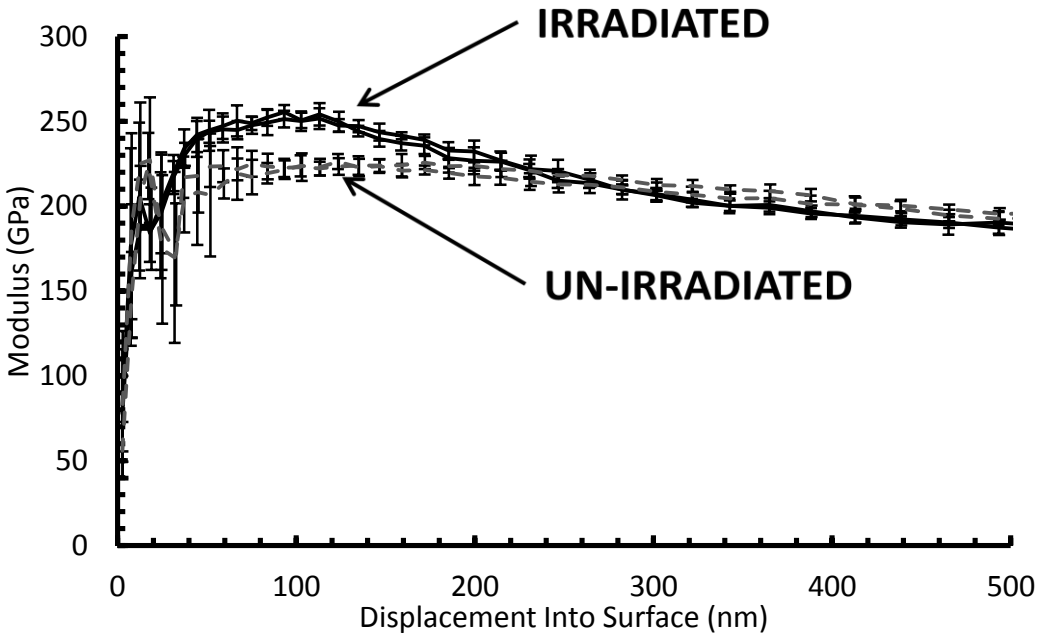

Figure 7.3 - Modulus versus indentation depth measured from indents produced in the un-irradiated and irradiated regions of two grains of Fe 5%Cr irradiated to a dose of 0.6dpa at a dose rate of 6 x 10^{-4}dpa/s and temperature of 300˚C. Error bars represent +/- one standard deviation.

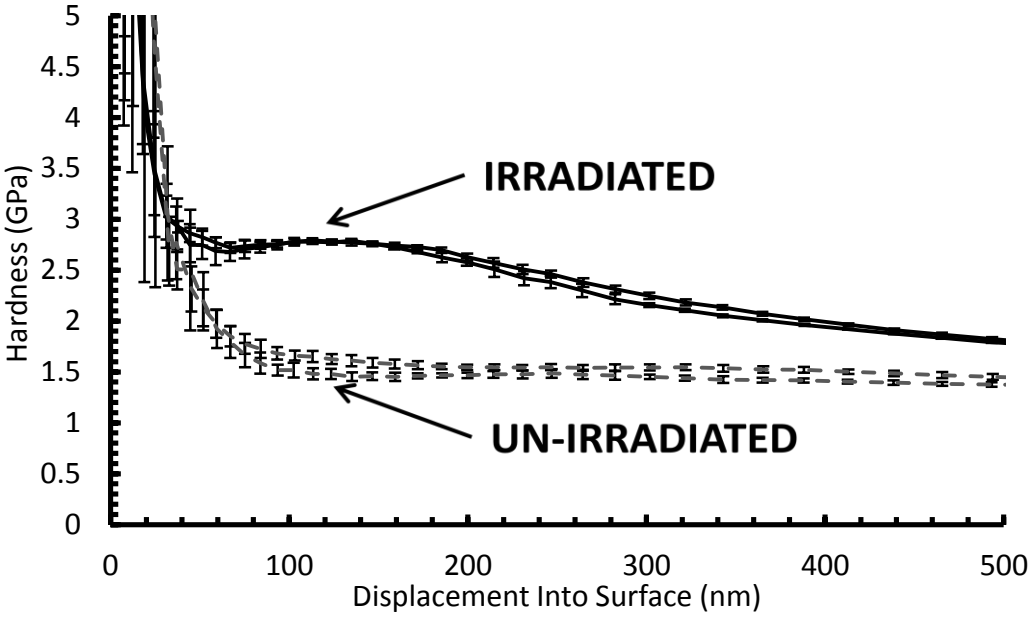

Figure 7.4 - Hardness versus indentation depth measured from indents produced in the un-irradiated and irradiated regions of two grains of Fe 5%Cr irradiated to a dose of 0.6dpa at a dose rate of 6 x 10^{-4}dpa/s and temperature of 300°C. Error bars represent +/- one standard deviation.

For each sample condition and grain the hardness calculated from arrays of indents was measured by averaging data between indentation depths from 50 to 200nm as defined in *chapter 5*. Same grain data for the two grains (*figures 7.3* and *7.4*) show little variation due to crystal anisotropy. The range of hardness variation due to differences in crystallographic orientation of the grains in which the indentation arrays were made can be identified by comparing hardness data in un-irradiated material. This includes several grains in un-irradiated regions of the same composition which were tested throughout the investigation. Average values for hardness (and standard deviation) for all tests in the un-irradiated material were 1.60GPa (0.09GPa) for pure Fe, 1.67GPa (0.07GPa) for Fe5%Cr, 1.94GPa (0.07GPa) for Fe10%Cr and 2.27GPa (0.16GPa) for Fe14%Cr. Un-irradiated hardness data are shown in *figure 7.5*. Hardness values across multiple grains in the irradiated material also

exhibited little scatter; thus, differences in hardness due to crystallography are minimal compared to those caused by irradiation.

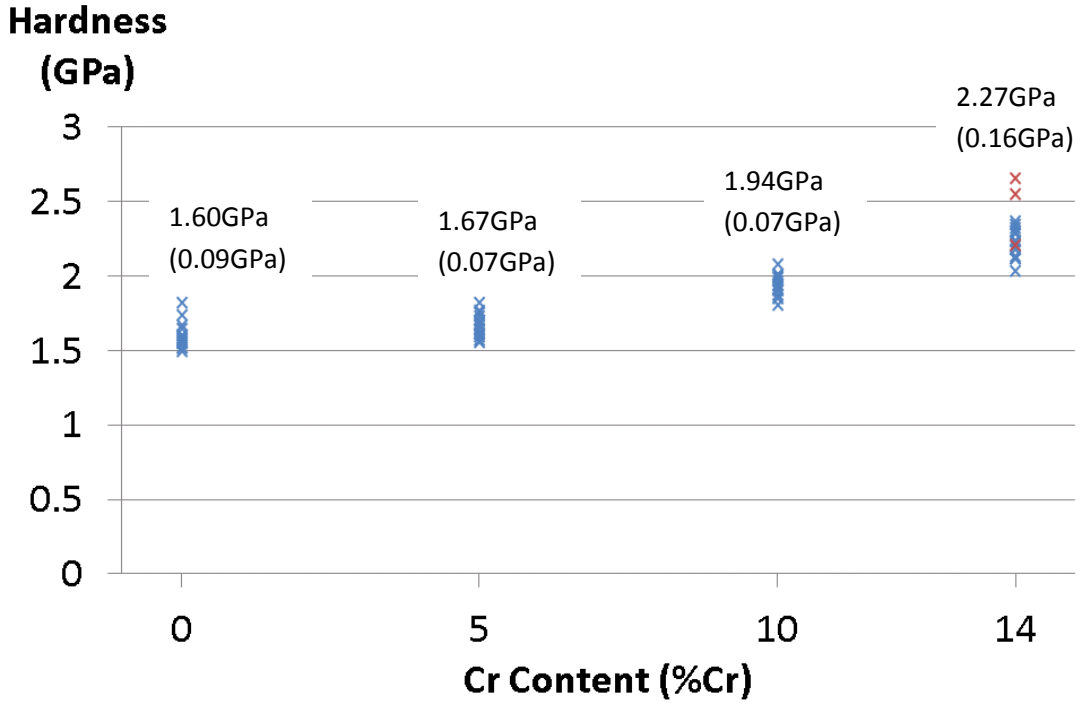

Figure 7.5 - Hardness values from un-irradiated regions of all samples tested with averages given in data labels and standard deviation in brackets. The red data points show un-irradiated material subjected to a temperature of 400˚C for 10 hours during the low dose rate implantation; the higher hardness in this material may have been caused by α' precipitation.

7.3.1 Irradiation Dose

Figure 7.6 shows the hardness of the un-irradiated and irradiated regions as a function of Cr content. For the un-irradiated material, there is a slight increase in hardness with increase in Cr content which is likely to be attributed to solute hardening. Irradiation hardening (ΔH) is clearly evident in all materials tested and increases as a function of dose. In contrast to the Fe-Cr alloys, pure Fe exhibited little additional hardening at doses greater than 0.6dpa.

Fe5%Cr exhibited the most irradiation hardening, which was 2.19GPa (224%) at a dose of 6dpa (HD). The irradiation hardening in Fe10%Cr and Fe14%Cr was less than the Fe5%Cr alloy with similar values of 1.58GPa (179%) and 1.65GPa (174%) respectively. The difference in hardness between the alloys irradiated at a dose of 0.6dpa (MD) and 6dpa (HD) decreases with Cr content.

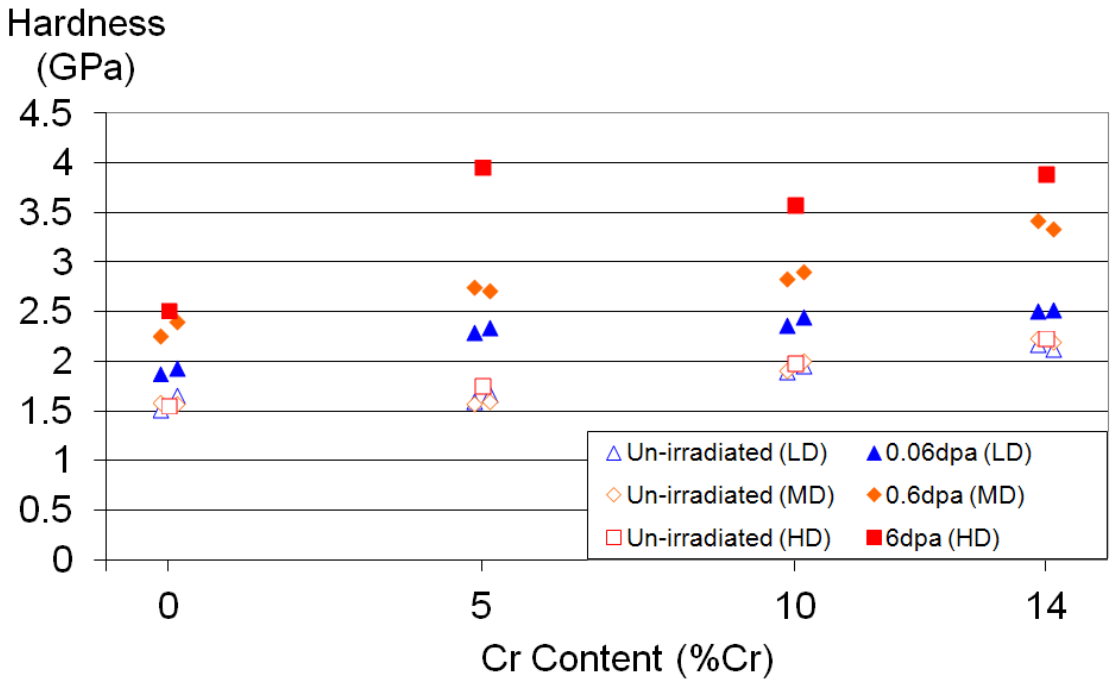

Figure 7.6 - Average hardness values for data produced between indentation depths of 50 and 200nm for all Fe and Fe-Cr alloys irradiated to doses of 0.06 (LD), 0.6 (MD) and 6dpa (HD) at a dose rate of 6 x 10^{-4} dpa/s (HDR) and a temperature of 300°C. Data for each %Cr are laterally spread for ease of visibility.

7.3.2 Irradiation Dose Rate and Temperature

Figure 7.7 shows the hardness of the un-irradiated and irradiated regions as a function of Cr content for all samples irradiated to the same dose of 0.6dpa. Average hardness values are plotted for two grains in each sample subjected to the high dose rate of 6 x 10^{-4} dpa/s (HDR) and low dose rate of 3 x 10^{-5} dpa/s (LDR) at temperatures of 300, 400 and 500°C. After irradiation at 300°C (*figure 7.7a*), irradiation hardening was clearly observed in all samples. Some Fe-Cr alloys exhibited a difference in irradiation hardening between the two dose rates and this difference was greatest for Fe5%Cr. The difference in hardness between low and high dose rates decreased with increasing Cr content and is not evident in Fe14%Cr. In addition, there were no effects of dose rate on irradiation hardening in pure Fe.

After irradiation at 400°C (*figure 7.7b*), hardening was clearly observed in all Fe-Cr alloys, but not in pure Fe. Similar to the irradiation at 300°C, irradiation hardening in Fe5%Cr was greater at the lower dose rate, and the 'dose rate effect' decreased with increasing Cr content. Unlike at 300°C, irradiation hardening of Fe14%Cr exhibited a dependence on dose rate. Negligible hardening was observed for all material irradiated at 500°C subjected to either dose rate (*figure 7.7c*).

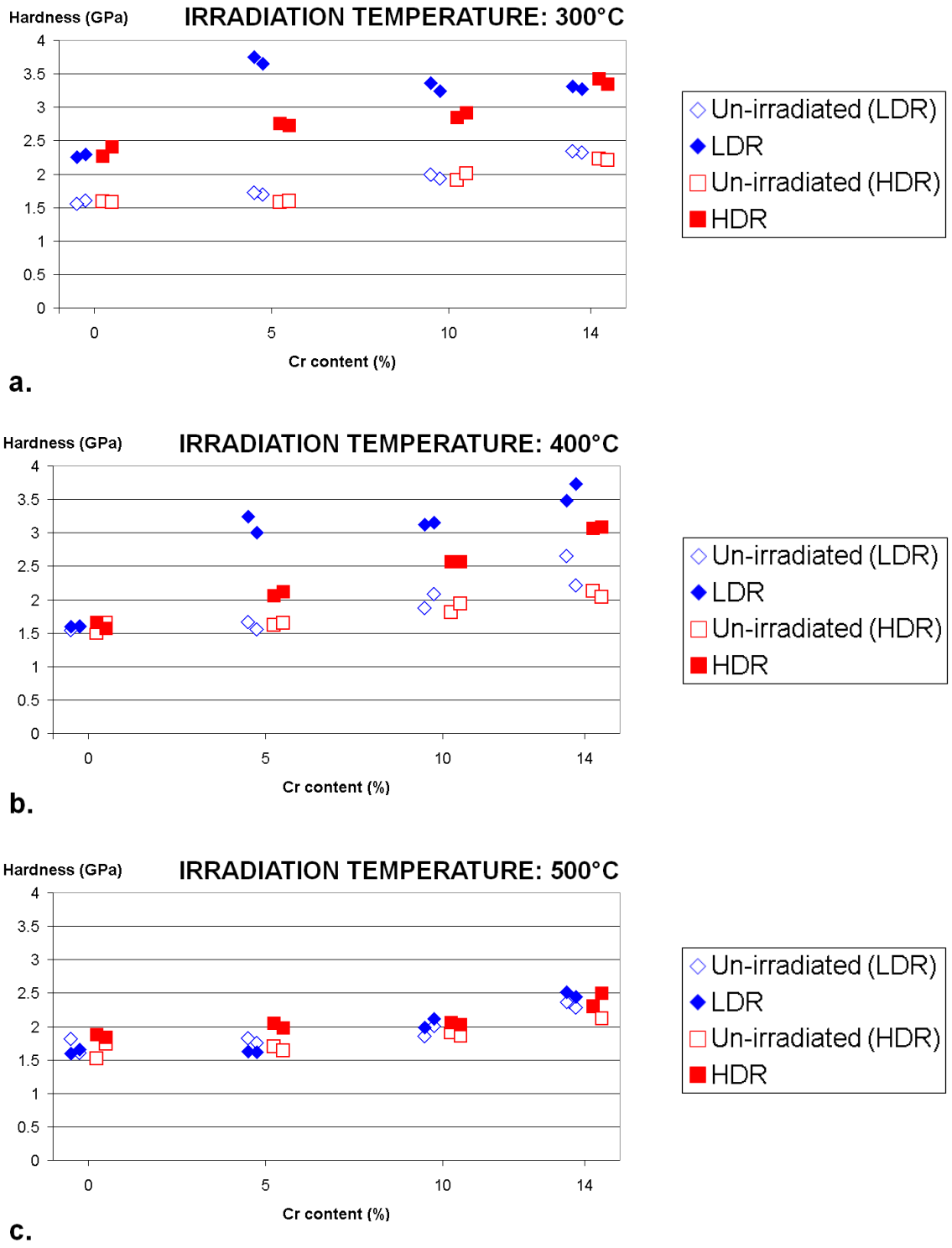

Figure 7.7 - Average hardness values for data produced between indentation depths of 50 and 200nm for an irradiation dose of 0.6dpa produced at temperatures of 300°C (a), 400°C (b) and 500°C (c). Data are for indentation arrays within the same grain for low dose rate (LDR: solid blue), high dose rate (HDR: solid red) and the un-irradiated regions (open symbols). Data for each %Cr are laterally spread for ease of visibility.

7.4 Micro-Cantilever Results

7.4.1 High Dose, High Dose Rate

All samples irradiated to 6dpa were analysed by testing arrays of ~12 waisted type beams in both the un-irradiated and irradiated regions of the same grain. Data were analysed by using progressive convergence approximation described in *section 4.2.4*, with 6 plastic match points of equal spacing as optimised and discussed in *section 5.3.2*. These results are given in *table 7.4* and *figure 7.8*.

Table 7.4 - Micro-cantilever beam results for tests within the un-irradiated and irradiated regions of the same grain for all samples subjected to a dose of 6dpa.

	UN-IRRADIATED				
Sample	**No. of Beams**	**Elastic Modulus (GPa)**	**SD**	**Yield Stress (GPa)**	**SD**
Pure Fe	12	181	9	1.13	0.11
Fe5%Cr	12	168	9	1.14	0.08
Fe10%Cr	12	182	13	1.33	0.16
Fe14%Cr	12	265	11	1.41	0.12
	IRRADIATED				
Sample	**No. of Beams**	**Elastic Modulus (GPa)**	**SD**	**Yield Stress (GPa)**	**SD**
Pure Fe	12	189	8	1.11	0.13
Fe5%Cr	10	160	7	1.20	0.06
Fe10%Cr	12	196	8	1.52	0.08
Fe14%Cr	12	250	13	1.59	0.18

No change was found in the measured elastic modulus between un-irradiated and irradiated material (*figure 7.8a*). A negligible increase in yield stress (*figure 7.8b*) is evident after irradiation in the Fe 10%Cr and Fe 14%Cr alloys, however in contrast to the nanoindentation data no or very little irradiation hardening is evident in all materials.

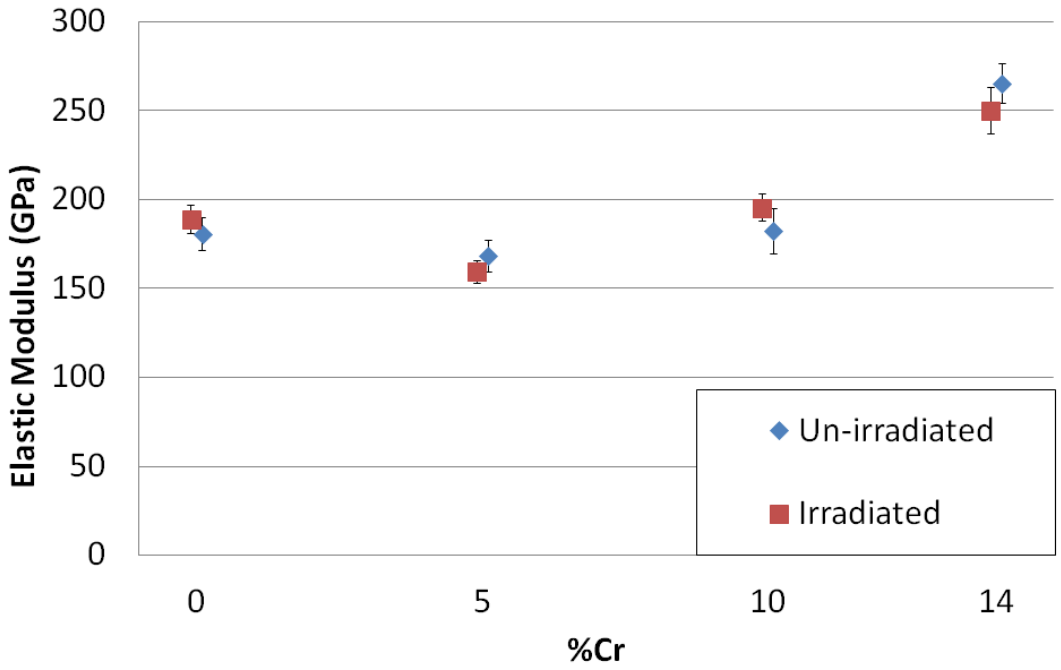

a.

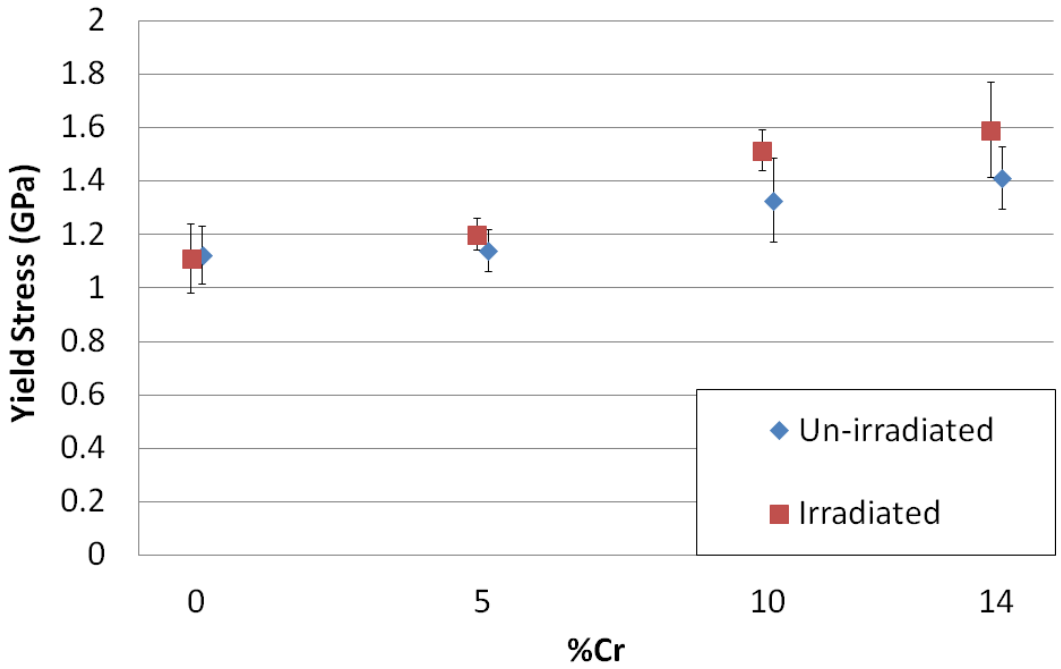

b.

Figure 7.8 - Elastic modulus (a) and yield stress (b) analysed by FEA simulation for beams tested within the un-irradiated and irradiated regions of the same grain in material irradiated to a dose of 6dpa at 300°C (HDR - 6 x 10^{-4}dpa/s). Data for each %Cr are laterally spread for ease of visibility.

7.4.2 Low Dose, Low Dose Rate

The Fe5%Cr samples subjected to irradiation at a dose of 0.6dpa at 300°C with the low dose rate was also analysed by testing waisted type beams. Results for the measured elastic modulus and yield stress are shown in *table 7.5*.

Table 7.5 - Waisted beams test results for Fe 5%Cr irradiated to 0.6dpa at 300 ˚C with the low dose rate (3 x 10^{-5}dpa/s).

	No. of Beams	Elastic Modulus (GPa)	SD	Yield Stress (GPa)	SD
UN-IRRADIATED	12	266	23	1.40	0.09
IRRADIATED	12	272	25	2.03	0.24

There were clear differences in the behaviour of beams tested in un-irradiated and irradiated regions of the LDR sample; the full stress-strain response as calculated by FEA matching is shown in *figure 7.9*.

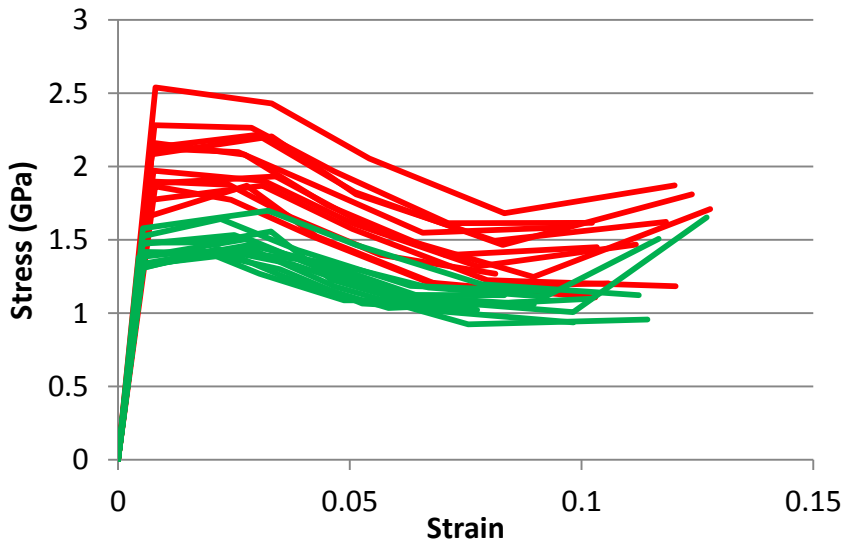

Figure 7.9 - Matched model stress-strain curves for 'waisted' type beams tested in the un-irradiated (green lines) and irradiated (red lines) regions of Fe 5%Cr irradiated to 0.6dpa at 300 ˚C with the low dose rate (3 x 10^{-5} dpa/s).

7.5 Microstructural Damage

7.5.1 TEM

Observations of the damage microstructure were undertaken by Mr S Xu of the University of Oxford. Kinematical bright-field (KBF) and dynamical two-beam diffraction conditions were used to characterise radiation damage. *Figure 7.10* shows damage structure in Fe5%Cr specimens irradiated at 300°C with the high dose rate and low dose rate. Damage in all foils had the form of dislocation loops with average sizes of 6.7nm for high dose rate sample, and 6.5nm for low dose rate sample. The dislocation loop densities were $16.1 \times 10^{21}/m^3$ for high dose rate sample and $9.72 \times 10^{21}/m^3$ for low dose rate sample (*table 7.6*). The samples had a similar thickness of approximately 145nm measured by using a convergent beam technique. Analyses were based on measurement of 542 loops for high dose rate and 327 loops for low dose rate.

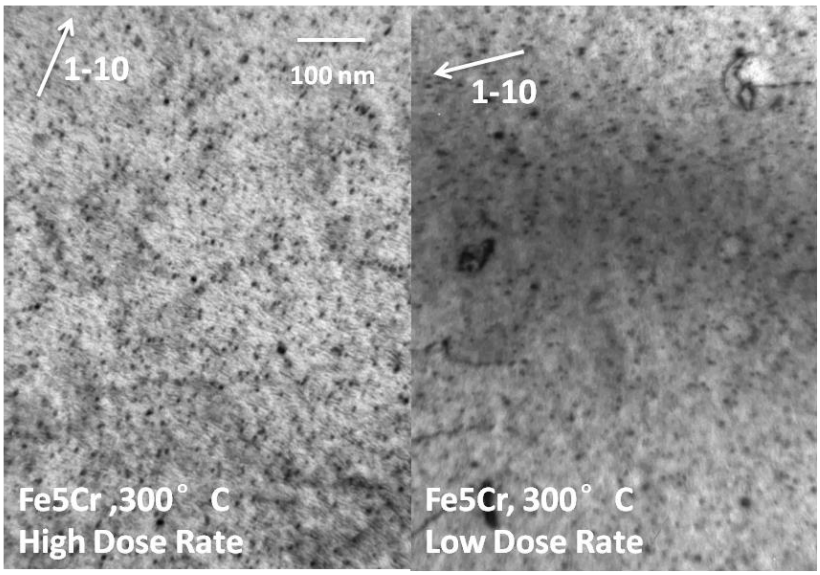

Figure 7.10 –TEM kinematical bright-field (KBF) micrograph for the Fe5%Cr alloy irradiated at 300°C with low dose rate and high dose rate. Both micrographs were taken near the [001] zone axis with g=1-10. Images provided by Mr S Xu of the University of Oxford.

A Burgers vector analysis of loops identified no significant difference between the HDR and LDR samples. All loops were found to be interstitial in nature. These results are shown in *table 7.6*.

Table 7.6 - Burgers vector analysis for Fe 5%Cr irradiated with both high and low dose rates at 300°C. Values given for both the fraction of loops in each sample and number of loops used in analysis. Data provided by Mr S Xu of the University of Oxford.

	HIGH DOSE RATE		LOW DOSE RATE	
	Fraction	**Number**	**Fraction**	**Number**
a<100>	66%	113	72%	103
1/2a<111>	34%	58	28%	40
Loop Density	$16.1x10^{21}/m^3$		$9.72x10^{21}/m^3$	

7.5.2 APT

Atom probe tomography was undertaken with assistance from Dr C Williams of the University of Oxford. Fe5%Cr specimens irradiated at 400˚C with the low and high dose rate were analysed by APT. *Table 7.7* shows the overall composition measurements for both types of alloy irradiated at 400˚C, including C and N interstitial impurities which may have been introduced during irradiation.

Table 7.7 - APT composition measurements for Fe5%Cr irradiated at 400˚C with the low and high dose rate.

Element	Low dose rate (at.%)	High dose rate (at.%)
Fe	94.74	94.7
Cr	5.26	5.31
N	0.045	0.02
C	0.02	0.02

Figure 7.11 shows the 3-D atom maps generated from the APT analysis of the alloys irradiated at 400˚C, with a corresponding proximity histogram showing the concentration of Cr from the core of an enriched region, outwards into the matrix. Areas of Cr enrichment were observed with Cr contents up to 15at. % identified in the alloy irradiated at 400˚C with the low dose rate (*figure 5a*). Areas of Cr enrichment were also observed in the alloy irradiated at 400˚C with a high dose rate, yet the size and number density of enriched Cr regions were significantly smaller than alloy irradiated with the lower dose rate. There are also traces of nitrogen in the regions of enrichment, yet there was no evidence of segregation of all other elements.

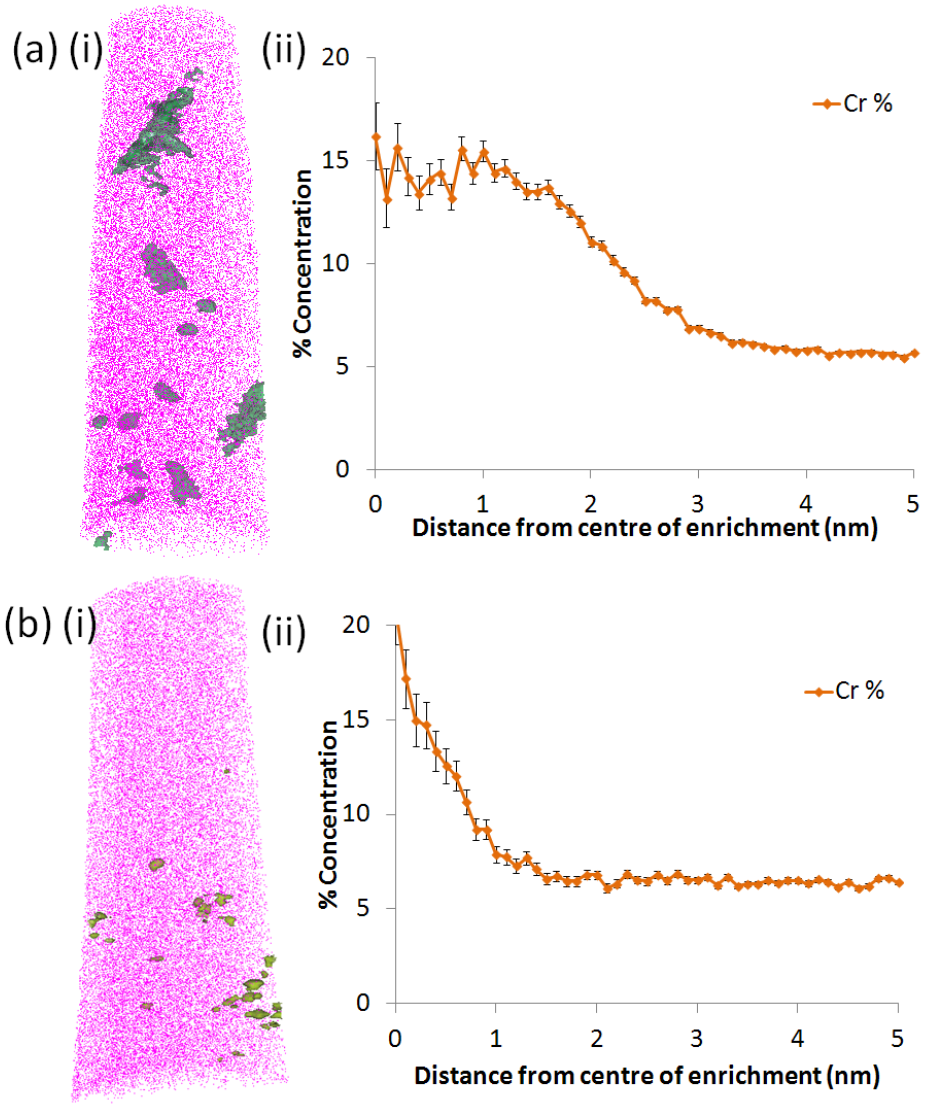

Figure 7.11 - APT data for the Fe5%Cr alloy irradiated at 400°C with the low dose rate (a) and high dose rate (b). Figure includes an atom map showing Fe atoms and a 0.5at.% CrN isoconcentration surface (i) and proximity histograms showing the variation in composition from the centre of enrichment outwards into the matrix (ii). Centre of enrichment is defined as the region of highest CrN concentration.

7.6 Discussion

This section explores the production of primary cascades and the evolution of damage in Fe and Fe-Cr alloys, the origin of irradiation hardening and the role of Cr in Fe-Cr alloys.

7.6.1 Cascade Damage in Fe and Fe-Cr Alloys

The elementary defects which exist after a cascade event and their corresponding mobility are the primary factors which determine the evolution of radiation damage in a crystalline material. Vacancies in iron have higher migration energy relative to that of interstitials, the increased mobility of the surviving fraction of SIAs may result in the formation and growth of SIA clusters producing the interstitial loops observed in *figure 7.10*.

TEM observations of iron and its alloys subjected to self-ion implantation have identified that the agglomeration of defects into visible clusters does not occur until doses at which cascade volumes begin to overlap, corresponding to ~0.01dpa [69]. At the relatively high dose rates corresponding to ion irradiation experiments, damage generated from a single cascade event remains in the form of point defects and clusters smaller than ~1nm (invisible in the TEM) until interaction with additional cascades. Assuming a cascade overlap dose of 0.01dpa [69] and using damage calculations produced by SRIM, the average duration between cascade overlap in the experiments reported here was ~17 seconds for the high dose rate and ~5.5 minutes for the low dose rate. Therefore the observed differences in hardening between both dose rates indicate that the effects of defect migration and

subsequent microstructural evolution occur over timescales greater than at least a few tens of seconds.

7.6.2 Defect Mobility and Damage Evolution

In these experiments, all materials were annealed producing large grains of approximately 150 to 300µm, with a low initial dislocation density. The low density of defect sinks and the relatively high dose rates used, suggest that all materials were likely to have been irradiated under a recombination-dominated regime (*section 2.4.1*). An increase in defect mobility with temperature is indicated in all irradiated materials as a decrease in hardening with increase in irradiation temperature, caused by a higher fraction of defect recombination. This is seen in *figure 7.12* which compares difference in irradiation hardening for all alloys with irradiation temperature. The 'dose rate effect', an increase in irradiation hardening in Fe-Cr alloys with decreasing dose rate, is reduced with increasing Cr content. It is likely that the pinning of defects by Cr [69, 89, 119, 141] reduces defect mobility and suppresses the differences in the evolution of damage between the two dose rates. Thus, the dose rate effect was not observed in Fe14%Cr irradiated at 300˚C, but was observed after irradiation at the higher temperature of 400˚C. This indicates an increase in defect mobility with temperature. The increase in defect mobility at higher temperatures may result in heightened rates of defects migrating to clusters/loops (reaction path (ii) as described in *section 2.4.1*) and enhance the Cr enrichment observed by APT in *section 7.5.2*. For the Fe14%Cr alloy irradiated at the low dose rate, the increased defect mobility at an irradiation temperature of 400°C resulted in slightly greater irradiation hardening than at 300°C. Interestingly, this was not observed in Fe14%Cr irradiated at 400˚C with the high dose rate and does not agree with the common trend that irradiation hardening increases as temperature decreases. The hardness in the un-irradiated region of the LDR Fe14%Cr sample

irradiated at 400˚C was also slightly higher than average (*figure 7.5*). The low dose rate implantations were conducted for a longer duration of ~10 hours (compared to <1hour for the high dose rate implantation), thus the higher hardness in the Fe14%Cr alloy may indicate the formation of alpha prime (α') in the un-irradiated region. This is discussed further in *section 7.6.5*.

At an irradiation temperature of 300˚C there was no effect of dose rate on hardening in pure Fe. Pure Fe irradiated at 400˚C exhibited no irradiation hardening, which suggests that the majority of radiation induced defects may annihilate by recombination at 400˚C in pure Fe. At an irradiation temperature of 500°C, negligible hardening was observed in all materials, which suggests that at this temperature the majority of defects annihilate by recombination during irradiation in the Fe-Cr alloys. Thus defects may overcome pinning by Cr and become mobile at this high irradiation temperature.

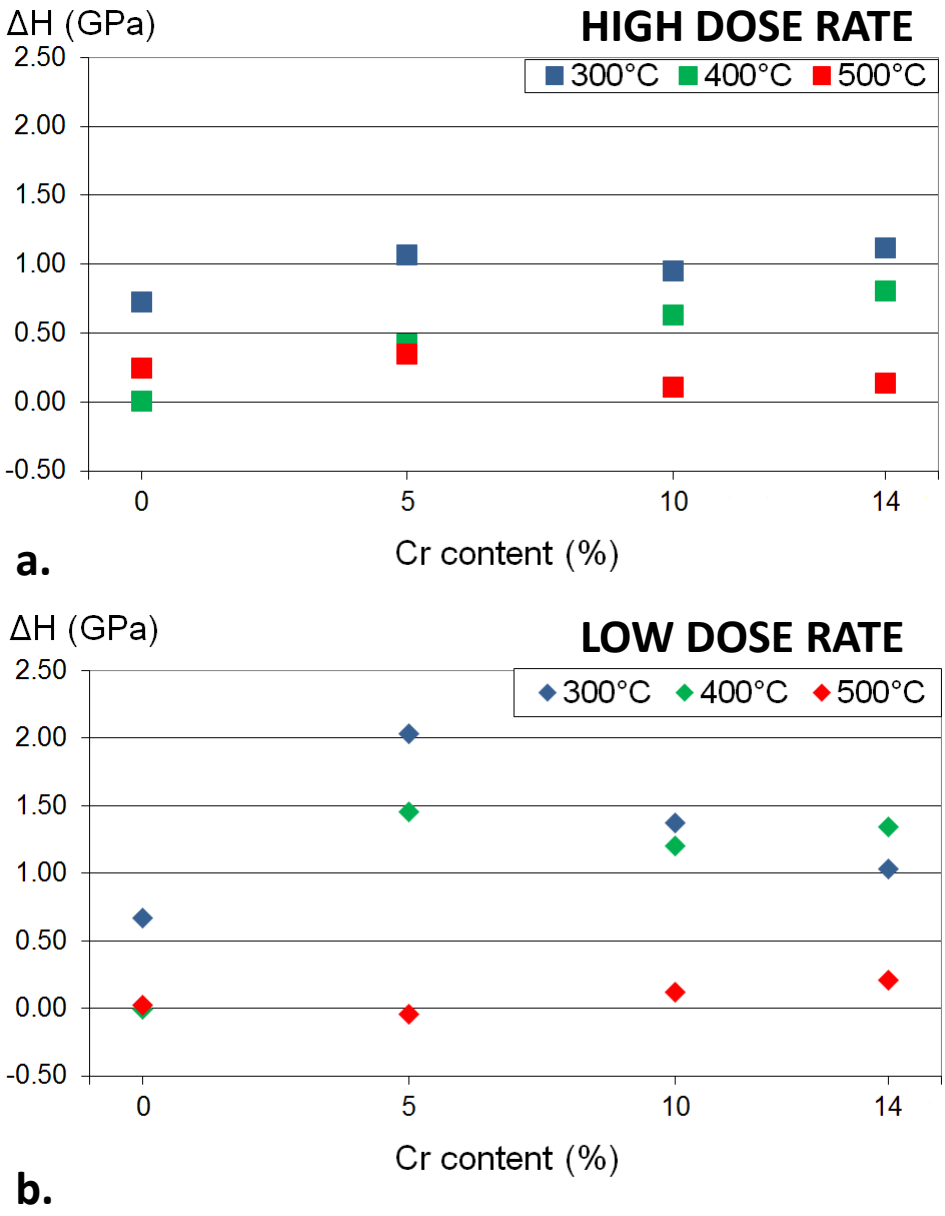

Figure 7.12 - Average irradiation hardening (ΔH) for materials subjected to high dose rate (a) and low dose rate (b) for irradiation temperatures of 300°C (blue), 400°C (orange) and 500°C (red). The reference value (ΔH=0) is that for un-irradiated material of the same composition.

7.6.3 Effects of Impurities

Similar investigations using nanoindentation to measure the mechanical properties of lower purity Fe-Cr alloys, have shown that irradiation hardening is saturated at a dose of approximately 1dpa in alloys with a Cr content greater than ~5% [91, 95]. Data reported by Hardie et al. [91] were produced using the same CSM indentation methods on the low purity alloys produced by CMCO as described in *section 5.1.1*. These data are plotted (with lines) on *figure 7.13* for a direct comparison with the UHP alloys. All un-irradiated materials exhibit the same hardness with Cr regardless of purity. With the exception of pure Fe, irradiation hardening is greater for all the UHP material. The saturation hardness of the high Cr, low purity alloys is similar to the hardness of UHP alloys irradiated to 0.6dpa. The decrease in further irradiation hardening from a dose of 0.6 to 6dpa with increasing Cr content may indicate that saturation doses for hardening decrease with an increasing Cr content as suggested by previous work [91, 95].

The impurities in the Fe-Cr alloys manufactured by CMCO have suppressed irradiation hardening, which may have been caused by a reduction in defect mobility (e.g. vacancy-carbon complexes have a higher migration energy compared to a single vacancy). Therefore, the additional hardening observed in the high purity alloys subjected to 6dpa is likely to be caused by the higher mobility of radiation induced defects in the absence of impurity atoms. The additional hardening may be linked to the Cr-enriched regions discovered by APT in *section 7.5.2*, thus impurities in pure Fe do not have the same influence on hardening. The increase in hardening in the low purity pure Fe may have been caused by additional phases (such as carbides) or Cottrell atmospheres surrounding dislocations and loops which develop during irradiation, however further work is required to understand this behaviour.

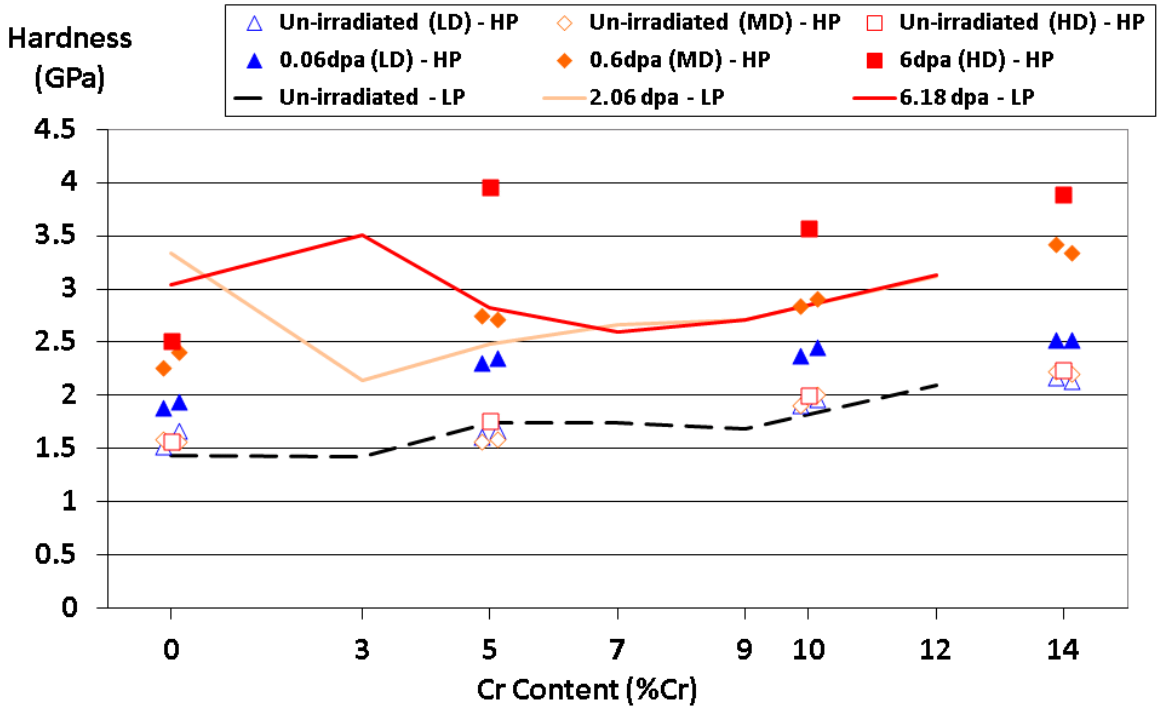

Figure 7.13 - Hardness data for ultra-high purity (UHP) alloys produced by EFDA (shown by data points), compared with hardness data for lower purity (LP) materials produced by CMCO [91] (shown by lines).

7.6.4 Irradiation Hardening

A previous study has identified that plastic deformation in Fe^{+} irradiated Fe-Cr alloys progresses via the annihilation of radiation induced defects by glissile dislocations, causing dislocation channelling shown in *figure 7.14* [91]. Channelling is associated with the annihilation of defects by reaction with glissile dislocations [73] and may result in decreased irradiation hardening. At irradiation temperatures of 300°C and 400°C, irradiation at a lower dose rate resulted in an increase in irradiation hardening of many Fe-Cr alloys. Despite this, the radiation damage microstructure observed in the TEM had a lower dislocation loop density in Fe 5%Cr irradiated with the low dose rate, compared to the same alloy irradiated with the high dose rate (*section 7.5.1*). Thus, the observed increase in irradiation hardening

at the lower dose rate is likely to be due to the evolution of defects more complex than simple dislocation loops, which strongly resist annihilation by glissile dislocations. The Cr-rich regions observed by APT in *section 7.5.2* were present at a high density in the Fe5%Cr alloy irradiated with the low dose rate and are likely to present such barriers to glissile dislocations. This is similar to the significant hardening associated with Cr-rich precipitate formation, known as "475°C embrittlement" in steels with >12%Cr [62, 63, 159]. The contribution of Cr-rich precipitates to hardening is also consistent with the lack of a dose rate dependence for hardening in pure Fe, where no Cr is present. In fact, the evolution of irradiation hardening in pure Fe with increasing dose indicates the hardening produced by dislocation loops alone. Thus, the small difference in hardening in pure Fe at 0.6dpa and 6dpa, suggest that the dislocation loop structure is near saturation at 0.6dpa. In comparison, the additional hardening in the Fe-Cr alloys at doses greater than 0.6dpa indicates that the presence of Cr has a significant effect.

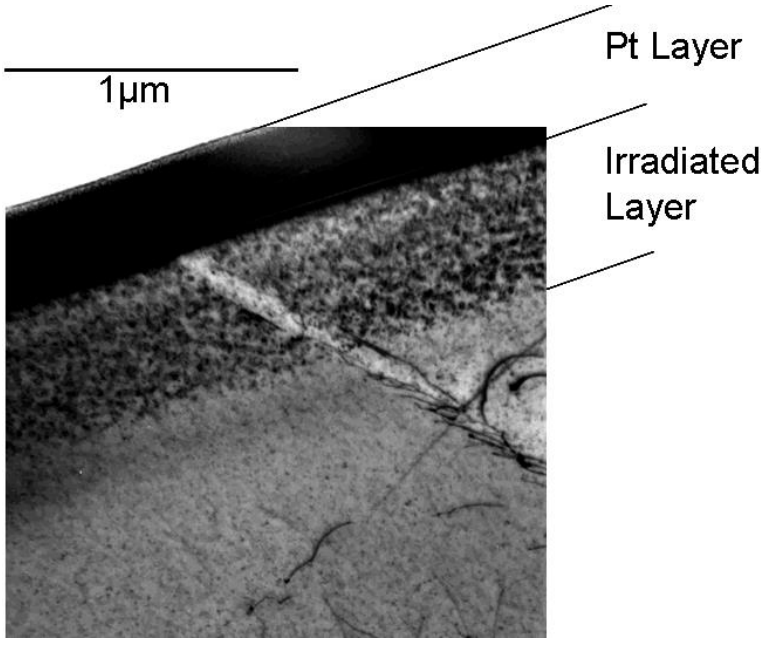

Figure 7.14 - Dislocation channelling in Fe 12%Cr irradiated to 6.18 dpa at 300°C. Figure from [91].

In a recombination - dominant system, a lower dose rate results in a smaller density of defects per unit volume per unit time and interaction between radiation induced defects will occur less frequently. This is likely to result in a smaller density of extended stable defect nucleation points (e.g. clusters and dislocation loops), with a larger number of defects migrating to each point. This is likely to have caused the observed reduction in loop density with decreasing dose rate in *figure 7.10* (also observed elsewhere [135]) and Cr segregation by heightened rates of radiation induced segregation (RIS). RIS may be suppressed by an increasing dose rate, due to a larger fraction of recombination or local clustering produced by the higher density of mobile defects. This compares well to the suppression of swelling and creep with increasing dose rate observed in austenitic stainless steels [133, 134].

The decrease of a dose rate effect with increasing Cr content may be the result of reduced mobility of radiation induced defects by pinning at Cr atoms in the lattice. Cr pinning may suppress RIS in alloys with increasing Cr content. This dependence on defect mobility is consistent with the onset of a hardening dependence on dose rate in Fe14%Cr as irradiation temperature is increased from 300°C to 400°C.

Analogous to the micro-cantilever results of Fe 6%Cr irradiated with neutrons (low dose rate) reported in Chapter 6, irradiation hardening was observable by micro-cantilever testing of the Fe5%Cr alloy irradiated to a dose of 0.6dpa with the low dose rate. It is likely that the same hardening mechanisms (Cr enrichment) are present of both materials, which result in the observation of irradiation hardening from micro-cantilevers with a depth of ~800nm. The absence of any significant irradiation hardening observed in micro-cantilever testing of all materials irradiated to a dose of 6dpa at the high dose rate, suggest that the response of

these beams was entirely dominated by size effects on mechanical behaviour. Therefore the hardening mechanisms in the 0.6dpa LDR Fe-Cr alloy are likely to be different from the 6dpa HDR Fe-Cr alloy, despite similar hardness measurements produced by nanoindentation.

7.6.5 Fe-Cr Phase Stability

The saturation of irradiation hardening in pure Fe is likely to occur when the growth and shrinkage of dislocation loops, become equal. Despite this, the ongoing migration of SIAs and vacancies to dislocation loops still occurs after the loop structure has saturated. Cr in irradiated Fe-Cr alloys can diffuse by both vacancy and interstitial mechanisms [238], thus the continuous diffusion of these point defects to loops during irradiation may provide the means for Cr enrichment. DFT calculations suggest that Cr has a high affinity with the interstitial dumbbell in the Fe-Cr system [238], thus the coalescence of interstitials into dislocation loops may result in regions of Cr enrichment at dislocation loops.

The enthalpy of mixing in Fe-Cr alloys changes sign from a negative to a positive at a composition of 8-10%Cr, although the exact composition where phase decomposition occurs (especially at low temperatures) is a subject of debate [157]. 475°C embrittlement in the absence of irradiation only occurs in alloys with >12%Cr. Thus, during irradiation at 300-400°C there is no known thermodynamic driving force for Cr segregation in the Fe5%Cr and Fe10%Cr alloys. Despite this, there have been a number of experimental observations of Cr clustering and enrichment at dislocation loops in Fe-Cr alloys with ≤10%Cr [175, 239-241]. The mechanisms which cause Cr enrichment in irradiated Fe-Cr alloys are not fully understood, however recent modelling has shown that Cr solubility in Fe changes under

hydrostatic pressure in the lattice [242]. This may provide the driving force for Cr migration to the stressed regions surrounding radiation induced defects such as dislocation loops within the lattice. Cr segregation to dislocation loops has been identified in an Fe 9%Cr alloy irradiated at 673K (400°C) to 1dpa, by the observation of moiré fringes within the loops in the TEM [243]. At present, it is not clear whether Cr enrichment is associated with dislocation loops from the experiments reported in this thesis and further work is required to understand this behaviour.

In the alloys with ≥10%Cr, alpha prime (α') precipitation not associated with dislocation loops may cause increased hardening [62]. The Fe14%Cr sample irradiated at 400°C at the low dose rate exhibited a slight increase in hardness in the un-irradiated region. This sample was held at 400°C for ~10 hours during the implantation, which may have initiated the early formation of α'; however further analysis is required to confirm this behaviour. The combination of RIS of Cr in alloys with a low Cr content, and α' formation in alloys with a high Cr content, may give rise to the observed minimum increase in ductile to brittle transition temperature in alloys containing approximately 9%Cr [31].

7.7 Summary

i. Nanoindentation hardness results increased slightly as a function of Cr content (0.05GPa/%Cr) and exhibited small dependence on crystal orientation. Hardness varied by ~0.1GPa across several grains.

ii. All samples exhibited irradiation hardening (ΔH) upon irradiation to doses as little as 0.06dpa. A negligible increase in irradiation hardening was observed in pure Fe at doses greater than 0.6dpa, which suggested that hardening was close to saturation at 0.6dpa. For the Fe-Cr alloys irradiation hardening was found to increase with dose up to 6dpa and was highest for Fe5%Cr with a dose of 6dpa at 2.19GPa or 224% (*figure 7.6*).

iii. A lower saturation dose and lower hardening is observed for alloys with high levels of impurities; this is likely to be a result of reduced defect mobility in the presence of impurity atoms.

iv. As shown in *figure 7.7*, significant differences in irradiation hardening were observed between the Fe-Cr alloys irradiated at a dose rate of $6x10^{-4}$dpa/s and those irradiated at $3x10^{-5}$dpa/s, whilst irradiation hardening in pure Fe was independent of dose rate.

    a. Irradiation hardening was greater in the alloys irradiated with the low dose rate. This difference in ΔH was largest for Fe5%Cr irradiated to 0.6dpa at 400°C and was ~0.4GPa (~26%) for the high dose rate and ~1.6GPa (~95%) for the low dose rate.

v. Data presented in *Figure 7.12* shows that irradiation hardening decreased with increasing irradiation temperature. This suggests that the recombination of defects increases with increasing irradiation temperature due to enhanced mobility.

vi. No irradiation hardening was observed in pure Fe irradiated at 400°C and Fe-Cr alloys irradiated at 500°C, suggesting complete recovery of cascade damage at these temperatures.

vii. In contrast to nanoindentation data, negligible hardening was observed from micro-cantilever testing in all materials irradiated to 6dpa at the high dose rate (*table 7.4*). This is likely to be caused by size effect mechanisms which have been shown to obscure irradiation hardening in beams with depths <1μm. Analogous to the neutron-irradiated (low dose rate) Fe6%Cr material reported in *chapter 6*, irradiation hardening was observed from cantilever tests of Fe5%Cr subject to 0.6dpa at the low dose rate.

viii. TEM results summarised in *section 7.5.1* identified that the material irradiated with the higher dose rate had a higher dislocation loop density despite the lower irradiation hardening measurements reported in *section 7.3.2*.

ix. APT data reported in *section 7.5.2* identified Cr-enriched regions in Fe5%Cr irradiated with the lower dose rate; radiation induced segregation of Cr is likely to produce the increased hardening observed in all Fe-Cr alloys irradiated with the lower dose rate. This observation is consistent with irradiation-hardening measurements of pure Fe, which were independent of dose rate.

8 DISCUSSION AND CONCLUSIONS

In the absence of a fusion relevant radiation environment, work conducted in this thesis addresses some of the current challenges in investigating materials for future fusion reactors such as DEMO (a demonstration nuclear fusion reactor). Accounting for the various challenges and limitations identified in the testing of micro-scale irradiated volumes in *chapter 5* and the simulation of fusion radiation conditions in *chapter 6*, the data presented in *chapter 7* provides some important insights into the possible effects of irradiation on steels. The results from these investigations have been discussed at the end of each chapter. The following text will provide a wide-ranging overview of the results and their future implications, in the context of materials research for fusion energy.

8.1 Simulation of Fusion Relevant Radiation Environment

A brief overview of available radiation sources is given in *section 2.2.2*. These include current fission reactors, charged particle accelerators and accelerator driven neutron sources. As discussed in *chapter 6*, these sources cover a wide range of dose rates, PKA energies and reaction cross-sections producing various levels of transmutation products. In addition to these physical differences, there are variations in the standard methods used for the characterisation of radiation conditions, resulting in inconsistent definitions of exposure and damage (*section 6.4.1*). These problems resulted in large differences in irradiation induced hardening between an Fe6%Cr alloy irradiated in a fission reactor and by ion implantation (*chapter 6*). The differences in damage calculations may be overcome by standardisation

across all irradiation methods, by defining a measurement of exposure to displacement inducing radiation damage, which is independent of particle energy and type as indicated by Stoller et al. [229]. However, the physical differences between radiation sources was confirmed in experiments reported in *chapter 7*, where the variation of dose rate alone produced significant differences in irradiation hardening in some Fe-Cr alloys.

The origin of the dose rate dependence of irradiation-induced hardening may be attributed to the presence of freely migrating defects produced within a single cascade event [232]. The rate of interaction between these point defects or small clusters is dependent on their mobility and is proportional to the square root of their density [129], thus increases in defect densities at the higher dose rates characteristic of ion implantation results in an increase in local clustering and recombination. This may suppress radiation-induced changes driven by the diffusion of point defects, such as swelling, creep and in the case of the Fe-Cr alloys described in *chapter 7*, radiation induced segregation. In addition, the density of freely migrating defects is controlled by the fraction of point defects and small clusters produced within a single cascade, which is dependent on cascade energy. Higher energy cascades produce an increased fraction of larger immobile clusters, which do not contribute to the radiation-induced changes associated with defect diffusion. Therefore the higher PKA energies produced by high energy fusion neutrons and heavy ion irradiation may result in decreased levels of swelling, creep and radiation-induced segregation at a given dose. Finally, differences in neutron energy spectra, particularly between fission and fusion neutrons, result in variations of transmutation reactions. For fusion neutrons, this may cause significant compositional changes and the production of transmutation He and H gases [50, 244], which contribute to radiation induced swelling, hardening and embrittlement. Strikingly, the levels of transmutation He produced in the Fe 6%Cr sample irradiated in the

ATR1 reactor were five times larger than that predicted for the fusion neutron energy spectrum. Due to the large volume of water causing neutron moderation, the energy spectrum for the ATR1 reactor exhibits a Maxwellian distribution of thermal neutrons with a peak at energies <1eV as shown in *figure 8.1*.

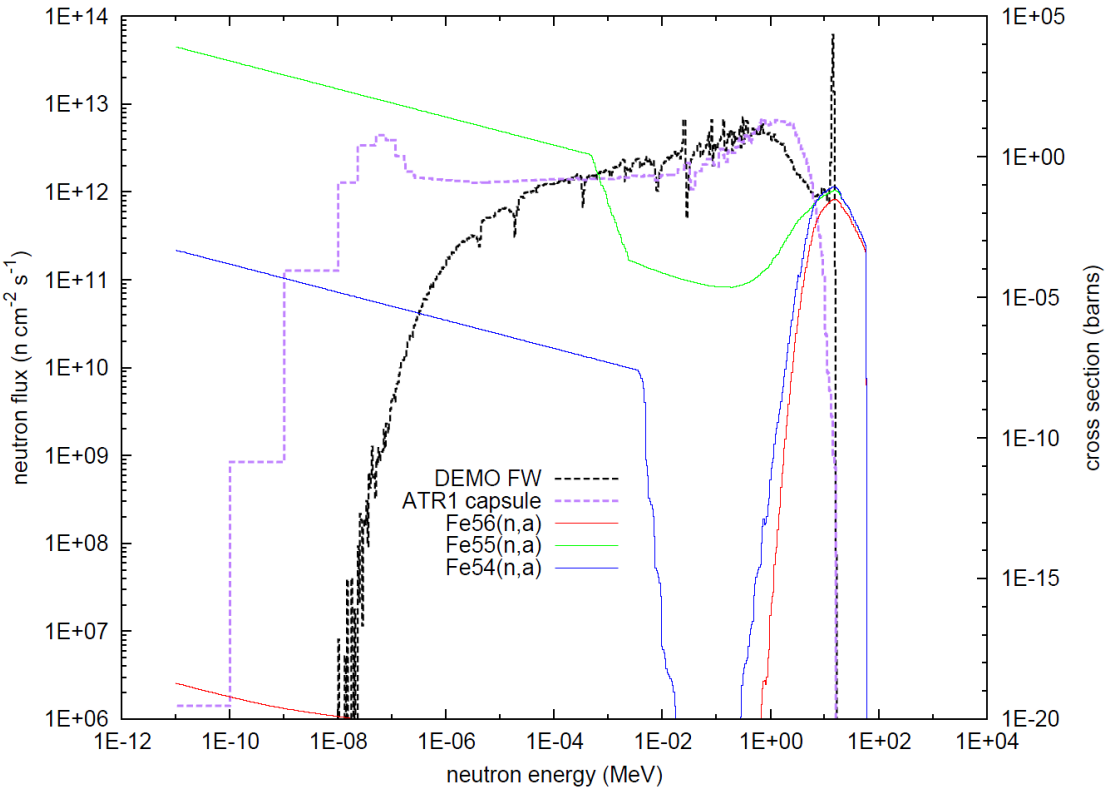

Figure 8.1 – Neutron energy spectra currently predicted for the DEMO first wall and the ATR1 reactor at INL. Solid lines show the neutron energy dependent reaction cross-sections for He production. Graph produced and supplied by Dr M Gilbert, CCFE.

As shown in *figure 8.1*, these thermal neutrons have a large cross-section for transmutation reaction with ^{55}Fe, producing large quantities of He in the Fe6%Cr. A fusion reactor has far less neutron moderators and the lower energy neutrons are non-existent in the currently predicted fusion neutron energy spectrum. Therefore, the production of transmutation He in

steels are either currently underestimated in a fusion reactor or are much greater in fission reactors. These spectral effects on inelastic reactions are concerning when considering the extensive efforts and expense allocated to the development of a 14MeV neutron source, an 'Early Neutron Source' (ENS), in the EU 'roadmap to the realisation of fusion energy' [245], which is primarily sought for producing fusion relevant levels of inelastic transmutation reactions. All ENS concepts are accelerator driven neutron sources with a peak at 14MeV, however a broad energy spectrum which may yield significantly different transmutation reactions in some materials. Furthermore, current recommendations from an EU Materials Assessment Group include the development of ENS concepts which can reach 30dpa by 2026 [246], however this requires accelerated dose rates and will not entirely reflect the radiation environment predicted for the first wall. Regardless of the development of a 14MeV neutron source, the sensitivity of materials to parameters such as dose rate observed in *chapter 7* necessitates the use of neutron irradiation for the qualification of fusion reactor materials.

8.2 Methods to investigate mechanical properties of irradiated materials

Before fusion power reaches a commercial scale, experimental materials research is limited to simulating radiation environments with sources such as fission reactors, charged particle implantation or accelerator driven neutron sources. In addition to limitations regarding the validity of simulation discussed in *section 8.1*, all of the above sources have common constraints in the volume of irradiated material. Furthermore, all proposed concepts for an 'Early Neutron Source' [246], a near-term smaller scale replacement of IFMIF, share similar limitations in sample volume. *Section 8.1* explains the necessity for the use of neutron irradiation, which will require an extensive research effort on active materials. Without

dedicated hot cell facilities, typical university restrictions on total activity also produce further limitations in the volume of active samples. Therefore, the investigation of mechanical properties of a wide range of irradiated materials required for fusion technology is limited to small specimen test technology, indentation methods and micro-mechanical testing for the foreseeable future.

8.2.1 Characteristics of nanoindentation and micromechanical testing

Of all methods available nanoindentation is the most commonly used and standardised technique, with procedures outlined in international standards such as ISO 14577 and ASTM E2546-07. Despite this, the comparison of nanoindentation methods and tip geometries in *chapter 5* identified a number of limitations. The selection of tip geometry requires a compromise between plastic zone size, the magnitude of pop-in events and the development of pile-up characteristic of each tip. The importance of these parameters is dependent on the volume of material available for investigation. For example, a Berkovich tip was used for the 800nm thick ion implanted layers investigated for this thesis; however larger volumes of material would facilitate testing with spherical tips. This would provide a test with a less complex stress state defined by Hertzian mechanics and allow for measurement of work hardening behaviour and size effects with the use of various tip radii.

The development of micro-mechanical testing has produced methods which benefit from simple uniaxial (pillars and tension specimens [98, 102]) and biaxial (cantilever specimens [221]) stress states and provide direct measurements of yield stress, work hardening and fracture properties [247]. Despite this, the data presented in *chapter 6* indicates that the

mechanical response of materials is increasingly dominated by size effects as the scale of test decreases. The inconsistent mechanical property data resulting from several nanoindentation and micro-cantilever methods shown in *figure 5.23*, illustrates the significant influence specimen size and geometry has on the measurement of mechanical properties on the micro scale.

The results reported in *section 6.3.2* identified that the influence of test size is dependent on the irradiation condition and the material composition, thus the dependence of size must be characterised for a given combination of material and irradiation conditions, if the extrapolation to macro-scale properties is to be attempted. An extrapolation using the data reported in *section 6.3.2* to Vickers hardness data was conducted with limited accuracy (*section 6.4.2*), which suggested that several different mechanisms controlling size effect were present across the specimen size range observed. Accurate extrapolation requires the understanding and superposition of several size effect mechanisms and data from a wider range of specimen size. With current technology and procedures, such analysis is highly consuming on time and resources.

The work in this thesis demonstrates that nanoindentation and micro-mechanical testing methods can produce mechanical property data which develops current understanding and knowledge regarding the behaviour of materials subject to irradiation. However, these methods produce unconventional data which is difficult to interpret and apply to the various failure mechanisms considered for reactor design. Continued development for the validation and standardisation of methods is required, to produce data which qualify in nuclear design codes such as SDC-IC and RCC-MR, and thus applicable to the development of future fusion reactors such as DEMO.

8.3 The Fe-Cr System

The data reported in this thesis (*figure 7.13*) and elsewhere [64, 80, 91, 95, 248] identify that irradiation hardening in Fe-Cr alloys exhibits a non-monotonic function of Cr content, with a minimum at approximately 9%Cr. As shown in *chapter 7*, this trend depends on dose, dose rate, temperature and impurity content. The increase in hardening with increasing Cr content in alloys >9%Cr is commonly attributed to the formation of α' by phase decomposition which may be enhanced by irradiation. The mechanisms producing the increase in hardening with decreasing Cr content in alloys <9%Cr are less certain, however APT results reported in *section 7.5.2* provide strong evidence for Cr segregation in irradiated Fe5%Cr. Cr enriched regions may be responsible for the increased irradiation hardening of Fe-Cr alloys subjected to lower dose rates by providing additional or strengthened obstacles to dislocation glide (as simulated by MD in refs.[72, 73]).

Cr is well within the solubility limit in alloys <9%Cr and the driving force for Cr segregation in low Cr alloys is anomalous to current understanding and is not predicted by modelling. This observation of radiation-induced segregation of a solute in alloys which are otherwise thermodynamically stable in the absence of radiation is not trivial. The mechanisms which result in segregation may be present and may have serious implications in other alloy systems. Due to higher PKA energies and dose rates, these mechanisms are likely to be obscured when using implantation methods and may be overlooked during the investigation and development of new alloys.

8.4 Conclusions

The work in this thesis investigates the simulation of fusion reactor conditions by ion implantation and the use of micron-scale mechanical testing methods for irradiated Fe and Fe-Cr alloys. Key results are summarised below:

(i) Irradiation hardening in Fe-Cr alloys increased with decreasing dose rate.
   a) Significant differences in irradiation hardening were identified between ion and neutron-irradiated Fe6%Cr.
   b) Irradiation hardening of pure Fe was not influenced by dose rate.
   c) Radiation-induced segregation of Cr was identified in Fe5%Cr after ion-irradiation at 400°C and a low dose rate ($3x10^{-5}$dpa/s).

(ii) Irradiation hardening is dependent on test specimen size.
   a) Irradiation hardening in ion-irradiated Fe6%Cr was completely obscured by size effects from micro-cantilevers with a depth <1µm.
   b) Irradiation hardening in neutron irradiated Fe6%Cr was observed for all micro-cantilever sizes (~0.5 to 7µm).
   c) For the ion-irradiated material, irradiation hardening measurements from micro-cantilevers with a depth ~800nm was only observed in Fe5%Cr irradiated with the lower dose rate.

Dose rate and size effects individually present significant challenges for mechanical property testing when using of ion implantation to simulate fusion reactor conditions. As discussed in *section 8.2*, the complex relationship between irradiation conditions (including dose rate),

material composition and test volume, suggest that the extrapolation to fusion reactor conditions and macro-scale properties is impossible. The use of neutron-irradiation produces larger volumes of irradiated material and can simulate fusion relevant dose rates if current fission reactors are used. The investigation of neutron irradiated material has significant practical constraints, such as the lack of available neutron sources for experimental research and the induced radioactivity of specimens. Due to safety implications and departmental restrictions on radioactive materials inventory, there are little resources available for the investigation of active neutron irradiated materials. For example, the ~6.5mg neutron-irradiated sample investigated in *chapter 6* was 90% of the Department of Materials activity limit. Thus, the value of a 14MeV neutron source will be limited without several dedicated research facilities for active materials such as the CAES in Idaho and the Materials Research Facility (MRF) currently in design phase at CCFE in Oxfordshire. These facilities are capable of investigating active materials from current and future neutron sources and will prove invaluable for the development of materials for future fusion devices such as DEMO.

9 REFERENCES

[1] A. Grübler, N. Nakićenović, Global energy perspectives to 2050 and beyond, World Energy Council, 1995.

[2] R. Toschi, Nuclear fusion, an energy source, Fusion Eng. Des. 36 (1997) 1-8.

[3] J.T. Houghton, L. Meira Filho, J.P. Bruce, H. Lee, B.A. Callander, E. Haites, Climate Change 1994: Radiative Forcing of Climate Change and an Evaluation of the IPCC 1992 IS92 Emission Scenarios, Cambridge University Press, 1995.

[4] G. Britain, Climate Change Act 2008: Elizabeth II, The Stationary Office, London (2008).

[5] Ofgem, Electricity Capacity Assessment 2012. 126/12 (2012) 1-93.

[6] J. Team, Fusion energy production from a deuterium-tritium plasma in the JET tokamak, Nucl Fusion. 32 (2002) 187.

[7] S. Cowley, Hot Fusion, Phys. World (2010) 46-51.

[8] D. Fasel, M.Q. Tran, Availability of lithium in the context of future D–T fusion reactors, Fusion Eng. Des. 75–79 (2005) 1163-1168.

[9] A. Gibson, JET Team, Deuterium-tritium plasmas in the Joint European Torus (JET): Behavior and implications, Phys. Plasmas. 5 (1998) 1839-1847.

[10] M. Dittmar, Nuclear energy: Status and future limitations, Energy. 37 (2012) 35-40.

[11] E.E. Bloom, S.J. Zinkle, F.W. Wiffen, Materials to deliver the promise of fusion power - progress and challenges, J. Nucl. Mater. 329-333 (2004) 12-19.

[12] D.J. Ward, S.L. Dudarev, Economically competitive fusion, Materials Today. 11 (2008) 46-53.

[13] P. Norajitra, L. Bühler, A. Buenaventura, E. Diegele, U. Fischer, S. Gordeey, E. Hutter, R. Kruessmann, S. Malang, A. Orden, G. Reimann, J. Reimann, G. Vieder, D. Ward, F. Wasastjerna, Conceptual design of the dual-coolant blanket within the framework of the EU power plant conceptual study (TW2-TRP-PPCS12): Final report, Wissenschaftliche Berichte FZKA ISSN 0947-8620. FZKA 6780 (2003).

[14] P. Schiller, Review of Materials Selection for Fusion Reactors, Journal of Nuclear Materials (The Netherlands). 206 (1993) 113-129.

[15] K. Ehrlich, R. Bullough, A. Kelly, J. Sheffield, P. Vandenplas, C. Windsor, E.A. Little, T.N. Todd, I. Cook, R.J. Hawryluk, The Development of Structural Materials for Fusion Reactors [and Discussion], Philosophical Transactions: Mathematical, Physical and Engineering Sciences. 357 (1999) 595-623.

[16] M.T. Robinson, Basic physics of radiation damage production, J. Nucl. Mater. 216 (1994) 1-28.

[17] T.D. Delarubia, M.W. Guinan, Progress in the Development of a Molecular-Dynamics Code for High-Energy Cascade Studies, J. Nucl. Mater. 174 (1990) 151-157.

[18] C.A. English, W.J. Phythian, A.J.E. Foreman, Considerations of Recoil Effects in Microstructural Evolution, J. Nucl. Mater. 174 (1990) 135-140.

[19] H.L. Heinisch, Computer-Simulation of High-Energy Displacement Cascades, Radiat. Eff. Defects Solids. 113 (1990) 53-73.

[20] G. Kinchin, R. Pease, The displacement of atoms in solids by radiation, Reports on Progress in Physics. 18 (1955) 1.

[21] G.S. Was, Fundamentals of radiation materials science: metals and alloys, Springer, 2007.

[22] M.J. Norgett, M.T. Robinson, I.M. Torrens, A proposed method of calculating displacement dose rates, Nucl. Eng. Des. 33 (1975) 50-54.

[23] J. Stiegler, L. Mansur, Radiation effects in structural materials, Annual review of materials science. 9 (1979) 405-454.

[24] L.K. Mansur, Theory and experimental background on dimensional changes in irradiated alloys, J. Nucl. Mater. 216 (1994) 97-123.

[25] E. Wakai, N. Hashimoto, Y. Miwa, J.P. Robertson, R.L. Klueh, K. Shiba, S. Jistukawa, Effect of helium production on swelling of F82H irradiated in HFIR, J. Nucl. Mater. 283-287 (2000) 799-805.

[26] P. Okamoto, H. Wiedersich, Segregation of alloying elements to free surfaces during irradiation, J. Nucl. Mater. 53 (1974) 336-345.

[27] P.R. Okamoto, L.E. Rehn, Radiation-induced segregation in binary and ternary alloys, J. Nucl. Mater. 83 (1979) 2-23.

[28] J.L. Boutard, A. Alamo, R. Lindau, M. Rieth, Fissile core and Tritium-Breeding Blanket: structural materials and their requirements, Comptes Rendus Physique. 9 (2008) 287-302.

[29] M. Gilbert, J. Sublet, Neutron-induced transmutation effects in W and W-alloys in a fusion environment, Nucl Fusion. 51 (2011) 043005.

[30] J. Henry, M.H. Mathon, P. Jung, Microstructural analysis of 9% Cr martensitic steels containing 0.5 at.% helium, J. Nucl. Mater. 318 (2003) 249-259.

[31] A. Kohyama, A. Hishinuma, D.S. Gelles, R.L. Klueh, W. Dietz, K. Ehrlich, Low-activation ferritic and martensitic steels for fusion application, J. Nucl. Mater. 233-237 (1996) 138-147.

[32] P. Fenici, A.J. Frias Rebelo, R.H. Jones, A. Kohyama, L.L. Snead, Current status of SiC/SiC composites R&D, J. Nucl. Mater. 258–263, Part 1 (1998) 215-225.

[33] E.T. Cheng, Concentration limits of natural elements in low activation fusion materials, J. Nucl. Mater. 258-263 (1998) 1767-1772.

[34] Y. Seki, T. Tabara, I. Aoki, S. Ueda, S. Nishio, R. Kurihara, Impact of low activation materials on fusion reactor design, Journal of Nuclear Materials (Netherlands).Vol.258-263. 258-263 (1998) 1791-1797.

[35] B.M. Oliver, H. Farrar IV, M.M. Bretscher, Tritium half-life measured by helium-3 growth, International Journal of Radiation Applications and Instrumentation.Part A.Applied Radiation and Isotopes. 38 (1987) 959-965.

[36] G.R. Hopkins, E.T. Cheng, Low activation fusion rationale, Nucl. Technol. /Fusion; (United States). 4:3 (1983) 528.

[37] E.E. Bloom, Low Activation Materials for Fusion Applications, Journal of Nuclear Materials. 122 (1984) 17-26.

[38] M. Okada, T. Noda, F. Abe, On the Development of Low-Activation Materials for Fusion Reactors, J.Nucl.Mater.Vol.169. (1989) 249-256.

[39] B.A. Loomis, D.L. Smith, Vanadium alloys for structural applications in fusion systems: a review of vanadium alloy mechanical and physical properties, J. Nucl. Mater. 191-194 (1992) 84-91.

[40] H. Matsui, K. Fukumoto, D.L. Smith, H.M. Chung, W. van Witzenburg, S.N. Votinov, Status of vanadium alloys for fusion reactors, J. Nucl. Mater. 233-237 (1996) 92-99.

[41] S.J. Zinkle, H. Matsui, D.L. Smith, A.F. Rowcliffe, E. van Osch, K. Abe, V.A. Kazakov, Research and development on vanadium alloys for fusion applications, J. Nucl. Mater. 258-263 (1998) 205-214.

[42] D.R. Diercks, B.A. Loomis, Alloying and impurity effects in vanadium-base alloys, J. Nucl. Mater. 141–143, Part 2 (1986) 1117-1124.

[43] M.L. Grossbeck, J.F. King, T. Nagasaka, S.A. David, Gas tungsten arc welding of vanadium alloys with impurity control, J. Nucl. Mater. 307-311 (2002) 1590-1594.

[44] G.R. Hopkins, R.J. Price, Fusion reactor design with ceramics, Fusion Eng. Des. 2 (1985) 111-143.

[45] P. Rocco, H.W. Scholz, M. Zucchetti, Silicon carbide and the new low activation requirements for a fusion reactor first wall, J. Nucl. Mater. 191-194 (1992) 1474-1479.

[46] P. Rocco, M. Zucchetti, Criteria for Defining Low Activation Materials in Fusion Reactor Applications, Fusion Engineering and Design (Switzerland). 15 (1992) 235-244.

[47] D.A. Petti, K.A. McCarthy, N.P. Taylor, C.B. Forty, R.A. Forrest, Re-evaluation of the use of low activation materials in waste management strategies for fusion, Fusion Eng. Des. 51 (2000) 435-444.

[48] D.L. Smith, M.C. Billone, S. Majumdar, R.F. Mattas, D.K. Sze, Materials integration issues for high performance fusion power systems, J. Nucl. Mater. 258-263 (1998) 65-73.

[49] A. Hasegawa, M. Saito, K. Abe, R.H. Jones, Helium implantation effects on mechanical properties of SiCf/SiC composites, J. Nucl. Mater. 253 (1998) 31-35.

[50] E.E. Bloom, The challenge of developing structural materials for fusion power systems, Journal of Nuclear Materials (Netherlands).Vol.258-263 (1998) Part A.

[51] E. Little, Void-swelling in irons and ferritic steels, I, mechanisms of swelling suppression. J, Nuclear Mater. 87 (1979) 11-24.

[52] E. Little, D. Stow, Void-swelling in irons and ferritic steels: II. An experimental survey of materials irradiated in a fast reactor, J. Nucl. Mater. 87 (1979) 25-39.

[53] D.S. Gelles, Microstructural examination of commercial ferritic alloys at 200 dpa, J. Nucl. Mater. 233-237 (1996) 293-298.

[54] Y. Katoh, M. Ando, A. Kohyama, Radiation and helium effects on microstructures, nano-indentation properties and deformation behavior in ferrous alloys, J. Nucl. Mater. 323 (2003) 251-262.

[55] F.A. Garner, M.B. Toloczko, B.H. Sencer, Comparison of swelling and irradiation creep behavior of fcc-austenitic and bcc-ferritic/martensitic alloys at high neutron exposure, J. Nucl. Mater. 276 (2000) 123-142.

[56] R.L. Klueh, M.A. Sokolov, K. Shiba, Y. Miwa, J.P. Robertson, Embrittlement of reduced-activation ferritic/martensitic steels irradiated in HFIR at 300°C and 400°C, J. Nucl. Mater. 283-287 (2000) 478-482.

[57] E. Lucon, R. Chaouadi, M. Decréton, Mechanical properties of the European reference RAFM steel (EUROFER97) before and after irradiation at 300 °C, J. Nucl. Mater. 329–333, Part B (2004) 1078-1082.

[58] B.v.d. Schaaf, C. Petersen, Y. De Carlan, J.W. Rensman, E. Gaganidze, X. Averty, High dose, up to 80 dpa, mechanical properties of Eurofer 97, J. Nucl. Mater. 386-388 (2009) 236-240.

[59] R.L. Klueh, J.M. Vitek, Elevated-temperature tensile properties of irradiated 214 Cr-1 Mo steel, J. Nucl. Mater. 126 (1984) 9-17.

[60] E. Gaganidze, H.C. Schneider, C. Petersen, J. Aktaa, A. Povstyanko, V. Prokhorov, R. Lindau, E. Materna-Morris, A. Möslang, E. Diegele, R. Lässer, R. Van der Schaaf, E. Lucon, Mechanical properties of reduced activation ferritic/martensitic steels after high dose neutron irradiation, Proc. of IAEA Fusion Energy Conference. Paper: FT/P2-1 (2008).

[61] R.L. Klueh, D.J. Alexander, Embrittlement of Cr□Mo steels after low fluence irradiation in HFIR, J. Nucl. Mater. 218 (1995) 151-160.

[62] P. Grobner, The 885° F (475° C) embrittlement of ferritic stainless steels , Metallurgical and Materials Transactions B. 4 (1973) 251-260.

[63] R.M. Fisher, E.J. Dulis, K.G. Carroll, Identification of the precipitate accompanying 885 F embrittlement in chromium steels, Trans. Metall. Soc. AIME. 197 (1953) 690.

[64] M. Matijasevic, A. Almazouzi, Effect of Cr on the mechanical properties and microstructure of Fe–Cr model alloys after n-irradiation, J. Nucl. Mater. 377 (2008) 147-154.

[65] G.R. Romanoski, L.L. Snead, R.L. Klueh, D.T. Hoelzer, Development of an oxide dispersion strengthened, reduced-activation steel for fusion energy, J. Nucl. Mater. 283-287 (2000) 642-646.

[66] L.V. Boccaccini, L. Giancarli, G. Janeschitz, S. Hermsmeyer, Y. Poitevin, A. Cardella, E. Diegele, Materials and design of the European DEMO blankets, J. Nucl. Mater. 329-333 (2004) 148-155.

[67] J.L. Boutard, M.J. Caturla, S.L. Dudarev, F. Willaime, Strategic Objectives for Fusion Materials Modeling and Experimental Validation 2010-2015. EFDA-D-2D4B78 (2009).

[68] S.J. Zinkle, Overview of the U.S. Fusion Materials Sciences Program, Fusion Science and Technology. 47 (2005) 821-828.

[69] Z. Yao, M. Hernández-Mayoral, M.L. Jenkins, M.A. Kirk, Heavy-ion irradiations of Fe and Fe–Cr model alloys Part 1: Damage evolution in thin-foils at lower doses, Phil Mag. 88 (2008) 2851.

[70] P. Hosemann, Y. Dai, E. Stergar, H. Leitner, E. Olivas, A. Nelson, S. Maloy, Large and Small Scale Materials Testing of HT-9 Irradiated in the STIP Irradiation Program, Exp Mech. 51 (2011) 1095-1102.

[71] D.J. Bacon, F. Gao, Y.N. Osetsky, Computer simulation of displacement cascades and the defects they generate in metals, Nuclear Instruments and Methods in Physics Research, Section B (Netherlands). 153 (1999) 87-98.

[72] D.J. Bacon, Y.N. Osetsky, Z. Rong, Computer simulation of reactions between an edge dislocation and glissile self-interstitial clusters in iron, Philos. Mag. 86 (2006) 3921-3936.

[73] D. Terentyev, Y.N. Osetsky, D.J. Bacon, Competing processes in reactions between an edge dislocation and dislocation loops in a body-centred cubic metal, Scr. Mater. 62 (2010) 697-700.

[74] C. Domain, C.S. Becquart, L. Malerba, Simulation of radiation damage in Fe alloys: an object kinetic Monte Carlo approach, J. Nucl. Mater. 335 (2004) 121-145.

[75] L. Gámez, B. Gámez, M.J. Caturla, D. Terentyev, J.M. Perlado, Object Kinetic Monte Carlo calculations of irradiated Fe–Cr dilute alloys: The effect of the interaction radius between substitutional Cr and self-interstitial Fe, Nuclear Instruments and Methods in Physics Research Section B: Beam Interactions with Materials and Atoms. 269 (2011) 1684-1688.

[76] P. Garin, M. Sugimoto, Status of IFMIF Design and R&D, Fusion Eng. Des. 83 (2008) 971-975.

[77] S. Ishino, Implications of fundamental radiation damage studies in the research and development of materials for a fusion reactor, J. Nucl. Mater. (Netherlands). 239 (1996) 24-33.

[78] F.A. Garner, H.L. Heinisch, R.L. Simons, F.M. Mann, Implications of neutron spectrum and flux differences on fission-fusion correlations at high neutron fluence, Radiation Effects and Defects in Solids. 113 (1990) 229-255.

[79] M. Kiritani, Radiation rate dependence of microstructure evolution, J. Nucl. Mater. 169 (1989) 89-94.

[80] C.D. Hardie, C.A. Williams, S. Xu, S.G. Roberts, Effects of irradiation temperature and dose rate on the mechanical properties of self-ion implanted Fe and Fe–Cr alloys, J. Nucl. Mater. 439 (2013) 33-40.

[81] M. Kiritani, T. Yoshiie, S. Kojima, Y. Satoh, K. Hamada, Fission--Fusion Correlation by Fission Reactor Irradiation With Improved Control, J. Nucl. Mater. 174 (1990) 327-351.

[82] P.J. Maziasz, R.L. Klueh, J.M. Vitek, Helium effects on void formation in 9Cr-1MoVNb and 12Cr-1MoVW irradiated in HFIR, J. Nucl. Mater. 141-143 (1986) 929-937.

[83] A.F. Rowcliffe, Neutron irradiation facilities for fission and fusion reactor materials studies, Nuclear Instruments and Methods in Physics Research Section A: Accelerators, Spectrometers, Detectors and Associated Equipment. 249 (1986) 26-33.

[84] E. Materna-Morris, A. Möslang, R. Rolli, H.-. Schneider, Effect of helium on tensile properties and microstructure in 9%Cr–WVTa–steel after neutron irradiation up to 15 dpa between 250 and 450 °C, J. Nucl. Mater. 386-388 (2009) 422-425.

[85] N. Hashimoto, R.L. Klueh, K. Shiba, Pros and cons of nickel- and boron-doping to study helium effects in ferritic/martensitic steels, J. Nucl. Mater. 307–311, Part 1 (2002) 222-228.

[86] C.M. Logan, D.W. Heikkinen, RTNS-II - a fusion materials research tool, Nuclear Instruments and Methods in Physics Research. 200 (1982) 105-111.

[87] R.S. Nelson, D.J. Mazey, J.A. Hudson, The use of ion accelerators to simulate fast neutron-induced voidage in metals, J. Nucl. Mater. 37 (1970) 1-12.

[88] M.R. Hayns, M.H. Wood, R. Bullough, A theoretical evaluation of dual-beam irradiation experiments, J. Nucl. Mater. 75 (1978) 241-250.

[89] M.L. Jenkins, Z. Yao, M. Hernández-Mayoral, M.A. Kirk, Dynamic observations of heavy-ion damage in Fe and Fe–Cr alloys, J. Nucl. Mater. 389 (2009) 197-202.

[90] G.E. Lucas, G.R. Odette, H. Matsui, A. Möslang, P. Spätig, J. Rensman, T. Yamamoto, The role of small specimen test technology in fusion materials development, J. Nucl. Mater. 367-370 (2007) 1549-1556.

[91] C.D. Hardie, S.G. Roberts, Nanoindentation of model Fe–Cr alloys with self-ion irradiation, J. Nucl. Mater. 433 (2013) 174-179.

[92] C.D. Hardie, S.G. Roberts, A.J. Bushby, Mechanical Behavior of Ion-Irradiated Fe-Cr Alloys Investigated by Spherical Indentation, Proc MRS. 1424 (2012).

[93] M. Ando, H. Tanigawa, S. Jitsukawa, T. Sawai, Y. Katoh, A. Kohyama, K. Nakamura, H. Takeuchi, Evaluation of hardening behaviour of ion irradiated reduced activation ferritic/martensitic steels by an ultra-micro-indentation technique, J. Nucl. Mater. 307-311 (2002) 260-265.

[94] F.M. Halliday, D.E.J. Armstrong, J.D. Murphy, S.G. Roberts, Nanoindentation and micromechanical testing of iron-chromium alloys implanted with iron ions, Advanced Materials Research. 59 (2008) 304-307.

[95] C. Heintze, F. Bergner, M. Hernández-Mayoral, Ion-irradiation-induced damage in Fe–Cr alloys characterized by nanoindentation, J. Nucl. Mater. 417 (2011) 980-983.

[96] C. Shin, H. Jin, M. Kim, Evaluation of the depth-dependent yield strength of a nanoindented ion-irradiated Fe–Cr model alloy by using a finite element modeling, J. Nucl. Mater. 392 (2009) 476-481.

[97] E.A. Marquis, J.M. Hyde, D.W. Saxey, S. Lozano-Perez, V. de Castro, D. Hudson, C.A. Williams, S. Humphry-Baker, G.D.W. Smith, Nuclear reactor materials at the atomic scale, Materials Today. 12 (2009) 30-37.

[98] D. Kiener, C. Motz, G. Dehm, R. Pippan, Overview on established and novel FIB based miniaturized mechanical testing using in-situ SEM, International journal of materials research. 100 (2009) 1074-1087.

[99] E.M. Grieveson, D.E.J. Armstrong, S. Xu, S.G. Roberts, Compression of self-ion implanted iron micropillars, J. Nucl. Mater. 430 (2012) 119-124.

[100] D. Kiener, P. Hosemann, S.A. Maloy, A.M. Minor, In situ nanocompression testing of irradiated copper, Nat Mater. 10 (2011) 608-613.

[101] J.R. Greer, J.T.M. De Hosson, Plasticity in small-sized metallic systems: Intrinsic versus extrinsic size effect, Progress in Materials Science. 56 (2011) 654-724.

[102] D. Kiener, C. Motz, G. Dehm, Micro-compression testing: A critical discussion of experimental constraints, Materials Science and Engineering: A. 505 (2009) 79-87.

[103] C. Abromeit, Aspects of simulation of neutron damage by ion irradiation, J. Nucl. Mater. 216 (1994) 78-96.

[104] L.K. Mansur, Correlation of neutron and heavy-ion damage: II. The predicted temperature shift if swelling with changes in radiation dose rate, J. Nucl. Mater. 78 (1978) 156-160.

[105] G.S. Was, Elastic Scattering, in: Fundamentals of Radiation Materials Science, Spinger, Springer-Verlag Berlin Heidelberg, 2007.

[106] G. Dearnaley, J.H. Freeman, R.S. Nelson, J. Stephen, Defects in Crystalline Solids, S. Amelinckx, R. Gevers, J. Nihoul (Eds.), Ion Implantation, 154 (1973).

[107] C. Erginsoy, G.H. Vineyard, A. Englert, Dynamics of Radiation Damage in a Body-Centered Cubic Lattice, Phys. Rev. 133 (1964) 595.

[108] F. Maury, M. Biget, P. Vajda, A. Lucasson, P. Lucasson, Anisotropy of Defect Creation in Electron-Irradiated Fe Crystals, Phys.Rev.B, Solid State. 14 (1976) 5303-5313.

[109] J.N. Lomer, M. Pepper, Anisotropy of Defect Production in Electron- Irradiated Iron, Phil Mag. 16 (1967) 1119-1127.

[110] N. Juslin, K. Nordlund, J. Wallenius, L. Malerba, Simulation of threshold displacement energies in FeCr, Nucl. Instrum. Meth. Phys. Res. B. Beam Interact. Mater. Atoms. 255 (2007) 75-77.

[111] J. Beeler, Displacement Spikes in Cubic Metals. Pt. 1. Alpha Iron, Copper, and Tungsten, Phys Rev. 150 (1966) 470-487.

[112] R.E. Stoller, G.R. Odette, B.D. Wirth, Primary damage formation in bcc iron, Journal of Nuclear Materials (Netherlands). 251 (1997) 49-60.

[113] E. Zarkadoula, S. Daraszewicz, D. Duffy, M. Seaton, I. Todorov, K. Nordlund, M. Dove, K. Trachenko, The nature of high-energy radiation damage in iron, Journal of Physics: Condensed Matter. 25 (2013) 125402.

[114] A.F. Calder, D.J. Bacon, A molecular dynamics study of displacement cascades in α-iron, J. Nucl. Mater. 207 (1993) 25-45.

[115] W.J. Phythian, R.E. Stoller, A.J.E. Foreman, A.F. Calder, D.J. Bacon, A comparison of displacement cascades in copper and iron by molecular dynamics and its application to microstructural evolution, J. Nucl. Mater. 223 (1995) 245-261.

[116] A.M. Stoneham, J.R. Matthews, I.J. Ford, Innovative materials for fusion power plant structures: separating functions, J Phys-Condens Mat. 16 (2004) S2597-S2621.

[117] R.E. Stoller, L.R. Greenwood, Subcascade formation in displacement cascade simulations: Implications for fusion reactor materials, J. Nucl. Mater. 271-272 (1999) 57-62.

[118] R. Dierckx, The importance of the PKA-energy spectrum for radiation damage simulation, J. Nucl. Mater. 144 (1987) 214-227.

[119] D.A. Terentyev, L. Malerba, R. Chakarova, K. Nordlund, P. Olsson, M. Rieth, J. Wallenius, Displacement cascades in Fe-Cr: A molecular dynamics study, J. Nucl. Mater. 349 (2006) 119-132.

[120] M. Tikhonchev, V. Svetukhin, A. Kadochkin, E. Gaganidze, MD simulation of atomic displacement cascades in Fe-10 at.%Cr binary alloy, J. Nucl. Mater. 395 (2009) 50-57.

[121] C. Bjorkas, K. Nordlund, L. Malerba, D. Terentyev, P. Olsson, Simulation of displacement cascades in Fe90Cr10 using a two band model potential, J. Nucl. Mater. 372 (2008) 312-317.

[122] J. Shim, H. Lee, B.D. Wirth, Molecular dynamics simulation of primary irradiation defect formation in Fe-10%Cr alloy, J. Nucl. Mater. 351 (2006) 56-64.

[123] www.hector.ac.uk. (2013).

[124] E. Zarkadoula, S. Daraszewicz, D.M. Duffy, M. Seaton, I.T. Todorov, K. Nordlund, M.T. Dove, K. Trachenko, Electronic effects in high-energy radiation damage in iron, arXiv preprint arXiv:1307.3385 (2013).

[125] N. Yoshida, A. Yamaguchi, T. Muroga, Y. Miyamoto, K. Kitajima, Characteristics of point defects and their clustering in pure ferritic steels, J. Nucl. Mater. 155-157 (1988) 1232-1236.

[126] R.E. Stoller, G.R. Odette, B.D. Wirth, Primary damage formation in bcc iron, J. Nucl. Mater. 251 (1997) 49-60.

[127] M.L. Jenkins, C.A. English, B.L. Eyre, Heavy-ion irradiation of α-iron, Phil Mag. 38 (1978) 97.

[128] S. Xu, TEM Characterisation of Heavy-Ion Irradiation Damage in Fe-Cr Alloys, DPhil Thesis (2009).

[129] S.L. Dudarev, M.R. Gilbert, K. Arakawa, H. Mori, Z. Yao, M.L. Jenkins, P.M. Derlet, Langevin model for real-time Brownian dynamics of interacting nanodefects in irradiated metals, Phys. Rev. B. 81 (2010) 224107-1-224107-15.

[130] T. Okita, T. Sato, N. Sekimura, F.A. Garner, L.R. Greenwood, The primary origin of dose rate effects on microstructural evolution of austenitic alloys during neutron irradiation, J. Nucl. Mater. 307-311 (2002) 322-326.

[131] S.L. Dudarev, J.-. Boutard, R. Lässer, M.J. Caturla, P.M. Derlet, M. Fivel, C.-. Fu, M.Y. Lavrentiev, L. Malerba, M. Mrovec, D. Nguyen-Manh, K. Nordlund, M. Perlado, R. Schäublin, H. Van Swygenhoven, D. Terentyev, J. Wallenius, D. Weygand, F. Willaime, The EU programme for modelling radiation effects in fusion reactor materials: An overview of recent advances and future goals, J. Nucl. Mater. 386–388 (2009) 1-7.

[132] C.H. Woo, B.N. Singh, The Concept of Production Bias and Its Possible Role in Defect Accumulation under Cascade Damage Conditions., Phys. Status Solidi B. 159 (1990) 609-616.

[133] J.L. Seran, J.M. Dupouy, Swelling of solution annealed 316 cladding in Rapsodie and Phenix, in: J.S.P. Brager (Ed.), Effect of Radiation on Materials: 11th International Symposium, ASTM, Baltimore, MD., 1982.

[134] G.W. Lewthwaite, D. Mosedale, The effects of temperature and dose-rate variations on the creep of austenitic stainless steels in the dounreay fast reactor, J. Nucl. Mater. 90 (1980) 205-215.

[135] T. Muroga, H. Watanabe, N. Yoshida, Correlation of fast neutron, fusion neutron and electron irradiations based on the dislocation loop density, J. Nucl. Mater. 174 (1990) 282-288.

[136] T. Okita, T. Sato, N. Sekimura, T. Iwai, F.A. Garner, The synergistic influence of temperature and displacement rate on microstructural evolution of ion-irradiated Fe–15Cr–16Ni model austenitic alloy, J. Nucl. Mater. 367-370 (2007) 930-934.

[137] L. Boulanger, Y. Serruys, Dislocation loops in Eurofer and a Fe–Cr alloy irradiated by ions at 350 and 550 °C at 3 dpa: Effect of dose rate, J. Nucl. Mater. 386–388 (2009) 441-444.

[138] L.K. Mansur, Theory and experimental background on dimensional changes in irradiated alloys, J. Nucl. Mater. 216 (1994) 97-123.

[139] M. Horiki, T. Yoshiie, M. Iseki, M. Kiritani, Invisible and visible point defect clusters in neutron irradiated iron, J. Nucl. Mater. 271-272 (1999) 256-260.

[140] Z. Yao, M.L. Jenkins, M. Hernández-Mayoral, M.A. Kirk, The temperature dependence of heavy-ion damage in iron: A microstructural transition at elevated temperatures, Phil Mag (2010) 1.

[141] P. Olsson, C. Domain, J. Wallenius, Ab initio study of Cr interactions with point defects in bcc Fe, Phys. Rev. B. 75 (2007) 1-12.

[142] Y.N. Osetsky, D.J. Bacon, A. Serra, B.N. Singh, S.I. Golubov, Stability and mobility of defect clusters and dislocation loops in metals, J. Nucl. Mater. 276 (2000) 65-77.

[143] S.L. Dudarev, R. Bullough, P.M. Derlet, Effect of the alpha-gamma phase transition on the stability of dislocation loops in bcc iron., Phys. Rev. Lett. 100 (2008).

[144] S.P. Fitzgerald, S.L. Dudarev, Dislocation pile-ups in Fe at high temperature, Proceedings of the Royal Society A: Mathematical, Physical and Engineering Science. 464 (2008) 2549-2559.

[145] I.M. Robertson, M.L. Jenkins, C.A. English, Low-dose neutron-irradiation damage in α-iron, J. Nucl. Mater. 108–109 (1982) 209-221.

[146] K. Arakawa, M. Hatanaka, E. Kuramoto, K. Ono, H. Mori, Changes in the Burgers vector of perfect dislocation loops without contact with the external dislocations, Phys. Rev. Lett. 96 (2006) 125506.

[147] J. Marian, B.D. Wirth, J.M. Perlado, Mechanism of formation and growth of< 100> interstitial loops in ferritic materials, Phys. Rev. Lett. 88 (2002) 255507.

[148] B. Eyre, R. Bullough, On the formation of interstitial loops in bcc metals, Philosophical Magazine. 12 (1965) 31-39.

[149] D. Terentyev, L. Malerba, P. Klaver, P. Olsson, Formation of stable sessile interstitial complexes in reactions between glissile dislocation loops in bcc Fe, J. Nucl. Mater. 382 (2008) 126-133.

[150] M.A. Kirk, I.M. Robertson, M.L. Jenkins, C.A. English, T.J. Black, J.S. Vetrano, The collapse of defect cascades to dislocation loops, J. Nucl. Mater. 149 (1987) 21-28.

[151] E.A. Little, D.A. Stow, Effects of chromium additions on irradiation-induced void swelling in α-iron, Metal Science. 14 (1980) 89.

[152] D.S. Gelles, Microstructural examination of neutron-irradiated simple ferritic alloys, J. Nucl. Mater. 108-109 (1982) 515-526.

[153] T. Tanaka, K. Oka, S. Ohnuki, S. Yamashita, T. Suda, S. Watanabe, E. Wakai, Synergistic effect of helium and hydrogen for defect evolution under multi-ion irradiation of Fe–Cr ferritic alloys, J. Nucl. Mater. 329-333 (2004) 294-298.

[154] S.J. Zinkle, L.E. Seitzman, W.G. Wolfer, Energy calculations for pure metals, Phil Mag. 55 (1987) 111.

[155] Y. Dai, Y. Foucher, M.R. James, B.M. Oliver, Neutronics calculation, dosimetry analysis and gas measurements of the first SINQ target irradiation experiment, STIP-I, J. Nucl. Mater. 318 (2003) 167-175.

[156] R. Schäublin, J. Henry, Y. Dai, Helium and point defect accumulation: (i) microstructure and mechanical behaviour, Comptes Rendus Physique. 9 (2008) 389-400.

[157] L. Malerba, A. Caro, J. Wallenius, Multiscale modelling of radiation damage and phase transformations: The challenge of FeCr alloys, J. Nucl. Mater. 382 (2008) 112-125.

[158] M.J. Marcinkowski, R.M. Fisher, A. Szirmae, Effect of 500 C Aging on the Deformation Behavior of an Iron-Chromium Alloy, Trans. Metall. Soc. AIME. 230 (1964) 676.

[159] T. Nichol, A. Datta, G. Aggen, Embrittlement of ferritic stainless steels, Metallurgical and Materials Transactions A. 11 (1980) 573.

[160] T. Muroga, M. Gasparotto, S.J. Zinkle, Overview of materials research for fusion reactors, Fusion Eng. Des. 61-62 (2002) 13-25.

[161] R. Lindau, A. Möslang, M. Rieth, M. Klimiankou, E. Materna-Morris, A. Alamo, A.-.F. Tavassoli, C. Cayron, A.-. Lancha, P. Fernandez, N. Baluc, R. Schäublin, E. Diegele, G. Filacchioni, J.W. Rensman, B.v.d. Schaaf, E. Lucon, W. Dietz, Present development status of

EUROFER and ODS-EUROFER for application in blanket concepts, Fusion Eng. Des. 75-79 (2005) 989-996.

[162] J. Yu, Q. Huang, F. Wan, Research and development on the China low activation martensitic steel (CLAM), J. Nucl. Mater. 367-370 (2007) 97-101.

[163] N. Baluc, D.S. Gelles, S. Jitsukawa, A. Kimura, R.L. Klueh, G.R. Odette, B. van der Schaaf, J. Yu, Status of reduced activation ferritic/martensitic steel development, J. Nucl. Mater. 367-370 (2007) 33-41.

[164] Y. Katoh, M. Ando, A. Kohyama, Radiation and helium effects on microstructures, nano-indentation properties and deformation behavior in ferrous alloys, J. Nucl. Mater. 323 (2003) 251-262.

[165] Y. Katoh, H. Tanigawa, T. Muroga, T. Iwai, A. Kohyama, The influence of helium co-implantation on ion-induced hardening of low activation ferritic steel evaluated by micro-indentation technique, J. Nucl. Mater. 271-272 (1999) 115-119.

[166] H. Ogiwara, A. Kohyama, H. Tanigawa, H. Sakasegawa, Helium effects on mechanical properties and microstructure of high fluence ion-irradiated RAFM steel, J. Nucl. Mater. 367-370 (2007) 428-433.

[167] F.W. Kunz, A.N. Holden, The effect of short-time moderate flux neutron irradiations on the mechanical properties of some metals, Acta Metallurgica. 2 (1954) 816-822.

[168] B.N. Singh, A. Horsewell, P. Toft, Effects of neutron irradiation on microstructure and mechanical properties of pure iron, J. Nucl. Mater. 271-272 (1999) 97-101.

[169] K. Suganuma, H. Kayano, S. Yajima, Mechanical properties changes of Fe-Cr alloys by fast neutron irradiation, J. Nucl. Mater. 105 (1982) 23-35.

[170] K. Suganuma, H. Kayano, Irradiation hardening of Fe-Cr alloys, J. Nucl. Mater. 118 (1983) 234-241.

[171] M.I. Luppo, C. Bailat, R. Schäublin, M. Victoria, Tensile properties and microstructure of 590 MeV proton-irradiated pure Fe and a Fe–Cr alloy, J. Nucl. Mater. 283-287 (2000) 483-487.

[172] S.I. Porollo, A.M. Dvoriashin, A.N. Vorobyev, Y.V. Konobeev, The microstructure and tensile properties of Fe–Cr alloys after neutron irradiation at 400°C to 5.5–7.1 dpa, J. Nucl. Mater. 256 (1998) 247-253.

[173] P.M. Rice, R.E. Stoller, Hardening Behavior of Ferritic Alloys at High Doses and After Thermal Aging, ORNL Technical Report. ORNL/TM-199/297 (2004).

[174] M.L. Hamilton, D.S. Gelles, Post-irradiation strength and deformation of ferritic Fe–Cr binary alloys, in: R.E. Stoller, A.S. Kumar, D.S. Gelles (Eds.), Fifteenth International Symposium on Effects of Radiation on Materials, ASTM STP 1125, ASTM, Philadelphia, 1993.

[175] C. Heintze, A. Ulbricht, F. Bergner, H. Eckerlebe, SANS investigation of neutron-irradiated Fe-Cr alloys, J. Phys. : Conf. Ser. 247 (2010).

[176] K. Farrell, T.S. Byun, Tensile properties of ferritic/martensitic steels irradiated in HFIR, and comparison with spallation irradiation data, J. Nucl. Mater. 318 (2003) 274-282.

[177] F.H. Hammad, M.K. Matta, K.E. Mohammed, Eeffect of fast-neutron irradiation on mechanical properties of iron and some iron binary solid solutions, J. Nucl. Mater. 108-109 (1982) 428-435.

[178] M.L. Hamilton, D.S. Gelles, P.L. Gardner, Post-irradiation deformation behavior in ferritic Fe–Cr alloys, in: A.S. Kumar, D.S. Gelles, R. Nanstad, E.A. Little (Eds.), Sixteenth International Symposium on Effects of Radiation on Materials, ASTM STP 1175, ASTM, Philadelphia, 1993.

[179] Z. Tong, Y. Dai, The microstructure and tensile properties of ferritic/martensitic steels T91, Eurofer-97 and F82H irradiated up to 20 dpa in STIP-III, J. Nucl. Mater. 398 (2010) 43-48.

[180] D.S. Gelles, R.E. Schäublin, Post-irradiation deformation in a Fe-9%Cr alloy, Mater. Sci. Eng. , A. 309-310 (2001) 82-86.

[181] J.F. Ziegler, M.D. Ziegler, J.P. Biersack, SRIM – The stopping and range of ions in matter (2010), Nucl. Instrum. Methods Phys. Res. B. Beam Interact. Mater. Atoms. 268 (2010) 1818-1823.

[182] W.C. ASTM International, Standard Practice for Measurement of Mechanical Properties During Charged-Particle Irradiation. E821 - 96(2009).

[183] H. Maeda, Accurate Bond Length Determination by EXAFS Method, J PHYS SOC JPN. 56 (1987) 2777-2787.

[184] V. Ashworth, W.A. Grant, R.M.P. Procter (Eds.), Ion implantation into metals: proceedings of the 3rd International Conference on the Modification of Surface Properties of Metals by Ion Implantation held at UMIST, Manchester, UK, 23-26 June 1981, 1st ed. ed., Pergamon Press, 1982, Oxford, Oxfordshire, 1982.

[185] M.R. VanLandingham, Review of Instrumented Indentation, J RES NATL INST STAN. 108 (2003) 249-265.

[186] W.C. Oliver, G.M. Pharr, An improved technique for determining hardness and elastic modulus using load and displacement sensing indentation experiments., J MATER RES. 7 (1992) 1564-1583.

[187] M.F. Doerner, W.D. Nix, A method for interpreting the data from depth-sensing indentation instruments. Journal of Materials Research, 1 , pp 601-609 doi:10.1557/JMR.1986.0601, JMR. 1 (1986) 601-609.

[188] N.A. Stillwell, D. Tabor, Elastic Recovery of Conical Indentations, Proc. Phys. Soc. London. 78 (1961) 169-179.

[189] I.N. Sneddon, The relation between load and penetration in the axisymmetric boussinesq problem for a punch of arbitrary profile, Int. J. Eng. Sci. 3 (1965) 47-57.

[190] T.T. Zhu, A.J. Bushby, D.J. Dunstan, Size effect in the initiation of plasticity for ceramics in nanoindentation, J. Mech. Phys. Solids. 56 (2008) 1170-1185.

[191] K.L. Johnson, Contact mechanics, Cambridge university press, 1987.

[192] J. Field, M. Swain, A simple predictive model for spherical indentation, Journal of Materials Research(USA). 8 (1993) 297-306.

[193] D. Di Maio, S.G. Roberts, Measuring fracture toughness of coatings using focused ion beam machined microbeams, JMR. 20 (2005) 299-302.

[194] G. Piazzesi, Photogrammetry with the scanning electron micrscope, J. Phys. E: Sci. Instrum. 6 (1973) 392-396.

[195] R.M. Langford, C. Clinton, In situ lift-out using a FIB-SEM system, Micron. 35 (2004) 607-611.

[196] D.W. Saxey, J.M. Cairney, D. McGrouther, T. Honma, S.P. Ringer, Atom probe specimen fabrication methods using a dual FIB/SEM, Ultramicroscopy. 107 (2007) 756-760.

[197] J.M. Gere, Mechanics of Materials, 5th SI Ed. ed., Nelson Thornes Ltd, Cheltenham, UK, 2002.

[198] M.A. Puso, J. Solberg, A stabilized nodally integrated tetrahedral, Int J Numer Methods Eng. 67 (2006) 841-867.

[199] D.E.J. Armstrong, Measuring Elastic, Plastic and Fracture Properties using Micro-Cantilever Testing, DPhil thesis (2009).

[200] ASTM Standard ASTM E521 - 96(2009), "Standard Practice for Neutron Radiation Damage Simulation by Charged-Particle Irradiation", ASTM International, West Conshohocken, PA, (2009).

[201] Aglient Technologies, http://cp.literature.agilent.com/litweb/pdf/5990-4907EN.pdf. 2013 (2009).

[202] Hysitron Corporation, http://www.hysitron.com/LinkClick.aspx?fileticket=bcq5arPC_GE%3d&tabid=429. 2013 (2010).

[203] A. Bolshakov, W.C. Oliver, G.M. Pharr, Influences of stress on the measurement of mechanical properties using nanoindentation: Part II. Finite element simulations, J. Mater. Res. 11 (1996) 760-768.

[204] C.L. Woodcock, D.F. Bahr, Plastic zone evolution around small scale indentations, Scr. Mater. 43 (2000) 783-788.

[205] N. Zaafarani, D. Raabe, R.N. Singh, F. Roters, S. Zaefferer, Three-dimensional investigation of the texture and microstructure below a nanoindent in a Cu single crystal using 3D EBSD and crystal plasticity finite element simulations, Acta Materialia. 54 (2006) 1863-1876.

[206] M. Rester, C. Motz, R. Pippan, The deformation-induced zone below large and shallow nanoindentations: A comparative study using EBSD and TEM, Phil Mag Lett. 88 (2008) 879-887.

[207] G.M. Pharr, W.C. Oliver, Measurement of thin film mechanical properties using nanoindentation., MRS Bulletin. 17 (1992) 28-33.

[208] H. Buckle, Use of the Hardness Test to Determine Other Material Properties, in: J.H. Westbrook, H. Conrad (Eds.), The Science of Hardeness Testing and Its Research Applications, American Society for Metals, Metals Park, Ohio. (1971) 453-494.

[209] A.C. Fischer-Cripps, Factors Affecting Nanoindentation Test Data, in: Nanoindentation, Springer Science, New York. (2011) 77-103.

[210] K.W. McElhaney, J.J. Vlassak, W.D. Nix, Determination of indenter tip geometry and indentation contact area for depth sensing indentation experiments, J. Mater. Res. 13 (1997) 1300-1306.

[211] T.Y. Tsui, G.M. Pharr, Substrate effects on nanoindentation mechanical property measurement of soft films on hard substrates, J. Mater. Res. 14 (1998) 292-301.

[212] A.J. Bushby, S.G. Roberts, C.D. Hardie, Nanoindentation investigation of ion-irradiated Fe–Cr alloys using spherical indenters, Journal of Materials Research. 27 (2012) 85-90.

[213] X. Hou, A. Bushby, N. Jennett, Direct measurement of surface shape for validation of indentation deformation and plasticity length-scale effects: a comparison of methods, Measurement Science and Technology. 21 (2010) 115105.

[214] K.O. Kese, Z.C. Li, B. Bergman, Method to account for true contact area in soda-lime glass during nanoindentation with the Berkovich tip, Materials Science and Engineering: A. 404 (2005) 1-8.

[215] D. Lorenz, A. Zeckzer, U. Hilpert, P. Grau, Pop-in effect as homogeneous nucleation of dislocations during nanoindentation, Phys. Rev. B. 67 (2003) 172101-1-172101-4.

[216] G.M. Pharr, J.H. Strader, W. Oliver, Critical issues in making small-depth mechanical property measurements by nanoindentation with continuous stiffness measurement, J. Mater. Res. 24 (2009) 653-666.

[217] W.C. Oliver, G.M. Pharr, Measurement of hardness and elastic modulus by instrumented indentation: Advances in understanding and refinements to methodology., JMR. 19 (2004) 3-20.

[218] W.D. Nix, H. Gao, Indentation size effects in crystalline materials: A law for strain gradient plasticity, J. Mech. Phys. Solids. 46 (1998) 411-425.

[219] J. Gong, A.J. Wilkinson, Anisotropy in the plastic flow properties of single-crystal α titanium determined from micro-cantilever beams, Acta Materialia. 57 (2009) 5693-5705.

[220] E. Van Der Giessen, A. Needleman, Discrete dislocation plasticity: a simple planar model, Modelling Simul. Mater. Sci. Eng. 3 (1995) 689-735.

[221] C. Motz, T. Schöberl, R. Pippan, Mechanical properties of micro-sized copper bending beams machined by the focused ion beam technique, Acta Materialia. 53 (2005) 4269-4279.

[222] J.T. Busby, M.C. Hash, G.S. Was, The relationship between hardness and yield stress in irradiated austenitic and ferritic steels, J. Nucl. Mater. 336 (2005) 267-278.

[223] B. Girault, A.S. Schneider, C.P. Frick, E. Arzt, Strength Effects in Micropillars of a Dispersion Strengthened Superalloy, Adv. Eng. Mater. 12 (2010) 385-388.

[224] D.S. Gelles, Microstructural examination of neutron-irradiated simple ferritic alloys, J. Nucl. Mater. 108–109 (1982) 515-526.

[225] G.E. Dieter, Mechanical metallurgy, McGraw-Hill New York, 1976.

[226] G. Speich, A. Schwoeble, W. Leslie, Elastic constants of binary iron-base alloys, Metallurgical Transactions. 3 (1972) 2031-2037.

[227] R. MacFarlane, D. Muir, The NJOY nuclear data processing system: Version 91. 1 (1994).

[228] J. Sublet, J. Eastwood, J. Morgan, The FISPACT-II User Manual CCFE-R(11)11 Issue 3, Tech. Rep. CCFE (2012).

[229] R. Stoller, M. Toloczko, G. Was, A. Certain, S. Dwaraknath, F. Garner, On the Use of SRIM for Computing Radiation Damage Exposure, Nuclear Instruments and Methods in Physics Research Section B: Beam Interactions with Materials and Atoms (2013).

[230] R. More, J. Spitznagel, Primary recoil spectra and subcascade effects in ion bombardment experiments, Radiation Effects. 60 (1982) 27-33.

[231] R.E. Stoller, The role of cascade energy and temperature in primary defect formation in iron, J. Nucl. Mater. 276 (2000) 22-32.

[232] H. Wiedersich, Effects of the primary recoil spectrum on long-range migration of defects, Radiation effects and defects in solids. 113 (1990) 97-107.

[233] L. Rehn, Production of freely-migrating defects, J. Nucl. Mater. 174 (1990) 144-150.

[234] S.S. Brenner, Tensile strength of whiskers, J. Appl. Phys. 27 (1956) 1484-1491.

[235] W.D. Nix, J.R. Greer, G. Feng, E.T. Lilleodden, Deformation at the nanometer and micrometer length scales: Effects of strain gradients and dislocation starvation, Thin Solid Films. 515 (2007) 3152-3157.

[236] T.A. Parthasarathy, S.I. Rao, D.M. Dimiduk, M.D. Uchic, D.R. Trinkle, Contribution to size effect of yield strength from the stochastics of dislocation source lengths in finite samples, Scr. Mater. 56 (2007) 313-316.

[237] J.L. Coze, Procurement of Pure Fe Metal and Fe-based Alloys with Controlled Chemical Alloying Element Contents and Microstructure: Final Report on Model Alloy Preparation. EFDA – Contract 06 – 1901 TW6 – TTMS 007- PUREFE (2007).

[238] P. Olsson, Ab initio study of interstitial migration in Fe–Cr alloys, J. Nucl. Mater. 386–388 (2009) 86-89.

[239] H. Takahashi, H. Kinoshita, S. Ohnuki, R. Nagasaki, F.A. Garner, D.S. Gelles, The influence of solute segregation on void swelling in Fe□Cr based alloys, J. Nucl. Mater. 155–157, Part 2 (1988) 908-911.

[240] S. Ohnuki, H. Takahashi, T. Takeyama, Void and precipitate structure in ion- and electron-irradiated ferritic alloys, J. Nucl. Mater. 122 (1984) 317-321.

[241] S.H. Babu, R. Rajaraman, G. Amarendra, R. Govindaraj, N.P. Lalla, A. Dasgupta, G. Bhalerao, C.S. Sundar, Dislocation driven chromium precipitation in Fe-9Cr binary alloy: a positron lifetime study, Philosophical Magazine (2012) 1-12.

[242] A.V. Ponomareva, A.V. Ruban, O.Y. Vekilova, S.I. Simak, I.A. Abrikosov, Effect of pressure of phase stability in Fe-Cr alloys, Phys. Rev. B. 84 (2011) 094422-1-094422-6.

[243] E. Wakai, A. Hishinuma, Y. Kato, H. Yano, S. Takaki, K. Abiko, Radiation-Induced α' Phase Formation on Dislocation Loops in Fe-Cr Alloys During Electron Irradiation, J Phys IV. 5 (1995) 277-286.

[244] S.J. Zinkle, Fusion materials science: Overview of challenges and recent progress, Phys Plasmas. 12 (2005) 058101.

[245] F. Romanelli, P. Barabaschi, D. Borba, G. Federici, L. Horton, R. Neu, D. Stork, H. Zohm, Fusion Electricity A roadmap to the realisation of fusion energy. EFDA Report (2013).

[246] D. Stork, P. Agostini, J.L. Boutard, D. Buckthorpe, E. Diegele, S.L. Dudarev, S. Gonzalez, A. Ibarra, C. Linsmeier, G. Marbach, B. Raj, M. Rieth, M. Rieth, M.Q. Tran, S.J. Zinkle, Assessment of the EU R&D Programme on DEMO Structural and High-Heat Flux Materials. EFDA(12)52/7.2 (2012) 187.

[247] F. Ericson, J. Schweitz, Micromechanical fracture strength of silicon, J. Appl. Phys. 68 (1990) 5840-5844.

[248] D. Terentyev, G. Bonny, C. Domain, G. Monnet, L. Malerba, Mechanisms of radiation strengthening in Fe–Cr alloys as revealed by atomistic studies, J. Nucl. Mater. (2013).